Proceedings of the 114th Annual Meeting of

The American Association of Variable Star Observers

Oregon Museum of Science and Industry
Portland, Oregon, United States
November 1-2, 2025

January 2026

ISBN 978-1-939538-77-2

The American Association of Variable Star Observers
185 Alewife Brook Parkway, Suite 410, Cambridge, MA 02138, USA

Proceedings of the AAVSO 114th Annual Meeting

Editor

Joyce A. Guzik

Los Alamos National Laboratory

Los Alamos, NM 87545, USA

The American Association of Variable Star Observers
185 Alewife Brook Parkway, Suite 410, Cambridge, MA 02138, USA

Proceedings of the AAVSO 114th Annual Meeting

Editor's Note

These articles were submitted as optional conference proceedings papers by participants of the 114th Annual Meeting of the AAVSO held November 1-2, 2025, at the Oregon Museum of Science and Industry, Portland, Oregon.

Eighteen articles were received, representing contributed oral and poster presentations. These articles have been edited but not peer reviewed. This proceedings volume also includes the abstracts for eleven additional invited and contributed talks and posters for which proceedings papers were not submitted.

Meeting abstracts were reviewed by a committee with members Joyce Guzik (chair), Tom Maccarone, Elizabeth Waagen, Kalée Tock, and Sebastián Otero, before being accepted for presentation at the meeting.

The full meeting schedule with program and links to abstracts can be found at https://www.aavso.org/114.

J.G. thanks Elizabeth Waagen for reviewing the draft of the entire proceedings volume and finding many items to correct.

We hope you enjoy reading this collection of articles and find inspiration for your own astronomy pursuits!

Proceedings of the AAVSO 114th Annual Meeting

Main entrance to the Oregon Museum of Science and Industry. Photograph courtesy M.O. Stevens. License.

Group Photo from 114th Annual Meeting; Photo credit: Robert Stephens

The American Association of Variable Star Observers
185 Alewife Brook Parkway, Suite 410, Cambridge, MA 02138, USA

Proceedings of the AAVSO 114th Annual Meeting

Table of Contents: Proceedings Papers

The American Association of Variable Star Observers
185 Alewife Brook Parkway, Suite 410, Cambridge, MA 02138, USA

Proceedings of the AAVSO 114th Annual Meeting

Table of Contents: Abstracts Only

The American Association of Variable Star Observers
185 Alewife Brook Parkway, Suite 410, Cambridge, MA 02138, USA

Radio Eyes on Variable Skies: Harnessing Archival Radio Data for AAVSO Research

Wayne F. Buck

Eastern Connecticut State University, 83 Windham St, Willimantic, CT 06226, USA;
buckw@easternct.edu

Subject Keywords

Radio astronomy, VLA, AAVSO 114th Annual Meeting

Abstract

I propose a closer collaboration between the AAVSO and radio astronomy community. Archival radio observations represent a powerful and underused resource for the AAVSO community. Incorporating these data can enhance the scientific value of AAVSO observations, expand member contributions into multi-wavelength astronomy, and foster closer collaboration with professional astronomers. In this way, AAVSO's established optical photometric capabilities can be paired with "radio eyes" to investigate the full range of physical processes driving variability in stars.

1. Introduction

The American Association of Variable Star Observers (AAVSO) has a long tradition of providing high-cadence, extended time-domain optical light curves of variable stars. These data have been invaluable for understanding stellar evolution, pulsation, magnetic activity, and mass loss, among others. Yet many of the same stars that AAVSO members observe optically are also detectable at radio wavelengths, where they reveal a complementary set of physical processes: magnetic reconnection in stellar flares, synchrotron jets in cataclysmic variables, thermal emission from nova ejecta, and maser emission from pulsating giants. These sources include cataclysmic variables, BL Lac AGNs, Algol-type binaries, flare stars, T Tauri stars, and X-ray binaries, among others.

Radio telescopes such as the Very Large Array (VLA), Atacama Large Millimeter/submillimeter Array (ALMA), and the Green Bank Telescope offer easily accessible radio archives containing radio detections of many variable stars already familiar to AAVSO observers. By cross-matching AAVSO targets with these surveys, members can extend their science from the optical into the radio regime—without the need to operate their own radio instruments.

These radio data have the potential to support development of targeted observing campaigns for long term optical monitoring, anticipate significant variable optical emissions, and provide opportunities for AAVSO members to explore science questions beyond the optical regime. In turn, AAVSO observations can support the selection and monitoring of targets by radio astronomers, partner with radio facilities to provide optical alerts to trigger opportunistic radio

observations and contribute to collaborative multiwavelength campaigns where optical and radio data are analyzed together.

For example, the Karl G. Jansky Very Large Array (VLA) in New Mexico has mapped large regions of the sky in several public surveys: the NRAO VLA Sky Survey (NVSS), Faint Images of the Radio Sky at Twenty-Centimeters (FIRST), and most recently the VLA Sky Survey (VLASS), which is currently in the process of conducting a fourth epoch of observations.

These surveys are fully archived and publicly accessible. By learning how to connect optical light curves from AAVSO with existing radio survey data, AAVSO members can expand their contributions to multiwavelength astronomy, test new hypotheses about stellar variability, and even help trigger future professional observing campaigns.

2. AAVSO-Radio Collaboration Strategies

In the following sub-sections, I describe three possible AAVSO-radio astronomy collaboration strategies. For each strategy, I reference current published work in the field that motivates and validates the strategy.

2.1 Optical monitoring of newly detected radio transients

Expand the scope of the current GCN/GRB alert program to include notices from radio telescopes on transients and other events that would benefit from optical follow up by AAVSO members. There are currently just a small number of radio observing programs that have the cadence and wide-field coverage to support time-domain data collection and timely multi-wavelength follow up. However, over the next few years many more (the Square Kilometer Array for instance) are coming online. These observing programs send out automated alerts, often machine readable. Now would be the time to prepare. An example of this growing time-domain capability in radio astronomy is Chen *et al*., 2025.

2.2 Optical monitoring of expected future radio transients

A program modeled on SNEWS that provides AAVSO members with target lists of sources that are currently radio quiet but are expected to experience a radio outburst and for which optical variability might serve as a precursor to such events. This is of growing interest in the radio astronomy community, motivated precisely because of the new time-domain observing capabilities that are coming online. An excellent review article is Murphy *et al.*, 2025.

2.3 Optical monitoring of historically and currently active radio sources

An ongoing observing campaign that focuses on sources that: a) are optically-variable, b) have significant radio emission, and c) for which ongoing photometric data can be of particular scientific use to the astrophysical community. A recent example can be found in Yiu *et al.*, 2024.

3. Science Objectives and Target Sources

Robust collaboration between AAVSO members and the radio astronomy community has the potential to make contributions to answer important outstanding science questions and the physics of a wide variety of astrophysical objects. Below I provide a short inventory of the object-types and the open science questions that optical photometry can support answering, as well as references to published work that underlines the value of the kind of data collected by AAVSO members.

3.1 AGNs/Quasar

Optical variability has been shown to be correlated with observed differences between radio and optical astrometry (I.e., positional variability) and thereby can help constrain AGN/quasar orientation and jet dynamics. For example: "Our results are consistent with the most positionally stable sources being blazars, a class of object in which the jet is oriented close to the line of sight and where relativistic beaming increases photometric variability and minimizes the projected offset between the optical and radio positions" (Lambert & Secrest, 2024).

According to the current model of AGN emission processes, optical EM originates as thermal emission from the accretion disk, while radio EM originates from jets. The lack of correlation between optical and radio variability supports this hypothesis. The evidence for this limitation of optical EM to the accretion disk is mixed, however. For example: "These results support the hypothesis that long-term optical variability in AGN is primarily governed by thermal emission from the accretion disk. Further investigations with larger samples are essential to refine these correlations and develop robust physical models integrating black hole properties, accretion disk physics, and multi-wavelength radiative transfer." (Jha *et al.,* 2025).

Our current understanding of the physical processes of AGNs – mass flows, mechanical, gravitational and radiation energy generation and how these interact over time – is limited. For an example, see Lin *et al.*, 2025.

3.2 Brown Dwarfs

Some brown dwarfs and other low mass stars emit in the radio and show correlated optical variability, but the mechanism is currently unknown. A richer set of optical photometry data can help constrain the possible mechanisms at work. For example: "Our data points to a likely association between radio and optical periodic variability in late-M/early-L dwarfs, although the underlying physical cause of this correlation remains unclear" (Harding *et al.*, 2013).

3.3 Flare Stars

The physical processes behind stellar flares and CMEs are poorly understood. A recent paper makes the case very succinctly: "Multiwavelength observations are crucial for understanding the physical processes of stellar flares and associated mass ejections, as different wavelengths probe

distinct aspects of magnetic energy release and plasma dynamics. Optical photometry captures continuum brightening and blackbody temperature evolution, tracing the heating of the lower atmosphere during flares" (Lu *et al.*, 2025).

3.4 Young Stellar Objects

YSOs are already a source of interest to the AAVSO. Long-term optical photometric monitoring of optically bright, radio-emitting YSOs could provide the accretion, rotational, magnetic, and disk-state context required to physically interpret radio variability and to identify the conditions under which radio emission is produced. For example: "We report the first detection of radio emission from V1298 Tau at different epochs using the JVLA. . . From a comparison with contemporary optical photometry, we found that the detected emission with the highest fluxes is located around a phase of minimum of the photospheric light curve" (Damasso *et al.*, 2025).

4. Conclusions

AAVSO members may not be aware that citizen science is an important part of radio astronomy. Indeed, the radio community provides citizen access to archival radio data and encourages citizen science proposals to gather new data from pointed observations on many radio telescopes. My intention here is to suggest that archival radio surveys offer a powerful, untapped resource for the AAVSO community. They allow members to go beyond optical light curves and explore radio counterparts of the very stars they have been monitoring for decades. Integrating radio survey data into AAVSO research will:

- Enhance the scientific return from existing AAVSO observations.
- Provide new opportunities for citizen science in the radio domain without requiring personal radio telescopes.
- Strengthen connections between amateur and professional astronomers through multiwavelength campaigns.

By "opening radio eyes" onto variable stars, AAVSO observers can help answer fundamental astrophysical questions, demonstrating once again the central role of the AAVSO in advancing variable star astronomy.

Acknowledgements

I wish to gratefully acknowledge the suggestions of Dr. Erik Carlson, University of Rhode Island, in the preparation of my presentation proposal and of the presentation itself. All errors, mistakes and infelicities are mine.

References

Chen, Y., Gaensler, B.M., Clarke, T., Peters, W., Polisensky, E., & Rose, K. 2025, *ApJ*, 987(2), 170.

Damasso, M., Morata, O., Kaur, S., Viganò, D., Melis, A., Murgia, M., Pilia, M., Lanza, A.F., Del Sordo, F., Antonietti, N. and Kansabanik, D. 2025, *A&A*, 696, A132.

Harding, Leon K., Gregg Hallinan, Richard P. Boyle, Aaron Golden, Navtej Singh, Brendan Sheehan, Robert T. Zavala, and Ray F. Butler. 2013, *ApJ*, 779(2), 101.

Jha, V.K., Bhattacharya, D. and Chand, H. 2025, arXiv preprint, arXiv:2508.06610.

Lin, J., Zheng, Z.Y., Ma, B., Long, L., Xie, Y., Lin, P., Lin, R. and Ji, X. 2025, *ApJS,* 281(2), 60.

Lu, H.P., Zhang, J.L., Tian, H., Zhang, L.Y., Chen, H.C., Zheng, J., Zhang, J.B., Wang, J.G., Inoue, S., Maehara, H. and Namekata, K. 2025, *ApJL*, 990(2), p. L32.

Murphy, T., & Kaplan, D.L. 2025, *PASA,* pp. 1-59.

Lambert, S. and Secrest, N.J. 2024, *A&A*, *684*, p. A93.

Yiu, T.W.H., Vedantham, H.K., Callingham, J. R., & Günther, M.N. 2024, *A&A*, 684, A3.

Have aCyg R: PEP Monitoring of Deneb

Tom Calderwood[1] and Erwin van Ballegoij[1,2]

[1]AAVSO, 185 Alewife Brook Parkway #410, Cambridge, MA, 02138, USA (tjc@cantordust.net); [2]KNWS Werkgroep Veranderlijke Sterren, De Rogge 6, 5384 XD Heesch, The Netherlands

Subject Keywords

Photometry, PEP; Alpha Cygni Variables; stars: individual (Deneb)

Abstract

Alpha Cygni variables generally exhibit photometric variations of only 0.1 magnitude or less. A successful photometry campaign with multiple observers must achieve high internal consistency with low uncertainties. With preliminary data on Deneb, we show that the AAVSO Photoelectic Photometry (PEP) group can produce such data.

1. Introduction

Deneb is among the most studied of the Cygni variables, but its great brightness and small range of variation make it a challenging photometric target. Old-school PEP is well suited to the study of this star. During the 2025 apparition (June to October) nine AAVSO PEP observers obtained 154 V band data points.

2. Observations

2.1 Method

The AAVSO PEP group operates Optec SSP photometers almost exclusively. For this project the model SSP-3 was used, its photodiode sensor being well suited to such a bright target. Telescopes of aperture 8 to 12 inches were employed. The brightness of Deneb was measured differentially in respect to HD 199629, an A0 giant. The PEP observing sequence typically samples the program star three times, each time bracketed by samples of the comparison star. The reduced magnitude is taken from the mean of the three differential measurements.

Historically, AAVSO PEP has reported uncertainties as the standard error of the samples. That metric overstates the precision achieved. In this study those uncertainties have been multiplied by 1.73, approximately converting the standard error to a standard deviation of the sample.

The comparison star was chosen to minimize transformation, the Δ(B-V) being 0.070 (Mermilliod et al., 1997). Observers would typically apply transformations of only a few millimagnitudes. Alpha Cygni stars undergo only slight color changes so the transforms were based upon the catalog BV colors rather than two-band measurements. The comparison star is 5° away from Deneb so an extinction correction was applied. Some observers measured nightly extinction,

while others used a fixed estimate. The extinction corrections are not readily available from most observers, but the second most prolific observer (32 data points) applied median absolute corrections of 0.006.

2.2 Results

Figure 1 presents the 2025 PEP light curve with the expanded uncertainties. The median uncertainty was 0.005 magnitudes. On 41 nights there were 2, 3, or 4 measurements reported. This permitted 107 same-night pairwise comparisons between observations. In 96 cases, the pairs agreed within their uncertainties for a 90% rate of consistency. In only two cases were both magnitudes reported by the same observer.

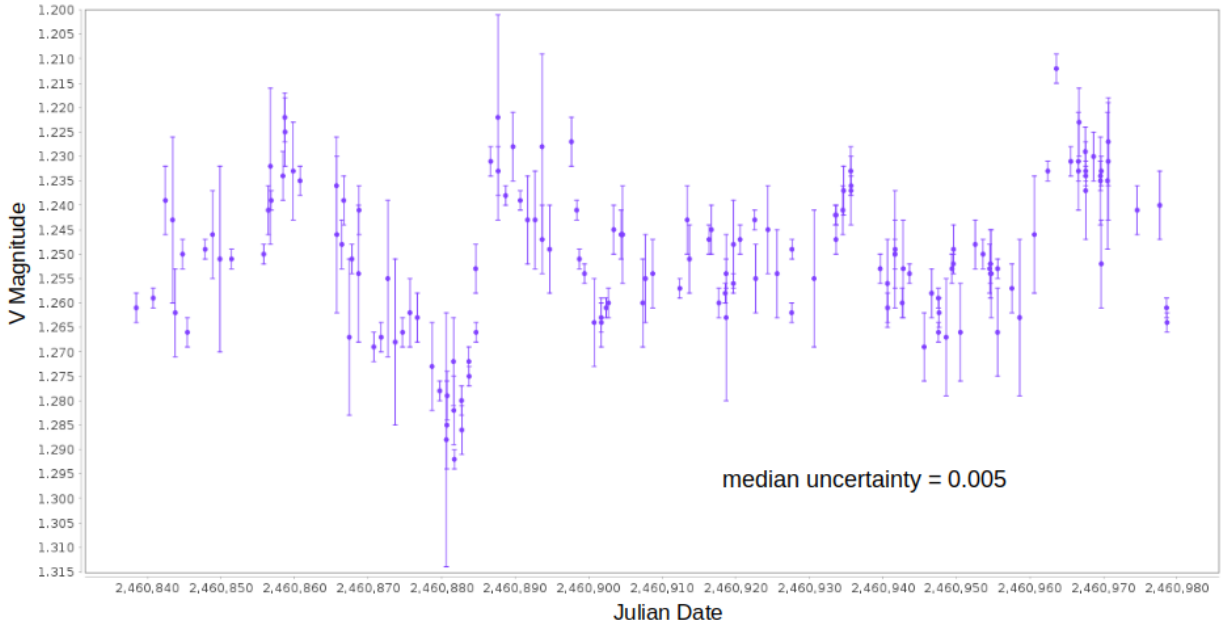

Figure 1. Deneb V band light curve, June-October 2025.

2.3 New uncertainties

With some admittedly limited data it is possible to illustrate that the new uncertainty metric is appropriate. The AAVSO International Database (Kloppenborg, 2025) contains some stars that were once thought variable but are now considered constant. Such stars, for which data may still be submitted, become convenient test targets. Figure 2 shows a light curve for HD 127700 with 27 data points from four observers. The weighted mean of the observations (V=4.244) is marked with the dashed line. Only four data points fail to have their uncertainties straddle the mean, missing by 2, 10, 14, and 18 mmag. The worst of these is known to have been acquired on a night with challenging sky conditions; the other large outliers are still under investigation.

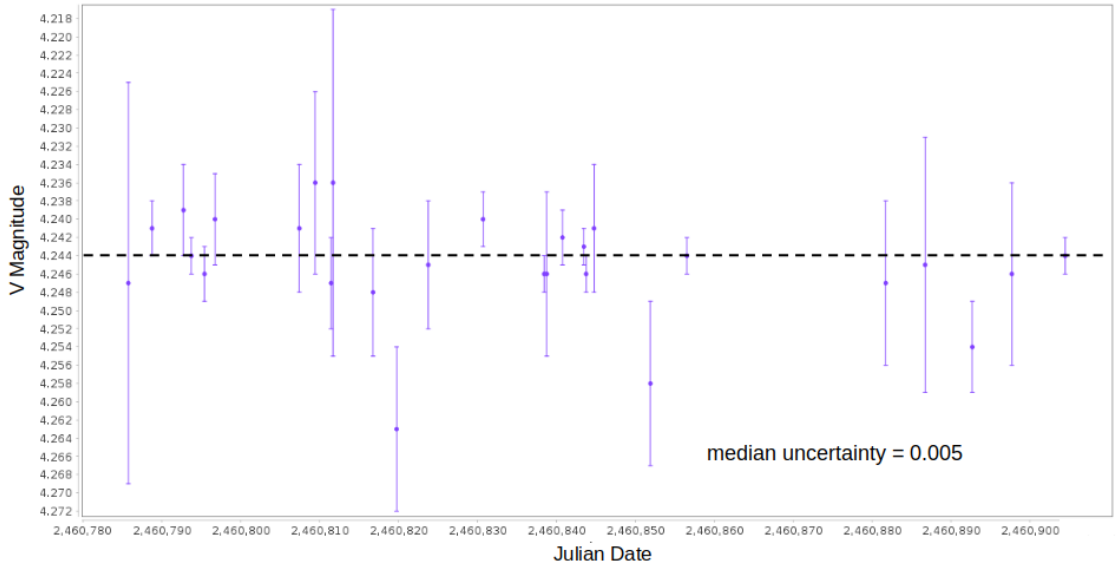

Figure 2. V band light curve of constant star HD 127700.

The comparison (HD 136726) was chosen for its very close BV color match. Some observers took data only in V band, others took BV data and inferred the color difference. The comparison is about 5° from the target star; extinction was compensated for.

Light curves like this can be used to diagnose problematic sources of photometry. We have already employed such a curve to identify an observer reporting systematically too-bright magnitudes. Constant stars can be found in the International Variable Star Index (Watson et al., 2006) by searching for "non-variables." It would be instructive for CCD observers to undertake an exercise like this!

3. Conclusions

The consistency and precision of PEP make it well-suited to the study of low amplitude variables by multiple observers. We plan a multi-year project to follow Deneb and other alpha Cygni stars. In the future AAVSO PEP will make standard deviation of the sample the default metric for uncertainty.

Acknowledgements

We gratefully acknowledge support from the late Gerald Persha, founder of Optec and designer of the SSP photometers.

References

Kloppenborg, B. 2025, https://aavso.org

Mermilliod, J-C., Hauck, B., Mermilliod, M. 1997, A&AS, 124, 349 (https://gcpd.physics.muni.cz)

Watson, C., Henden, A., Price, A. 2006, SASS, 25, 47

Turning Attention to Wolf Rayet Stars

Stephen P. Cook

Project Worldview, 910 Oak Terrace Dr., Prescott, AZ 86301 USA; scook@projectworldview.org

Subject Keywords

AAVSO International Database; Wolf Rayet stars; Eclipsing Binaries; Photometry, CCD

Abstract

Other than the thousands of visual observations of several Wolf Rayet (WR) stars made by legendary Royal Astronomical Society of New Zealand and AAVSO observer Albert Jones (JA) between 1997 and 2011, citizen scientist observers have seemingly neglected these highly luminous, extremely massive, evolutionary short-lived, and relatively rare objects. Beginning in August 2025, the author sought to help rectify that. Intrigued by the obvious periodicity evident in several light curves plotted from JA observations, he began by subjecting them to period search analysis. With the possible exception of dust obscuration "eclipse" notable in CV Ser, he was unable to link periods the DFT-based routine found strong signals for with known binary star orbital periods. He followed that with 2.5 months (August—October 2025) of V filter photometry of 22 WR stars in an effort to extend Jones' style monitoring with higher precision data. Whether due to his much shorter baseline, or to his targets' inactivity, other than for V5097 Sgr he saw no large amplitude, seemingly periodic variations. The magnitudes of many of the WRs observed were confined within an essentially constant 0.1 magnitude range consistent with a VSX listing. This excludes V460 Sct and WR 142, which exhibited variations far exceeding the listed VSX V magnitude range. Likewise, both V460 Sct and V4578 Sgr were seen at average magnitude far brighter than VSX average values, the latter by 0.8 magnitudes. Finally, the author determined at least two times of minima (TOM) for each of the three northern hemisphere WR stars that are also eclipsing binaries. These data are especially important for CX Cep, given its sparsely populated O-C diagram and observational challenges it presents.

1. Introduction

Wolf-Rayet stars are the descendants of OB stars that have lost their hydrogen envelopes and are burning helium in their cores prior to exploding as supernovae.How'd they lose their hydrogen envelopes? Either through binary interactions or through strong stellar winds coupled with episodic mass loss. Some WRs lose one solar mass every 100,000 years—nearly a billion times the rate at which our Sun loses mass via the solar wind.

Inspired by 1) James Webb Space Telescope (JWST) images of rapidly expanding, concentric dust rings around binary star WR 140 (= V1687 Cyg,) accompanied by the suggestion that the carbon in our bodies might ultimately come from such a long ago source, and 2) a *Wikipedia* article about WR 104 (=V5097 Sgr) and speculations about how its end-of-life core collapse supernova or

gamma ray burst could conceivably affect life on Earth, I began investigating the citizen scientist contribution to understanding these extraordinarily hot, luminous and massive objects. A search of *JAAVSO* using "Wolf-Rayet stars" and "variable star research" netted just two papers—the most recent from 2017. While the AAVSO International Database –henceforth referred to as AAVSO DB (Kloppenborg 2025) —includes tens of thousands of WR observations, I found many of these are of a handful of stars. And that several bright objects in the 227-member 2001 VIIth catalogue of galactic WRs (van der Hucht 2001) —an update of the 1981 catalogue that introduced "WR" designations— have none. And that the impressive log of visual observations of WR stars made by Albert Jones was generally not being added to after his death in 2013.

While my own observations of such objects began in 1968 with challenging visual observations of the eclipsing binary CQ Cep, I too had neglected them. Vowing to fix that, I put together a list of 22 WR stars—see Table 1—roughly divided between those classed WN and WC, depending on whether their spectra are dominated by emission lines of ionized nitrogen or carbon—and recently began CCD V filter photometry of them. I anticipated documenting these stars' mundane doings and perhaps being lucky enough to see some extraordinary ones. Such as capturing dust obscuration events—like the 2017 *JAAVSO* report (Stubbings and Williams 2017) of a three-magnitude fading of (WC9 type) WR 76, previously thought to be non-variable. And perhaps helping to answer several questions.

"Can long-term monitoring uncover periodicity associated with binary star orbital periods?" "And, where something else—pulsation— is the source of light variation, might a few nights of observations detect this?" Noteworthy in this regard: the Canadian space telescope finding a 5.3-day period for QR Sge (Chene and Moffat 2010). While the Variable Star Index (VSX 2025) and General Catalogue of Variable Stars (GCVS 2025) catalogue entries typically depict WR stars with small light variation ranges and—if cited at all—short periods, AAVSO DB based light curve plots of JA observations document larger ranges, in some cases a decreasing amplitude, and suggest longer periods. The key question here: "Are they real?" Skeptics may link seeming periods to seasonal spacing of observations—even to full moon interference—and attribute decreases in amplitude to changes in Jones' eyesight.

Other questions: "Although WC stars are hotter, more evolutionarily advanced, and—as carbon dust ejectors—more 'glamorous' than WN stars, are the latter more optically variable, as one study (Fahed et al. 2009) found?" "Are the WR stars at the lower temperature end of the classification scheme (WC9 or WN8) more likely to show optical variability than their hotter (WC5 or WN5) relatives?" And are the hottest, most evolutionary advanced (and rarest with only a handful known in our Galaxy) of the WR stars—namely the WO stars, with prominent lines of ionized oxygen—especially active? Their hottest members—such as WR 142 listed in Table 1—have surface temperatures of around 200,000 K.

Besides intrinsic variations, study of the extrinsic variations in the four WRs that are also EBs (see Table 2) are critically important. Recognizing this, and noting the relative sparseness of TOMs in O-C diagrams of these objects, one wonders, "Why have citizen scientists seemingly neglected these objects?"

Observations of eclipsing binary stars (EBs) represent the best way to get stellar masses. Thus, Lowell Observatory astronomers recently announced (Schindler 2025) that they'd determined that one of those four objects—the southern hemisphere member of the quartet known as NGC3603 A1— is perhaps the most massive binary in the Galaxy. It consists of two WR stars—one of 93.3 solar masses, the other with 70.4 solar masses.Perhaps the most notable AAVSO-linked contribution to observing an eclipsing WR came with "BVRI Photometry of the CX Cep system" (Hutton, Henden, and Terrell 2009). The detailed light curve it reported was used in Wilson-DeVinney model-based characterization that depicted the system as consisting of a 36.8 solar mass O5 star and a 25.4 WN5 star. Sadly, since then, before my own observations, only one TOM has been reported for CX Cep: for a 2015 eclipse based on 66 observations from F. Agerer. (Hubscher 2017). Unfortunately, this TOM is highly uncertain given the reported 0.0362-day error.

Table 1. Wolf Rayet Stars Observed by S. Cook, 2025

Star name	WR#	Sp Type	# obs	Star name	WR#	Sp Type	# obs
V1402 Aql	123	WN8	48	V1035 Sco	86	WC7	61
V1485 Aql	121	WC9	52	WR 88 Sco	88	WC9	55
CQ Cep	155	WN5.5	162	V460 Sct	116	WN9	78
CX Cep	151	WN5	226	CV Ser	113	WC8	125
NSV 25991 Cep	156	WN8	37	QR Sge	124	WN8	64
V444 Cyg	139	WN5.5	180	V4072 Sgr	103	WC9	63
V1042 Cyg	135	WC8	46	V4578 Sgr	105	WN8	112
V2180 Cyg	130	WN8	47	V 5097 Sgr	104	WC9	111
V2183 Cyg	141	WN5	76	V5101 Sgr	106	WC9	72
V2547 Cyg	143	WC5	50	V5976 Sgr	107	WN8	79
WR142 Cyg	142	WO2	75	V378 Vul	125	WC7	69

Table 2. Wolf Rayet Stars that are also Eclipsing Binaries, data from VSX unless noted

Star name	V mag range	Var type	Epoch, 2400000+	Period, day	Secondary min V mag range
CQ Cep	8.63-9.12	EB/DM/WR	32456.6654	1.64124475	none
CX Cep	12.09-12.24	EB/WR	44451.4234	2.126897	12.09-12.16
V444 Cyg	7.92-8.22	EA/WR	41164.348	4.2124528	7.92-8.06
NGC 3603 A1	11.12-11.57	EA	50513.52	3.77265	none

Notes: Epoch and period listed in Table 2 are ephemeris elements from Krakow "O-C and Up-To-Date Linear Elements of Eclipsing Binaries" (Kreiner 2004) except for NGC 3603 A1. While the most observable WRs that are EBs are listed here, there are a few others, and rumors of at least one more.

Finally, let's recognize that the physical nature of WR stars, their typical large distances, surrounding nebulae, and their often dusty local environment, can limit what citizen scientists working in optical wavelengths can contribute to their study. Such work is hampered by WR peak energy output in the far ultra-violet, by local absorption / surrounding dust reradiating in the infra-red, by typical thousands of light years' worth of interstellar dust dimming their light by

several magnitudes and heavily reddening it. Often the space-based telescopes that professionals use to make X-ray, UV and infrared observations are better suited for observing WR stars. In the last five years the infrared sensitive JWST, well-suited for investigating WR stars, has boosted interest in these objects with associated press releases and pretty, sometimes dynamic, pictures and videos. Certainly, this rekindled my interest and may generally spur citizen scientist WR star observations.

2. Methods

2.1 Period Search Analysis

This was conducted for a handful of stars using a Discrete Fourier Transform (DFT) based period search analysis program (Belserene 1988).

2.2 Photometry

For a total of fifty nights between JD 2460904—2460978, I did CCD differential photometry on the twenty-two WR stars listed in Table 1—collecting a total of 1888 images. I used a 130 mm f/5 reflector equipped with a ZWO ASI533 CMOS imager and V filter, working at a 5300 ft elevation suburban sky site in Prescott, AZ. Typically at least three images of a star were made on a given night, separated by roughly 60 seconds. Four or five images, rather than three, were typically made for fainter stars. Many more images were taken for the three northern hemisphere WRs that are EBs as part of time series photometry spanning many hours, with images spaced typically three minutes apart. All images were 30 second exposures. While the images were created using ZWO ASI Studio deep sky imaging software, they were measured individually using Astro Image J 5.3 software.

3. Results—Summary

3.1 Period Search Analysis

My period search analysis of 3185 of JA observations of DI Cru, V1035 Sco, CV Ser, and V1485 Aql most notably produced periods of 27.316 days for CV Ser and 340.15 days for V1485 Aql. The former is remarkably close to the 29.7 day known orbital period—but also suggests a possible full moon effect. Likewise, is the period the software found for V1485 Aql (with a signal of very high strength) real, or just due to seasonal spacing of observations? Attempts at performing such analysis for my observations—most notably for QR Sge in search of the reported 5.3-day period—found no strong signals.

3.2 Photometry

The stars observed, spectral type and total number of observations are listed in Table 1. Other than for V5097 Sgr, where I recorded V magnitude variation of nearly two magnitudes in seeming periodic fashion, none of the stars exhibited more than a 0.5 V magnitude variation. Many varied

little more than 0.1 V magnitude. But there were a few exceptions, and one star, CV Ser, surprised by being remarkably constant—with no dust obscurations observed at predicted times despite making additional observations searching for them. For V1485 Aql, where previous analysis found that strong signal for a 340-day periodicity in JA observations, I found seemingly random variation of less than 0.2 V magnitudes.

I did see variations in V460 Sct and WR 142 far exceeding listed VSX V magnitude ranges. For details, see the comments following their light curves in the next section. My observations of V460 Sct put it at an average brightness (of 12.96 V) — 0.53 magnitude brighter than the (13.49 V) VSX average value. The V4578 Sgr average magnitude of 12.212 V I found, based on 112 images gathered on 30 nights of observations, exceeded the VSX value by an even greater value. (Note its uncertainty: associated standard deviation = 0.053 and standard deviation divided by the square root of the number of images = 0.005.) This value is 0.758 V magnitudes brighter than VSX listed value of 12.97 V (based on 12.92 to 13.02 V magnitude range.) Given that DR9 for APASS lists it at V=12.24, perhaps the hypothesis that the VSX value is in error is a better one than that V4578 Sgr has brightened substantially?

Other average magnitude value discrepancies, such finding QR Sge 0.419 magnitudes brighter than VSX suggested average, and V2547 Cyg 0.30 magnitudes fainter than its DR9 for APASS listed value of V=11.27, are small enough to be explained by hypothesizing use of poorly determined comparison star magnitudes.

For the WRs that are also EBs, my observations determined two TOM for primary eclipses of CQ Cep, two TOM for primary eclipses of CX Cep, two TOM for primary eclipses of V444 Cyg, and one TOM for a secondary eclipse of V444 Cyg. Of these seven TOMs, getting the ones for CX Cep was especially challenging. Based on 17 images made on JD2460955, an out of eclipse V magnitude of 12.204 (with standard deviation of 0.0302 and standard deviation divided by the square root of the number of images = 0.007) was computed. Comparing that with data in Figure 4 and Figure 5 suggests an amplitude around 0.10 V magnitude, less than the 0.15 V given in the VSX but consistent with what Hutton, Henden, and Terrell found. See the light curves in section 4.2 and section 5.2 for comments and additional discussion.

Details of all my observations, including comparison and check stars used and their instrumental magnitudes, can be found in the AAVSO DB under observer code CK. Unlike what I sometimes do in submitting eclipsing binary star observations where I might combine analysis of multiple images and report “normal points”, for WR stars I have reported only my raw observations. But to highlight a few stars of particular interest—and help draw out the signal from the noise—in figures that follow I have used the raw observations to produce normal points, listing them in tables and depicting them in light curves.

4. Results and Comments: Normal Point Based Light Curves for Stars of Interest

4.1 For WR stars showing Intrinsic Variations

S. Cook observations of V5097 Sgr

		uncertainty			uncertainty
JD	Ave mag	Std dev/ sqrt N	JD	Ave mag	Std dev/ sqrt N
904.7052	12.913	0.04	950.6146	13.623	0.052
906.7058	12.861	0.017	952.6511	13.878	0.064
908.6453	12.784	0.05	953.6163	14.152	0.044
914.6578	13.028	0.011	954.6022	13.871	0.049
917.7152	12.92	0.008	955.6255	13.958	0.034
919.6319	12.84	0.025	956.6089	13.871	0.049
924.6243	12.713	0.022	957.5962	13.999	0.031
927.6255	12.669	0.015	960.6504	13.432	0.037
928.7218	12.631	0.029	961.6245	13.319	0.027
932.6227	12.713	0.018	963.6017	13.138	0.008
934.6279	12.639	0.02	965.5934	13.102	0.021
938.6395	12.67	0.012	967.6016	13.196	0.02
942.6786	12.678	0.009	971.5837	13.199	0.014
945.6581	12.905	0.019	973.578	12.93	0.019
949.6079	13.536	0.058	978.5711	13.026	0.023

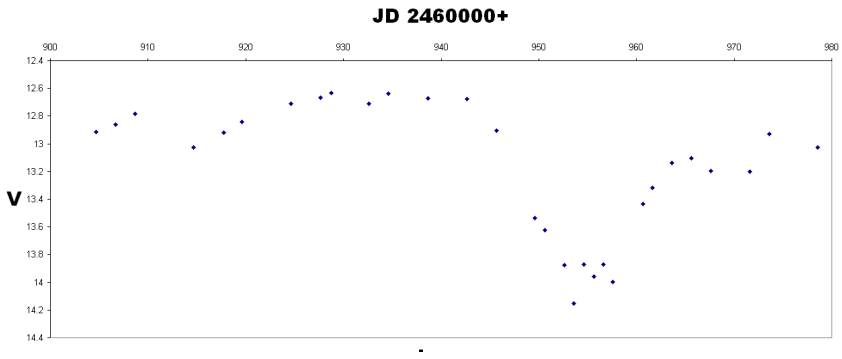

Figure 1. Observations of V5097 Sgr, V magnitude vs. JD date

***Comment**:* The 111 raw observations of mine found in the AAVSO DB have been used to create the 30 normal points listed above and plotted in the light curve. V magnitudes range from 12.631 to 14.152— values which span a significant part of the 12.6 to <14.8 range listed in the VSX. The periodicity hinted at in the light curve, which spans 74 days, can be evaluated in terms of a reported 241.5-day orbital period. And the minimum recorded around JD 2460953.6 conceivably interpreted as a dust obscuration event associated with the WC9 member of this system.

This data point was obtained from averaging fluxes measured on five images that spanned five minutes. It represents an increase of 0.209 magnitude from the previous night's value and is 0.270 magnitude brighter than the following night's brightness— a flux change of roughly 25%. This represents a significant increase followed by decrease in the star's optical region energy output (centered at around 5000 Angstroms = 500 x 10^{-9} m = 500 nm wavelength) in a short (one day) time. One wonders what happened to the star's overall energy during this outburst? Note, for surface temperature of 200,000 K, according to Wien's Law (assuming black body radiators) given in equation (1)

$$\lambda_{Peak} = 2.878 \times 10^{7} \text{ Angstroms deg K / Ts} \qquad (1)$$

WR 142's peak output would occur around 144 Angstroms = 14.4 nm. This is so far in the extreme short wavelength ultra-violet that it approaches the 10 nm beginning of the x-ray region of the electromagnetic spectrum. Of course, reddening by interstellar dust will shift it back toward the optical region a bit.

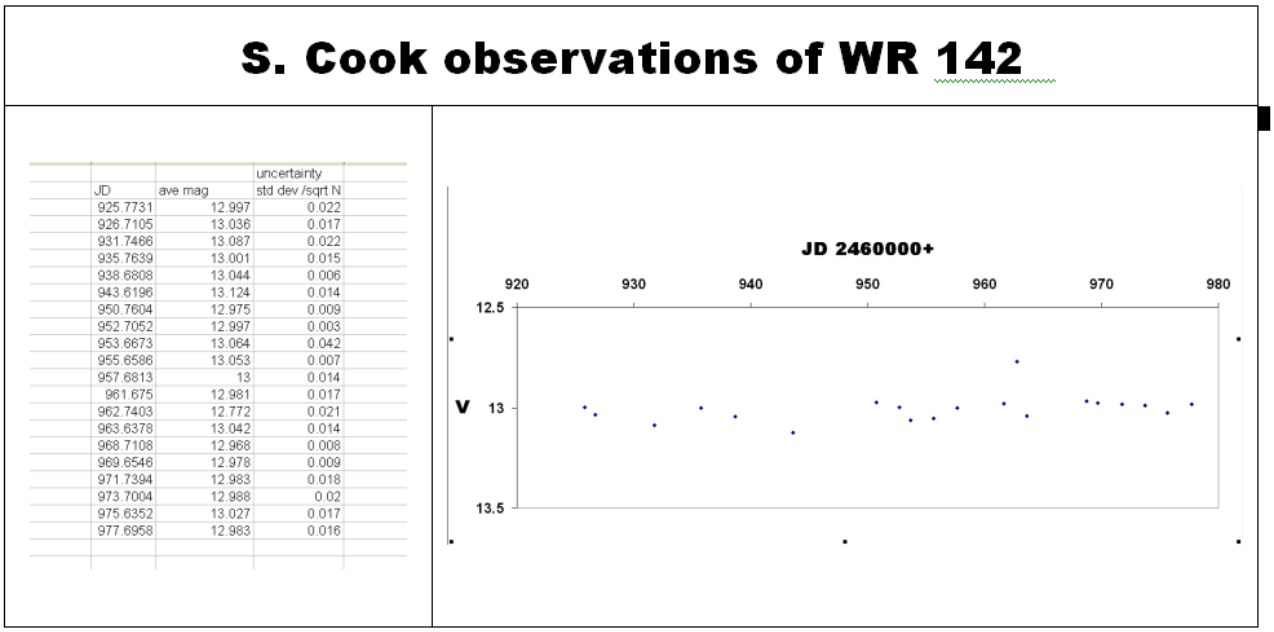

	JD	ave mag	uncertainty std dev /sqrt N
	925.7731	12.997	0.022
	926.7105	13.036	0.017
	931.7466	13.087	0.022
	935.7639	13.001	0.015
	938.6808	13.044	0.006
	943.6196	13.124	0.014
	950.7604	12.975	0.009
	952.7052	12.997	0.003
	953.6673	13.064	0.042
	955.6586	13.053	0.007
	957.6813	13	0.014
	961.675	12.981	0.017
	962.7403	12.772	0.021
	963.6378	13.042	0.014
	968.7108	12.968	0.008
	969.6546	12.978	0.009
	971.7394	12.983	0.018
	973.7004	12.988	0.02
	975.6352	13.027	0.017
	977.6958	12.983	0.016

Figure 2. Observations of WR 142, V magnitude vs. JD date

Comment: The 75 raw observations of mine found in the AAVSO DB have been used to create the 20 normal points listed above and plotted in the light curve. For 19 of the 20 nights represented, it shows the WR 142 V magnitude confined to a range between 12.968 and 13.124. Note this 0.156 V magnitude range is over five times greater than the 12.96 to 12.99 or 0.03 range listed in VSX. But of more interest—and what stands out in the figure—is the 12.772 V magnitude recorded at JD 2460962.7403.

S. Cook observations of V460 Sct

JD	ave mag	uncertainty std dev /sqrt N
924.6525	12.792	0.046
928.744	12.996	0.01
930.6554	12.823	0.024
934.6139	12.855	0.005
938.6506	12.938	0.027
941.6121	12.885	0.017
945.6675	13.022	0.021
949.6138	12.983	0.027
952.6441	12.913	0.035
953.6373	13.031	0.031
954.6085	12.853	0.005
955.6363	12.83	0.014
956.6125	13.164	0.022
957.6067	12.97	0.029
960.6446	12.853	0.033
961.6372	12.768	0.029
963.6125	12.849	0.021
967.6132	12.811	0.019
971.5969	12.835	0.021
976.5682	12.853	0.014
978.5826	12.756	0.019

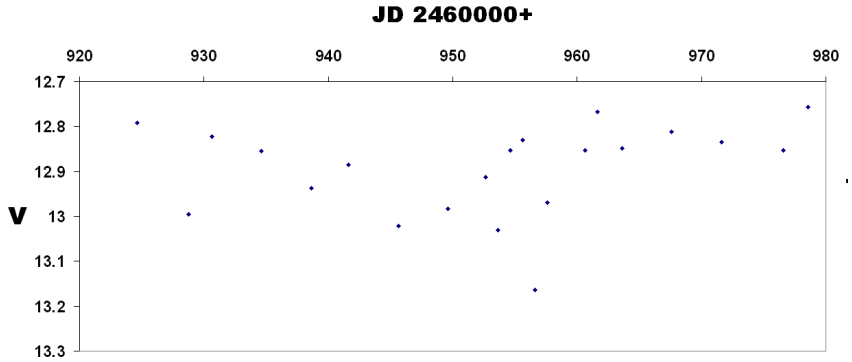

Figure 3. Observations of V460 Sct, V magnitude vs. JD date

Comment: The 78 raw observations of mine found in the AAVSO DB have been used to create the 21 normal points listed above and plotted in the light curve. The extremes values of 13.164 (with uncertainty 0.022) on 24060956 and 12.756 (with uncertainty 0.019) were each based on averaging fluxes measured on four images. They define a range of 0.408 V magnitude—nearly twice the (from 13.38 to 13.60 V) 0.22 V magnitude range listed in VSX. Note they also put the star at an average brightness of (12.96 V) that's 0.53 magnitude brighter than the (13.49 V) VSX average value. Even so, I recorded it fainter than did observer HMB on June 1, 2023 / JD2460096.8 in observations reported to the AAVSO DB. Those 40 listed V observations covered 3.46 hours and confined it within a 12.777 to 12.838 V magnitude range.

4.2 For WR and Eclipsing Binary CX Cep

S. Cook observations of CX Cep

JD	Ave mag	Uncertainty std dev /sqrt N
928.614	12.222	0.025
928.622	12.233	0.009
928.633	12.241	0.011
928.642	12.243	0.015
928.649	12.238	0.021
928.655	12.236	0.01
928.665	12.242	0.016
928.674	12.248	0.017
928.686	12.254	0.009
928.701	12.266	0.011
928.710	12.296	0.019
928.723	12.295	0.015
928.734	12.302	0.013
928.748	12.300	0.011
928.764	12.300	0.011
928.778	12.296	0.024
928.785	12.297	0.009
928.791	12.294	0.018
928.795	12.289	0.03
928.805	12.267	0.026
928.814	12.253	0.013
928.827	12.199	0.047

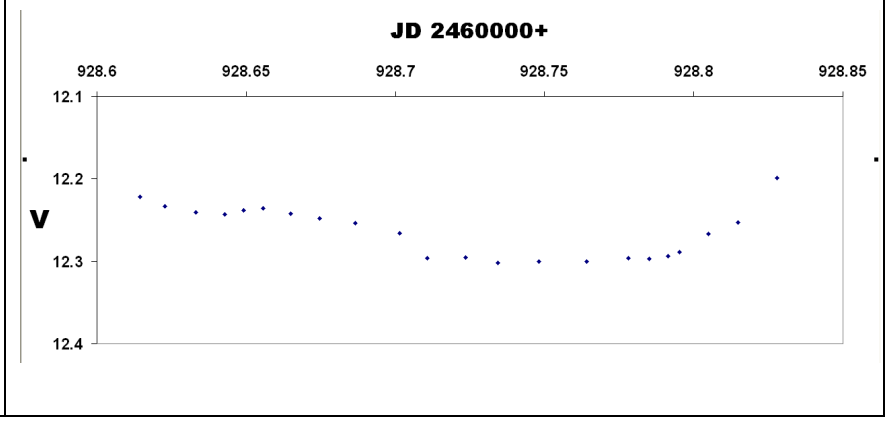

Figure 4. CX Cep V magnitude vs. time on JD day 2460928 from phased analysis

Comment: The 126 raw observations of mine found in the AAVSO DB for dates JD 2460928, JD 2460930, JD 2460960, and JD2460962 have been phased using period 2.126907 days to place all of them as if they were made on JD 2460928 and used to create the 22 normal points listed above and plotted in the light curve. While the mean error associated with the TOM determined using the Kwee-van Woerden method is a respectable —given the challenges that observing this system poses as discussed by Hutton, Henden, and Terrell—0.0027 days, the minimum pictured in the above light curve looks much "flatter" than the one they present. The "pieced together" (from four nights of observations) nature of that may be responsible, or its intrinsic variations, which Hutton, Henden, and Terrell put at the 0.02 V magnitude level, may be the culprit.

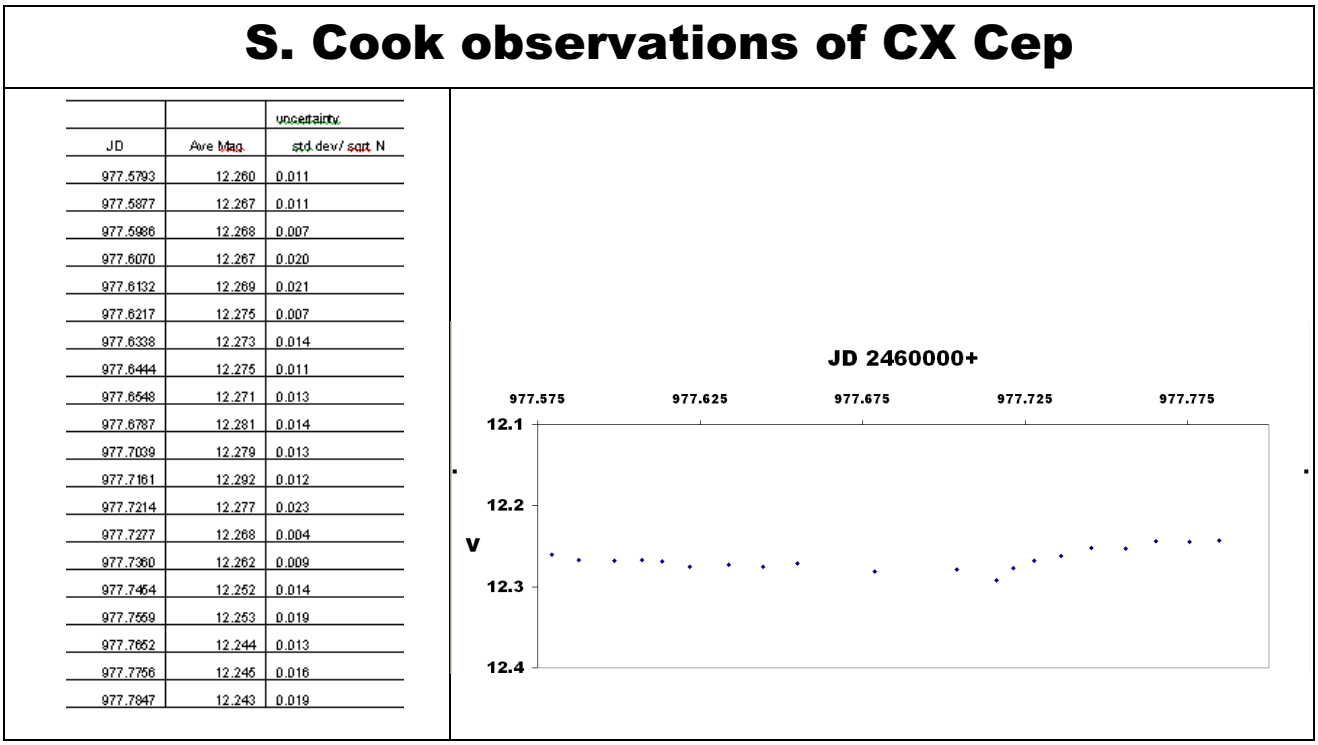

JD	Ave Mag	uncertainty std dev/ sqrt N
977.5793	12.260	0.011
977.5877	12.267	0.011
977.5986	12.268	0.007
977.6070	12.267	0.020
977.6132	12.269	0.021
977.6217	12.275	0.007
977.6338	12.273	0.014
977.6444	12.275	0.011
977.6548	12.271	0.013
977.6787	12.281	0.014
977.7039	12.279	0.013
977.7161	12.292	0.012
977.7214	12.277	0.023
977.7277	12.268	0.004
977.7360	12.262	0.009
977.7464	12.252	0.014
977.7569	12.253	0.019
977.7652	12.244	0.013
977.7756	12.245	0.016
977.7847	12.243	0.019

Figure 5. CX Cep V magnitude vs. time on JD day 2460977

Comment: The 83 raw observations of mine found in the AAVSO DB for this JD 2460977 date have been used to create the 20 normal points listed above and plotted in the light curve. The mean error associated with the TOM determined using the Kwee-van Woerden method is 0.0024 day and the light curve—in contrast to the Figure 4 one—looks more like the one provided by Hutton, Henden, and Terrell. Note both Figure 4 and Figure 5 light curves show the slight asymmetry—where the coming out of eclipse side is slightly brighter than the going into eclipse side—that Hutton, Henden, and Terrell reported.

5. Followup / Suggestions for Future Work / Conclusions

5.1 Monitoring Intrinsic Activity in WR stars

While some may conclude that my 2.5 months of rather intensive monitoring of 22 WRs produced nothing particularly exciting or unexpected, I disagree. What I did see and described above (and in what follows) provides motivation enough for me to plan on repeating it in the future. And what I didn't see —namely VSX reported large V magnitude ranges for objects such as V5101 Sgr (3.3 mag. range) and V4026 Sgr (1.5 mag. range) —spurs me to keep watching.

I believe my observations established that the stars whose light curves are presented in section 4.1—namely V460 Sct, V5097 Sgr and WR 142 —especially warrant observation. The last two are members of a surprising number of WR stars that have their own Wikipedia articles—many of them surprisingly detailed and well-referenced. While the one for V5097 Sgr—found under its WR 104 designation—refers to the expectation that it will "within the next few hundred thousand years…experience a core collapse supernova," the one for WR 142 reports "it is estimated to

explode as a supernova in approximately 2,000 years." Knowing how short 2,000 years is on stellar evolution time scales and of the uncertainties involved, that prediction is enough to get me to keep watching WR 142. Also knowing, from Figure 2, that it's currently shows signs of being restless provides additional motivation.

In general, I urge citizen scientists to rectify their seeming neglect of WR stars. Observing them offers both the exciting potential for making observations important to documenting catastrophic explosions waiting to happen, and the opportunity to contribute to answering the questions I posed in the Introduction.

In particular, my observations of WC9 star V5097 Sgr and WN9 star V460 Sct seem to reinforce the suggestion in one of those questions that WR stars at the cooler end of the WR classification temperature are more optically active than hotter WC and WN stars. And my observations of WO2 star WR 142 reinforce the suggestion (in another question) that the very hottest WR stars might be very active.

5.2 Observations of WRs that are also Eclipsing Binaries

The seven TOMs referred to in section 3.2 will be published in an upcoming JAAVSO paper such as previous TOM of EBs lists: (Cook 2023) and (Cook 2025).

Mass transfer by WRs that are members of binary star systems drives orbital period change. For EBs, the rate of that change, commonly referred to as P dot, is gauged by fitting a parabola through the points in a O-C diagram. Consider CX Cep in this regard.

Evidence exists that the period of CX Cep is changing: Based on their observations, Hutton, Henden, and Terrell concluded in 2009 that a 2.126891-day period provided a better linear equation value (on which to base future ephemeris predictions on) than the 2.126870-day period published in a 1982 paper. Likewise, my own 2025 TOMs suggest that a still slightly larger value of 2.126932 days now works better. It would be nice to determine P dot for CX Cep from its O-C diagram, but sadly the existing database is not sufficient to do this: more TOMs over the next few years are needed.

In general, observations to determine TOMs for WRs that are also EBs are needed to both maintain up to date ephemeris elements for predicting future TOM and for avoiding gaps in O-C diagrams.

References

Belserene, E. P. 1988 Sky & Telescope, September 1988, p. 288

Chene, A. and Moffat, A. 2010 Proceedings IAU Symposium, No. 272

Cook, S. 2023, JAAVSO 51, #1, pp. 138-140

Cook, S. 2025, JAAVSO 53, #1, pp. 61-65

Fahed, R., et al. 2009, Mon. Not. Royal Astron. Soc. 392, p. 376

GCVS 2025 / General Catalogue of Variable Stars https://sai.msu.su/gcvs/gcvs

Hubscher, J. 2017, Inf Bull Var Stars 62, #6196, January 20, 2017, p. 11

Hutton, K., Henden, A. and Terrell, D. 2009, Publ. Astron. Soc. Pac. 121, pp. 708-715

Kloppenborg, B. AAVSO, 2025 observations from the AAVSO International Database, http://www.aavso.org/

Kreiner, J. M. 2004, Acta Astron. 54, p. 207, https://www.as.up.krakow.pl/ephem

Kwee, K. K., and van Woerden, H. 1956, Bull. Astron. Inst. Netherlands 12, p. 327

Nelson, B. 2025, O-C files, http://www.aavso.org/bob-nelsons-o-c-files

Schindler, K. Lowell Observatory press release, August 22, 2025, https://lowell.edu/astronomers-reveal-massive-binary-star-system-in-milky-way

Stubbings, R. and Williams, P. 2017, JAAVSO 45, #1, pp. 57-59

Van der Hucht, K. 2001, New Astronomy Reviews 45, #3, pp. 135-232

VSX 2025 / International Variable Star Index, https://www.aavso.org/vsx

Polarimetry of Variable Stars with PICSARR-2

Daniel V. Cotton, Glenn Henderson, Kim Sumagang, and Eric C. Haase

Monterey Institute for Research in Astronomy, 200 Eighth Street, Marina, CA 93933, USA; dc@mira.org

Jeremy Bailey

University of New South Wales, Sydney, NSW, 2052, Australia; j.bailey@unsw.edu.au

Subject Keywords

Instrumentation: polarimeters; techniques: polarimetric; stars: binaries: symbiotic; stars: variables: general; stars: individual (ζ Peg, ζ Cas, ε Per, T CrB, AC Her, μ Cep, λ Cep)

Abstract

We describe the upgraded Polarimeter using Imaging CMOS Sensor and Rotating Retarder 2 (PICSARR-2) and characterize its performance for stellar polarimetry on a 36-inch telescope. In the SDSS *g'*, *r'* and *i'* filters a precision of σ_p= 5.7 ppm on bright stars is recorded using a fast modulation rate corresponding to frame exposures of 12 ms; accounting for the internal errors in the individual observations gives e_p= 1.3 ppm – better than any other instrument in the World. Longer frame rates are required for stars with *m* > 5, but the recorded errors only underperform a photon shot noise derived extrapolation for *m* > 8, when even longer frame exposures are required. Stars as faint as *m* = 11 were observed. The position angle precision is measured as 0.0845 degrees, and there is very good agreement between observations made by both the PICSARR-2 and HIPPI-2 instruments. This makes PICSARR-2 an excellent instrument to explore stellar variability due to a range of phenomena; examples of many in current programs are presented.

1. Introduction

1.1 Linear Polarimetry

Conceptually, linear polarization describes the average orientation of photons in a beam, where the orientation of each photon may be thought of as the position angle, perpendicular to the direction of travel, of the oscillation in the wave that describes it. If the photons are randomly aligned, then the beam will be essentially unpolarized. If all of the photons are aligned the same way, the beam is polarized, with *p*=100%, at the preferred position angle, θ. If there are a mix of photon alignments then the beam is partially polarized, with *p* and θ given by the vector sum of the constituent photons.

For convenience, astronomers often work with Stokes parameters, *Q* and *U*, which are the vector components of polarized flux (Stokes 1851). Unlike the x and y vector components of projectile velocity, for instance, the Stokes parameters are not perpendicular, but separated by 45 degrees. This is because polarization is only a pseudo vector, with orientation but no direction. Thus, in the Equatorial system, 0 degrees (North) corresponds to Stokes *Q* and 45 degrees to Stokes *U*; 90 degrees (East) is -*Q* and 135 degrees is -*U*. The total flux is usually labelled as Stokes *I*, and the normalized Stokes parameters given the lowercase characters $q = {}^{Q}/_{I}$ and $u = {}^{U}/_{I}$. Typically, one first gets the Stokes parameters from an instrument by making intensity measurements of the polarized components at four position angles, so that $q = \frac{I_0 - I_{90}}{I_0 + I_{90}}$, $u = \frac{I_{45} - I_{135}}{I_{45} + I_{135}}$, and then converts to *p* and θ. To convert between the two systems: $p = \sqrt{q^2 + u^2}$, and $\theta = \frac{1}{2}\tan^{-1}\left(\frac{u}{q}\right)$.

1.2 Stellar Polarimetry

Polarimetry is a valuable tool in variable star studies, but one that has been chronically under-utilized. Stars are net linearly polarized when their light is scattered asymmetrically, either from the stellar atmosphere itself – *photospheric polarization* – or from the gas and dust that surrounds them – *circumstellar polarization*. Polarimetry is particularly good at revealing details of geometry in unresolved systems, as well as particle size and other properties, where conventional techniques are inadequate.

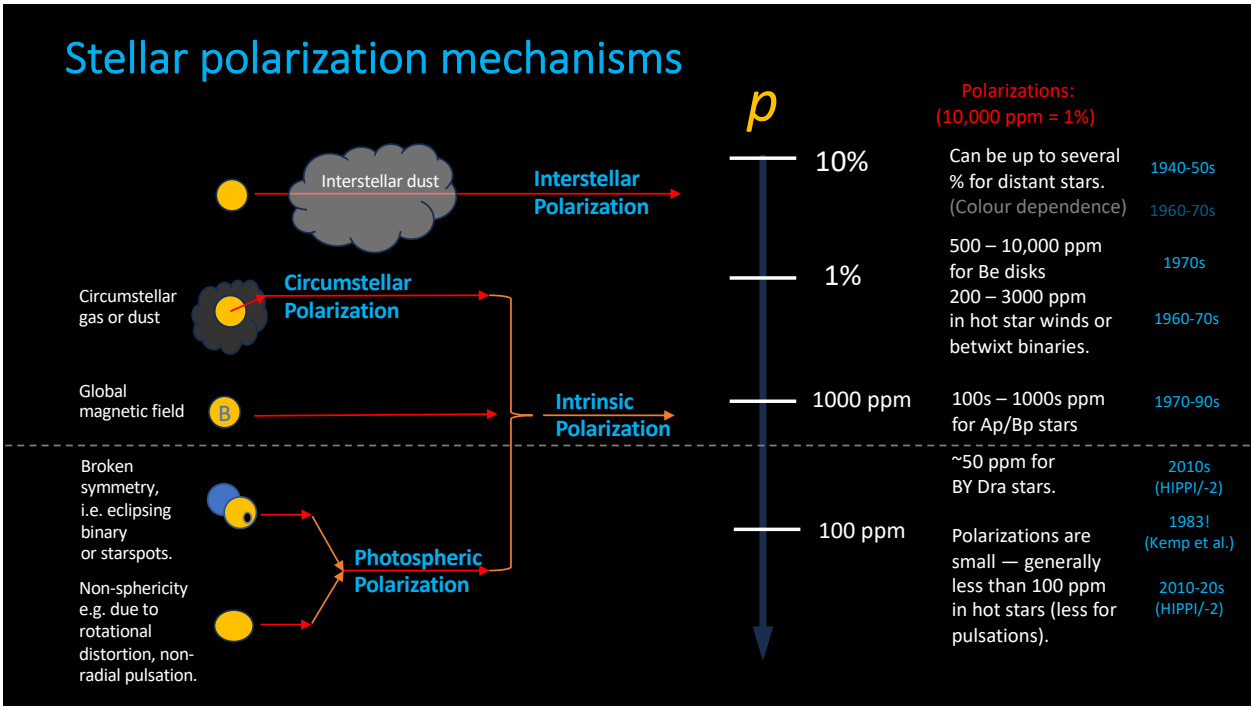

Figure 1. A summary of selected polarization mechanisms, the era of their initial discovery and investigation, and the typical polarizations associated with them.

Figure 1 highlights some of the ways starlight is polarized. All but interstellar polarization and rotational distortion lead to a time varying polarimetric signal. Spectropolarimetry (also making use of Stokes *V* – circular polarization) has mostly superseded broadband linear polarimetry in studies of magnetic phenomena, but otherwise these are all still areas of active research for the type of instrument we describe in this paper. For a complete summary of the development and applications of stellar polarimetry prior to the current decade and a half, the interested reader is directed to Clarke (2010).

Conventional polarimeters have a best precision of about 100 parts-per-million (ppm). Study of the mechanisms below the dashed line in *Figure 1* requires a high precision polarimeter. This is a dual beam instrument that employs rapid modulation, so that perpendicular components of polarization (e.g., I_0 and I_{90}) are measured both at the same time, and again in the same optical path within a time frame less than the characteristic seeing noise. CCD detectors, first developed in the 1980s, are not capable of such rapid modulation without large amounts of read noise. So, until recently, a polarimeter ciould either be efficient (i.e., in the QE sense) or achieve high precision through other less efficient detector technologies. Consequently, high precision polarimeters tended to be exotic, and have some unique drawback that limited their use.

Consider, for instance, the most successful of these instruments, HIPPI (Bailey et al. 2015) and HIPPI-2 (Bailey et al. 2020), which were used to discover three of the electron-scattering photospheric polarization mechanisms (Cotton et al. 2017, Bailey et al. 2019, Cotton et al. 2022a). It achieved precisions of ~3-4 ppm – compared to the 8 ppm of the next best instruments – through the use of ferro-electric liquid crystal modulators and photo-multiplier tube detectors. On a 1-m class telescope its operation was limited to stars with $\mathrm{m} < 10$ (Cotton et al. 2022b). The low detector efficiency along with significant observing overheads limited high-cadence studies to the brightest stars.

The advent of CMOS sensors for astronomy has significantly advanced the state of the art, since now fast modulation can be achieved without appreciably sacrificing efficiency.

1.3 The PICSARR Polarimeter

First commissioned in 2021, the *Polarimeter using Imaging CMOS Sensor and Rotating Retarder* (PICSARR; Bailey et al. 2023) made high precision stellar polarimetry feasible on small telescopes. Its 3D-printed plastic case, off-the-shelf optics and hardware, and inexpensive CMOS camera – of the type marketed to amateur astrophotographers – made it inexpensive and belied its high performance. It features a MgF_2 Wollaston prism analyzer that directs the orthogonally polarized components of starlight onto the detector – which typically takes data at a rate of 83 fps. In front of that in the light path is a ZWO electronic filter wheel and a super-achromatic half-waveplate modulator that is rotated by a belt-driven mechanism to provide fast modulation – smoothly varying the polarization state measured by each beam.

Five PICSARR-class instruments are currently in operation, across four institutions, on telescopes with apertures ranging in size from 8 to 36 inches. Chief among their applications are programs

to study variable stars, including eclipsing and non-eclipsing close binaries, β Cep variables, α Cyg variables, Long Period Variables, Be stars and other eruptive variables. Most of these are still in progress, but there are papers on Deneb (Cotton et al. 2024a), and Venus (Bailey et al., submitted). The second of these also makes use of the imaging functionality of the instrument.

Three of these polarimeters, that we denote PICSARR-2, incorporate a hollow core stepper motor to smoothly accomplish the rapid modulation needed for high precision. This is a significant improvement on the original belt drive system, which enables longer frame exposures for the observation of fainter targets, and smoother operation improved imaging and stability on bright targets. The purpose of the current paper is to describe the upgraded instrument, report its performance, and provide brief examples of the variable star research being done with it.

In Section 2.1 we first describe the instrument, focusing on changes from the original PICSARR. In section 2.2 the methods of calibration are described in an instructional manner. Similarly, in Section 2.3 we relate the results of performance characterization tests. In Section 3, examples of current observing programs are given. The conclusions are in Section 4.

2. Methods

2.1 The PICSARR-2 Polarimeter

The three copies of PICSARR-2 currently in operation incorporate subtle differences in their componentry and design. The first two were built by one of us (JB), the third, to be described here, was fabricated at the Monterey Institute for Research in Astronomy (MIRA). The instruments' modular design allows for differing modulators and detectors. MIRA's instrument also includes minor layout changes to accommodate the short back-focal distance of the Cassegrain port of the Guidance and Acquisition Package (GAP) on the MIRA 36-inch telescope.

What distinguishes PICSARR-2 from PICSARR is the use of a Faulhaber DM66200H hollow-core stepper motor to spin the half-waveplate modulator, which is housed within it. The motor features 200 steps of 1.8 degrees, but for smoother operation uses 1/16 micro-steps. This replaces the previous belt-drive system. Through the use of a custom electronics board, the motor can be manually stepped into one of 16 fixed positions corresponding to spacings of 22.5 degrees (equal to 45 degrees in position angle), or continuously rotated at rates corresponding to frame exposures of 12, 50, 200, or 500 ms; where there are 16 frames per complete waveplate rotation *block* (always processing data as complete blocks serves to cancel instrumental effects).

The modulator is held in its own cradle mounted within the motor; it is press fit against a spring washer. Three screws are used to adjust the tilt of the modulator within its cradle for better optical alignment; the adjustment plate these screws pass through was machined out of aluminum after the plastic version was found to be insufficiently rigid (see the left panel of *Figure 2*). This mechanism has substantially reduced beam motion as a function of rotation angle compared to PICSARR.

On MIRA's 36-inch telescope the instrument is attached to an aluminum mounting plate affixed directly to the Cassegrain face of the GAP. The mounting plate incorporates a turntable that allows adjustment of the position angle on the sky of the detector (*Figure 2* right panel). The modulator assembly and the camera assembly, incorporating all the other optics, are attached to the mounting plate separately. In this way, the plate and the mass of the GAP act to damp vibrations induced by the motor in the modulator assembly.

Figure 2. Left: partially assembled PICSARR-2, with the electronics board top left, modulator assembly at bottom left, the camera assembly at bottom right, and the 2-inch eyepiece adapter for smaller telescopes on the top right. Right: PICSARR-2 attached to its black and silver aluminum mounting plate on MIRA's 36-inch telescope GAP. In this configuration, the modulator assembly is within the GAP.

Rotation of a half-waveplate is a common way to achieve fast modulation in polarimetry. What is often overlooked though are the mechanical considerations in doing this effectively. Vibration from the rotating parts can act like seeing noise in its effect on the images at the detector, and it increases in frequency as the modulation rate is increased. A motor with a smooth action, along with giving consideration to vibration damping, are therefore vital considerations.

For the observations reported here, PICSARR-2 was configured with a Thorlabs AHWP05M-580 achromatic half-waveplate modulator, a MgF_2 Wollaston prism analyzer, and made use of an SDSS *ugriz* filter set by Chroma. Two runs were completed with two different cameras, the ZWO ASI 462MM and the ZWO ASI 662MM. The ASI 662MM has a larger dynamic range at the cost of a greater read noise compared to the ASI 462MM but otherwise these are very similar cameras. We designate the runs MOP2025JUL and MOP2025SEP, where the first two letters are an observatory/telescope code (for MIRA's 36-inch telescope at its Oliver Observing Station), P stands for PICSARR, and the remainder refers to the month the instrument was first mounted. The MOP2025JUL run is split into an A and B sub-run as a result of a minor set-up change.

Figure 3 shows the transmission of the filter set, the optical components, and the Quantum Efficiency (QE) of the ASI 462MM camera. The modulator batch was specially characterized by

Thorlabs in the region 400 to 850 nm. Outside this range its performance has been estimated based on the data available from previous batches. Similarly, the camera QE is estimated outside of 400 to 1000 nm based on data from Sony on chips of the same generation.

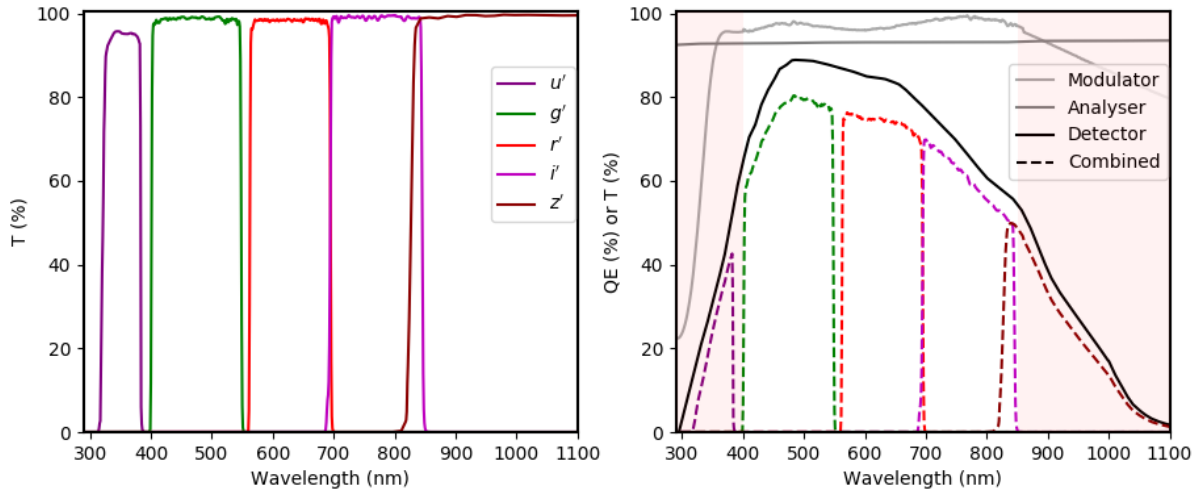

Figure 3. Left: Chroma SDSS filter transmission as a function of wavelength. Right: the relative response of PICSARR-2 in each filter when taking account of the ASI 462MM camera QE and the transmission of the other optical components. Note: pink shaded regions are estimated from second order data.

2.2 Calibration

Polarimeter characterization and calibration is very important for making reliable measurements that can be compared to the work of others. The basis of this is an accurate bandpass model as a function of wavelength. With PICSARR-2 we have mostly relied on manufacturer data for the transmission of each optical component and the detector quantum efficiency (QE) (*Figure 3*), as well as the modulator's modulation efficiency and fast-axis deviation. However, we always regard this data as approximate until verified on-sky against established standard stars and corrections applied where indicated.

For any broadband linear stellar polarimeter, there are two on-sky calibrations that must be performed for every new mounting of the instrument: measurement of the telescope polarization, and a position angle calibration. We perform these first before other characterization and then iterate to establish the performance of the instrument.

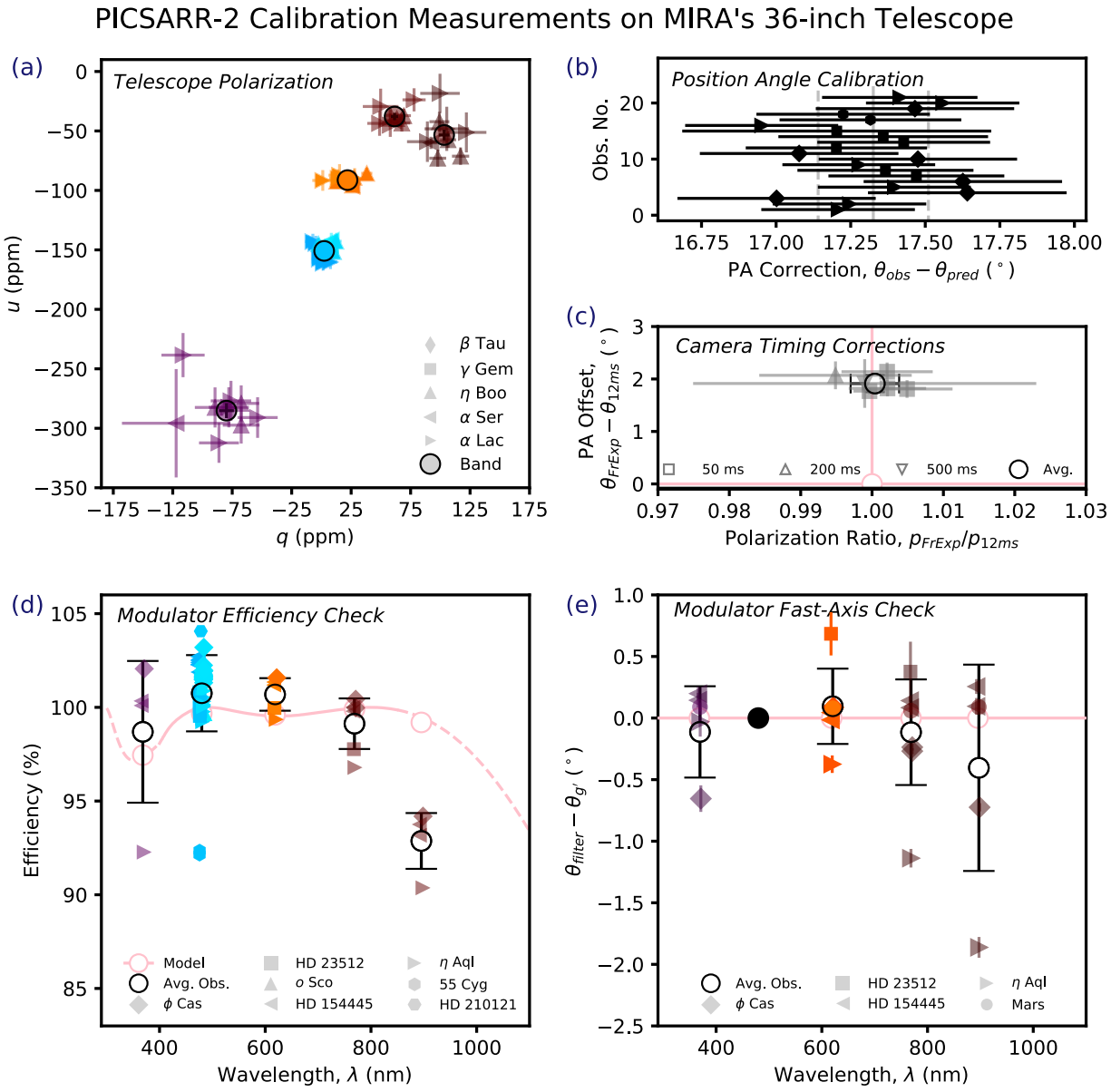

Figure 4. PICSARR-2 calibration measurements on MIRA's 36-inch telescope. (a) Telescope polarization in u', g', r', i', and z' bands for run MOP2025JUL, (b) position angle calibration for run MOP2025SEP, (c) camera timing corrections for the ASI 662MM, (d, e) moduator efficiency and fast-axis checks, respectively, for the Thorlabs AHWP05M-580. An explanation of the symbols can be found in the sections 2.2.1, 2.2.2, 2.2.3, 2.2.4 and 2.2.5 respectively.

2.2.1 Telescope Polarization

The first calibration is the telescope polarization (TP) measurement, which defines the zero point of Stokes *q* and *u*. It needs to be determined independently for each for each passband used. The simplest method is to take the straight average of several observations of low polarization standard stars, the result of which is subtracted from all the other observations in the same

passband. *Figure 4*(a) shows the TP data for our MOP2025JUL run; the standards used are listed in the key, these are assumed to have no polarization. In reality these stars have small polarizations, the knowledge of which places a limit on the accuracy obtainable.

In *Figure 4*(a) the TP data is shown in the Equatorial frame (See section 1.1). However, if the TP is significant, one should first make these calculations in the instrument frame and subtract the results before a position angle calibration (see Section 2.2.2). The slope of $TP_{[q/u]}$ with wavelength limits the accuracy of this method. If it is large compared to the needed accuracy, then a second order correction for the color of the stars (standards and science targets) may be needed. Here, the implied TP difference between blue and red stars is smaller than the nominal errors for a typical observation of the brightest stars (see Section 2.3.2).

2.2.2 Position Angle Calibration

The instrumental *Q* and *U* axes are a function of the layout of instrument hardware components. The position angle calibration rotates the Q-U frame from that of the instrument to the Equatorial frame (See Section 1.1). This is accomplished by a comparison of the observed position angle, θ, of high polarization standard stars to their predicted values – determined from literature parameters. The simplest method would take as a prediction previously observed values in the same band and take a straight average of all observations. We use a more sophisticated method explained fully in Cotton et al. (2024b), that takes account of wavelength and time dependence, and weights each measurement according to the RMS sum of the measured error, the known variability in the standard, and an instrument-telescope precision, $\eta(\epsilon_i\theta)$, which is the median of error-corrected standard deviations in measurements of the same stars during the same run with the same instrumental set-up. From the MOP2025JUL A and B runs, we calculated this parameter to be 0.0845 degrees – about half the adopted value for HIPPI-2 on the same telescope.

Figure 4(b) depicts graphically the position angle calibration for the MOP2025SEP run. The symbols corresponding to the standards used can be found in the key of *Figure 4*(d). The vertical grey line shows the adopted value, and the dashed lines +/- the weighted standard deviation, 0.185 degrees, whereas the nominal RMS error in the determination is 0.0681 degrees. These values are comparable to the potential error that might be introduced if a TP subtraction was not carried out first. For any given standard this could be estimated, assuming the TP offset is p_e, as $\theta_e = 28.65\left({}^{p_e}/_{p}\right)$ degrees, where p_e is the error in polarization and p the standard's nominal polarization – typically several percent.

2.2.3 Camera Timing Corrections

The cameras used with PICSARR-2 employ a rolling shutter: each row of pixels is read out in sequence. To achieve the fastest modulation speeds the modulator is rotated continuously, resulting in a slight rotation between rows. We correct for this using a formula for frame rotation determined empirically from repeat standard observations made previously with the original

PICSARR using the ASI 462MM: $\theta_{row} = \frac{0.6252}{FrExp} b(\frac{h}{2} - y)$, where *b* is the pixel binning of the camera (i.e., 2 for 2x2), *h* the window height in pixels, *y* the average row center of the star for the video sequence, and *FrExp* the frame exposure in ms. For the ASI 662MM an adjustment is made to account for the maximum frame rate difference.

The rolling shutter correction is less important with PICSARR-2 than PICSARR because the optics are better aligned resulting in less circular motion of the star on the detector. Additionally, we are now able to employ autoguiding directly from the SHARPCAP (www.sharpcap.co.uk) display using the TCS HELPER program written by Logan Barrett (www.mira.org/software.htm), which keeps the star images much closer to the target pixel.

Because the modulator is driven continuously at a high rate, the row readout can lead to a modulation efficiency loss or position angle rotation when the readout time is a significant fraction of the total. In *Figure 4*(c), we plot data obtained from sequential measurements made of the same standards with different frame rates for the ASI 662MM camera. By the polarization ratio, p_{FrExp}/p_{12ms}, measured, these show no significant efficiency loss. However, there is a small position angle offset of 1.913 degrees for the fastest 12 ms frame rate.

2.2.4 Modulator Efficiency Check

To check the accuracy of the lab data provided on the Thorlabs AHWP05M-580 modulator efficiency, in *Figure 4*(d) we plot the measured polarization of standard stars in different passbands as a percentage of the predicted value (derived from Cotton et al. 2024b), with the modulator efficiency correction removed. The modelled efficiency is shown by the pink line. It is clear that there is a significant scatter in the literature polarizations of the standards. Nevertheless, the *z'* band data is significantly different from the prediction – which had to be estimated from prior modulator batch data in the corresponding wavelength range – and so we scale this band by a factor of 1.0721 to compensate. We could scale the other bands as well to get better agreement, but it is not certain that this would lead to greater accuracy.

2.2.5 Modulator Fast-Axis Check

A waveplate induces a phase shift between two orthogonal polarizations of light through birefringence, i.e., through a refractive index difference between the fast-axis and slow-axis of the crystal(s). A half-waveplate rotates the plane of polarization by flipping the polarization direction around the fast-axis. To modulate the polarization, PICSARR-2 rotates the half waveplate, continuously changing the angle of the fast-axis relative to the incoming light. In some modulator designs, the angle of the fast-axis can vary with wavelength. For an accurate measurement this behavior must be characterized and included in a bandpass model.

The AHWP05M-580 is an achromatic half-waveplate. Therefore, its fast-axis should not change as a function of wavelength. In PICSARR, a super-achromatic version was used, which did vary quite a lot, requiring a more complex bandpass model for corrections. (Thorlabs generously

recharacterized a SAHWP05M-700 modulator for us after initial observations revealed a significant discrepancy with the nominal lab data.) It may also have contributed to position angle imprecision through chromatic aberration apparent at high airmass.

In *Figure 4*(e) we check that there really is no fast-axis deviation with wavelength. Observations of the same standard in different bandpasses are made in sequence, and the difference in position angle between the *g'* band and the other filters are calculated (data from Cotton et al. 2024b). We also included an observation set of the planet Mars as an additional standard – to first order Solar system bodies have polarizations that are either parallel or perpendicular to the Sun-Target-Observer plane, regardless of wavelength. The error bars show the standard deviations for each passband – there are no significant deviations. In fact, our observations serve to highlight that the wavelength dependence of θ for some standards is poorly characterized. HD 154445 looks to be the best standard, with deviations comparable to the Martian data.

We note in passing, that planetary data can serve as an alternative to high polarization standard stars for position angle calibration. If using this method the observer should carefully calculate the angle of the scattering plane relative to the equatorial frame at the time of the observation. One should also keep in mind that the polarization will periodically flip between plane parallel and perpendicular, and that this does not occur at the same phase for every passband.

2.3 Performance Characterization

2.3.1 Position Angle Precision & Accuracy

Position angle precision and accuracy are important, not just for observations of large polarization variables, but also for small polarization variables at distances large enough to have significant interstellar polarization. The data from different observing runs can only be combined reliably, regardless of the nominal errors on the individual observations, if the telescope position angle is accurately established.

Figure 5(a) presents repeat observations of three high polarization standards, across all three sub-/runs (delineated by the dashed red lines), as differences from the model predicted position angle – indicated by the horizontal blue lines. The height of the grey backing around the blue lines represents the established variability of each standard across a 10-year period (Cotton et al. 2024b). The number of observations falling beyond the grey area is fewer than expected for a normal distribution. The red data points and error bars at the right of frame show the mean observation and standard deviation; this is a formal match for expectations in all three cases.

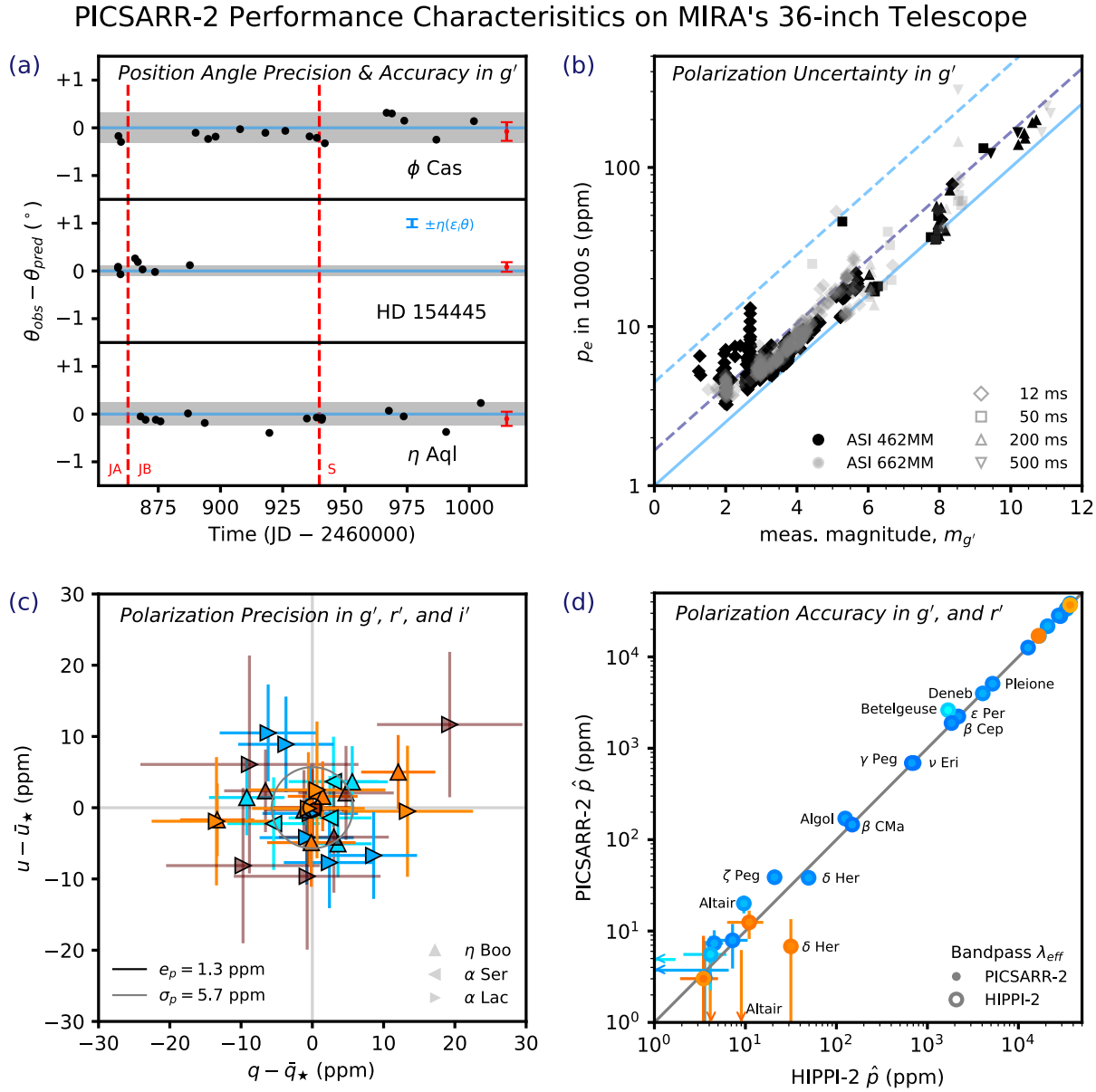

Figure 5. Performance characteristics of PICSARR-2 on MIRA's 36-inch telescope. (a) Position angle accuracy and precision in g', (b) polarization uncertainty in g', (c) polarization precision in g', r' and i', (d) polarization accuracy in g' and r'. An explanation of the symbols can be found in the text in Sections 2.3.1, 2.3.2, 2.3.3 and 2.3.4 respectively. In panels (c) and (d) the colors reflect the effective wavelengths of the passbands, and account for star color.

2.3.2 Polarization Uncertainty

Figure 5(b) presents the errors for all of the stellar data acquired in *g'* with PICSARR-2 on MIRA's 36-inch telescope. These are plotted against the measured magnitude of the star offset such that the median measured magnitude matches the median literature derived value in *g'* from our bandpass model. The nominal errors are determined statistically from the standard deviation of

each individual measurement of *q* and *u* from the 16-frame blocks that make up a video sequence. Most, but not all, observations are 16 minutes (4x4 min = 960 s). For convenience, all the errors have been scaled to a 1000 s equivalent exposure using $e_2 = e_1\sqrt{\frac{t_2}{t_1}}$. Upward outliers are the result of rejected blocks which are still counted in the total exposure time. Blocks can be rejected when the signal is too low (e.g., clouds), too high (a single saturated pixel), when the Ordinary (O) star image is too far from the target pixel or the O and Extraordinary (E) beam spacing is anomalous (from, e.g., poor seeing or tracking errors), or due to time sequence errors.

The performance of the two cameras is plotted in different shades in *Figure 5*(b). There are more upward outliers for the ASI 462MM camera for bright stars. Many of these points correspond to blocks rejected by saturation, often in variable seeing conditions. The larger full well depth of the ASI 662MM (38.2 ke$^-$ vs. 11.2 ke$^-$ for the ASI 462MM) reduces such instances. However, this comes at the cost of a larger read noise, and so the ultimate performance is not quite as good (black points below grey). At Gain 0 the read noise is 7 e$^-$ for the ASI 662MM and 2.5 e$^-$ for the ASI 462MM and decreases quickly with gain. A High Contrast Gain (HCG) mode, which significantly lowers the read noise, doesn't kick-in until a much higher gain for the ASI 662MM; for specific values at other gains see ZWO's documentation.

Neither trend in camera data is entirely smooth. Where longer frame exposures are chosen, read noise is reduced, but faster frame rates better reduce the effects of seeing noise, so there is a trade off, and this setting, along with the Gain, is chosen by the observer at the time of the observation based on the prevailing conditions. Around $m = 5$, the slower 50 ms frame exposure is preferred (square symbols), and this corresponds to a slight increase in nominal error. Another step is noticeable around $m = 8.5$, where the 200 ms frame exposure (up triangle) is necessary.

The solid blue diagonal line represents a purely photon-limited error increase for a system with 1 ppm error at $m = 0$; the instrument's best performance matches this for magnitudes about 3 to 8.5 but begins to deviate for both fainter and brighter stars, as expected. The same bright star deviation was seen with HIPPI-2, where it was mainly attributed to centering imprecision (Bailey et al. 2020, Cotton et al. 2022b), but here read noise is probably a larger contributor. The dashed purple line is the equivalent photon-limited trend offset to correspond with the performance of HIPPI-2 on the same sized telescope (based on Bailey et al. 2020). In terms of exposure time, PICSARR-2 is performing about twice as well, which is attributable to the relative detector efficiencies. However, if one considers HIPPI-2's observing overheads, the performance is almost four times better (Cotton et al. 2022b).

For comparison purposes, a dashed blue diagonal line is drawn in *Figure 5*(b) that scales the solid line for a telescope aperture of 8 inches (20 cm) – the smallest telescope used with PICSARR-2.

2.3.3 Polarization Precision

The instrument's precision is established by making repeat observations of bright low polarization stars across multiple nights. For comparison with Bailey et al. (2023) we have

combined data sets from the *g'*, *r'* and *i'* bands in *Figure 5*(c). The average standard deviation of *q* and *u* for each set plotted in this figure is σ_p = 5.7 ppm, which is comparable to the individual observation errors. This figure would likely improve with longer observations. The metric e_p seeks to establish the scatter independent of the nominal errors by a root-mean-square subtraction of the average error of each set (see Bailey et al. 2020) – this is a check of whether the nominal errors are really representative under these conditions. We calculate e_p = 1.3 ppm. This is an improvement on both the figures of 11 and 17 ppm for PICSARR on smaller telescopes (14-inch and 8-inch respectively; Bailey et al. 2023) and HIPPI-2 on the same telescope (1.7 ppm; Cotton et al. 2022b), which makes PICSARR-2 the World's most precise stellar polarimeter by this metric.

2.3.4 Polarization Accuracy

One measure of the instrument's polarization accuracy was already presented in *Figure 4*(d) as the agreement between the modelled and measured modulator efficiency. Yet, a precise determination was difficult because of the spread in the results for different standards. We contend this is a consequence of errors in the literature values rather than imprecision of the instrument. To test this, in *Figure 5*(d) we plot mean PICSARR-2 observations against those in common with HIPPI-2 in the same bands (*g'* and *r'*). The data has been debiased by the RMS subtraction of the errors as:

$$\hat{p} = \begin{cases} \sqrt{p^2 - p_e^2}, p > p_e \\ 0 \qquad\quad , p \leq p_e \end{cases}.$$

The plotted grey line has a slope of 1; the slope of a line fit to the points is 1.0051 +/- 0.0001. The r^2 value is 0.99994. Together with the small error in the slope, this demonstrates a very consistent relationship. This agreement is good but indicates that PICSARR-2 is measuring slightly higher polarizations. This is to be expected, given the data presented in *Figure 4*(d), since the modulator efficiency of HIPPI-2 is determined by fitting to the standard literature values, which are slightly high compared to our bandpass model prediction.

In *Figure 5*(d) we have labelled all of the stars, not either low polarization or high polarization standards (and Altair which we have sometimes used as a standard). The log-log scale emphasizes lower polarization objects. The most apparent outliers are the known polarimetric variables Betelgeuse (Schwarz 1986) and Algol (Kemp et al. 1983), for which we only have one or two observations with one or both instruments.

3. Science Examples

3.1 Pulsating Stars

The main observing program for PICSARR-2 on MIRA's 36-inch telescope aims to do polarimetric asteroseismology on bright β Cep and Slowly Pulsating B-type (SPB) variables. This pushes the performance of the instrument to the limit. Many hundreds of observations per star are required to detect pulsations with amplitudes expected to be ≈20 ppm or less (Cotton et al. 2022a). A

Fourier analysis is required to identify different pulsation periods. Then the data has to be combined with high precision photometry and high-resolution spectroscopy to make mode assignments (in terms of *l* and *m*), which ultimately allows modelling of the interior of the star. The focus is on B-type stars because traditional asteroseismology techniques alone are unable to identify the pulsation modes, and polarimetry offers complimentary data. *Figure 6* shows example data for three ~3rd magnitude stars in the program.

3.1.1 ζ Pegasi

One of the stars, ζ Peg, exhibits no significant polarization variability. The Q-U plot in *Figure 6*(b) includes 64 *g'* data points from the MOP2025JUL run, displaying less scatter than the standards used to estimate the instrument's precision in *Figure 5*(c). This is an SPB star with a single low amplitude ($\Delta m \approx 0.001$) photometric mode with a period of 22.952 ± 0.804 h (Goebel 2007). We do not expect a detectable signal from it, so the result provides more evidence of the instrument's capability.

3.1.2 ζ Cassiopeiae

The second example is ζ Cas. Neiner et al. (2003) found a non-radial pulsation mode with *l* = 2 +/- 1 at P = 1.57 d, so it is a good candidate for a significant polarimetric signal. However, the star also has a weak dipole magnetic field ranging from about -150 to +150 G (Briquet et al. 2016). Modulated by its 5.37 d rotational period this produces a characteristic double peaked phase curve – *Figure 6*(d) – with an amplitude of ~200 ppm. This signal will have to be removed to search for the signature of pulsation.

3.1.3 ε Persei

The final example, ε Per, shows clear variability. In the single night example shown in *Figure 6*(f) there is a signal with up to 100 ppm amplitude. This star is a hybrid pulsator with four dominating photometric periods of 4.47, 3.84, 3.04 and 2.26 h, which are thought likely to be non-radial modes with *m* = -3, -4, -5 and -6 respectively (Gies & Kullavanijaya 1988). Any or all of these modes might produce a large sinusoidal polarimetric signal of the type seen in *Figure 6*(f), and beating between them is likely responsible for the larger range of the time series in *Figure 6*(e).

3.2 Other Stars

There are many other types of stars that make interesting objects for polarimetric study. The ability to make many observations over a long period of time is important in such work. In this regard the time available to small observatories and skilled amateurs is a significant advantage. Some examples are presented in *Figure 7*.

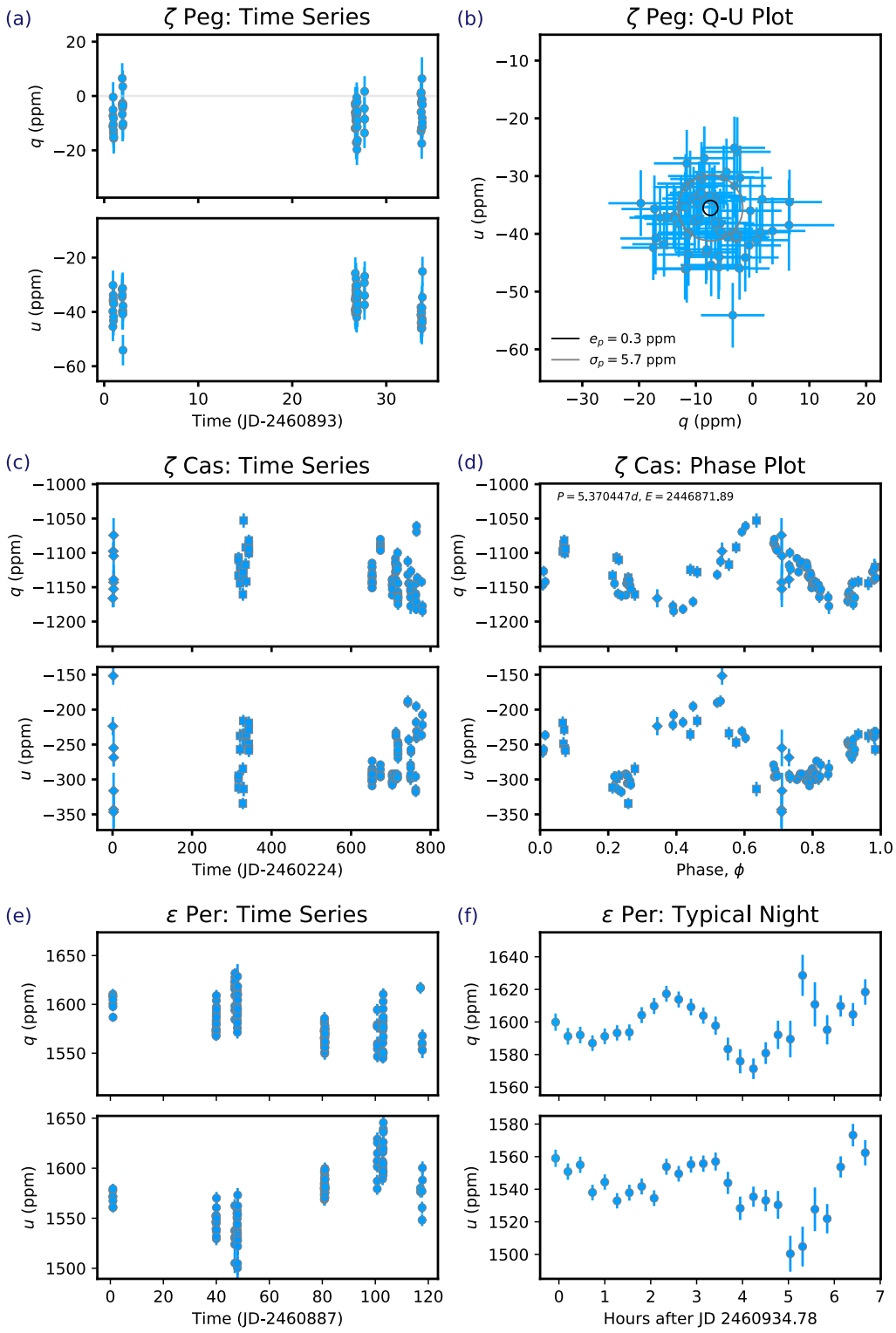

Figure 6. Example data from the pulsating star program. PICSARR-2 data from MIRA's 36-inch telescope is shown as circles, earlier PICSARR data from the same telescope as squares, and PICSARR/-2 data from other smaller telescopes as diamonds. All observations were made in the g' filter.

3.2.1 T Coronae Borealis

T CrB, the *Blaze Star*, is (currently) the faintest variable star we are observing. It is the brightest example of a recurrent nova with outbursts observed in 1886 and 1946 and another outburst expected soon (Schneider, 2025). Previous polarization observations (Nikolov, 2022) showed interstellar polarization and no variability. In *Figure 7*(a) we see a convincing change in polarization for passbands in the visual range, with those in the near-infrared showing more stability. T CrB is a binary system consisting of a red giant transferring material onto a white dwarf companion. We suspect that the variable polarization may be due to light reflected between the two binary components and if so this would allow us to determine the orientation of the binary orbit on the sky. This would then provide valuable information to help understand any structure seen in the outflowing gas when the outburst occurs.

3.2.2 AC Herculis

AC Her is a member of the RV Tauri class of variables. These are solar type stars in their final stages of evolution. AC Her shows pulsations with a period of 75 days, and these are known to be accompanied with surprisingly large variations in polarization (Henson et al. 1985; Nook et al. 1990). The polarization amplitudes can be as large as 1 per cent (10000 ppm) at blue wavelengths and this is confirmed by our PICSARR observations in *Figure 7*(b). The large polarization variations of RV Tauri stars are something of a mystery as most pulsating stars show only small polarization amplitudes (as described in Section 3.1).

3.2.3 μ Cephei

First found variable in 1858, μ Cep is an M2 supergiant classified as an SRc type, with prominent periods near 860 and 4400 d (Kiss et al. 2006). Its polarimetric variability has also been known for a long time (Grigorian 1966); it correlates, at least, to the shorter photometric period (Polyakova 2003). The large amplitude, wavelength dependence, and slow polarimetric variability seen in *Figure 7*(c) are typical of this type of star. The most often invoked mechanisms relate to absorption and scattering from convective cells (hotspots) and/or circumstellar dust (Schwarz 1986), though a companion star within the extended dust shell has also been proposed to explain the same behavior in Betelgeuse (Karovska et al. 1985), which is also an SRc type M2 supergiant.

3.2.4 λ Cephei

A program examining variability in early-type supergiants is nearing completion. It includes both stars that vary slowly like Deneb (Cotton et al. 2024a) and stars that vary quickly like λ Cep (Hayes 1978). The favored mechanism in these instances is a clumpy stellar wind that acts as an asymmetric scattering medium propagating outward from the star. Data from a five-night run is presented in *Figure 7*(d) that shows the star's long-established night-to-night polarization changes, as well as faster variability. In addition to similar stochastic behavior, ζ Pup, which has a similar spectral type, demonstrates a persistent polarimetric periodicity (Bailey et al. 2024).

This speaks to the nature of the wind generation, and so it is a matter of interest as to whether similar behavior is present in λ Cep and other related stars.

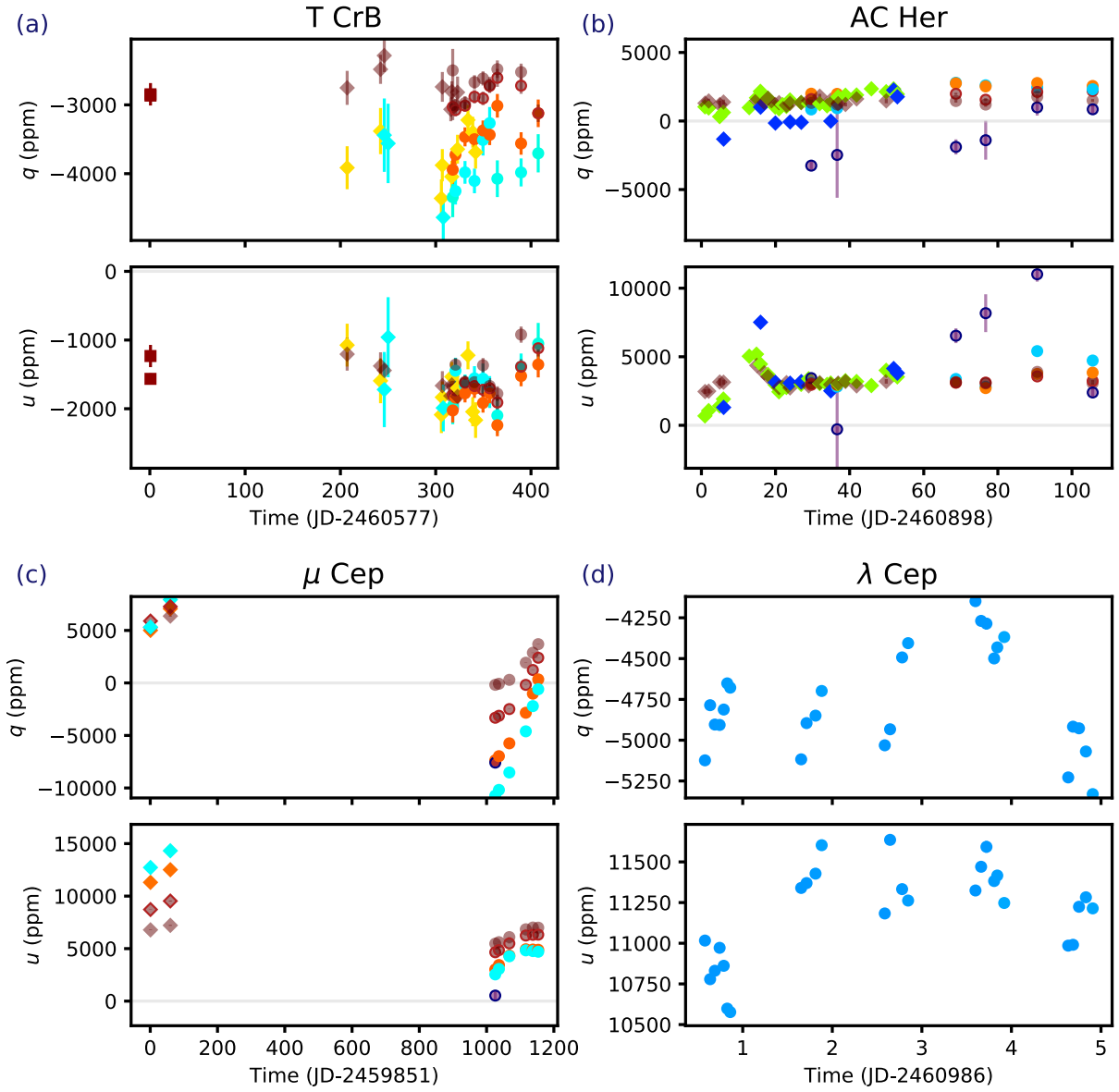

Figure 7. Four variable stars observed with PICSARR-2 on MIRA's 36-inch telescope (circles), with PICSSARR on the same telescope (squares), and PICSARR/-2 on smaller telescopes (diamonds). The colors represent λ_{eff} of the passband. Many of the observations of T CrB (a) and AC Her (b) have been made by one of us (JB) with the 8-inch telescope at Pindari Observatory in Sydney, Australia. Some of these observations use non-SDSS bands, i.e., the Bessel B and I bands, and a Luminance filter from Chroma, which is essentially g'+r' – these points show up as yellow in panel (a) and green in panel (b). To help distinguish i' from z', the former uses a red marker edge color, and the latter brown.

4. Conclusions

We have built a copy of the PICSARR-2 instrument and thoroughly tested it on MIRA's 36-inch telescope. Of the two cameras used, the ZWO ASI 462MM provides better performance on fainter stars, but the ZWO ASI 662MM is a better choice for bright star work. The instrument's polarization precision is about a factor of 8 improved over the best reported for the original PICSARR, and the position angle precision is also very much better.

The main observing program for PICSARR-2 is focused in B-type pulsating stars. A relatively large polarization signal attributable to non-radial pulsations is seen in ε Per, but no significant polarization was detected in observations of ζ Peg. The main polarization signal from ζ Cas results from its weak magnetic field.

Of the examples of joint programs with other PICSARR instruments on smaller telescopes, the highlight is polarization variability detected from T CrB for the first time.

Acknowledgements

Max Anthony Velasquez, Logan Barrett, Jean Perkins and Ievgeniia Boiko assisted with some of the PICSARR-2 observations used in the paper. Ain De Horta contributed some comparison observations made at Western Sydney University's Penrith observatory. Discussions with Derek Buzasi and Conny Aerts helped formulate the target list for the pulsating star program. A study by Richard Hubbard helped determine the best synthetic aperture radii to use. We would like to thank Robin Glover of SharpCap for his responsiveness in making changes to the program to suit PICSARR, and Matt Jennings of Thorlabs for his invaluable assistance organizing characterization of the AHWP05M-580 modulator.

The adaption of PICSARR-2 for MIRA's 36-inch telescope is supported by NSF grant AST 2320626; observations of β Cep and SPB stars with the instrument are supported by NSF grant AST 2407635. We also thank the Friends of MIRA for their support.

References

Bailey, J., Kedziora-Chudczer, L., Cotton, D.V., et al. 2015, *Mon. Not. R. Astron. Soc.* **449**, 3064.

Bailey, J., Cotton, D. V., Kedziora-Chudczer, L., De Horta, A., and Maybour, D. 2019, *Nature Astron.* **3**, 363.

Bailey J., Cotton, D. V., Kedziora-Chudczer, L., De Horta, A., and Maybour, D. 2020, *Publ. Astron. Soc. Aust.* **37**, ID e0004.

Bailey J., Cotton, D. V., De Horta, A., Kedziora-Chudczer, L., and Shastri, O. 2023, *Mon. Not. R. Astron. Soc.* **520**, 1938.

Bailey, J., Howarth, I. D., Cotton D. V., et al. 2024, *Mon. Not. R. Astron. Soc.* **529**, 374.

Bailey J., Cotton, D. V., Bott, K., and Boiko, I., submitted to *Icarus*.

Briquet, M., Neiner, C., Petit, P., Leroy, B., and de Batz, B. 2016, *Astron. Astrophys.* **587**, ID A126.

Clarke, 2010, *Stellar Polarimetry*, Wiley, Darmstadt.

Cotton, D. V., Bailey, J., Howarth, I. D., et al. 2017, *Nature Astron.* **1**, 690.

Cotton, D. V., Buzasi, D. L., Aerts, C., et al. 2022a, *Nature Astron.* **6**, 154.

Cotton, D. V., Bailey, J., Larson, J. et al. 2022b, *Res. Not. Am. Astron. Soc.* **6**, ID 209.

Cotton, D. V., Bailey, J., Perkins, J., Buzasi, D. L., and Boiko, I. 2024a, *Astrophys. J. Lett.*, ID L43.

Cotton, D. V., Bailey, J. Kedziora-Chudczer, L., et al. 2024b, *Mon. Not. R. Astron. Soc.* **535**, 1586.

Gies, D. R., Kullavanijaya, A. 1988, *Astrophys. J.* **326**, 813.

Goebel, J. H. 2007, *Publ. Astron. Soc. Pac.* **119**, 483.

Grigorian, K. H. 1966, *Comm. Byurakan Astrophys. Obsv.* **37**, 18.

Hayes, D. P. 1978, *Astrophys. J.* **219**, 952.

Henson, G. D., Kemp, J. C., and Kraus, D. J. 1985, *Publ. Astron. Soc. Pac.* **97**, 1192.

Karovska, M., Noyes, R. W., Rodder, F., Nisenson, P., and Stachnik, R. V. 1985, *Bull. Am. Astron. Soc.* **17**, 598.

Kemp, J. C., Henson, G. D., Barbour, M. S., Kraus, D. J., and Collins, G. W., II. 1983, *Astrophys. J.*, L85.

Kiss, L. L., Szabó, G. M., and Bedding, T. R. 2006, *Mon. Not. R. Astron. Soc.* **372**, 1721.

Neiner, C., Geers, V. C., Henrichs, H. F., et al. 2003, *Astron. Astrophys*. **406**, 1019.

Nikolov, Y. 2022, *New Astron.* **97**, ID. 101859.

Nook, M. A., Cardelli, J. A., and Nordsieck, K. H. 1990, *Astron. J.* **100**, 2004.

Polyakova, T. A. 2003, *Astrophys.* **46**, 18.

Schwarz, H. E. 1986, *Vistas Astron.* **29**, 253.

Schneider, J. 2025, *Res. Not. Am. Astron. Soc.* **8**, ID 272.

Stokes, G. G. 1851, *Trans. Cambridge Philos. Soc.* **9**, 399.

Periodic Growth and Dissipation of the Circumstellar Disk of the Be Shell Star *omicron Andromedae*

Harry R. Diz

Saint Simons Island, Georgia; hrickdiz@gmail.com

Subject Keywords

Spectroscopy; Be shell star; Hα emission line; omicron Andromedae

Abstract

A 32-year spectral history of the Be shell star *omicron Andromedae* was compiled by obtaining spectral profiles from the BeSS database in addition to those acquired by the author. The Hα line (6562.8Å) was examined and its features quantified in 235 spectral profiles. The star is viewed edge-on, and thus the light from the star reaches us having travelled through its glowing disk. As a result the spectrum provides information about the photosphere of the star as well as information about the disk. In fact, the presence of emission lines (spectral lines that are brighter than the continuum) is evidence of the existence of the disk and its extent. The formation of Be star disks is believed to be the result of the ejection of material from the surface of the rapidly rotating star. It was found that there have been four cycles of formation and dissipation of disks around this star during the study period. The average lifespan of a disk was estimated to be 8 to 10 years with a new disk beginning to grow as soon as the previous disk had dissipated. The current disk is predicted to dissipate in approximately 18 months (summer 2027) based on the recent history and status of the disk.

1. Introduction

The purpose of this study was to document and report the recent history of the formation and dissipation of the circumstellar disk around the Be shell star *omicron Andromedae*. The source of information about the existence and behavior of the circumstellar disk is provided by the spectrum of the star, particularly the H alpha (Hα) spectral line at 6565.8 Å resulting from absorption and/or emission by hydrogen.

1.1 Be and Be shell stars

Be stars are described in the excellent review by Rivinius et al. (2013) as spectral type B non-supergiant stars that have, or have had, Balmer emission lines in their spectra. They rotate at a high rate resulting in an oblate spheroid shape with the equatorial diameter being greater than the diameter through the poles. The rapid rotation affects the spectrum by producing broad spectral lines due to the Doppler effect. Be stars typically have a circumstellar disk, which is the source of the emission lines. While the mechanism responsible for creating a disk is still debated (Porter & Rivinius 2003, Labadie-Bartz 2025), there is a consensus that the disks are formed from

matter ejected from the surface of the star rather than from material gained from some external source. The emission lines, particularly the Hα spectral line, take on various configurations depending on our line of sight relative to the axis of rotation (Figure 1). Notice the presence of a double peak, i.e., 'wings', in Figure 1-B & C. When the star is viewed edge-on, as in Figure 1C, the star is said to be a shell star since the star itself is obscured by circumstellar material. The shell spectral lines such as the Hα line studied here are reported by Escolano et al. (2015) to be emitted from the innermost region of the rotating disk. Additionally, Carciofi (2010) explained that "*the reason the spectra of Be stars show continuum excess or emission lines is that the dense disc material acts as a pseudo-photosphere that is much larger than the stellar photosphere*." He continues: "*for the optically thick Hα and Brγ lines the disc emission only fills in the photospheric absorption profile when the disc size is about 5 R. Both lines have pseudo-photospheres that extend up to about 20 R.*"

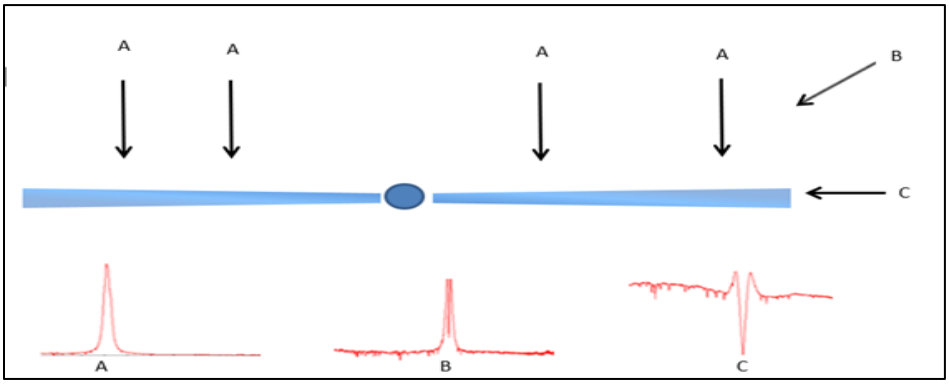

Figure 1. Schematic representation of a rapidly rotating Be star with a circumstellar disk, along with typical spectral profiles of the Hα region, as viewed from various perspectives. As the viewing angle becomes larger, as in the progression through B to C in the figure, the Doppler effect tends to separate the light coming from the portion of the disk that is rotating toward us (violet shifted) from the light from the portion that is moving away from us (red shifted). (After Rivinius et al. 2013).

1.2 Omicron Andromedae

The Be shell star *omicron Andromedae* (o And) is viewed by us almost perfectly edge-on. It is also known as HR 8762 and HD217675, and has been well studied (see, among others, Stagg et al. 1985, Stagg et al. 1988, Hill et al. 1989, Sareyan et al. 1998, Briot et al. 2002, Clark et al. 2003). o And is listed in the Simbad database (Wenger et al. 2020) as spectral type B6IIIpe, with a radial velocity of -14±0.9 km s^{-1}, at a distance of 211 pc. The V magnitude is listed in the International Variable Star Index (AAVSO 2025) as variable in the range 3.55 – 3.89, with a projected rotational velocity (v sin i) of 300 km/s.

o And is a multiple star group, consisting of possibly four stars (two pairs). Mitrofanova et al. (2021) determined the orbital period of the A-B pair to be 118 years. The B component is 2.3 magnitudes fainter than the A component and does not have emission lines in its spectrum. The o And A star may have a small close companion with an orbital period of 5.6 yrs, but there is some

controversy about its existence (Olevic and Cvetkovic 2006, Zhuchkov et al. 2010, Tokovinin 2018). It is assumed for purposes of this current study that the variation in the Hα line reported here is not complicated by the presence of the B star and/or B's close companion. Henceforth, this report pertains to the primary star "A" only.

Researchers over the years have attempted to determine the periodicity of o And's photometric variations (see references in Stagg et al. 1988). The light curve (Figure 2) of o And is a double-wave curve with a short period of ~0.84d reported by Bossi et al (1977) and longer period of 1.57 days (Harmanec 1987, Stagg et al. 1988). Recent analysis of TESS data (Caldwell et al. 2020) for this star by this author found a dominant 1.56 day period.

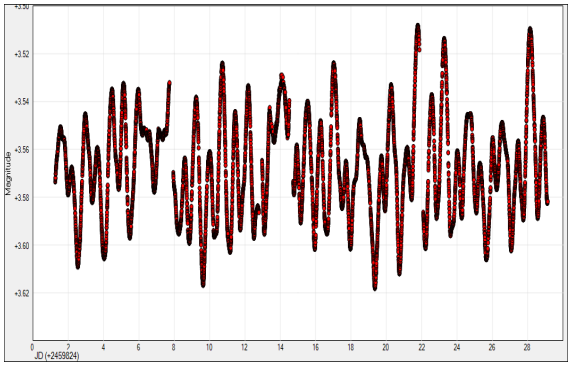

Figure 2. Light curve for o And using TESS data showing complex character. (TESS sector # 56, 2022-09-01 to 2022-09-30)

1.3 o And Spectra

The spectra below are typical spectra from the star o And. The rapid rotation of the star results in a broadening of the line due to the Doppler effect, with shorter wavelengths (violet) to the left and longer (reddish) wavelengths to the right. It should be noted that the Hα line is complex and the star's rotational velocity is usually not estimated by examination of this line. The spectrum presented below in Figure 3 was obtained in July 2013 and shows no indication of emission and therefore no evidence of the existence of a disk. The spectrum in Figure 3 is overlaid on the spectrum of a different B star that has never exhibited emissions for comparison purposes.

The spectrum presented in red in Figure 4 was obtained on August 24, 2023, and is superimposed on the spectrum from July 11, 2013. This spectrum shows emission due to the presence of a disk which is Doppler shifted such that there is a V wing (violet shifted, disk rotating towards us), while the portion of the disk rotating away from us is shifted toward the red end of the visible spectrum, i.e. the R wing. The greater the velocity, the greater the shift. Since the peaks are shifted less than the outer extent of the wings, the most intense light must be coming from portions of the disk that are moving slower than the light from the faster moving portion of the disk close to the star's surface. The disks around Be stars are believed to be 'Keplerian' in nature (Carciofi 2011, Rivinius et al. 2013, Labadie-Bartz et al. 2018, Labadie-Bartz et al. 2022, Labadie-Bartz et al. 2025), that is, they obey Kepler's laws in which objects farther out from the center of rotation move more slowly than objects close to the center. (For example, Mercury moves at a higher velocity

in its orbit than does Neptune.) We can therefore infer that the most intense Hα emission is from well out onto the circumstellar disk, perhaps in the range of 5 to 15 stellar radii as suggested by Rivinius et al. (2013).

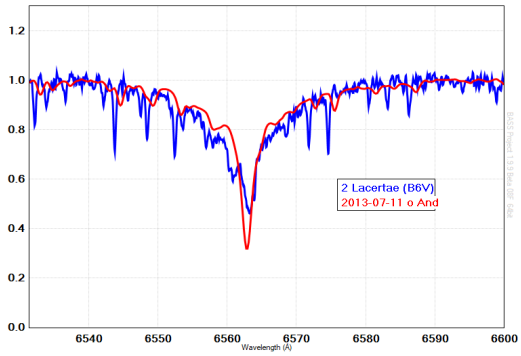

Figure 3. The Hα line is located at 6562.8Å. The other lines are telluric lines caused by the Earth's atmosphere. The spectrum of o And (red) was obtained on July 11, 2013; for comparison, a spectrum of 2 Lacertae, a B star of the same spectral type as o And but with no emission history is provided as a comparison.

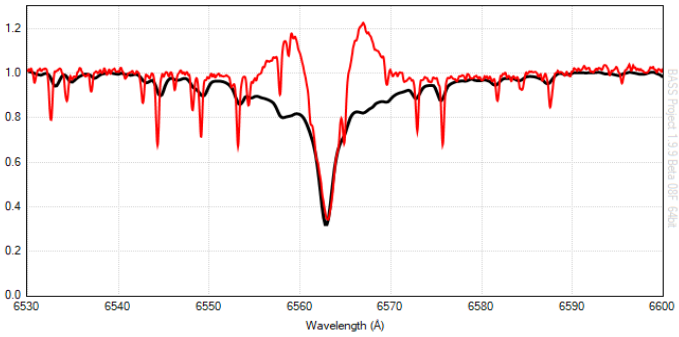

Figure 4. The spectrum in red was obtained on August 24, 2023 and is superimposed on the (black) profile from July 2013.

The central depression is due to absorption in the photosphere and the innermost regions of the disk. The shape of the profile, with its deep central depression, is a complex phenomenon, and the astrophysics of this shape is beyond the scope of this paper. The interested reader is referred to Hummel (1994) and Hanuschik et al. (1996).

2. Data Sources

There were two sources of spectra for this study: the BeSS database, and spectra acquired personally by the author. The BeSS database (Neiner et al. 2007) is populated with spectra obtained, processed, and uploaded by various amateur astronomers around the world. For this study 110 spectra dating as far back as 1994 were downloaded and found to be applicable and usable in this project, providing a 32-year history of this star. The downloaded spectra had signal-to-noise (SNR) values ranging from 77 to 549, as well as R values (resolving power) ranging from about 8,000 to 17,000. The steps used to derive quantitative data from these spectra are

described later. In addition, the author personally obtained 125 spectra of o And during an intensive study of its short-term behavior during 2023 to 2025. These spectra typically had an R value of 14,000, and SNR values ranging from 82 to 381.

2.1 Instrumentation

The author's observations were obtained with a backyard system consisting of a 203 mm Schmidt-Cassegrain telescope with a StarEx spectroscope (Buil 2025). The spectroscope was equipped with a 2400 L/mm holographic grating, a 35 µm slit, and a cooled ASI183MM-Pro camera by ZWO, Inc. The nominal resolving power (R) was about 14,000 at 6563 Å.

2.2 Processing and quantification of line profile features

The raw exposures acquired by the author were processed using SpecInti (Buil and Desnoux, 2025) into 1D profiles following conventional processing practices. The continuum of each profile, including those from the BeSS database, was rectified (flattened) using a tool in the ISIS software (Buil, 2021). All profiles were imported into the BASS software (Paraskeva 2024) where the wavelength calibrations were confirmed or adjusted using the telluric line at 6516.50Å, scaled the same vertically, and the continuum normalized to 1.0. The BASS software was then used to measure the features of the Hα region.

The metrics of interest were the intensity of each of the wings and the depth of the Hα central depression as recommended in Trypsteen and Walker (2017) for the analysis of double peaked profiles as shown in Figure 5. Clark et al. (2003) stated that "the intensity of the shell feature (a function of the disc density integrated along the line of sight) rather than the total EW provides a better indication of the mass content of the circumstellar disc for o And." Hummel and Vrancken (1995) used the intensity of the peaks and central depression of the Hα line in their study of non-axisymmetric Be star disks. This measurement approach was also used by Escolano et al. (2015).

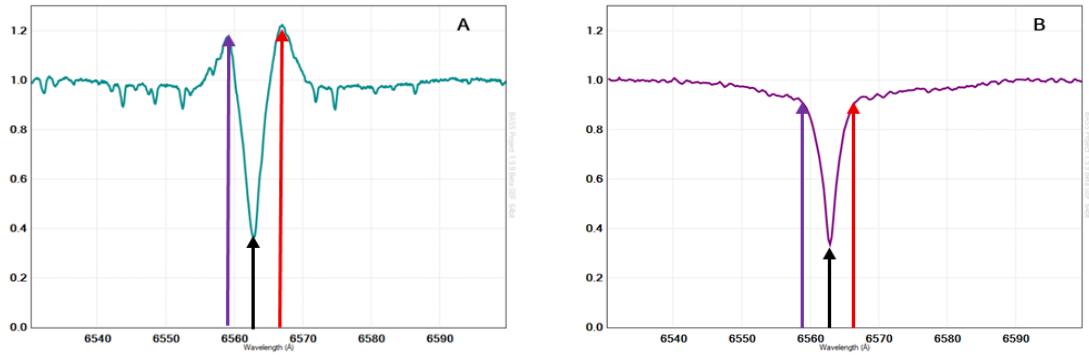

Figure 5. Illustration of how the features of the Hα line were measured, both when wings were present (A) and when they were not (B). The continuum was rectified and normalized to a value of 1.0.

The wavelength regions used for searching for the peak values were 6557Å to 6560Å for the V wing and 6566Å to 6567.5Å for the R wing. It was found that the V and R wing peaks always occurred in these regions regardless of peak height. The central depression was deliberately forced to be exactly 6562.8Å. Henceforth, this report will refer to the intensities of the V and R 'regions' because when the emission peaks are absent, as shown in Figure 5B, the measurements represent the descending portion of the broadened absorption line. For convenience, the intensity measurements were then converted to a value above or below the continuum by subtracting 1.0 from the measured value.

3. Results and Discussion

The intensities of the V and R regions for all spectral profiles have been plotted in Figure 6. This dataset began on July 25, 1994 (Julian Date 2449559). In the following charts, an adjusted JD has been provided setting JD 2449550 as day 0. The charts are also provided with the time in years after that JD. The existence of the disks and their density/extent are here inferred from the intensity values, knowing that this is a crude approximation.

Over this 32-year historical period, we observe that there have been four disks. Unfortunately, there are gaps in the data, especially for the first disk and the second disk. The third and fourth disks are well defined, except there is an unfortunate data gap for the assumed maximum point of the fourth disk. The minima are well defined in every case. In each cycle, there is steady growth, with some isolated periods of brief increase/decrease of the disk, to a maximum before the disk begins to dissipate. We do not see a lag at the minimum points before the next disk begins to form. The current hypothesis for Be star disk formation is that mass ejections from the photosphere add material to the disk which is incorporated and circularized into the disk. It then either eventually falls back into the photosphere or is lost to space (Carciofi 2011, Labadie-Bartz et al. 2018, Labadie-Bartz et al. 2022, Labadie-Bartz et al 2025). Thus the disk exists as a dynamic balance between gains and losses of matter.

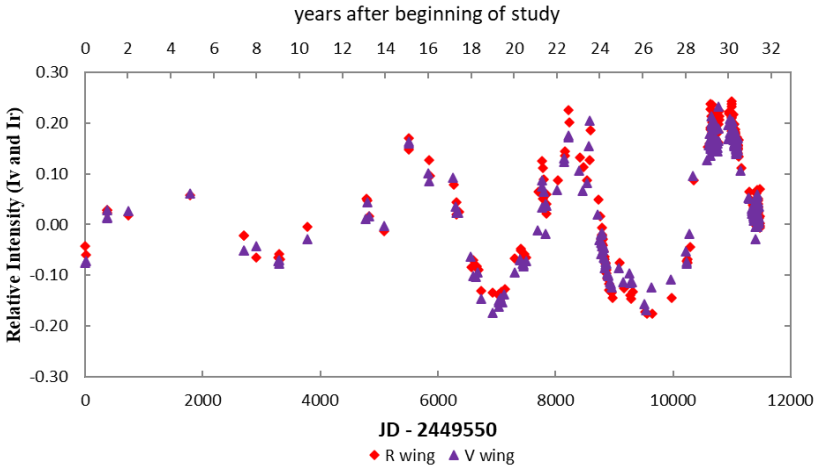

Figure 6. Measurements of the peak values are presented for both the V region and the R region for each of the 235 spectra in the dataset. Each datapoint represents the measured intensity of the peak above or below the continuum, which was normalized to a value of 1.0.

In general, it appears that the peak intensity of the disks increased with each successive disk, and the dissipation of the disks became more complete at the end of Disk 2 and Disk 3 compared to Disk 1. We have not yet reached the complete dissipation of the current disk.

Disk 1: The first data point in our dataset is - 0.06 relative intensity units. The minimum point at the end of the first disk cycle is - 0.073 at day 3310 (August 8, 2003, year 9.06). If the formation and dissipation of the disk was symmetrical, then the peak intensity of Disk 1 would have occurred at around 4.5 years. Unfortunately, we have a gap between the observations at 2.02 years and 4.9 years and so we cannot confirm that supposition. Example profiles have been provided for the earliest observation of the star, the maximum profile, and the profile at the end point of Disk 1. Notice that the shoulders of profiles A and C in Figure 7 are a bit squared off when compared to the profiles presented in Figure 3. This suggests that the disk may not have been completely absent on these dates. Acknowledging the incompleteness of the data for this first disk, it appears that it lasted for a minimum of nine years.

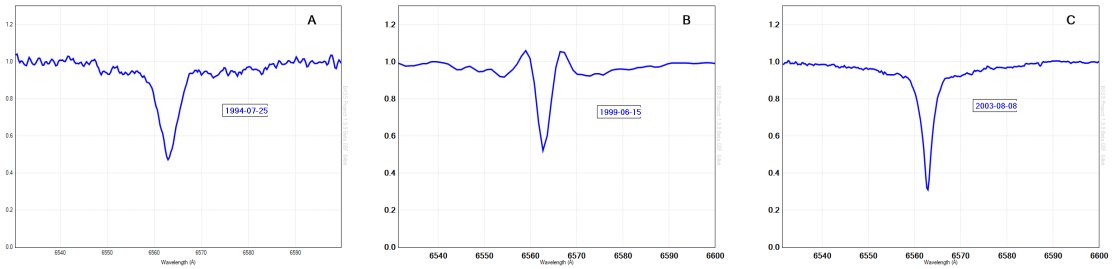

Figure 7. Profiles illustrating the evolution of the Hα line and the life cycle of the first disk in our history. A: July 25, 1994, B: June 15, 1999; C: August 8, 2003.

Disk 2: This disk reached its maximum intensity in August 2009, as shown in Figure 8 and 9B. The record of growth of this disk was unfortunately incomplete. The growth phase lasted for about 6 years until reaching a maximum intensity at Year 15.2. It then took another 4 years for the disk to dissipate, for a total elapsed time of about 10 years. This asymmetric pattern shows that the rate of growth of the disk was slower than the dissipation phase. Additionally, the dissipation of Disk 2 appears to be more complete compared to the previous minimum since the 'shoulders' we observed in the 2003 profile are absent in the 2013 profile (Figure 9C). The C profile from Figure 7 is copied as the A profile in Figure 9 below for ease of comparison.

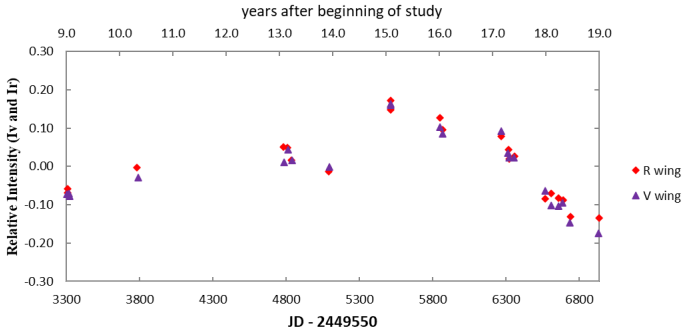

Figure 8. Lifecycle history of disk 2 showing a peak intensity in August 2009 at year 15.2.

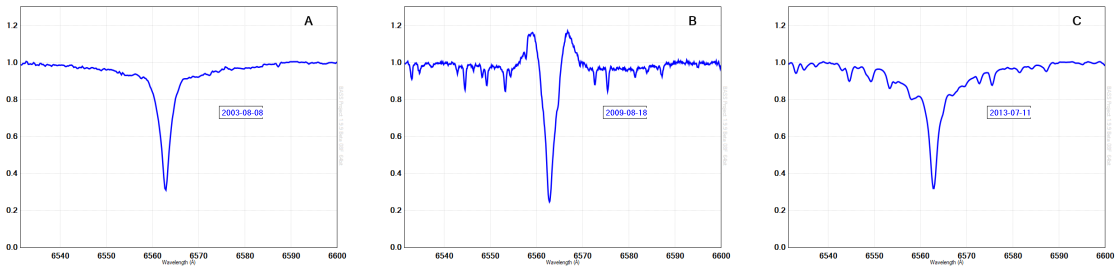

Figure 9. Profiles illustrating the evolution of the Hα line and the life cycle of the second disk in our history. A: August 8, 2003, B: August 18, 2009; C: July 11, 2013.

Disk 3: The disk that began to form in 2013 (year 18.98) grew until January 2017 (year 22.5), when it dissipated slightly for about nine months (minimum at year 23.4), and then quickly brightened again, reaching a second peak in January of 2018. There was also variation in the intensity of the disk in 2015 (year 21), which shows rapid disk growth and dissipation before growth continued again. These variations are presented in detail in Figure 10 and make it difficult to specify a single maximum for this disk cycle. Notice that during the peak on day 8,227 (year 22.5) the R wing was brighter than the V wing, while the peak at day 8,596 was for the V wing. These variations between the V wing and the R wing are typical for this and many other Be stars and are discussed in detail in Diz (2024), Diz (2025), Carciofi (2010), and many of the other sources cited herein. After the peak in January 2018 (year 23.5), the disk began a period of continuous dissipation until reaching a minimum less than three years later in September 2020 (year 26.16). Again, this record indicates that the growth of this disk (~ 4.5 years) was slower than was the dissipation phase (~ 3 years) for a total lifetime for this disk of about 7 years. Spectral profiles for this disk are presented in Figure 11. Notice that the C profile in Figure 11 does not have the 'shoulders' noted at an earlier disk endpoint. This suggests that the disk had completely dissipated.

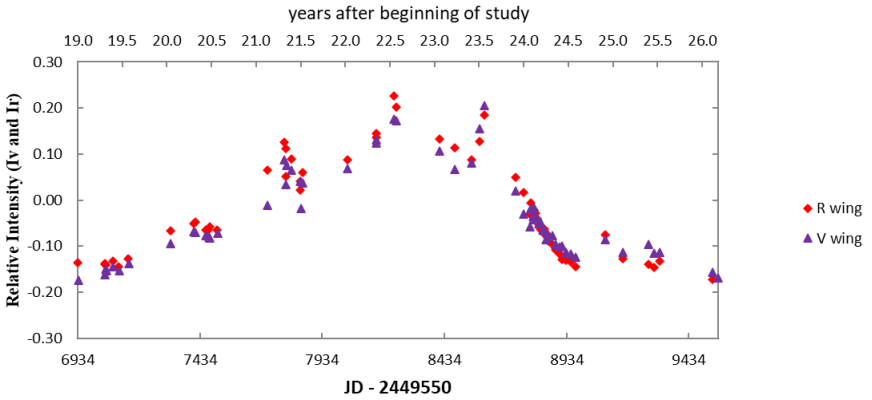

Figure 10. Lifecycle of disk 3. There were several episodes during which disk growth was followed by dissipation, and then growth again, ultimately reaching a peak intensity at year 22.5, with lesser peaks at year 21.3 and year 23.5.

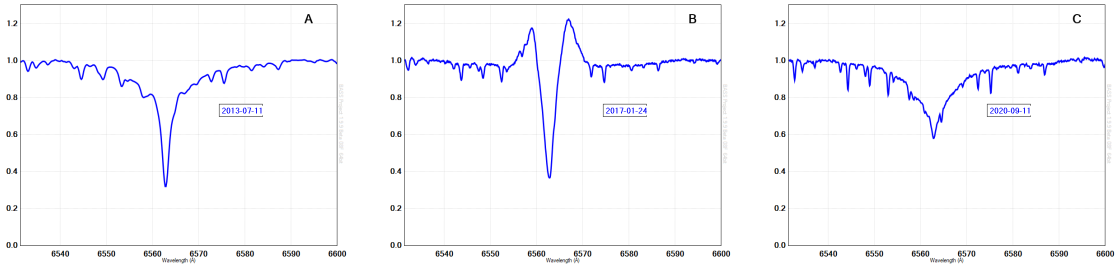

Figure 11. Profiles illustrating the evolution of the Hα line and the life cycle of the third disk in our history. A: July 11, 2013, B: January 24, 2017; C: September 11, 2020.

Disk 4: The record for Disk 4 is incomplete because it has only partially dissipated as of this writing. The growth of Disk 4 began in September 2020. A possible peak intensity was recorded on December 18, 2023 (day 10,747, year 29.42) and again in August 2024. Unfortunately, there is a data gap of about six months when the star was unobservable from the author's location and no spectra were available from the BeSS database. It is reasonable to assume that we missed the peak intensity of this disk cycle during this gap.

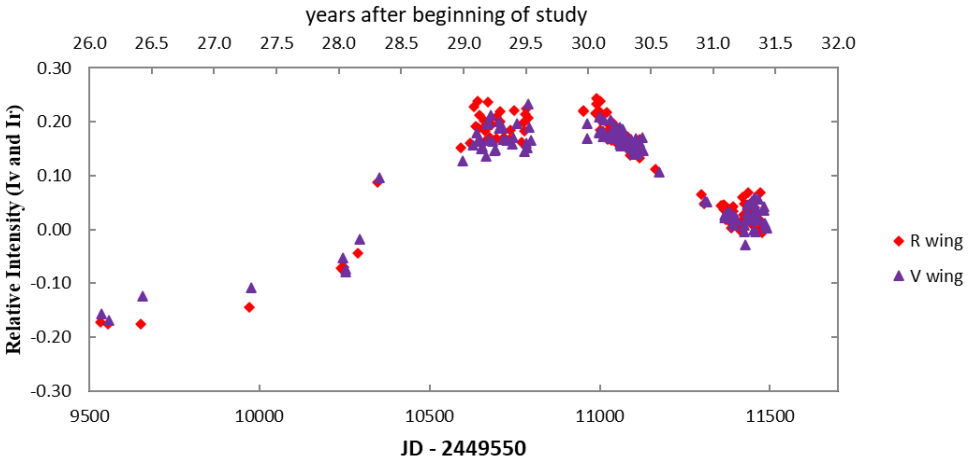

Figure 12. Lifecycle of Disk 4. The growth phase of this disk appears curvilinear but lacked the intermittent growth/dissipation seen previously. In this case there was a gap that may have been the time of peak intensity. It appears that a pause in dissipation and some slight regrowth was occurring as our dataset reached its end.

Representative spectral profiles for disk 4 are presented in Figure 13. The A profile from October 3, 2024, was among the highest peaks observed during the Disk 4 cycle. Slightly more than a year later, the emission peaks had diminished as shown in profile B, observed on December 20, 2025.

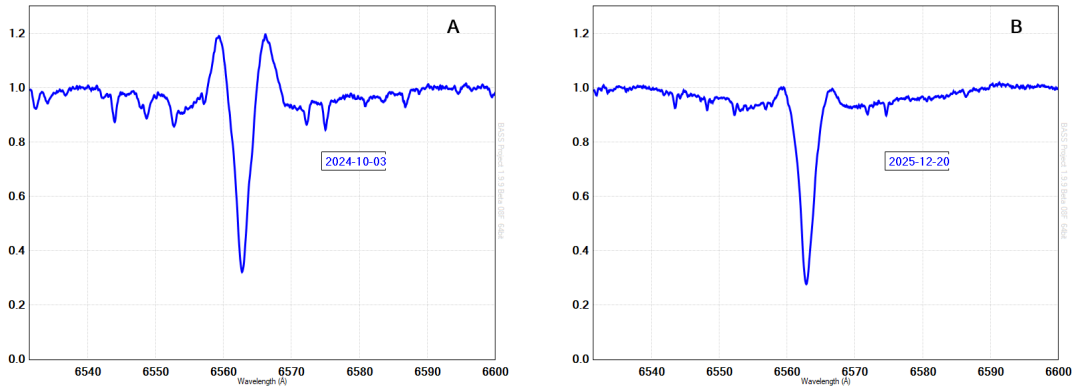

Figure 13. Spectral profiles for disk 4. Profile A was obtained in October 2024 near the peak intensity of disk 4, and profile B was the final profile obtained in the study in December 2025.

4. The Central Depression

The astrophysics of the shape and depth of the central depression of the Hα line is complex as has been mentioned above. The velocity, temperature, and density of the photosphere and of the gases of the disk affect the absorption/emission of photons and are not uniform either from time to time or from place to place. The influence of the kinematics of the disk, the temperature, and the density of the circumstellar gases on absorption/emission are beyond the scope of this paper, and the reader is referred to the literature already referenced. An additional factor influencing the data presented below is that the continuum of each spectrum was normalized to 1.0. Some information may have been lost that would have been of interest if the absolute flux of each spectrum had been determined. That was not possible with the limited information available.

Figure 14 presents the depth of the central depression superimposed on the wing intensity (here the intensities of the two wing regions have been averaged to simplify the chart). The general trends of the two datasets mirror one another, but in most cases there is an offset such that the central depression depth pattern leads that of the wings. This is obvious for Disks 2, 3, and 4, but it is not clear that this holds true for Disk 1. This may or may not be due to incomplete data coverage. For Disk 2, the delay between minima was 20 months; for Disk 3, it was 26 months. For Disk 4, a minimum in the central depression depth was reached in August 2025. If this pattern holds, we may see the end of Disk 4 sometime in the spring or summer of 2027. Interpretation of the relationship between the central depression depth and the growth/dissipation behavior of the disk is best left to more competent astrophysicists.

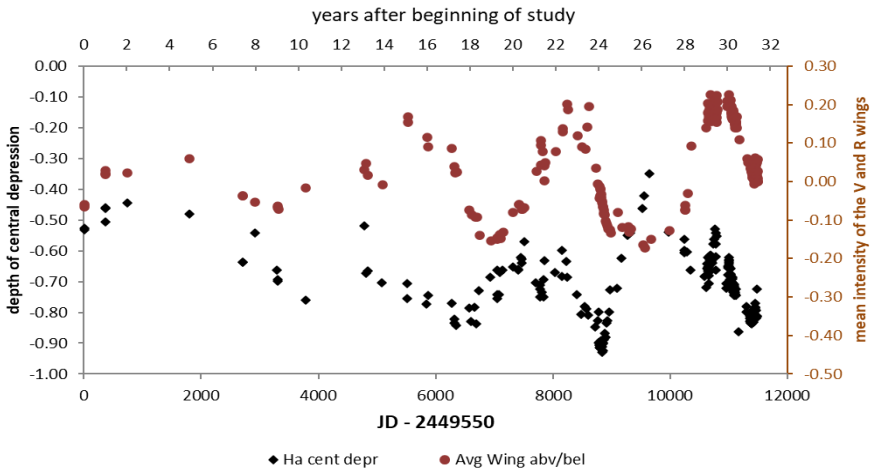

Figure 14. The 32-year history of the depth of the central depression (black), along with the mean of the intensities of the V and R regions (red).

5. Conclusion

The current explanation for disk building is that the momentum from the eruption/ejection of matter from the star's surface combined with the lessened surface gravity at the equator (due to the equatorial bulge), and centrifugal force due to the rapid rotational velocity is sufficient to place material into orbit around the star, forming the disk. Therefore, eruptions of matter from the photosphere are the prerequisite for disk formation.

In our study of the thirty-two-year history of the Be star *omicron Andromedae*, we see that the star has built and lost its circumstellar disk four times for an average of disk lifetime of about eight years. The data suggests that the star goes through eruptive episodes lasting about four to five years that result in disk building. This is followed by about three to four years during which eruptions cease or become less frequent, such that new material is not added at a sufficient rate to counter the continuous loss of material that either falls back to the surface or evaporates into space. Rarely, if ever, is a dynamic equilibrium achieved, at least in this brief history of this star, that results in a stable long-lasting disk.

Acknowledgements

This research has made use of the SIMBAD database, operated at CDS, Strasbourg, France. This research has made use of the International Variable Star Index (VSX) database, operated at AAVSO, Cambridge, Massachusetts, USA. My sincere thanks are offered to the amateur astronomers who contributed spectra to the **BeSS** database, operated at LESIA, Observatoire de Meudon, France: http://basebe.obspm.fr. Specifically, spectra of o And that were used in this study were contributed by (in no particular order): K. Graham, C. Sawicki, M. Leonardi, E. Barbotin, J. Guarro, J. Montier, T. Garrel, P. Lailly, N. Montigiani, M. Mannucci, F. Houpert, J. Daglen, J-N. Terry, E. Bryssinck, A. Stiewing, A. Gendron, V. Desnoux, C. Buil, O. Thizy, J. Ribeiro, P. Shlatter, A. Favaro, A. de Bruin, R. Leadbeater, D. Mohrbacher, E. Bernard, V. Anzallo, S. de Visscher.

References

AAVSO. 2025, The International Variable Star Index (VSX) of the American Association of Variable Star Observers. https://www.aavso.org/.

Bossi, M., Guerrero, G., Mantegazza, L. 1977, *Astronomy and Astrophysics, Suppl. Ser*., **29**, 327.

Briot, D., Chauville, J., and Guerrero, G. 2002, in *ASP Conference Series*, Vol. **259**. pp. 250-251.

Buil, C. 2021, ISIS (Integrative Spectrographic Innovative Software), https://buil.astrosurf.com/isis-software.html

Buil, C. 2025, The Solex/Starex Project: http://www.astrosurf.com/solex/sol-ex-etoiles.html .

Buil, C. and Desnoux, V. 2025, SpecINTI and SpecINTI Editor: website retrieved April 2025, http://www.astrosurf.com/solex/specinti1_en.html.

Caldwell, D.A., et al. 2020, TESS Science Processing Operations Center (SPOC) data, accessed via the Mikulski Archive for Space Telescopes (MAST).

Carciofi, A. C. 2010. *Proceedings IAU Symposium No. 272,* Neiner, Wade, Meynet, Peters, eds.

Carciofi, A. C. 2011, in *IAU Symposium, Active OB Stars: Structure, Evolution, Mass Loss, and Critical Limits*, ed. C. Neiner, G. Wade, G. Meynet, & G. Peters, Vol. **272**, 325–336

Clark, J. S., Tarasov, A. E., and Panko, E. A. 2003, *Astron. Astrophys.* **403**, 239-246.

Diz, H.R. 2024. *JAAVSO*, Volume **52**(2), pp 202-215.

Diz, H. R. 2025. *Proceedings for the 44th Annual Conference of the Society for Astronomical Sciences,* Ontario, CA; J. Martin and R. Buchheim, eds. pp 7-16.

Escolano, C. et al. 2015, *Astron. Astrophys.* **576**, A112

Hanuschik, R. W., Hummel, W., Sutorius, E. Dietle, O., and Thimm, G. 1996, *Astron. Astrophys. Suppl. Ser.* **116**, 309-358.

Harmanec, P. 1987, in *Proc. 10th European Regional Astronomical Meeting of the IAU, Publication of the Astronomical Institute of the Czechoslovak Academy of Sciences*, Publication No. 70, Astrophysics, ed. P. Harmanec, (Praha: Czechoslovak Academy of Sciences), p. 171.

Hill, G. M., Walker, G. A. H., Dinshaw, N., Yang, S., and Harmanec, P. 1988, *Publ. Astron. Soc. Pacific* **100**, 243

Hummel, W. 1994, *Astron. Astrophys.* **289**, 458-468.

Hummel, W. and Vrancken, M., 1995, *Astron. Astrophys.* **302**, 751-764.

Labadie-Bartz, J., Carciofi, A., et al. 2022, *Astron. J.* **163**, 226.

Labadie-Bartz, J., Chojnowski, S. D., et al. 2018, *Astron. J.* **155**, 53.

Labadie-Bartz, J. et al. 2025, *Astron. Astrophys.* **699**, A82

Mitrofanova, A., Dyachenko, V., Beskakotov, A., Balega, Yu, Maksimov, A., Rastegaev, D. 2021, *Astron. J.* 1**62** (4), 156.

Neiner, C., de Batz, B., Mekkas, A., Cochard, F., & Martayan, C. 2007, in SF2A-2007: *Proc. Annual meeting of the French Society of Astronomy and Astrophysics*, eds. J. Bouvier, A. Chalabaev, & C. Charbonnel, 538.

Olevic, D. and Cvetkovic, Z. 2006, *Astron. J.* **131**, 1721-1723.

Paraskeva, J. 2024, BASS: Basic Astronomical Spectroscopy Software, https://groups.io/g/BassSpectro

Porter, J. and Rivinius, T. 2003, *Publ. Astron. Soc. Pacific* **115,** 1153

Rivinius, T., Carciofi, A., and Martayan, C. 2013, *Astron. Astrophys. Review* **21**, 69.

Sareyan et al. 1998, *Astron. Astrophys.* **332**, 155-164.

Stagg, C. R., Bozic, H., Fullerton, A., Gao, W.W., Guo, Z. H., Harmanec, P. 1985, *J. Roy. Astron. Soc. Canada* **79**, 243.

Stagg, C.R., Bozic, H., Fullerton, A.W., et al. 1988, *Mon. Not. Roy. Astron. Soc*. **234**, 1021-1049.

Tokovinin, A. 2018, *Astrophys. J. Suppl. Ser.* **235** (1), 6

Trypsteen, M.F. and Walker, R. 2017, *Spectroscopy for Amateur Astronomers*, Cambridge University Press, Cambridge, UK

Wenger, M., Ochsenbein, F., Egret, D., Dubois, P., Bonnarel, F., Borde, S., Genova, F., Jasniewicz, G., Laloë, S., Lesteven, S., & Monier, R. 2000, The SIMBAD astronomical database, *Astron. Astrophys. Supplement Series* **143**, 9-22.

Zhuchkov, R., et al. 2010, *Astron. Rep*. **54** (12), 1134-1149

Bridging Education and Discovery: A High School Program in Variable Star Research

Ian Doktor

Edmonton Public Schools, 8950 163 Street, Edmonton, AB, T5R-2P2, Canada;
ian.doktor@epsb.ca

Subject Keywords

Citizen Science, Education, Outreach, Robotic Telescopes, Inquiry

Abstract

This article describes a three-course high school astronomy program at Jasper Place High School (Edmonton, Alberta) designed to bridge classroom learning and authentic participation in astronomical discovery. Over seven years, students have conducted close to twenty inquiry-focused research projects involving exoplanet transits, cataclysmic and pulsating variable stars, and spectroscopic studies of galaxies. Using robotic telescope networks such as SkyNet and AAVSOnet—supplemented by their own observations—students developed research proposals, acquired and reduced data, performed photometric and spectroscopic analyses, and publicly disseminated their results through astronomy clubs, science fairs, and contributions to variable-star databases. Grounded in a five-phase inquiry cycle, the program demonstrates how citizen-science–based photometry can foster scientific literacy, data-analysis skills, and long-term engagement with STEM while enabling high school students to make genuine contributions to astronomy research.

1. Introduction

Variable star astronomy, unlike many other scientific disciplines, is well positioned to allow students and citizen scientists to make real contributions to scientific discovery (Christian et al., 2012; Straub, 2016). Astronomy is an ideal science for students to engage in authentic research experiences where they can develop discipline related knowledge and skills, as well as make contributions to the development of new astronomy knowledge. Providing high school students with these learning opportunities is the primary goal of the astronomy program that will be described in this paper.

Preparing students to be future astronomers requires more than teaching them the necessary science content. Participating in scientific discovery requires an inquiring mind and developing the skills and attitudes necessary for that inquiry is often overlooked in traditional science education programs. According to Pedaste et al. (2015) one approach to developing the necessary attributes for scientific discovery comes from an Inquiry cycle which consists of 5 key phases:

1) Orientation – Students are introduced to a question or problem
2) Conceptualization – Students formulate a research question, generate hypotheses, and broaden their interest in the problem.
3) Investigation – Students conduct background research and gather data. This is then followed by data analysis and interpretation.
4) Conclusions – Based on their investigations, students draw inferences and summarize their findings.
5) Discussion and reflection – Students share their findings with peers, teachers, and the public.

Using this inquiry cycle as a framework for astronomy education, students at Jasper Place High School in Edmonton, Alberta have completed several citizen science projects focused on variable star research. The astronomy program described below allowed students to observe and analyze variable stars, contribute to variable star databases, and develop enduring relationships with professional astronomers, while at the same time being active participants in the process of scientific discovery.

Each of the three astronomy courses offered use inquiry cycles as a model for inquiry in science education. The three courses involve increasingly sophisticated astronomy knowledge and skills and are arranged as:

1) Astronomy 15 – Introduction to Astronomy
2) Astronomy 25 – Introduction to Astrophotography
3) Astronomy 35 – Astronomy Research

The purpose of these three courses is to bridge classroom learning and authentic scientific contribution through investigations that have made use of AAVSOnet and photometric data analysis.

2. Program Design and Pedagogical Framework

Astronomy 15 is designed as an introductory course in astronomy that includes a diverse range of topics from stargazing, the solar system, stellar evolution, variable stars, and cosmology. Students learn how to construct and use telescopes, the foundations of star gazing and the celestial sphere, and are introduced to the HR-diagram, Hubble's Law, and the nature of light. Learning activities include tools such as Stellarium, the AAVSO Variable Star Plotter, and a variety of citizen science projects hosted at www.zooniverse.org.

Astronomy 25 shifts the focus from astronomy knowledge to astrophotography. Students are required to participate in stargazing and are instructed in the use a variety of cameras – ranging from the cameras available on cell phones to DSLRs to astronomy specific CMOS and CCD cameras. After acquiring their own images (or using previously taken photos), students apply calibration frames, before processing and editing the results. Additionally, students are taught

about the operations and architecture of modern digital cameras including sensor linearity, noise, and pixel size.

Astronomy 35 is centered around inquiry-based astronomy research. The first task for students is to write a research proposal related to a problem or question in astronomy. Past topics have included using the companion star of Cygnux X-1 to better understand the black hole itself, exoplanet transit observations, and investigating the nature of Tabby's star. The research project then involves students conducting a literature review and creating an observation plan. After gathering data, students reduce and analyze the data before sharing it through presentations in school and at local astronomy clubs, writing reports, and entering in local science fairs.

The astronomy research course is designed around an inquiry cycle which focuses on the five phases discussed above (Orientation, Conceptualization, Investigation, Conclusion, and Discussion). This framework provides students with a useful scaffold where they are first introduced to different types of variable star research, generate their own questions, design and carry out a research plan, and summarize their results. Student autonomy is central to this approach and ensures students take ownership of their learning.

3. Research in Practice

The tools available through AAVSO (and other organizations like Skynet) have been instrumental in allowing this type of inquiry project to be accessible to high school students. In using AAVSOnet, for example, students are expected to write a short research proposal. This proposal includes a short explanation of their project, the object of interest, and the observation times. After a proposal has been accepted and students begin to acquire data, students then analyze their data using a variety of tools which have included IRIS, Muniwin, and VPhot.

Over the past seven years students have completed close to twenty different research projects. A notable project example from 2022 involved two grade 12 students who observed transit of a Qatar-9b using AAVSOnet. Their results were used to create the light curve shown in Figure 1.

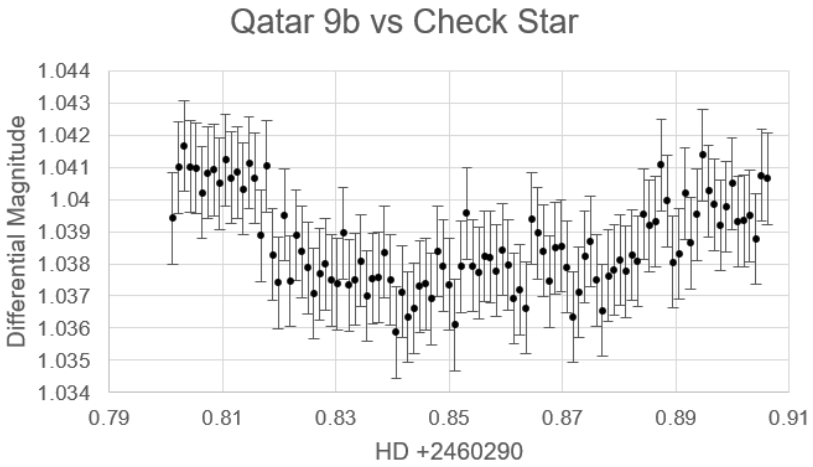

Figure 1. Students' Light Curve of Qatar 9b

In 2024 a different group of students made observations of HD226868 as it orbits Cygnus-X1. The results of their analysis allowed them to estimate the mass of the Cygnus X-1 black hole. Part of their results are shown in Figure 2.

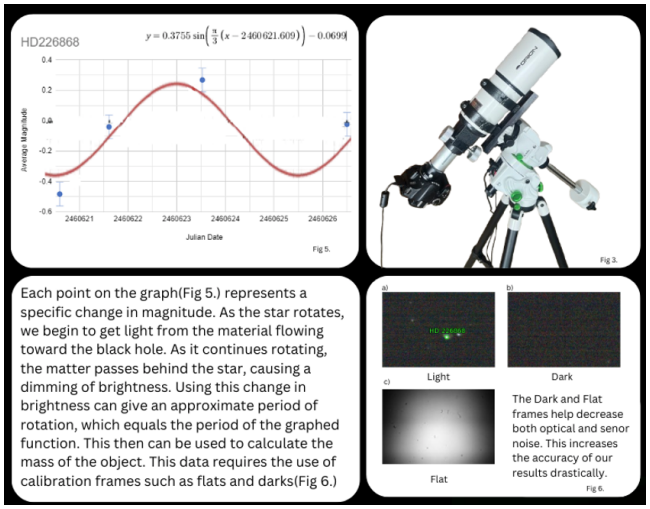

Figure 2. Sample Student Work from a Project Involving Cygnus X-1

Other projects included spectroscopic observations of galaxies, allowing students to recreate Hubble's Law, shown in Figure 3.

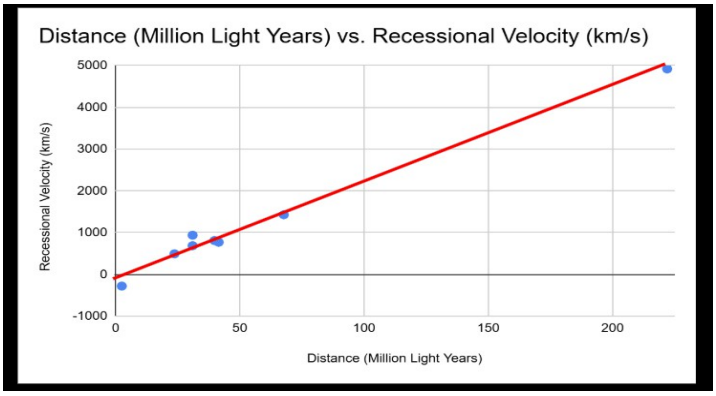

Figure 3. Students' Analysis of Spectroscopic Observations

During the past seven years, students have completed dozens of similar research projects. The culminating activity of each project is for students to share their knowledge. Over the years this has taken many forms including entries into Science Fairs, presentations at local astronomy group meetings, contributing to variable star databases, and publishing articles related to their work (e.g. Noshin, 2017).

4. Outcomes and Educational Impact

High school astronomy research such as these projects can have both educational and scientific impact. On the educational side, students demonstrated improved data literacy, reasoning, and

epistemological understanding of science. These observations are supported by Price and Lee (2013) who reported that astronomy related citizen science projects have positive impacts on students' Scientific Literacy.

Looking at the results from a purely science standpoint, students can contribute to variable star databases. In addition, this type of early participation in real world science fosters long term engagement with STEM related disciplines (Archer & DeWitt, 2020). High school students who participate in authentic, astronomy focused research are more likely to continue into a STEM related career.

5. Conclusions and Future Directions

Variable star astronomy is uniquely positioned to engage high school students in authentic research activities. As this course sequence demonstrates, students can participate in all aspects of the research process including proposal writing, gathering and analyzing data, forming conclusions, and sharing their results. Such citizen science photometry projects improve students' engagement with STEM as well as producing valuable scientific results.

Despite the success of this program, the entire area of secondary science astronomy research is relatively unstudied. Not only does this suggest further research from the science education community is needed, but it presents organizations like AAVSO with an important opportunity to aid students' development from enthusiastic amateurs to professional scientists.

References

Archer, M., & DeWitt, J. (2021). Thanks for helping me find my enthusiasm for physics: The lasting impacts "research in schools" project can have on students, teachers, and schools. *Geoscience Communication. 4*(2), 169–188. https://doi.org/10.5194/gc-4-169-2021

Atiah, N., Dang, H., Sewell, G., Funk, R., Vaiji, K., & Shahid, T. (2018). Introduction to photometry. *JRASC, 112*(3), 116–120.

Christian, C., Lintott, C., Smith, A., Fortson, L., & Bamford, S. (2012). *Citizen science: Contributions to astronomy research*. *arXiv* preprint arXiv:1202.2577.

Pedaste, M., et al. (2015). Phases of inquiry-based learning. *Educational Research Review, 14*, 47–61.

Price, A., & Lee, H.–S. (2013). Changes in participants' scientific attitudes and epistemological beliefs during an astronomical citizen science project. *Journal of Research in Science Teaching, 50*(7), 628-654. https://doi.org/10.1002/tea.21090

Straub, M. C. P. (2016). Giving citizen scientists a chance: A study of volunteer-led scientific discovery. *Citizen Science: Theory and Practice, 1*(1), 5. https://doi.org/10.5334/cstp.40

The Extraordinary Intermediate Polar DW Cnc

Juan Echevarría, Alejandro Ruelas, and Ivan Mora Zamora

Instituto de Astronomía, UNAM, Universidad Nacional Autónoma de México, Instituto de Astronomía, AP 70-264, CDMX 04510, México; jer@astro.unam.mx

Subject Keywords

AAVSO International Database; Photometry, CCD; Cataclysmic Variables; stars: individual (DW Cnc)

Abstract

We present a review of the latest years of observations of DW Cancri, an extraordinary intermediate polar with only an 86 min orbital period. The disappearance and reappearance of its 38 min spin period, the high and low state, and the detection of mini-outbursts are highlighted. The contribution of the AAVSO and its database has been crucial to the understanding of the nature of this unusual object, including the recent interpretation of two short outbursts as a micro nova.

1. Introduction

Cataclysmic Variables (CVs) are interactive binaries in which a white dwarf (WD), accretes matter from a late-type secondary which fills its Roche Lobe. An accretion disc is formed around the compact star (e.g., Warner 1995).

DW Cnc was discovered by Stepanyan (1982), but it was identified as a variable star, possibly of the U Gem type, with high and low magnitude states in the V band ranging from $15 < V < 17.5$. It was designated as DW Cnc by Kholopov et al. (1981) and later classified as a dwarf nova in a low-resolution spectrum that presents intense Balmer and weak He I lines (Khopylov et al. 1988). Rodríguez-Gil et al. (2004) identified DW Cnc as a magnetic cataclysmic variable and found an orbital period of 86.10 ± 0.05 min, as well as another period of 38.58 ± 0.02 min which appeared to modulate the Hydrogen and He I lines. They proposed that DW Cnc was a VY Scl magnetic system, as well as a CV intermediate polar: they associated the second period of 38.6 min with the spin period of the primary star. Simultaneously, Patterson et al. (2004) also found an orbital period of 86.1 minutes and a spin period of 38.6 min, as well as a period of 69.9 min, associated with the beat period. The first detection of a short outburst was made on January 2007 by Crawford et al. (2008); DW Cnc had an increase in magnitude of the order of 4 mag reaching a maximum V magnitude of about 11.36. Segura Montero et al. (2020) observed DW Cnc in a low state and found that the spin signal was almost absent. They suggested that this may be due to a substantial decrease in the mass transfer and consequently a decrease in magnitude, which was confirmed by the AAVSO database. Such suggestion or prediction was confirmed by Duffy et

al. (2022) and Ramírez et al. (2022) who observed the recovery of the system and the return of the 38-minute spin signal. A recent paper by Veresvarska et al. (2025) present an interpretation of two 4 magnitude amplitude short outbursts, in 2007 and 2024, as evidence of micro-nova events.

2. The Initial Problem

The initial problem that prompted us to work on this object was the fact that the spin period found by Patterson et al. (2004) and Rodriguez-Gil (2004) was totally absent in our first spectroscopic observations in January 2021 (see Montero et al. 2020). After a careful power spectrum analysis, we concluded that the system was probably in a low state and therefore unable to transfer enough matter to jump the magnetic field of the white dwarf. To justify this hypothesis, we proposed that the mass transfer from the secondary was *blocked* and, if so, the light curve should show a decrease in magnitude. We searched in the AAVSO database and found that in fact there was a magnitude decrease of about 2 mag. Figure 1 shows the AAVSO light curve for near thirty years.

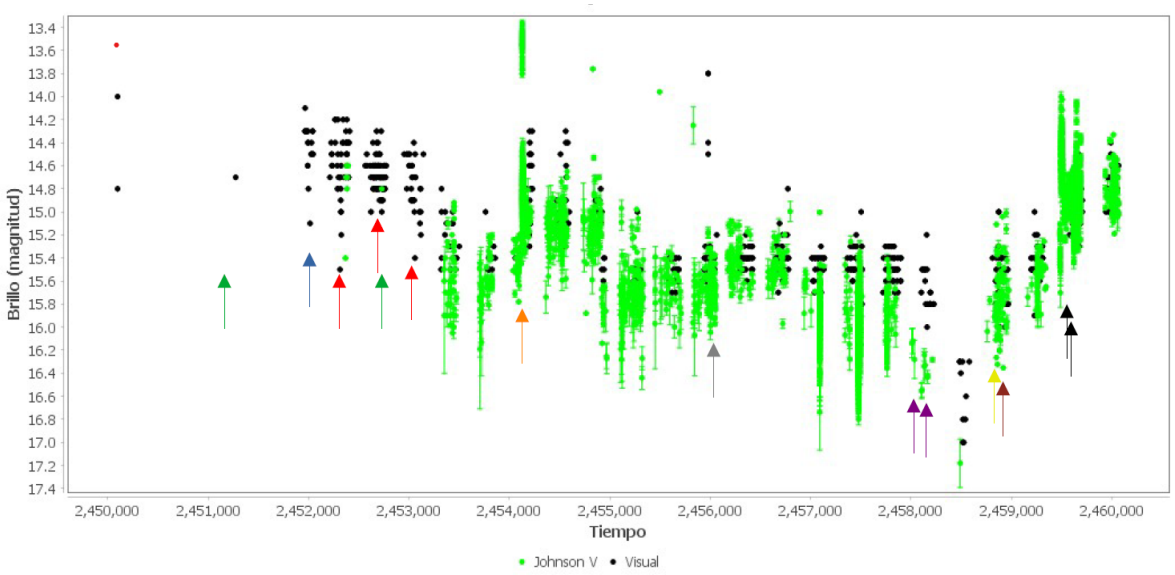

Figure 1. 30-year AAVSO light curve for DW Cnc.

It is clear that during 2018-2019 the system went into a low state, which agrees with our hypothesis.

3. Recovery to a High State?

In Segura Montero et al. (2020), we predicted that, once in the high state, the spin period should reappear. This was partially true as seen in the results by Duffy et al. (2022) and Ramirez et al. (2022); see the last three arrows in Figure 1. The spin signal was detected, but not with the strength observed by Patterson et al. (2004).

4. Back to Normal and More!

Figure 2 shows our last observations made with OPTICam, an optical camera that observes in three channels, with filters selected from the sloan filters, attached to the 2.1m telescope at San Pedro Mártir Observatory.

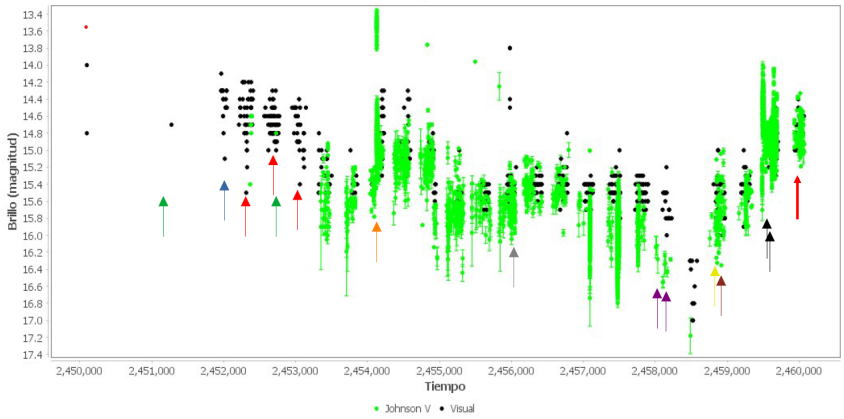

Figure 2. The extended AAVSO light curve of DW Cnc includes now our OPTICam observations (red arrow).

In these observations we were able to detect in full the spin period. The results shown in Figure 3 were not published by us alone, since they were requested by the Durham group and used as a collaboration to propose a complementary interpretation, which is explained in the next section.

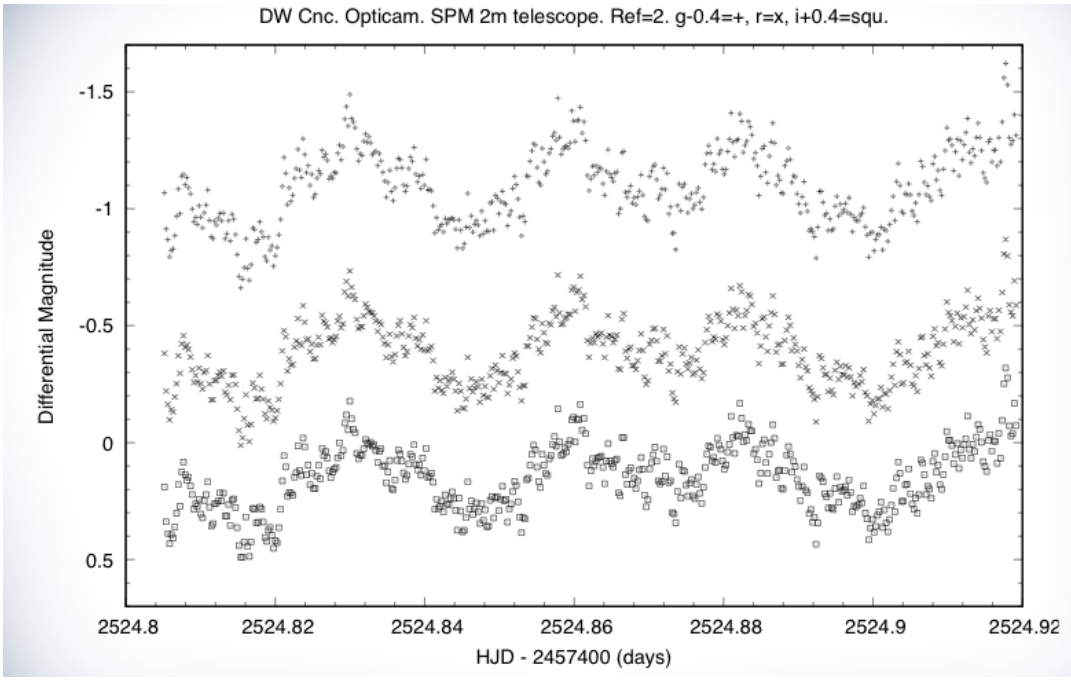

Figure 3. An example of the g, r, I light curves obtained with OPTICam, December 2022.

5. A Micro Nova with Negative Superhumps?

Combining our OPTICam data with *TESS, ASAS-SN* and *ATLAS* observations, Veresvarska et al. (2025) published an interesting interpretation of two 4 mag short outbursts, the first observed by Crawford et al. in 2007 and the second detected by *ASAS-SN* in late 2021, as shown in Figure 4.

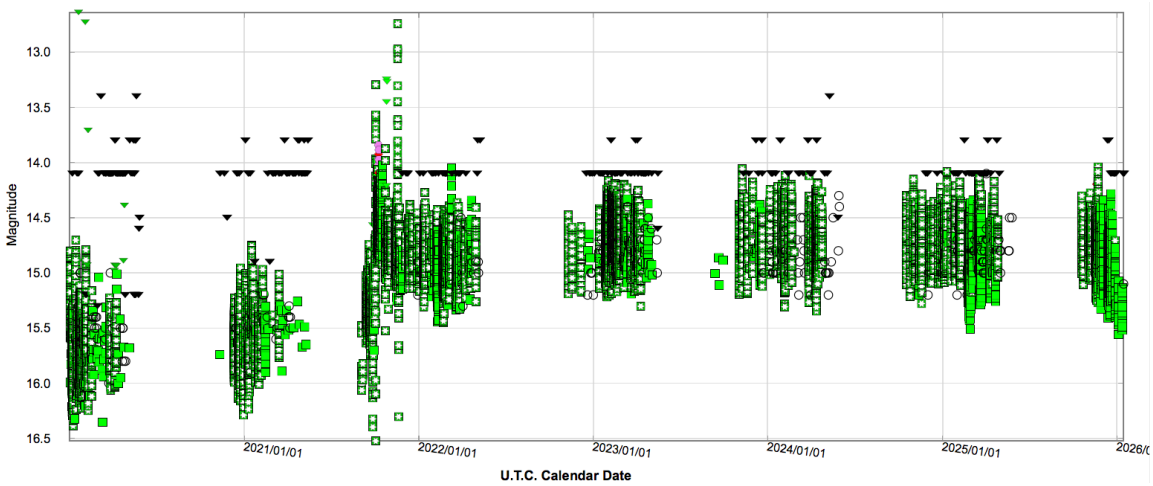

Figure 4. The AAVSO DW Cnc light curve around the second short outburst.

Veresverska et al. (2025) also discuss all frequencies detected with all the instrumental arrays and note also the presence of a frequency of 16.92 c/d which is associated with a negative superhump.

6. Conclusions

DW Cnc is an intermediate polar, now well studied, that shows a complex behavior as shown in the 30-year AAVSO light curve.

We have presented solid data that support our explanation of a two-year low mass transfer episode from the secondary star, which in turn results in a two-magnitude decrease; hence the lack of the spin signal that originates from the magnetic poles of the white dwarf.

We presented new data from TESS, ASAS-SN, ATLAS and OPTICam. A new short outburst of around 4 mag was reported, similar to the one in 2007, that leads to the interpretation of a micro-nova outburst and a negative superhump.

References

AAVSO. 2000-2025 observations from the AAVSO International Database http://www.aavso.org).

Crawford et al. 2008, *J. Am. Assoc. Var. Star Obs.* **36**, 60
Duffy et al. 2022, *MNRAS*, **510**, 1002
Kholopov et al. 1981, *Information Bulletin on Variable Stars*, 2042, 1
Khopylov et al. 1988, *Astrofizika* **28**, 287
Patterson et al. 2004, *Publications of the Astronomical Society of the Pacific* **116**, 516
Ramírez et al. 2022, Revista Mexicana de Astronomía y Astrofísica **58**, 47
Rodríguez-Gil et al. 2004, *Monthly Notices of the Royal Astronomical Society* **349**, 367
Segura Montero, O., Ramírez, S. H., & Echevarría, J. 2020, *MNRAS* **494**, 4110
Stepanyan, D. A. 1982, *Peremennye Zvezdy* **21**, 691
Veresvarska et al. 2025, *MNRAS,* **539**, 2424
Warner, B. 1995, *Cataclysmic Variable Stars*, Vol. 28, Cambridge Univ. Press, Cambridge

Revolutionizing Eruption Predictions for T Coronae Borealis and Other Recurrent Novae Using Machine Learning

Julian Elihu

Great Neck North High School, Great Neck, NY, 11023, United States

Abstract

Recurrent novae, such as T Coronae Borealis (T CrB), are binary star systems that undergo cyclical thermonuclear eruptions due to the accretion of material onto a white dwarf. Predicting these eruptions is challenging because of irregular light curves and complex accretion dynamics, and traditional methods often lack precision, with predictions for T CrB's imminent eruption ranging from 2023-2027. This study applies machine learning techniques to significantly improve eruption predictions, using T CrB as a case study. Historical photometric light curve data from multiple recurrent novae were collected from the American Association of Variable Star Observers database. A Long Short-Term Memory neural network, augmented with an attention mechanism, was developed to model the time-series data and predict the time until the next eruption. Validation using pre-eruption data from RS Ophiuchi's 1985 and 2021 eruptions yielded prediction errors of 5.99 and 13.89 days, respectively. Attention-based visualizations highlighted a pre-eruption dip in brightness as a key predictor, computationally confirming previously observed astrophysical phenomena. This approach enables astronomers to allocate resources effectively, capturing critical pre-eruption data where the model signals heightened eruption probability while also improving our understanding of accretion dynamics and stellar evolution. Astronomers can conduct targeted follow-up on these critical epochs, potentially capturing the thermonuclear runaway in real time and collecting crucial spectral data. Finally, as recurrent novae are potential progenitors of Type Ia supernovae, these advancements refine our understanding of galactic evolution and cosmic distance measurements.

1. Introduction

1.1 Novae

Novae are among the most luminous and dynamic astronomical phenomena, offering critical insights into stellar evolution and the mechanisms governing binary star systems (Shara et al., 2018). These sudden outbursts result from thermonuclear explosions on the surface of white dwarfs accreting material from companion stars, leading to dramatic increases in brightness that can outshine entire galaxies (Figure 1; Starrfield et al., 2020). Understanding novae is essential for astrophysics and cosmology, as they contribute to the chemical enrichment of galaxies and serve as models for studying extreme physical processes (Schaefer, 2010).

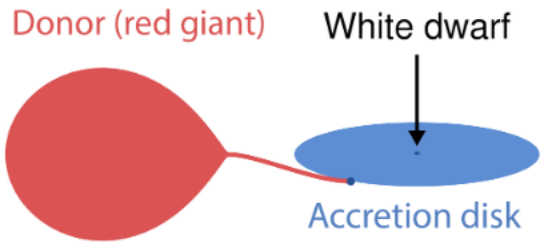

Figure 1. A cataclysmic variable. The binary system consists of a white dwarf accreting material from its Roche lobe-filling companion star via the inner Lagrangian point. The accreted matter forms an accretion disk around the white dwarf, where angular momentum is dissipated before accreting onto the compact object. As hydrogen accumulates on the white dwarf's surface, the temperature and pressure increase until a thermonuclear runaway occurs, ejecting the outer layers and causing the observed brightness.

1.2 Recurrent Novae

Recurrent novae (RNe), a subset of these systems, are distinguished by their cyclical eruptions within decades, compared to the millennia-scale recurrence timescales of classical novae (Schaefer, 2010). These systems provide unique opportunities to study nova evolution in real-time, offering insights into mass transfer processes, accretion dynamics, and thermonuclear runaways (Darnley et al., 2012). These systems also hold cosmological significance, as some RNe are potential progenitors of Type Ia supernovae, the "standard candles" for measuring cosmic distances (Shara et al., 2018). Despite their significance, only ten RNe have been identified in the Milky Way, limiting the statistical power of observational studies (Schaefer, 2010).

1.3 Prediction Challenges

Predicting eruptions in RNe remains a significant challenge due to the irregularity and complexity of their light curves and the stochastic nature of accretion and ignition processes (Collazzi et al. 2009; Shara 1989; Schaefer et al., n.d.). Traditional models rely on observational data such as the star's brightness, spectral properties, and changes in orbital dynamics (Pagnotta & Schaefer, 2014). While observational studies have identified possible pre-eruption behaviors, such as dips or rises in brightness, these methods often lack precision, leaving the timing and intensity of future eruptions uncertain and offering limited generalizability (Shara et al. 2018). The scarcity of pre-eruption data and the system-specific nature of observed behaviors further complicate prediction efforts (Shara, 1989).

1.4 T Coronae Borealis

T Coronae Borealis (T CrB) stands out among RNe due to its relatively short recurrence period and proximity to Earth (Schaefer, 2023). With recorded eruptions in 1787, 1866, and 1946, T CrB exhibits an approximate recurrence interval of 80 years (Schaefer, 2019). Its symbiotic nature—a white dwarf accreting matter from a red giant companion—adds complexity to its accretion dynamics, making it an invaluable system for studying accretion processes, disk instabilities, and

thermonuclear runaways (Zamanov et al., 2023; Lyster, 2024). The anticipated next eruption of T CrB presents a unique opportunity for detailed observation; however, predictions for its timing vary widely, ranging from as early as 2023 to as late as 2027 (Schaefer, 2019; Luna et al., 2020; Schaefer et al., 2023).

The uncertainty in predicting T CrB's next eruption underscores the limitations of current predictive models (Schaefer, 2019). These models are hindered by incomplete observational data and the inherent unpredictability of the physical processes involved (Shara et al., 2018). This lack of precision complicates efforts to allocate observational resources effectively and to capture critical pre-eruption data (Zheng et al., 2024).

1.5 Machine Learning

Recent advances in machine learning (ML) offer promising avenues for improving eruption predictions in RNe (Baron, 2019). ML algorithms excel at identifying patterns in large datasets that may not be apparent through traditional analytical methods (Feigelson & Babu, 2012). In astrophysics, ML has been successfully applied to classify variable stars, detect exoplanets, and analyze gravitational waves (Huertas-Company et al., 2018). Applying ML to historical light curves and spectral data of novae could uncover predictive features that forecast accuracy and provide novel insights into the underlying mechanisms of eruption (Masci et al., 2014). Despite its potential, the application of ML in predicting nova eruptions remains largely unexplored.

1.6 Objectives

This study aims to improve eruption forecasting for recurrent novae through data-driven analysis while maintaining physical interpretability. By identifying trends linked to eruption events in RNe, this study will (1) develop a predictive framework capable of forecasting the timing of eruptions in recurrent novae, with T Coronae Borealis as a primary case study, (2) identify and interpret the key temporal features in nova light curves that drive eruption predictions, and (3) evaluate the predictive performance of the framework using historical eruptions of other recurrent novae and apply the validated model to forecast the next eruption of T Coronae Borealis.

2. Methodology

2.1 Data Collection

Historical light curve data were collected for multiple recurrent novae to develop a predictive model for recurrent nova eruptions. Specifically, data for T Coronae Borealis (T CrB), RS Ophiuchi (RS Oph), U Scorpii (U Sco), T Pyxidis (T Pyx), and V3890 Sagittarii (V3890 Sgr) were obtained from the American Association of Variable Star Observers (AAVSO) database (Table 1). These datasets consist of visual magnitude measurements recorded over several decades by a global network of observers.

Table 1. Summary of Collected Data for Recurrent Novae.

Purpose	**Star Name**	**Eruption year**	**Selected Dates** MM/DD/YYYY	**Data Points**
Training	T Pyxidis	1966	01/06/1962 - 12/25/2013	2694
Training	T Pyxidis	2011	01/01/2007 - 12/31/2013	3130
Training	T Coronae Borealis	1946	01/26/1942 - 12/30/1948	2637
Training	V3890 Sagittarii	2019	01/30/2015 - 12/02/2021	2702
Training	U Scorpii	2022	02/16/2018 - 12/10/2024	2206
Training	RS Ophiuchi	2006	01/25/2002 - 11/24/2008	6854
Testing*	RS Ophiuchi	2021	01/02/2017 - 12/01/2023	5416
Testing*	RS Ophiuchi	1985	01/31/1981 - 12/01/1987	6793
Testing	T Coronae Borealis	2026 (anticipated)	01/02/2021 - 04/01/2025	10,280

* The pre-eruption data of RS Ophiuchi's 1985 and 2021 eruptions were used as a validation metric to test the model's predictive accuracy. Then an additional portion of the data for one year after the eruption is implemented into training dataset for the final prediction task for T CrB.

For each nova, the selected time spans included approximately four years prior to known eruptions and one year following eruption, ensuring that both pre-eruption behavior (including quiescent variability and brightness dips) and post-eruption recovery phases were captured. All observation times were converted to Julian Dates to maintain temporal consistency across systems.

Additionally, part of the AAVSO T CrB photometric dataset included the researcher's original observations of the system using the Skynet Fan Mountain Observatory telescope, accessed at the Pisgah Astronomical Research Institute.

2.2 Data Preprocessing

All outliers caused by observational noise or inconsistent measurements were removed using statistical thresholds for magnitude deviations, as provided by the AAVSO. Star names were standardized by stripping extra spaces and converting them to uppercase for consistency across datasets. Magnitudes were z-score normalized on a per-star basis to account for differences in baseline brightness and variability amplitude among systems. This normalization preserves relative variability while preventing brighter systems from dominating model training.

Then, a binary system indicated each nova event with an eruption flag so the model could identify eruption events within the time series data. Pre- and post-eruption magnitudes were indicated with a 0, and magnitudes during the eruption were marked with a 1.

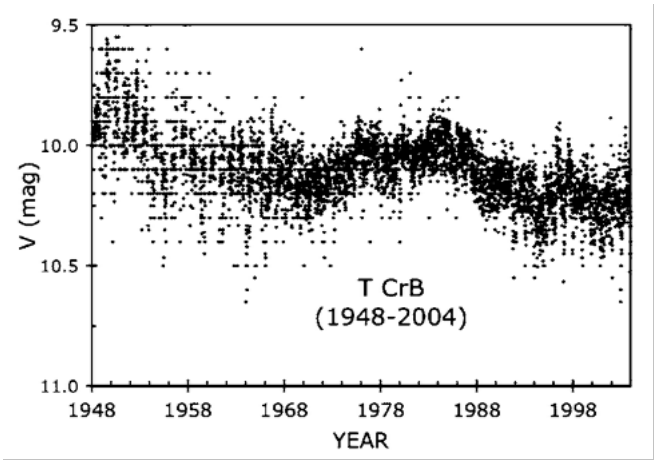

Figure 2. T CrB in the 60 years of quiescence following the 1946 eruption. This light curve is composed of nearly 80,000 observations made by AAVSO observers of T CrB, with an amplitude of approximately 0.25 magnitudes on a decadal timescale (Collazzi et al., 2009).

Because of the variability in post-eruption quiescent magnitudes, there was no precise method of identifying eruption thresholds. However, Collazzi et al. (2009) asserts that the densely sampled light curves (Fig. 2) allowed for consistent analysis with minimal impact from these variations. Finally, the data was partitioned into training and testing sets, ensuring no overlap between the periods used for training and evaluation to avoid data leakage.

2.3 Feature Engineering

A crucial step involved calculating a new feature: Time Until Next Eruption. For each observation, this feature represented the time difference (in Julian days) between the observation date and the date of the next known eruption. This continuous target variable was essential for training the regression model to predict the timing of future eruptions. The calculation was automated using Python scripts with NumPy operations, iterating through each star's data sorted by Julian Date.

2.4 Model Development

A Long Short-Term Memory (LSTM) neural network was selected due to its proven effectiveness in modeling time-series data and capturing long-term dependencies (Hochreiter & Schmidhuber, 1997). The model was implemented using Python with the TensorFlow Keras library.

Each input sequence consisted of 30 time steps, with the features described above provided at each step. The network architecture includes the following as can be seen in Figure 3:

- An Input Layer configured to accept sequences of 30 time steps, each containing three features:
    - Julian Date (relative, normalized)
    - Normalized magnitude
    - Star identifier
    - Eruption flag
- Hidden Layers:
    - First LSTM layer with 64 units
    - Second LSTM layer with 32 units
    - Both layers were designed to capture complex temporal patterns in the light curve data
- Dropout Layers applied after each LSTM layer with a dropout rate of 20% to mitigate overfitting by randomly disabling a fraction of the neurons during training.
- An Output Layer: A single neuron providing a regression output to predict the Time Until Next Eruption.

The model was trained using the Huber loss function, which balances sensitivity to small errors with robustness against outliers, and optimized using the Adam optimizer. To evaluate and improve the model's generalizability, 5-fold cross-validation was employed. Hyperparameter tuning was performed using grid search methods to optimize the number of LSTM units (tested values included 32, 64, and 128 units), dropout rates (rates ranged from 10% to 30%), and learning rates (adjusted between 0.001 and 0.01). The optimal combination was determined based on the lowest validation loss achieved during cross-validation.

2.5 Attention Mechanism and Interpretability Design

To ensure that predictions were physically interpretable, an attention mechanism was integrated on top of the final LSTM layer prior to the regression output. This mechanism assigns a learnable weight to each of the 30 time steps within an input sequence, allowing the model to emphasize temporally important regions of the light curve when generating predictions. The attention weights provide a global interpretability measure, indicating which phases of the pre-eruption light curve—such as long-term quiescent trends or short-term brightness dips—contribute most strongly to eruption forecasts. These weights were extracted after training and visualized across the full prediction dataset to identify consistent temporal patterns. A schematic of the full model architecture is shown in Figure 3.

In addition to attention, SHapley Additive exPlanations (SHAP) were applied to quantify local feature importance for individual prediction windows. SHAP values were computed for each feature at each time step, measuring how strongly that feature pushed the model toward predicting an earlier or later eruption. This allowed fine-grained attribution of predictive influence to specific magnitude deviations within the light curve.

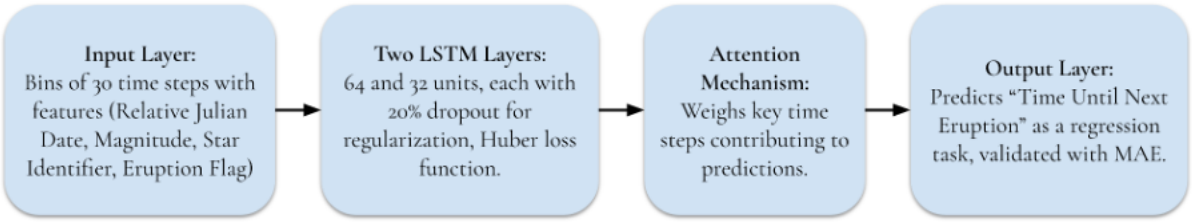

Figure 3. Schematic of the LSTM architecture. Graphic by author.

2.6 Model Evaluation

After training, the model's predictive performance was evaluated on the test dataset. The Mean Absolute Error was used to measure the average magnitude of the errors by comparing the model's predicted Time Until Next Eruption with the actual values in the test dataset.

The prediction process was fully automated, allowing for seamless integration of new light curve data into the pipeline. Sequences of 30 observations were prepared automatically, and the model predicted the time until the next eruption. This process was repeated for all sequences in the test dataset.

Results were visualized using matplotlib, including loss curves showing training and validation loss across epochs, predicted vs. actual time-to-eruption values for test data, and a plot of predicted time-to-eruption over the test period.

3. Results & Discussion

3.1 Model Validation with RS Ophiuchi

To evaluate the predictive capabilities of the LSTM model, pre-eruption data from RS Ophiuchi's (RS Oph) 1985 and 2021 eruptions were used as test cases before including their entire datasets in the training process. This approach provided an opportunity to assess the model's generalization to unseen data from a recurrent nova not initially included in the training set. The model's predictions for RS Oph's eruption dates were compared to the actual observed eruption dates determined by peak brightness magnitudes (Table 2).

Table 2. Model Predictions for RS Ophiuchi Eruptions

	Actual Eruption Date*	Predicted Eruption Date	Error
Test 1	2446093.95 (01/28/1985)	2446099.94 (02/03/1985)	5.99 days
Test 2	2459436.37 (08/09/2021)	2459450.26 (08/23/2021)	13.89 days

* The actual eruption date was determined by analyzing the peak brightness magnitude for each nova event.

Considering the complex and stochastic nature of nova eruptions, these results demonstrate a promising level of accuracy for predictive modeling in astrophysics. The relatively low prediction errors suggest that the model effectively captured the temporal patterns leading up to RS Oph's eruptions. The better accuracy for the 1985 eruption compared to the 2021 event may be attributed to differences in data quality, sampling rates, or intrinsic variations in the nova's behavior. While there is no established standard for acceptable error margins in time-series predictions of astrophysical events, errors of less than two weeks are considered highly valuable for planning observational campaigns. The model's performance indicates its potential utility for astronomers aiming to capture transient events.

3.2 Training Behavior and Model Stability

The training and validation loss curves exhibit smooth convergence with minimal divergence between training and validation loss (Figure 4). This behavior suggests that the model learned stable temporal patterns without overfitting to noise or individual systems. The absence of late-epoch validation loss increases further supports the generalizability of the learned representations.

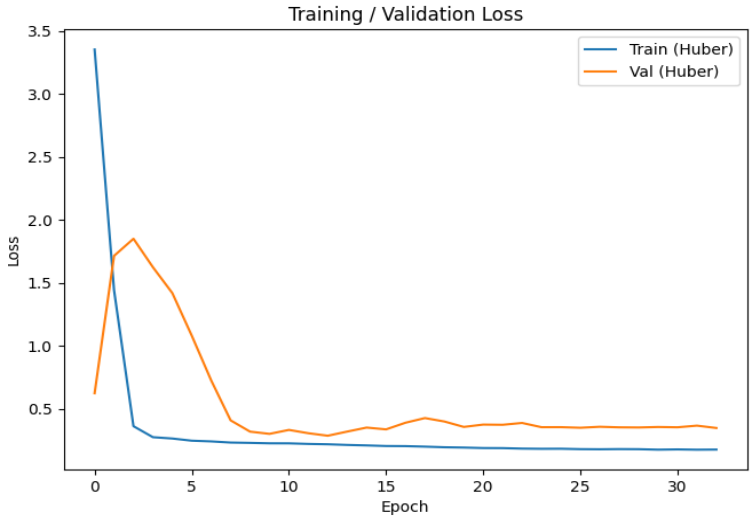

Figure 4. Graph of the training and validation loss during model development. Generated by matplotlib.

The use of dropout regularization and Huber loss likely contributed to this stability by limiting sensitivity to outliers and reducing over-reliance on individual observations. These results provide confidence that the model's predictive success is not an artifact of memorization but rather reflects consistent structure in the pre-eruption light curves.

3.3 Shared Pre-eruption Behaviors Across Recurrent Novae

A key factor contributing to the model's performance is the similarity in pre-eruption behaviors among the recurrent novae included in the training dataset. Notably, T CrB, RS Oph, T Pyx, and V3890 Sgr all exhibit a characteristic pre-eruption dip in brightness (Figures 5A and 5B).

These pre-eruption dips are indicative of alterations in the accretion rate and disk instability, serving as potential precursors to thermonuclear runaways (Collazzi et al., 2009; Zheng et al., 2024). The model's ability to recognize these patterns across different systems enhances its predictive accuracy. With the ability to input additional data of stars with other pre-eruption behaviors, the model is extremely generalizable, as it would be able to recognize the accretion dynamics of other systems as well.

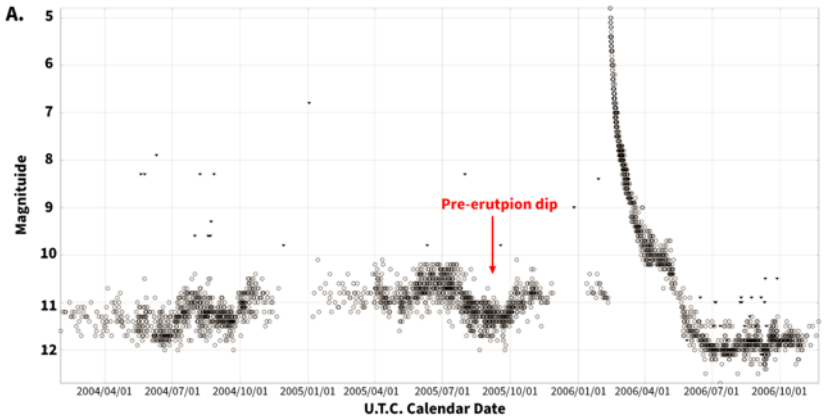

Figure 5A. The light curve of RS Oph during the time surrounding its 2006 eruption, plotted from AAVSO data. The pre-eruption dip, highlighted by a red arrow, is indicative of changes in the accretion dynamics preceding the eruption. Graphics by author.

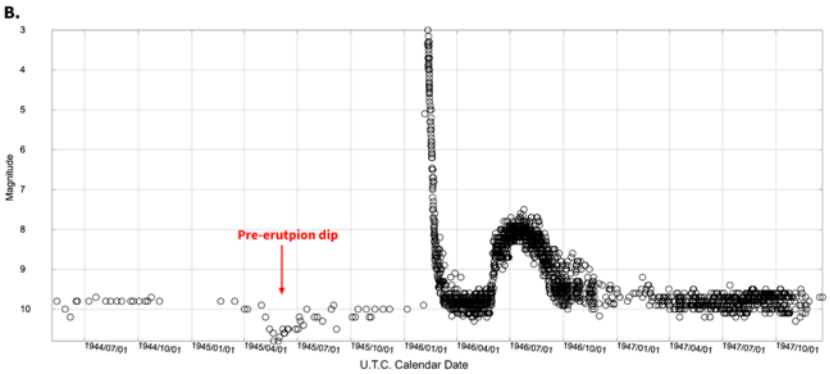

Figure 5B. The light curve of nova T CrB during the time surrounding its 1946 eruption, plotted from AAVSO data.

3.4 Prediction for T Coronae Borealis

Using the latest pre-eruption data from T CrB (2021–2025), the model predicts the next eruption to occur on September 3, 2026 (JD 2461287.2) with an estimated uncertainty of approximately

±20 days. This prediction falls well within previously proposed eruption windows while significantly narrowing the uncertainty from multiple years to a few months (Figure 6). The narrowing of the prediction window is of particular importance for observational planning, as it enables targeted, high-cadence monitoring during a physically motivated time interval rather than continuous long-term surveillance. The quoted uncertainty reflects both model variance and the limited number of pre-eruption training examples.

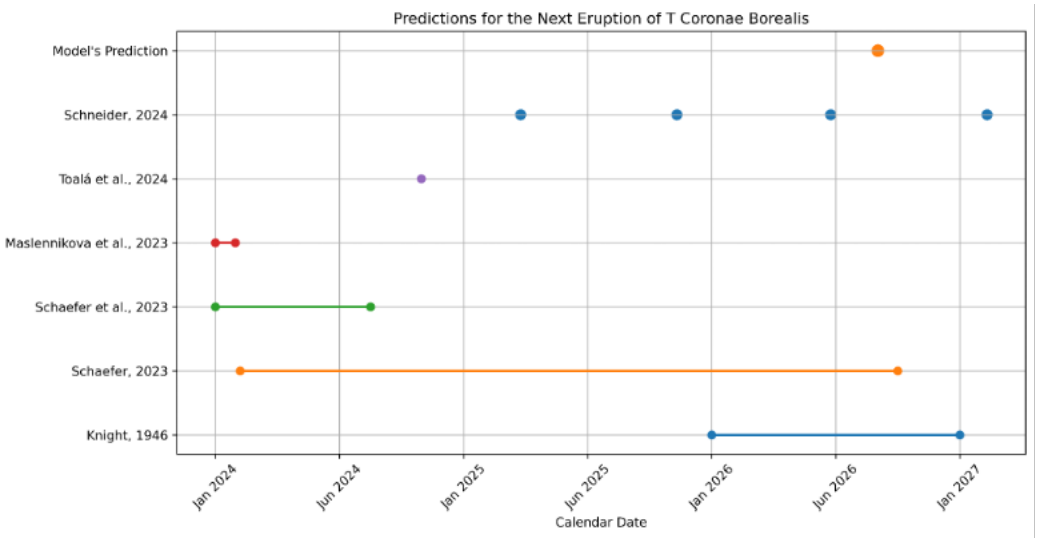

Figure 6. Comparison of published predictions for the timing of the next eruption of the recurrent nova T CrB. Knight (1946) predicted a future eruption broadly between 2026 and 2027. Schaefer (2023) estimated an eruption window spanning mid-February 2024 to late September 2026. Schaefer et al. (2023) narrowed the expected eruption to January 2024 through mid-August 2024, while Maslennikova et al. (2023) proposed a more specific timing near January 2024 from optical and infrared diagnostics. From X-ray evolution, Toalá et al. (2024) predicted an eruption near late October 2024. Schneider (2024) identified several discrete candidate dates—27 March 2025, 10 November 2025, 25 June 2026, and 8 February 2027—arising from periodicity-based modeling. The red marker denotes the prediction from this work, placing the eruption on 3 September 2026. Graphic by author.

3.5 Temporal Focus Identified by the Attention Mechanism

The attention-weight analysis provides a global view of which temporal regions of the light curve most strongly influenced eruption predictions. The attention map computed across the full T CrB prediction dataset (Figure 7) reveals a clear concentration of weight in the final several time steps preceding eruption, corresponding to the months immediately before the predicted outburst.

This region aligns closely with the timing of the observed pre-eruption dip reported in T CrB and other recurrent novae. Importantly, the model does not uniformly weight the entire light curve, suggesting that it is not responding to generic variability but to specific, temporally localized features. The attention results therefore indicate that the model's predictions are driven by astrophysically meaningful intervals rather than arbitrary fluctuations.

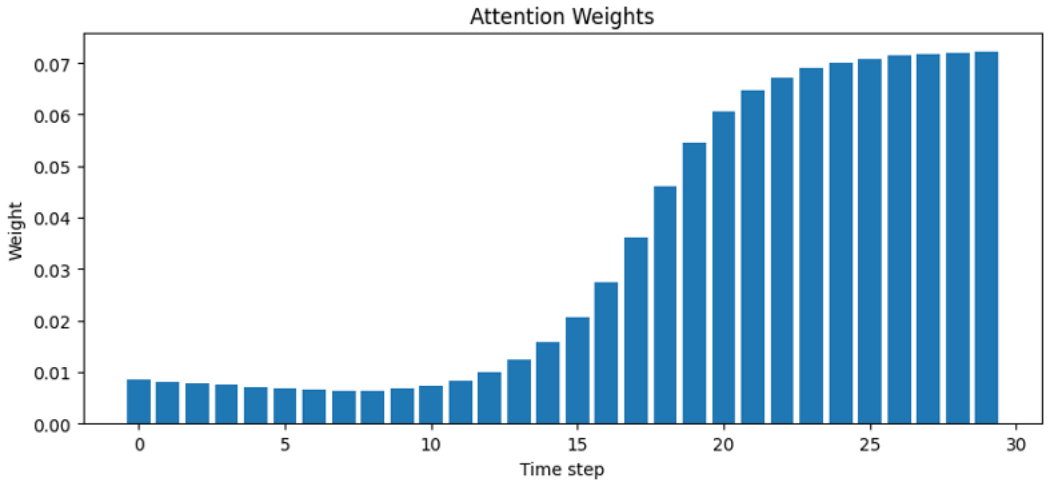

Figure 7. Global attention weights of LSTM model for 30 time steps over entire range of T CrB prediction dataset. Graphic by author.

Further, SHapley Additive exPlanations (SHAP) were used to quantify feature-level contributions to individual eruption-time predictions. When the top SHAP-ranked features are mapped back onto the modern T CrB light curve, they coincide with the most pronounced segments of the pre-eruption dimming behavior. This provides quantitative evidence that localized brightness dips act as strong predictive signals, consistent with prior observational reports of pre-eruption dips in recurrent novae (Collazzi et al., 2009; Schaefer et al., 2023) and with interpretations linking such dimming to accretion-disk reconfiguration preceding thermonuclear runaway (Zamanov et al., 2023).

3.6 Limitations

A primary limitation of this study is the severe scarcity of pre-eruption training data, which is itself a direct consequence of the intrinsic unpredictability of recurrent nova systems. Recurrent novae erupt irregularly on decadal timescales, and even well-monitored systems spend the vast majority of their lifetimes in quiescence. As a result, only a handful of eruptions have been observed with sufficiently dense photometric coverage in the critical pre-eruption phase. This limits both the number of labeled training examples and the diversity of pre-eruption behaviors available to the model. Consequently, while the model is able to learn shared, physically meaningful precursors such as pre-eruption brightness dips, its predictive performance and uncertainty estimates are ultimately constrained by the rarity and stochastic nature of these events. Expanding long-term, high-cadence monitoring across a larger population of recurrent novae will be essential for further improving model robustness and reducing predictive uncertainty.

4. Future Research

Incorporating data from ultraviolet, infrared, and X-ray observations could provide a more comprehensive understanding of the pre-eruption state of novae. Spectroscopic data, in particular, can reveal changes in the accretion disk's properties and the white dwarf's atmosphere that precede eruptions (Shen et al., 2023). Integrating these data types could enhance the model's predictive accuracy and provide deeper insights into the underlying physical mechanisms.

Also, applying the model to a broader range of novae, including classical and dwarf novae, would assess its applicability to different systems. Adjustments to the model architecture or inclusion of additional features may be necessary to accommodate varying behaviors, but such efforts could significantly advance our understanding of cataclysmic variables and novae as a whole (Mistry et al., 2023).

Finally, accuracy could be improved by establishing a real-time prediction system that continuously updates as new data becomes available.

5. Conclusions

This study demonstrates that data-driven methods can meaningfully advance eruption forecasting for recurrent novae while remaining grounded in physical interpretation. By applying an interpretable machine-learning framework to historical photometric light curves, the model successfully predicted past eruptions of RS Ophiuchi within days and produced a constrained forecast for the next eruption of T Coronae Borealis on September 3, 2026. This represents a substantial reduction in uncertainty compared to traditional empirical predictions, which typically span several years.

Notably, the integration of attention mechanisms provides confidence that the model is capturing genuine astrophysical phenomena, not random fluctuations. The model consistently emphasizes the same pre-eruption brightness dips that have been reported observationally for decades, providing the first quantitative, computational confirmation that these features are predictive. This alignment between model focus and known accretion-driven behavior further strengthens confidence in the astrophysical validity of the predictions.

6. Implications

The ability to predict nova eruptions with heightened accuracy has profound implications for observational astronomy. Accurate forecasts enable astronomers to allocate observational resources more effectively, saving cost, time, and resources. This preparedness is crucial for studying the onset of eruptions, which offers invaluable insights into the physical processes such as shock formation, particle acceleration, and nucleosynthesis (Kuo-Chuan et al., 2015; Zheng et al., 2024). Equally important is the role of interpretability in enabling adoption of machine-learning methods within the astrophysical community. Transparent attribution of predictions to

physically meaningful features ensures that ML-based forecasts can be evaluated, trusted, and compared directly with theoretical expectations. This interpretability is essential for extending such approaches to other transient phenomena, including dwarf novae, symbiotic outbursts, and accretion-driven variability in compact binaries.

The principal limitation of the present framework—the scarcity of densely sampled pre-eruption data—arises from the inherent unpredictability and rarity of recurrent nova eruptions. Expanding long-term photometric coverage across a broader population of systems will be critical for improving model robustness, refining uncertainty estimates, and capturing a wider diversity of pre-eruption behaviors.

T CrB's relative proximity to Earth and its brightness amplify the importance of precise predictions, as detailed observations can significantly enhance our understanding of recurrent nova systems and their role in galactic chemical evolution. Some RNe, such as RS Oph, are too far from Earth to collect well-measured spectral data. Hence, their related particle acceleration mechanisms are not well understood. However, T CrB's recent outburst was nearly ten times optically brighter than RS Oph (Zheng et al. 2024). Thus, T CrB plays an especially significant role, as it serves as a natural laboratory for examining the interactions between other RNe, as well as other white dwarfs and their companion stars, contributing to a deeper comprehension of stellar evolution and mass transfer physics (Kuo-Chuan et al., 2015). By predicting eruptions, astronomers can capture critical data that might otherwise be missed, facilitating studies that could reveal new aspects of accretion dynamics and thermonuclear processes.

Moreover, recurrent novae are potential progenitors of Type Ia supernovae, which are essential "standard candles" for measuring cosmic distances and studying the expansion of the universe (Wang & Han, 2012). Improved predictive models for nova eruptions, therefore, have significant implications for cosmology. By enhancing our ability to anticipate and observe these events, we can refine distance measurements and improve our understanding of fundamental cosmological parameters.

The model's prediction narrow error margins represent a significant improvement over previous estimations, which often spanned several months or years. This level of precision can revolutionize the scheduling of observations and maximize the scientific return from transient events (Wallerstein et al., 2008).

Looking forward, this work provides a foundation for real-time eruption forecasting pipelines that continuously ingest new observations and update predictions dynamically. Such systems could transform how transient events are monitored and transform current observational strategies. More generally, this study highlights the potential of interpretable machine learning as a powerful complement to theoretical and observational approaches, enabling new insights into complex, non-linear astrophysical systems that have long resisted precise prediction.

References

AAVSO. 2025, observations from the AAVSO International Database (http://www.aavso.org).

Baron, D. (2019). *MACHINE LEARNING IN ASTRONOMY: A PRACTICAL OVERVIEW* (pp. 1–10, 28–30). Tel-Aviv University School of Physics and Astronomy. https://arxiv.org/pdf/1904.07248

Collazzi, A. C., Schaefer, B. E., Xiao, L., Pagnotta, A., Kroll, P., Klaus Löchel, & Henden, A. A. (2009). THE BEHAVIOR OF NOVAE LIGHT CURVES BEFORE ERUPTION. *The Astronomical Journal*, *138*(6), 1846–1873. https://doi.org/10.1088/0004-6256/138/6/1846

Darnley, M. J., Ribeiro, M., Bode, M. F., Hounsell, R. A., & Williams, R. P. (2012). ON THE PROGENITORS OF GALACTIC NOVAE. *The Astrophysical Journal*, *746*(1), 61–61. https://doi.org/10.1088/0004-637x/746/1/61

Feigelson, E., & Jogesh Babu, G. (2012). *Statistical Methods for Astronomy*. https://arxiv.org/pdf/1205.2064

Hochreiter, S., & Schmidhuber, J. (1997). Long Short-Term Memory. *Neural Computation*, *9*(8), 1735–1780. https://doi.org/10.1162/neco.1997.9.8.1735

Huertas-Company, M., Primack, J. R., Dekel, A., Koo, D. C., Lapiner, S., Ceverino, D., Simons, R. C., Snyder, G. F., Bernardi, M., Chen, Z., Domínguez-Sánchez, H., Lee, C. T., Margalef-Bentabol, B., & Tuccillo, D. (2018). Deep Learning Identifies High-z Galaxies in a Central Blue Nugget Phase in a Characteristic Mass Range. *The Astrophysical Journal*, *858*(2), 114. https://doi.org/10.3847/1538-4357/aabfed

Juie Shetye, Verwichte, E., Stangalini, M., & Doyle, J. G. (2020). Chandra Observations of Candidate Sub-Parsec Binary Supermassive Black Holes. *The Astrophysical Journal*, *860*(110). https://doi.org/10.3847/1538-4357

Kuo-Chuan Pan (潘國全, Ricker, P. M., & Taam, R. E. (2015). SIMULATIONS OF THE SYMBIOTIC RECURRENT NOVA V407 CYG. I. ACCRETION AND SHOCK EVOLUTIONS. *The Astrophysical Journal*, *806*(1), 27–27. https://doi.org/10.1088/0004-637x/806/1/27

Luna, G. J. M., Sokoloski, J. L., Mukai, K., & M. Kuin, N. P. (2020). Increasing Activity in T CrB Suggests Nova Eruption Is Impending. *The Astrophysical Journal*, *902*(1), L14. https://doi.org/10.3847/2041-8213/abbb2c

Lyster, T. (2024). *The Jewel in the Crown*. Aavso.org; AAVSO Blog. https://www.aavso.org/blog/T-CrB-jewel-in-the-crown

Mistry, D., Copperwheat, C. M., Darnley, M. J., & Olier, I. (2023). Machine Learning applications for Cataclysmic Variable discovery in the ZTF alert stream. *Monthly Notices of the Royal Astronomical Society*, *527*(3), 8633–8658. https://doi.org/10.1093/mnras/stad3768

Pagnotta, A., & Schaefer, B. E. (2014). IDENTIFYING AND QUANTIFYING RECURRENT NOVAE MASQUERADING AS CLASSICAL NOVAE. *The Astrophysical Journal*, *788*(2), 164. https://doi.org/10.1088/0004-637x/788/2/164

R. Zamanov, S. Boeva, Latev, G. Y., E. Semkov, M. Minev, Kostov, A., Bode, M. F., V. Marchev, & D. Marchev. (2023). Accretion in the recurrent nova T CrB: Linking the superactive state to the predicted outburst. *Astronomy and Astrophysics*, *680*, L18–L18. https://doi.org/10.1051/0004-6361/202348372

Schaefer, B. E. (2010). COMPREHENSIVE PHOTOMETRIC HISTORIES OF ALL KNOWN GALACTIC RECURRENT NOVAE. *The Astrophysical Journal Supplement Series*, *187*(2), 275–373. https://doi.org/10.1088/0067-0049/187/2/275

Schaefer, B. E. (2023). The recurrent nova T CrB had prior eruptions observed near December 1787 and October 1217 AD. *Journal for the History of Astronomy*, *54*(4), 436–455. https://doi.org/10.1177/00218286231200492

Schaefer, B. E., Kloppenborg, B., & Waagen, E. O. (n.d.). *Announcing T CrB pre-eruption dip*. Www.aavso.org; AAVSO. https://www.aavso.org/news/t-crb-pre-eruption-dip

Schneider, J. (2024). When will the Next T CrB Eruption Occur? *Research Notes of the AAS*, *8*(10), 272. https://doi.org/10.3847/2515-5172/ad8bba

Shafter, A. W., Henze, M., Rector, T. A., Schweizer, F., Hornoch, K., Orio, M., Pietsch, W., Darnley, M. J., Williams, S. C., Bode, M. F., & Bryan, J. (2015). RECURRENT NOVAE IN M31. *The Astrophysical Journal Supplement Series*, *216*(2), 34. https://doi.org/10.1088/0067-0049/216/2/34

Shara, M. M. (1989). Recent progress in understanding the eruptions of classical novae. *Publications of the Astronomical Society of the Pacific*, *101*(635), 5–5. SAO/NASA Astrophysics Data System. https://doi.org/10.1086/132400

Shears, J. H. (2024). An Independent Discovery of the 1946 Eruption of the Recurrent Nova T Coronae Borealis and an Early Prediction of a Future Outburst. *Research Notes of the AAS*, *8*(6), 157–157. https://doi.org/10.3847/2515-5172/ad566b

Starrfield, S., Iliadis, C., & Hix, W. R. (2016). The Thermonuclear Runaway and the Classical Nova Outburst. *Publications of the Astronomical Society of the Pacific*, *128*(963), 051001. https://doi.org/10.1088/1538-3873/128/963/051001

Toalá, J., Id, O., González-Martín, Id, A., Sacchi, Id, D., & Vasquez-Torres. (2024). The X-ray rise and fall of the Symbiotic Recurrent Nova System T CrB. *MNRAS*, *000*, 1–12.

Wallerstein, G., Harrison, T. N., Ulisse Munari, & Vanture, A. D. (2008). The Metallicity and Lithium Abundances of the Recurring Novae T CrB and RS Oph. *Publications of the Astronomical Society of the Pacific*, *120*(867), 492–497. https://doi.org/10.1086/587965

Wang, B., & Han, Z. (2012). Progenitors of type Ia supernovae. *New Astronomy Reviews*, *56*(4), 122–141. https://doi.org/10.1016/j.newar.2012.04.001

Zheng, J.-H., Zhang, H.-M., Liu, R.-Y., Zha, M., & Wang, X.-Y. (2024). Probing the nova shock physics with future gamma-ray observations of the upcoming outburst from T Coronae Borealis. *Journal of High Energy Astrophysics*, *43*, 171–177. https://doi.org/10.1016/j.jheap.2024.07.007

Alpha Cygni Variables as Seen from the Transiting Exoplanet Survey Satellite

Joyce A. Guzik[1], Claire Whitley[1,2], Nova Moore[1,3], Madeline Marshall[1], and Jason Jackiewicz[4]

[1]Los Alamos National Laboratory, Los Alamos, NM (joy@lanl.gov); [2]University of New Mexico, Albuquerque, NM; [3]New Mexico Institute of Mining and Technology, Socorro, NM; [4]New Mexico State University, Las Cruces, NM

Subject Keywords

Alpha Cygni Variables; AAVSO International Database; NASA TESS Spacecraft

Abstract

The Alpha Cygni (ACYG) variables are blue-white supergiants which display low-amplitude brightness variations of around 0.1 magnitude. The prototype Deneb shows quasi-periodic variations of around 12 days, interrupted by intervals of erratic variability, and occasionally large excursions in amplitude. To gain insight on the behavior of these variables, we examined 27-day light curves from the Transiting Exoplanet Survey Satellite (TESS) for 75 ACYG variables south of the ecliptic plane which are being revisited by TESS in 2025-2026. We use the web-based TESS Extractor app for screening TESS light curves. We identified ten stars with similarities to Deneb that may be good candidates for ground-based monitoring. We approximated the location of these stars on the Hertzsprung-Russell diagram, and find most lie below the Luminous Blue Variables, are cooler than the β Cephei variables, and are hotter than the RV Tauri stars. We also compare light curves processed with several different pipelines available on the Mikulski Archive for Space Telescopes (MAST) and comment on their utility for ACYG stars.

1. Introduction

Alpha Cygni (ACYG) variables are luminous supergiants of spectral types O, B, and A which show low-amplitude (around 0.1 mag or less) photometric variability (e.g., van Genderen et al. 1989, Richardson et al. 2010). The prototype α Cyg (Deneb), with visual magnitude 1.21-1.29, exhibits alternating phases of quasi-periodic and erratic variability (see, e.g., Abt et al. 2023, Guzik et al. 2024a, 2024b, 2025), raising the question of whether similar behaviors are common among other members of the class. These variations have potential to provide insights into the evolutionary state and processes in the envelopes and atmospheres of massive stars nearing the ends of their lives.

The small-amplitude variations and quasi-periodicities of days to more than a month make ACYG variables challenging targets for ground-based observing. Since the variations do not strictly repeat in period or amplitude like classical variable stars such as Cepheids or RR Lyrae stars, it is not possible to phase data from sparse observations to create a light curve. Light curves spanning several months or years are necessary to search for abrupt excursions or changes from erratic to

quasi-periodic variability, as seen in Deneb. Ideally, a photometric data point around once per night is required, but seasonal visibility and cloudy skies make this goal difficult to attain. In addition, visual observing and perhaps even CCD photometry cannot obtain the necessary precision (0.01 mag) to characterize ACYG variations. The AAVSO Photoelectric Photometry (PEP) team has had good success in observing Deneb and will be targeting other ACYG variables (see Calderwood and van Ballegoij, these proceedings).

Ongoing observations by the NASA Transiting Exoplanet Surve Satellite (TESS, Ricker et al. 2015) spacecraft may be useful for characterizing ACYG variables. TESS was launched April 18, 2018 into a 13.7-day lunar resonance orbit around Earth. TESS's four CCD cameras have 2048 x 2048 pixels, with 21 arc seconds per pixel, and together cover 24° x 96° strips of the sky, called sectors. Photometric time series are taken for each sector for 27.4 days at a time. TESS's primary mission is to search for planets around nearby, mostly M-dwarf, stars using the planet transit method. 705 confirmed planets and 7703 candidates have been discovered as of October 2025.[1]

TESS surveyed sectors south and north of the ecliptic plane during its first two years of operation. The cadence for full-frame images was 30 minutes for years 1-2, then was shortened to 10 minutes for years 3-4, and subsequently has been 3.3 minutes. Observations through Sector 90, taken in March/April 2025, were available by the end of August when this paper was being prepared.

To obtain TESS light curves, the raw pixel data must be processed to subtract backgrounds, check for contamination from nearby stars in the field of view, detrend, remove outliers, and calculate error bars. We used the web-based TESS Extractor app (Serna et al. 2021) to screen TESS light curves and identify stars with behavior similar to Deneb's. The Mikulski Archive for Space Telescopes (MAST) includes light-curve products processed using different processing pipelines. For ACYG variables, it is important to remove artificial trends while not removing real variability. We compare example light curves from several pipelines along with the TESS Extractor results and discuss our preferences for obtaining TESS ACYG light curves.

2. TESS Observations of ACYG Variables

At prior AAVSO meetings, we reported TESS observations of Deneb. Abt et al. (2023), Guzik et al. 2024a,b and Guzik et al. 2025 discuss the special 2-minute cadence high-level science product (HLSP) light curves available at the Mikulski Archive for Space Telescopes (MAST).[2] The Deneb light curve shows mostly irregular variations in Sector 41, and resumption of the quasi-periodic 12-day variations during Sector 55, continuing into Sector 56 (Figure 1).

[1] https://exoplanetarchive.ipac.caltech.edu/
[2] https://archive.stsci.edu

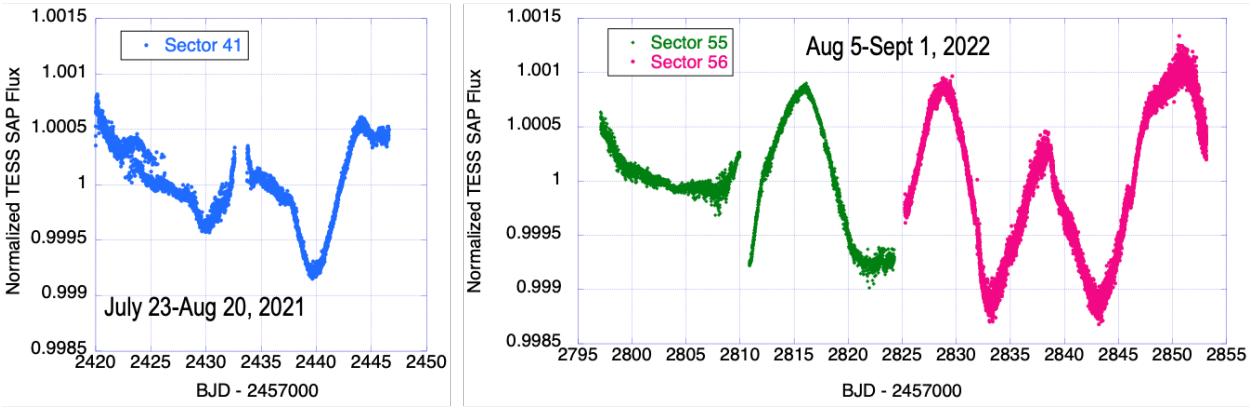

Figure 1. Deneb photometry from TESS spacecraft as presented by Abt et al. (2023). Variations with quasi-period around 12 days resume around day 2810 in Sector 55 data.

In March 2025, we proposed via the TESS General Investigator Program to obtain light curves for 75 out of 186 stars classified as ACYG variables in the AAVSO International Variable Star Index[3] which will be observable by TESS during Cycle 8, Sectors 97-107, Sept. 2025-Sept. 2026. These targets, positioned south of the ecliptic plane, span TESS magnitudes 0.7 (Rigel) to 12.6. Figure 2 shows the planned observing fields in ecliptic and equatorial coordinate views. For this Cycle, the fields of view of consecutive sectors will overlap at middle latitudes, so it will be possible to obtain coverage for some ACYG variables for at least two consecutive sectors, or 54 days, an advantage for monitoring the changing behavior of these stars.

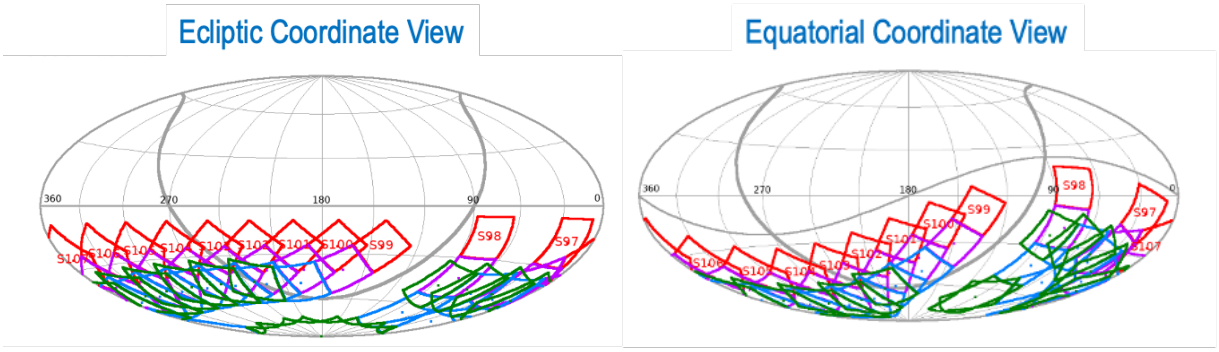

Figure 2. TESS fields of view for Cycle 8, Sectors 97-107, to be observed south of the ecliptic plane, September 2025-September 2026.[4]

3. Light Curve Analysis Using TESS Extractor

All 75 targets have one or more prior 27-day sector of TESS observations. We used the web-based application TESS Extractor[5] (Serna et al. 2021) to screen these data.

[3] https://vsx.aavso.org/
[4] https://tess.mit.edu/observations/
[5] https://www.tessextractor.app/

The TESS Extractor graphical interface is easy to use, and one does not need to know programming languages such as python, or how to process target pixel files or full-frame images. A disadvantage is that obtaining a light curve for a single 27-day sector for a given star via the interface may take several minutes. TESS Extractor has a bulk download request option, but this option was unavailable during the summer of 2025 when we were working on this project.

Figure 3 shows a screen shot of the TESS Extractor application page. While the TESS full-frame images are partially corrected before release for, e.g., CCD camera effects and cosmic rays, additional detrending is needed to remove additional systematic effects, mainly scattered light from the Earth and Moon, but also spacecraft pointing jitter and changes in detector sensitivity because of temperature variations (see, e.g., Hattori et al. 2022). To obtain detrended data, one should select the option noted by the red arrow. Target names can be entered by TESS Input Catalog (TIC) number, but the software also recognizes many other common star names, such as Deneb or Rigel. After entering the star name, one then clicks the 'Resolve Target' button, and, after the target is found, one can choose using the drop-down menu which TESS sector to process.

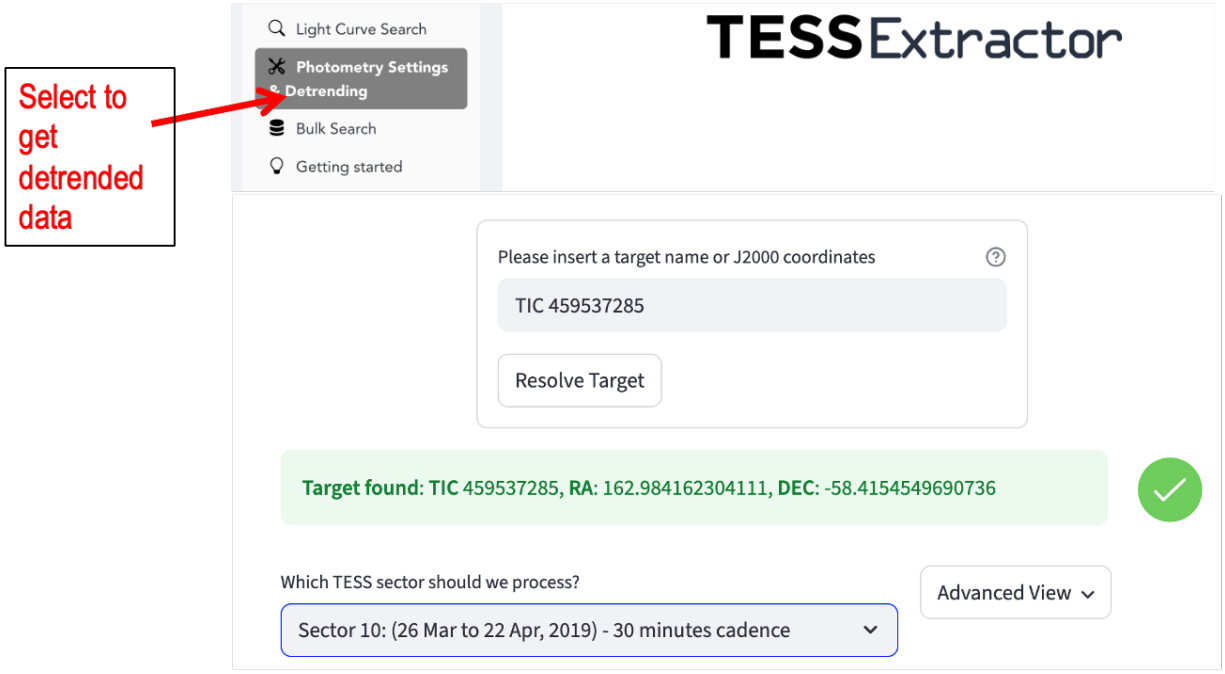

Figure 3. Screen shot of user interface for TESS Extractor[6] online interactive application.

Figure 4 shows a screen shot of the resulting 'simple aperture photometry' light curve (blue dots) and the trends based on photometry of other pixels in the field of view surrounding the star. Scrolling further in the analysis screen, the detrended light curve, a Lomb-Scargle periodogram, and some plots phased by the significant periods are shown (Figure 5). Text files with the time-

[6] https://www.tessextractor.app/

series detrended light curve and the Lomb-Scargle periodogram can be downloaded using the buttons below the plots.

Note that the periods in Figure 5 (right) are labeled as 'rotation' periods. However, for ACYG variables, these are not rotation periods, just significant periods in the 27-day light curve. For TIC 459537285, the light curve is not strictly periodic, although periods of 4.9 and 7.3 days are identified, but a time-series length of only 27 days is insufficient to characterize the variability of this star. The period identified at 0.010 days may be an alias of the 30-minute cadence, since 30 minutes = 0.0208 days, or two times 0.0104 days.

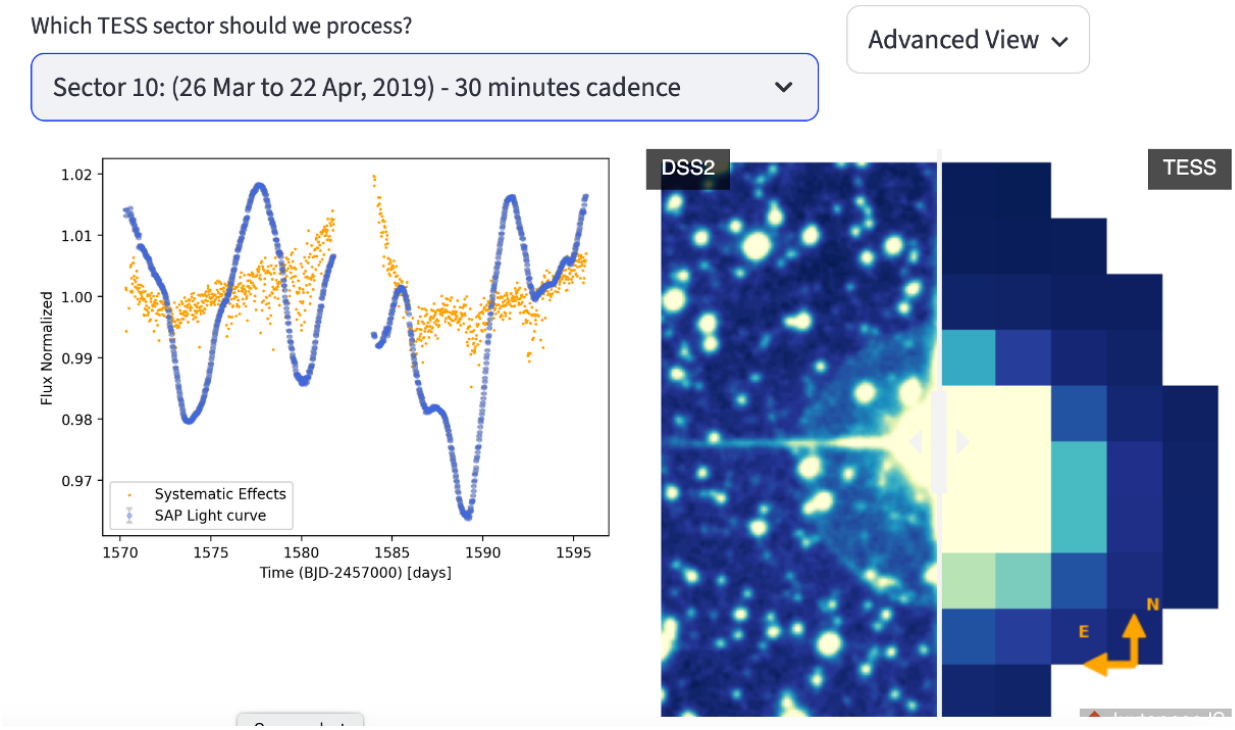

Figure 4. Screen shot of TESS Extractor light curve for TIC 459537285, Sector 10, showing the simple aperture photometry light curve (blue), systematic effects used for detrending (yellow), and a split image of the Digitized Sky Survey-2 (DSS2)[7] field (left) and the TESS pixels sampled (right).

We used TESS extractor to obtain at least one light curve for each of the 75 stars in our sample for initial screening. Our objectives were to maximize the possibilities for long-term ground-based monitoring, but also science return, so we were looking for:

- Bright stars (magnitude < 8)
- Larger-amplitude variations (greater than 0.02 mag)
- Quasi-periodicities longer than a day
- Evidence for changes in variability analogous to those seen in Deneb

[7]https://archive.eso.org/dss/dss/

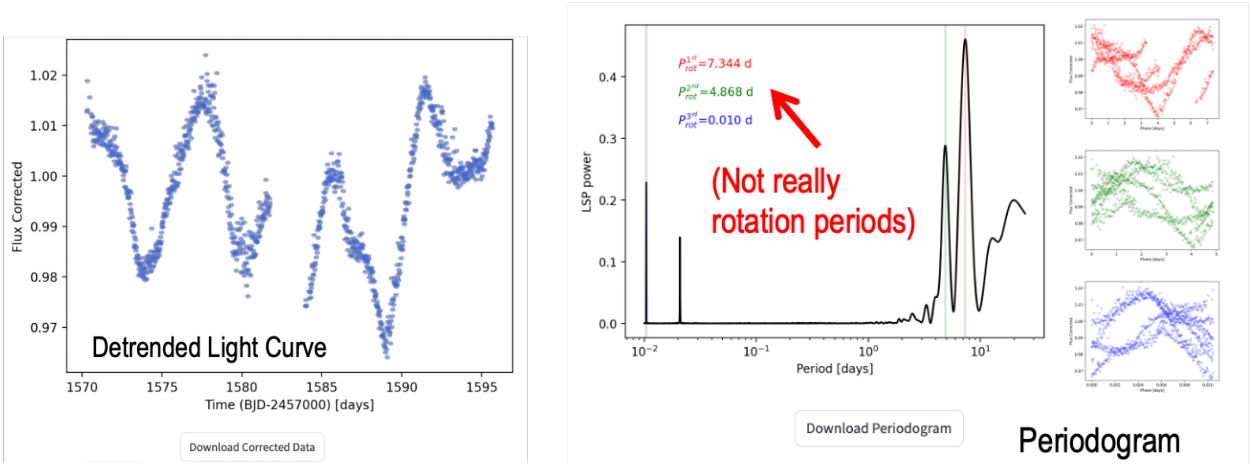

Figure 5. Screen shot of TESS Extractor detrended normalized light curve for TIC 459537285, Sector 10, and Lomb-Scargle periodogram along with subplots phasing the data by period. This star is not strictly periodic, although two quasi-periods at 4.9 and 7.3 days are found in this 27-day light curve. The period at 0.010 days is possibly an alias of the 30-minute observing cadence.

After previewing all 75 stars, we selected eight bright targets (TESS magnitudes 0.7–7.3) for further study. We also selected for follow-up two fainter (11th magnitude) stars near the south ecliptic pole having many consecutive sectors of TESS observations. Table 1 lists the ten targets selected. For these targets, we used TESS Extractor to process light curves for the available sectors as of August 2025 and downloaded the detrended light curve data. The light curve data files contain the time as barycentric Julian Date - 2457000, the normalized flux, and the flux uncertainty, typically around 10^{-4}. Note that a variation of around 0.1 or 10% in flux corresponds to a variation of around 0.1 stellar magnitudes. Below, we show a few highlights from our light curve search. We chose to replot the light curves rather than use the TESS Extractor plots directly since we wanted to plot the data on the same x and y axis scale to better compare light curve variations between sectors.

3.1 TIC 231308237 (Rigel)

The well-known star Rigel in Orion, spectral type B81a, is an ACYG variable. It is the brightest of the ACYG variables, with TESS magnitude 0.706.

Figure 6 shows the normalized flux vs. time from TESS Extractor for TESS Sectors 5 and 32. The observing cadence is not the same for each Sector, but it appears that Rigel had entered a time of lower-amplitude and longer-period variability in Sector 32 compared to Sector 5. Without intervening observations, it is impossible to know whether and when Rigel's variability changed its character. We are hoping that Rigel can be monitored by ground-based observers, e.g., the AAVSO PEP team (see Calderwood and van Ballegoij, these proceedings).

We should also caution that we have not ruled out the possibility that the normalized flux from the TESS light curves for Rigel, or any other ACYG variable discussed here, is not actually varying between observed TESS sectors; the star's position on different CCD cameras and pixels in each

sector, or changes in camera performance and background noise levels, could also change the normalized flux. Long-term ground-based monitoring and comparison of TESS Extractor results with those of other processing pipelines would help to confirm amplitude changes.

It is also likely that the default choice of TESS pixels to integrate over is not optimum for a star as bright as Rigel. The TESS Extractor and other software, e.g., lightkurve[8] do have the option to adjust the selection of pixels included in the analysis.

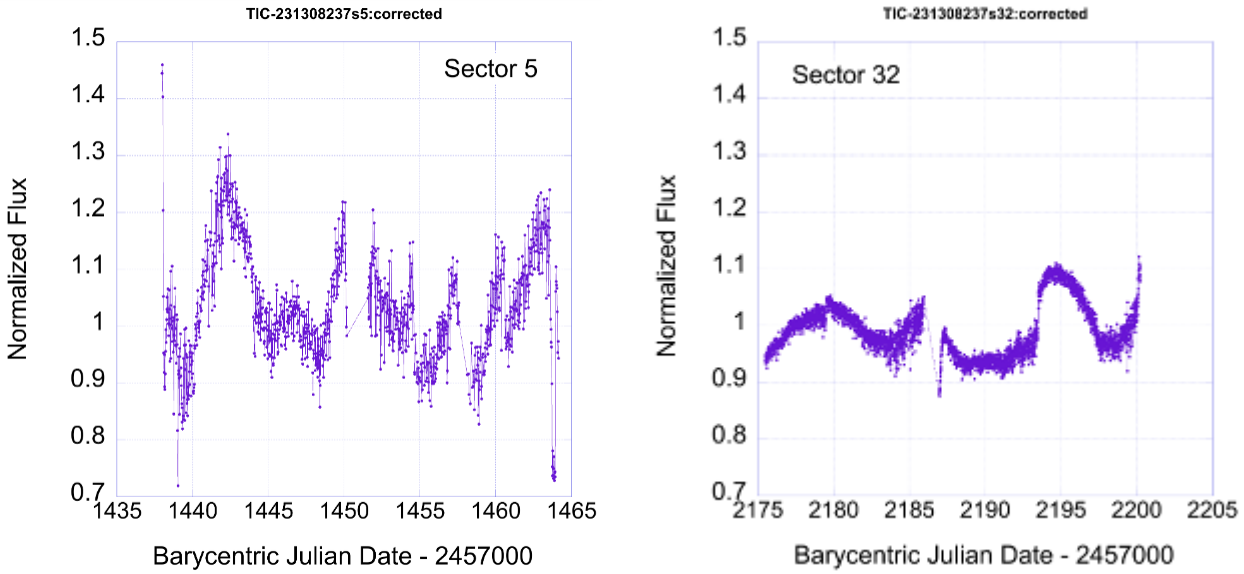

Figure 6. Normalized flux vs. time for TESS Extractor data for TIC 231308237 (Rigel) for Sectors 5 and 32. The light curve appears more regular and seems to have decreased in amplitude in Sector 32. However, given the gap in the time series between Sector 5 and 32, it is not possible to determine when the change in light curve behavior occurred. See text for other caveats.

3.2 TIC 304894154

This star has spectral type B3Ib and TESS magnitude 6.56. Figure 7 shows the TESS Extractor light curves on the same x and y scale for Sectors 10, 11, 63, 64, and 90. The variability appears to have lower amplitude in Sector 10, then increases in amplitude in Sectors 11, 63 and 64. There is a large excursion in Sector 90, followed by variability with a more defined period of around 3 to 4 days. Again, continuous coverage between these data gaps would have been useful to discern trends.

[8] https://lightkurve.github.io/lightkurve/

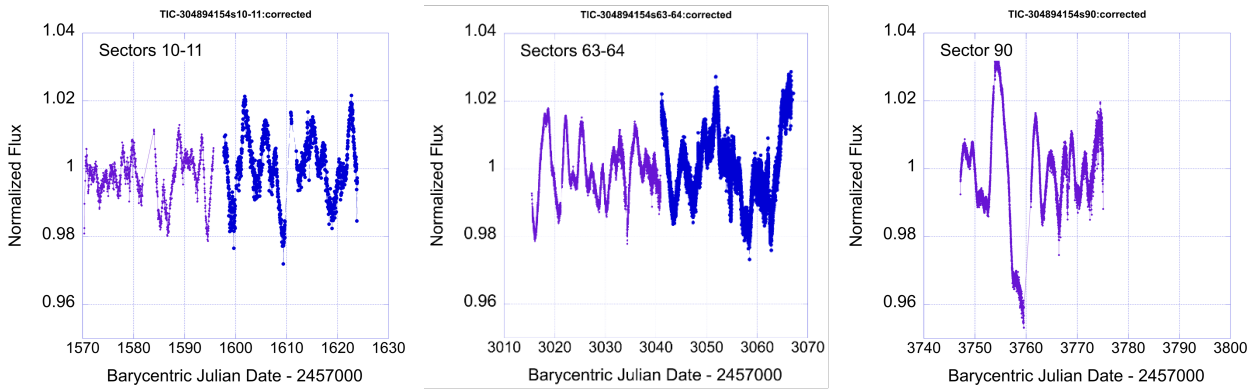

Figure 7. Normalized flux vs. time for TIC 304894154 TESS Extractor data for Sectors 10, 11, 63 64, and 90. The light curve seems to have increased in amplitude during Sectors 11, 63, and 64, and there is a large excursion during Sector 90. The light curve is more regular/periodic during Sector 63 and the end of Sector 90.

3.3 TIC 457766442

This star has TESS magnitude 5.61, and spectral type A2Iab, nearly the same spectral type as Deneb. Figure 8 shows the TESS Extractor light curves plotted on the same x and y axes scales for Sectors 36, 37, 63, 64, and 90. The amplitudes seem to be larger in Sectors 63-64. The Sector 63 data appear to be noisy, and we have traced this problem to noise in the TESS Extractor detrending algorithm for this sector—the noise is not present in the raw light curve or in light curves found on MAST using other processing pipelines. When the light curve is more regular, e.g., in Sectors 37 and 64, a periodicity of around 10 days can be discerned, similar to Deneb's 12-day quasi-period, which also varies in coherence with time. Again, without more continuous coverage, it is impossible to tell whether/when the amplitudes and periodicities changed character between sectors.

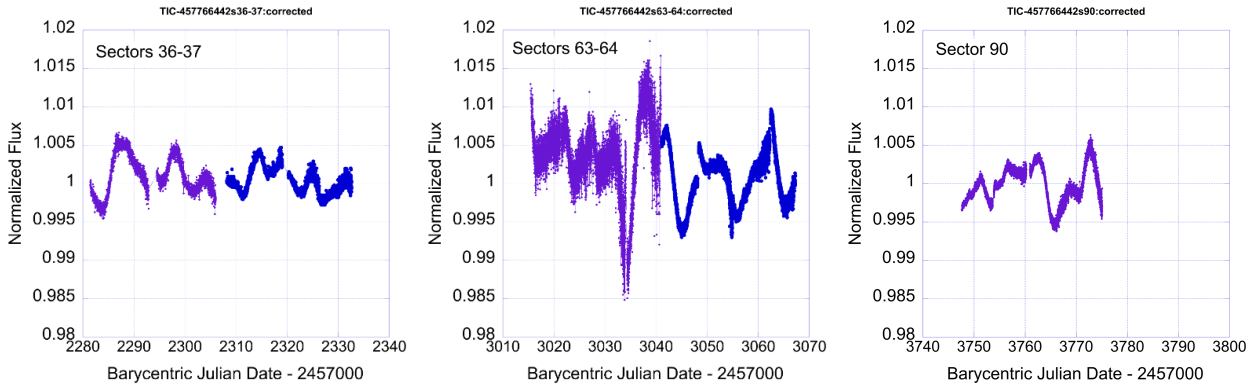

Figure 8. Normalized flux vs. time for TESS Extractor data for TIC 457766442 for Sectors 37, 67, 63, 64, and 90. The light curve seems to have increased in amplitude in Sectors 63 and 64 compared to earlier and later sectors.

4. ACYG variables on the Hertzsprung-Russell Diagram

We attempted to place the ten ACYG variables of Table 1 on the Hertzsprung-Russell (H-R) diagram relative to other named variable star classes. Figure 9 shows the variable star H-R diagram reproduced from Jeffery et al. (2025), with the location of the ten ACYG stars shown by red diamonds. We also included two estimates for the location of Deneb, reflecting the large uncertainty in Deneb's distance. These locations are only approximate, because it is not straightforward to calculate the star's luminosity. To do so requires knowing the star's distance, sometimes derived from parallax measurements, which have large uncertainties. Also, one needs to know the star's visual magnitude and apply a bolometric correction appropriate for the star's spectral type to obtain the absolute bolometric magnitude. We used the SIMBAD database, but also the MAST interface where the Gaia DR3 (Gaia collaboration 2023) and TESS Input Catalogs (Stassun et al. 2019) could be queried to find distance and effective temperature estimates. For most of the stars, there were several values in the literature, catalogs, or databases, which sometimes differed significantly from each other, so we used our judgement to choose a reasonable value. We estimated the Bolometric Correction (BC) using a plot of BC vs. spectral type found in Wikipedia[9] from the Landolt-Börnstein handbook (1982). We did not take into account interstellar reddening/extinction.

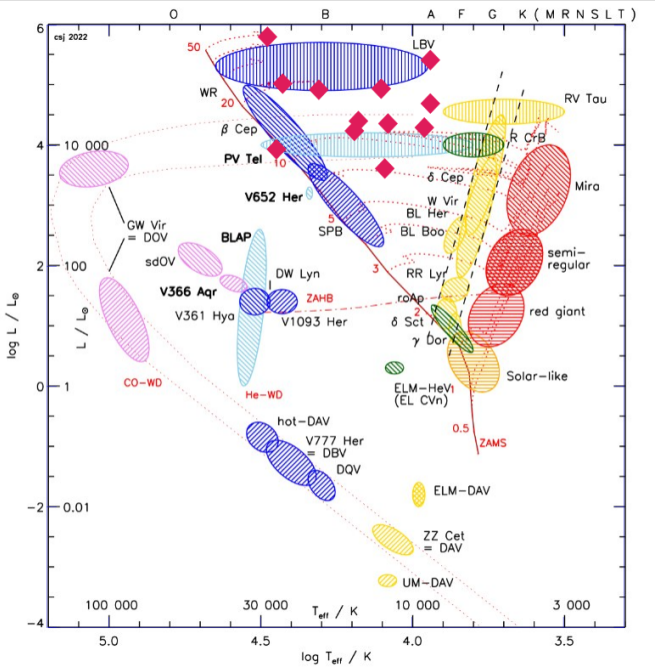

Figure 9. Hertzsprung-Russell Diagram of pulsating variable star types reproduced from Jeffery (2025), Figure 1. Overlaid are estimated locations of ten ACYG stars from our study (red diamonds), along with two locations for Deneb based on two different distance estimates. The ACYG variables mostly are located below the LBV variables, to the right of the β Cep variables, and left of the RV Tauri stars, but are close to the locations of these stars, indicating that the ACYG variables may be related to these variable star types in terms of variability mechanisms and evolutionary state.

[9] https://en.wikipedia.org/w/index.php?title=Bolometric_correction&oldid=1317225345

ACYG variables may not be a homogenous class and may have different evolution states and causes of variability. Based on the spectral types and luminosities of well-known ACYG variables Deneb and Rigel on the H-R diagram, we expected to find ACYG stars below the Luminous Blue Variable (LBV) region, and between the β Cep and RV Tauri variable star regions. For the most part, the ten stars fell within this region. LBVs are supergiant stars more massive than ACYG variables which show microvariations, outbursts, and sometimes giant eruptions (Humphreys and Davidson 1994; Guzik and Lovekin 2014). RV Tauri variables are semiregular yellow supergiants which have light curves with alternating shallow and deep minima and periodicities of 20-90 days (Bódi and Kiss 2019). β Cep variables are main-sequence spectral type O and B stars of with masses 7-20 solar masses, which pulsate in multiple low-order radial and nonradial pressure and gravity modes, with periods of 0.1-0.3 days (Stankov and Handler 2005). The proximity of these variable star types on the H-R diagram to the ACYG variables may indicate some commonality in terms of mechanisms for variability.

5. MAST High-Level Science Products

Processed TESS light curves for many prior sectors for all 75 ACYG stars proposed for TESS Cycle 8 observations are available as HLSPs at the MAST portal.[10] Most light curve products are available as *fits* binary files, and a learning curve is required to locate, download and process the data using additional software tools. We developed a Jupyter Notebook[11] using astroquery[12] python tools to read the fits files and plot the light curves. Figure 10 shows a screen shot of the MAST web site. One can enter the target name, e.g., by TIC number, and view the list of data products available for download. We recommend selecting either TESS light curve products or target pixel files, and avoiding the full-frame image files, which have very large file sizes. There is also a 'cart' where files can be selected and placed for later bulk downloads.

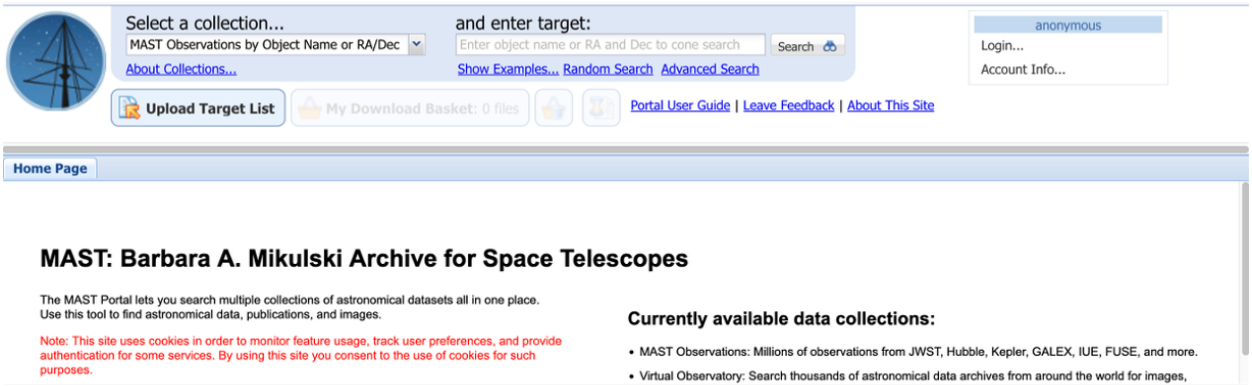

Figure 10. Screen shot of interface for TESS data search using MAST.

[10] https://mast.stsci.edu/portal/Mashup/Clients/Mast/Portal.html
[11] https://jupyter.org/
[12] https://astroquery.readthedocs.io/en/latest/

The MAST offerings include many High-Level Science Products (HLSPs) created using different processing 'pipelines', which are not the same as the TESS Extractor pipeline. A non-exhaustive list of these includes:

- QLP: Quick Look Pipeline
- SAP/PDCSAP: Simple Aperture Photometry / Pre-Search Data Conditioning Simple Aperture Photometry
- SPOC: Science Processing Operations Center pipeline
- Eleanor Lite
- TASOC: TESS Asteroseismic Science Operations Center pipeline
- TGLC: TESS Gaia Light Curve, makes use of Gaia data for crowded fields

Except for the Quick Look Pipeline data, light curves are available for only a few stars for a few sectors. Table 1 lists available sectors for our ten stars from the QLP, PDCSAP, and Eleanor Lite pipelines. SPOC data were available for only TIC 30106140, and TASOC and TGLC data were available only for the faintest two stars. *An advantage of proposing stars to observe via the TESS General Investigator Program is that the SAP/PDCSAP-processed light curves are made available on MAST a few months after the observations are taken.*

Some pipelines are preferable to others for studying stellar variability. To intercompare results for different pipelines, for our ten stars of interest (Table 1) we examined light curves for the same sector using several pipelines. Note that even the 'raw' light curves shown below usually have been pre-processed in some way, e.g., normalized, artifacts and trends common to most pixels in the field removed, etc.

Figure 11 compares the 'raw' and detrended light curve for the Quick Look Pipeline for Sector 68 for TIC 179508685. The raw light curve (left) shows that the star has a 1.658-day periodicity, along with a longer higher-amplitude modulation superimposed. However, the Quick Look Pipeline detrending algorithm is intended to remove stellar variability to facilitate searching for planet transits, so one can see that the detrended light curve (right) is nearly flat.

Figure 12 shows the raw and detrended light curves for TIC 179508685 for Sector 10 from the Eleanor Lite pipeline. While the raw light curve has some artifacts at the beginning of the first and second half of the sector, the 1.658-day period is visible as well as the longer-period modulation. The Eleanor Lite corrected light curve has retained the shorter periodicity but has removed the longer-period modulation. The Eleanor Lite pipeline also appears to have introduced some noise and did not remove anomalous data at the beginning of the first and second half of the observing sector.

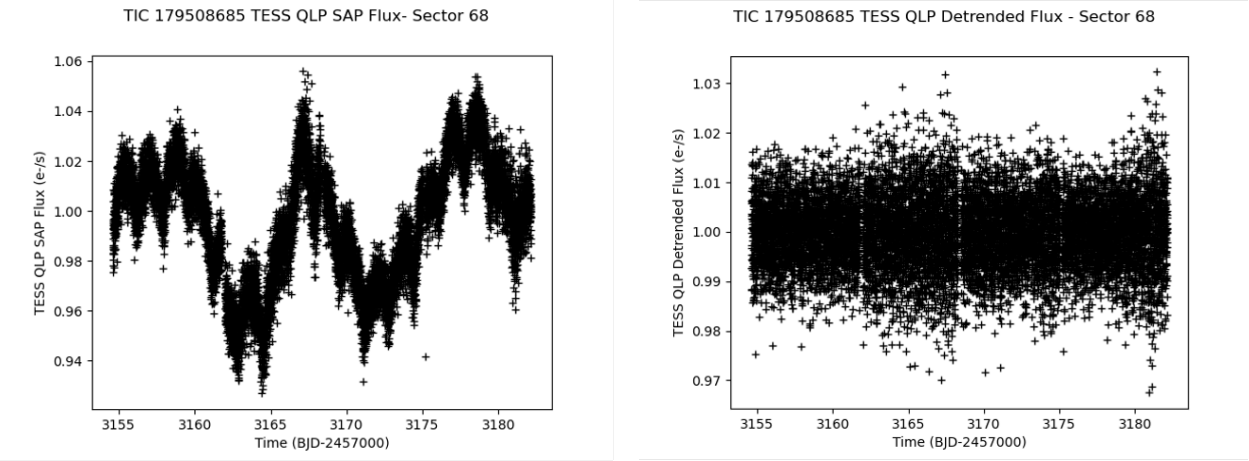

Figure 11. Raw (left) and detrended (right) TIC 179508685 light curves for Sector 68 from the Quick Look Pipeline. A 1.658-day periodicity along with a longer-period modulation can be seen in the raw data; however, the detrended data removes both the short and long-period variability.

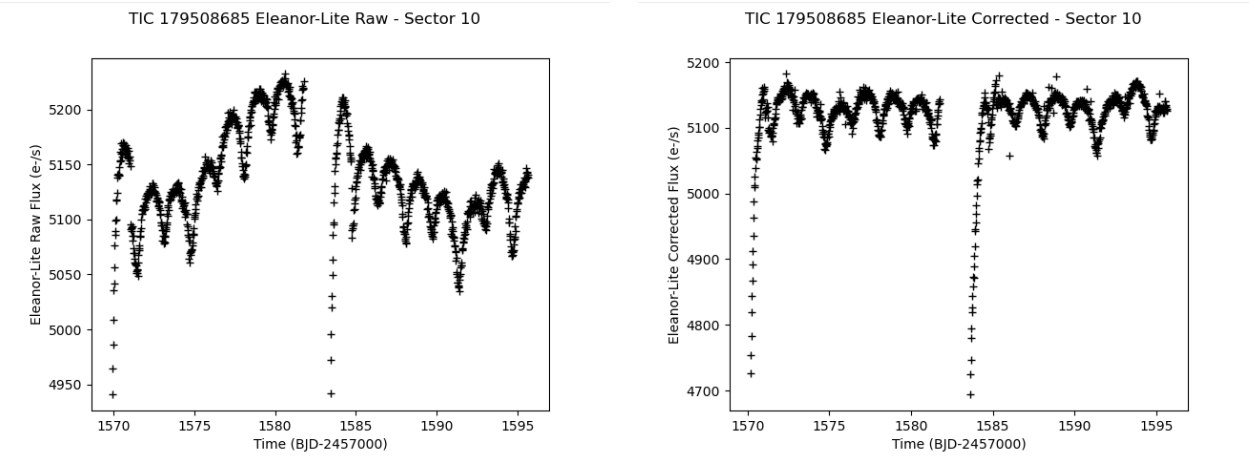

Figure 12. Raw (left) and corrected (right) light curves from Eleanor Lite pipeline for TIC 179508685 for Sector 10. A 1.658-day periodicity with a longer-period modulation can be seen in the raw data. The Eleanor Lite corrected light curve flattens this long-term trend while retaining the shorter-period variation. The corrected light curve also retained artifacts at the beginning of each half-sector and has a few data points that must be cleaned.

We next discuss the SAP/PDCSAP pipeline light curves that are made available for stars targeted as part of the TESS General Investigator program. Figure 13 shows the SAP (raw) and PDCSAP (corrected) light curve for TIC 459537285 during Sector 10. The light curve is not normalized, but it appears that the flux levels are shifted in the PDCSAP data. There seems to have been a slight amount of detrending, and small light curve segments in the PDCSAP data have been deleted at the beginning of each half-sector, even though these data do not look anomalous in the SAP light curve. While the PDCSAP light curve is usable and does not seem to have smoothed out real variations, we recommend comparing the SAP and PDCSAP light curves; our prior experience with SAP/PDCSAP products for Cepheid variable light curves showed that the PDCSAP pipeline sometimes removed real periodic variations.

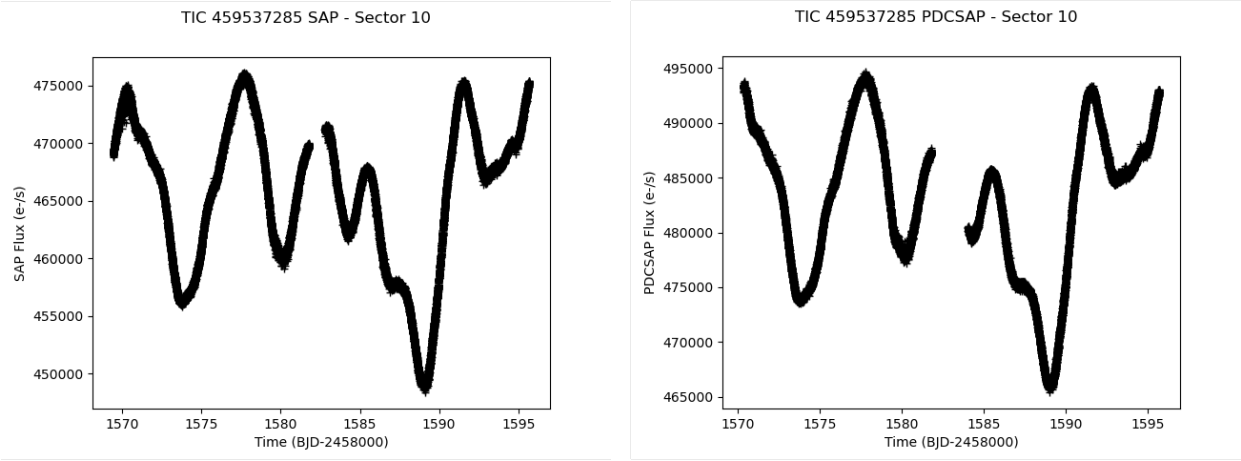

Figure 13. TIC 457537285 Sector 10 SAP (left) and PDCSAP (right) light curves. The two light curves are very similar, except that the PDCSAP flux is higher and segments of data at the beginning of each half sector have been deleted.

Figure 14 shows the 'raw' and 'corrected' light curves from the Eleanor Lite pipeline for TIC 459537285 during Sector 10. The raw Eleanor Lite light curve seems to have an obvious upward trend. The corrected light curve was so noisy that we had to replot the data and zoom in manually. The trend is flattened in the corrected data, but more cleaning would be needed to remove bad data points. Note that Figure 14 and Figure 13 can be compared to see the results for this star using two different pipelines. While some of the same features can be discerned, there are also significant differences, emphasizing the need for accurate long-term monitoring of these stars to establish an absolute amplitude scale.

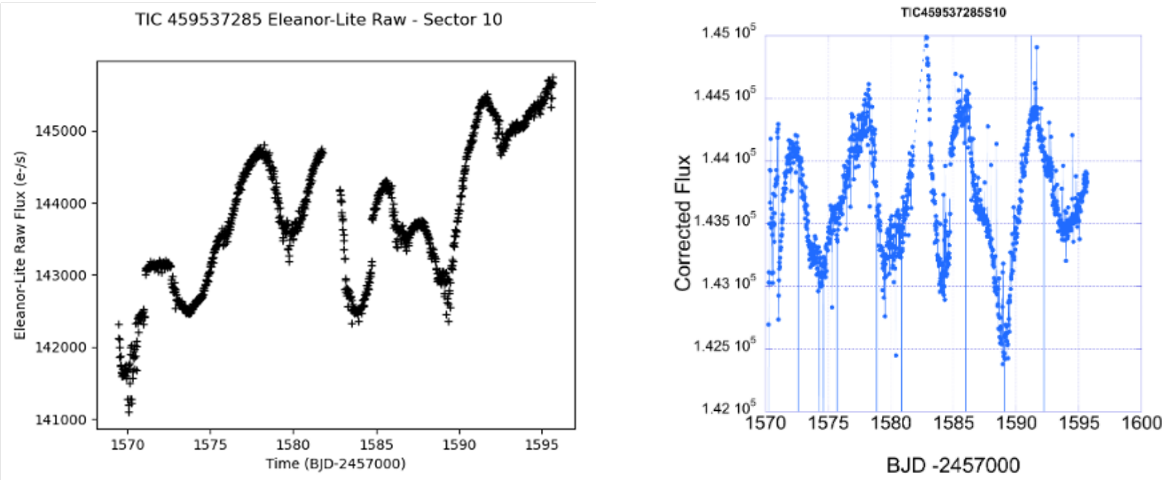

Figure 14. TIC 4959537285 Sector 10 Eleanor-Lite pipeline raw (left) and corrected (right) light curves. The raw light curve has an upward trend that was removed in the corrected light curve, but the corrected curve has many bad data points that need to be cleaned. The corrected light curve is very similar to the SAP and PDCSAP light curves of Figure 13.

To summarize our recommendations regarding light curves processed using various data pipelines available on MAST:

Quick Look Pipeline (QLP): The raw light curve is useful for a 'quick look' but may still contain trends. However, the detrended light curve is not useful for variable stars since the long-term trends and pulsation-like variations are removed to optimize searches for transiting exoplanets.

SAP/PDCSAP: This pipeline is very useful, and light curves are made available on MAST for all targets requested via the General Investigator program. We recommend comparing the SAP (simple aperture photometry) and PDCSAP (corrected) light curves to be sure that real trends and pulsations have not been removed in the PDCSAP light curve.

Eleanor Lite: This pipeline removes longer-period trends which may be real from the corrected light curve but retains shorter-period variations. Also, the resulting corrected light curves are often noisy and have bad data points, requiring further cleaning.

Table 1. Ten ACYG variables selected for follow-up after screening light curves using TESS Extractor. TESS Magnitudes are from the TESS Input Catalog 8.2 (Stassun et al. 2019). Spectral types are from the SIMBAD database.[13] High-Level Science Product light curves processed by several different pipelines are available for some of the stars and some sectors at MAST.[14]

TIC	TESS Magnitude	Spectral Type	TESS Extractor	QLP	SAP/PDC SAP	Eleanor Lite	Notes
			Sectors Available				
231308237	0.706	B8Ia	5, 32	5, 32		5	Rigel
317046099	6.57*	B2Ia	10, 11, 37, 38, 64	10, 11, 37, 38	10, 37, 38, 64	10	V808 Cen
337793038	5.24	O8Iaf	12, 39, 66, 90	12, 39, 66	12, 39, 66		V973 Sco
457766442	5.61	A2Iab/b	36, 37, 63, 64, 90	36, 37, 63, 64	36, 37, 63, 64		
459537285	8.66*	B8Ia	10, 36, 37, 63, 64, 90	10, 36, 37, 63, 64	10	10	V523 Car
304894154	6.56	B3Ib/II	10, 11, 63, 64, 90	10,11,63,64	10	10	
458076250	6.64	B0.7Ib	10, 36, 37, 63, 64, 90	36, 37, 63, 64			V513 Car
460279488	7.32	B8Iab	10, 11, 36, 37, 63, 64, 90	10, 11, 36, 37, 63, 64		10	V508 Car
30106140	11.037	B5Ia+	1-39, 61-69, 87-90	32 sectors, 1-69	23 sectors, 27-88	1,2,3,4, 6,7,8,9, 10	
179508685	11.365	OB D	1-13, 27-39, 61-69, 87-90	30 sectors, 2-69		2,3,4,5, 6,7,8,9, 10	1.658-day period with longer-period modulation

*TESS Input Catalog magnitudes were not correct; V magnitude from SIMBAD is listed instead.

We did not show example light curves from the SPOC, TASOC, TGLC pipelines here. The SPOC pipeline is the overarching processing pipeline that produces the SAP/PDCSAP light curves, and

[13] https://simbad.u-strasbg.fr/simbad/

[14] *https://mast.stsci.edu/portal/Mashup/Clients/Mast/Portal.html*

it is not clear what the differences might be between SPOC and SAP/PDCSAP light-curve products. Of the ten stars in Table 1, only TIC 30106140 had SPOC light curves available on MAST. The TASOC pipeline is excellent for pulsating variable stars, but light curves are not available on MAST for most ACYG stars and are available only for early TESS sectors. The TGLC pipeline makes use of Gaia DR3 (Gaia Collaboration 2023) data for position corrections for stars in crowded fields and clusters and looks promising. For the ten stars in Table 1, TGLC light curves are available only for the faintest two stars and for early sectors.

6. Summary and Future Work

We are only in the initial stages of exploring the large number of TESS light curves available for ACYG variables. However, the TESS time-series length of 27 days per sector leaves long gaps between observations for most of the targets. Detrending the light curves and placing them on the same absolute scale to compare sectors is challenging. Longer-term, more continuous monitoring by ground-based observers as well as observations overlapping in time with the TESS observations are needed to fill in the time-series gaps and verify changes in amplitude or large excursions found in the TESS data.

We plan to continue analysis of the existing TESS light curves for all 75 targets proposed for TESS Cycle 8, including the new light curves from Cycle 8 as they become available. Even though ACYG variables are not strictly periodic, we plan to examine Fourier transforms of existing time-series data to determine whether significant quasi-periodicities are present. We also plan to identify ACYG stars to propose for TESS General Investigator Cycle 9 observations.

We have identified a few ACYG stars for follow-up by the AAVSO ground-based PEP observing program. We also plan to search for ACYG light curve data from other sources, such as from the prior NASA *Kepler* (Borucki et al. 2008) and K2 (Howell et al. 2018) missions, and the Solar Mass Ejection Imager (Jackson et al. 2004, Clover et al. 2011, Guzik et al. 2025).

We also plan stellar evolution and pulsation modeling (see Moore and Guzik 2025). We hope that these studies will lead to a better understanding of the origin of the variability and the evolutionary state of Deneb and the ACYG variables.

Acknowledgements

This work makes use of data from NASA's Transiting Exoplanet Survey Satellite (TESS), obtained from the Mikulski Archive for Space Telescopes (MAST). We also acknowledge use of Gaia DR3 and SIMBAD databases. We made use of open-source software including astroquery python tools and TESS Extractor. We thank Philip Masding (British Astronomical Association) for suggesting TESS Extractor. We acknowledge support from Los Alamos National Laboratory, managed by Triad National Security, LLC, for the U.S. DOE's NNSA Contract #89233218CNA000001. This research has made use of the International Variable Star Index (VSX) database, operated at AAVSO, Cambridge, Massachusetts, USA.

References

Abt, H.A., Guzik, J.A., and Jackiewicz, J. 2023, The Abrupt Resumptions of Pulsations in α Cygni (Deneb), PASP **135**, 1054, 124201

Bódi, A. and Kiss, L.L. 2019, Physical Properties of Galactic RV Tauri Stars from Gaia DR2 Data, ApJ **872**, 60, doi: 10.3847/1538-4357/aafc24

Borucki, W.J., et al. 2010, *Kepler* Planet-Detection Mission: Introduction and First Results, Science **327**, 5968, doi: 10.1126/science.1185402

Clover, J.M., et al. 2011, Epsilon Aurigae light curve from the Solar Mass Ejection Imager, AAS Meeting Abstracts **217**, 257.02

Gaia Collaboration, Gaia Data Release 3, 2023, Summary of the content and survey properties, A&A **674**, A1, https://doi.org/10.1051/0004-6361/202243940

Guzik, J.A., Abt, H., Jackiewicz, J., and Kloppenborg, B.K. 2024a, Abrupt Periodic Pulsation Resumptions in Deneb, Proceedings of the 112th Annual Meeting of the AAVSO, https://www.aavso.org/112, doi: 10.48550/arXiv.2410.23936

Guzik, J.A., Kloppenborg, B., and Jackiewicz, J. 2024b, Deneb and the Alpha Cygni Variables, Society for Astronomical Sciences Symposium on Telescope Sciences 2024 proceedings, eds. J.C. Martin, R.K. Buchheim, R.M. Gill, W. Green, and J. Menke, https://socastrosci.org/wp-content/uploads/2024/08/2024-Proceedings_Ver1.3d.pdf, doi: 10.48550/arXiv.2410.23985

Guzik, J.A., Kloppenborg, B., Richardson, N., Jackiewicz, J., Morrison, N., Calderwood, T., and Pigulski, A. 2025, Abrupt Pulsation Resumptions in Deneb: An Update, Proceedings of the 113th Annual Meeting of the American Association of Variable Star Observers, Huntsville, AL, Nov. 8-10, 2024, www.aavso.org/113, arXiv:2503.20058

Guzik, J.A. and Lovekin, C.C. 2014, Pulsations and Hydrodynamics of Luminous Blue Variables, doi: 0.48550/arXiv.1402.0257

Hattori, S., et al. 2022, The unpopular Package: A Data-driven Approach to Detrending TESS Full-frame Image Light Curve, AJ, 163, 284, doi: 10.3847/1538-3881/ac625a

Howell, S.B., et al. 2014, The K2 Mission: Characterization and Early Results, PASP **136**, 398, doi: 10.1086/676406

Humphreys, R.A. and Davidson, K. 1994, The Luminous Blue Variables: Astrophysical Geysers, PASP **106**, 1025

Jackson, B.V., et al. 2004, The Solar Mass Ejection Imager (SMEI) Mission, Sol. Phys. **225**, 177

Jeffery, C.S. 2025, Linear and non-linear models for large-amplitude radial pulsation in faint blue stars (BLAPs), MNRAS **538**, issue 4, 2952-2988, https://doi.org/10.1093/mnras/staf401

Landolt-Börnstein, Numerical Data and Functional Relationships in Science and Technology - New Series, 1982, eds. L.H. Aller, et al., Group 6 Astronomy and Astrophysics, Stars and Star Clusters, Springer, Berlin, Heidelberg, New York, Band 2b, S.453

Moore, A.H. and Guzik, J.A. 2025, MESA Modeling of Blue Supergiants and Alpha Cygni Variables, Proceedings of the 113th Annual Meeting of The American Association of Variable Star Observers (www.aavso.org/113), ed. J.A. Guzik, ISBN 978-1-939538-72-7

Richardson, N.D., et al. 2011, A Five-Year Spectroscopic and Photometric Campaign on the Prototypical α Cygni Variable and A-Type Supergiant Star Deneb, AJ **141**, 17,

doi:10.1088/0004-6256/141/1/17

Ricker, G.R., et al. 2015, Transiting Exoplanet Survey Satellite, Journal of Astronomical Telescopes, Instruments, and Systems, Volume 1, id. 014003

Serna, J., et al. 2021, Stellar Rotation of T Tauri Stars in the Orion Star-forming Complex, ApJ **923**, 177, doi: 10.3847/1538-4357/ac300a

Stankov, A. and Handler, G. 2005, Catalog of Galactic β Cephei Stars, ApJSS **158**, 193, doi: 10.1086/429408

Stassun, K., et al. 2019, The Revised TESS Input Catalog and Candidate Target List, AJ **158**, 138, doi: 10.3847/1538-3881/ab3467

van Genderen, A., et al. 1989, Light variations of massive stars (alpha Cygni variables). IX., A&AS **79**, 263

The Red Dwarf Group: Five Years of Coordinated Photometric and Spectroscopic Observations on M-Dwarf Flares

Gary Hawkins

Coordinator, Red Dwarf Group; Director, Blossom Valley Small Telescope Observatory;
astrogary8@gmail.com

Abstract

Over the past five years, the Red Dwarf Group (RDG) has conducted coordinated, high-cadence photometric and spectroscopic observations of flare activity on nearby M-dwarf stars. These efforts, involving amateur and professional astronomers worldwide, have yielded over 400,000 observations of key targets such as EV Lacertae and AD Leonis. Using a proprietary tool called PhotoStats, RDG participants have derived flare energies, temperature evolution, and frequency distributions with increasing precision. This paper summarizes the observing strategy, data analysis methods, and major findings from 2021–2025, including several "monster" flares whose bolometric energy is estimated to have exceeded 10^{35} erg.

1. Introduction

M-dwarf stars, or red dwarfs, form the majority of the stellar population in the Milky Way, comprising roughly of 75% of all stars [1]. Despite their diminutive size and cool temperatures, they are dynamic laboratories for magnetic activity. Many host exoplanets in their habitable zones, but frequent and energetic flares can dramatically affect planetary atmospheres and potential biosignatures. Understanding these stellar outbursts is thus crucial for both stellar astrophysics and astrobiology.

The Red Dwarf Group (RDG) is a collaborative consortium of amateur and professional astronomers focused on long-term, high-cadence monitoring of active M-dwarfs. The mission of the RDG is to gather photometric and spectroscopic data, quantify flare energy distributions, and refine color-temperature models. This program contributes directly to the AAVSO International Database (AID) and seeks to bridge the gap between small observatories and academic research.

M-dwarf flares are unpredictable and transient, with rise times of seconds to minutes and decay phases extending over hours. During such events, the flare region may heat from a few thousand kelvin above the photosphere to 10,000–20,000 K, temporarily shifting the emission peak from red to blue and ultraviolet wavelengths [2]. This phenomenon not only alters the apparent brightness but also provides insight into the underlying magnetic reconnection processes driving these flares.

2. Observing Program

2.1 History

The RDG has focused observation primarily on EV Lacertae (EV Lac) and AD Leonis (AD Leo) to ensure adequate coverage across time zones and to protect against adverse weather conditions at observing sites. EV Lac and AD Leo are well known for their intense and frequent optical and UV flares, strong Hα emission, and rapid rotation. Their proximity and brightness make them ideal candidates for both photometric and spectroscopic campaigns. Their placement in the sky is ideal as it allows one to be observed while the other is not available.

The RDG network currently includes over twenty active observers, primarily in North America and Europe. Members utilize a wide variety of telescopes ranging in aperture from 50mm to 0.4m. Some of those observatories are remote and autonomous. The Blossom Valley Small Telescope Observatory is an example of one of the more modest setups within the RDG. It consists of an 8-inch SCT mounted on a Skywatcher EQ-6R Pro German Equatorial Mount (GEM). The 8-inch SCT at the BVSTO employs a x0.63 focal-reducer and is typically used in combination with a ZWO ASI 533MC CMOS color camera [3]. The author is also investigating if the use of small aperture scopes including a Williams Optics 51mm and the SeeStar S50 smart telescope can provide useful data.

Due to the rapid increase of observed flux for the leading edge of many flares, photometric measurement cadences of 30 secs or less are mandated by the RDG, while maintaining a minimum SNR = 100. Spectroscopic data, collected using low- to medium-resolution spectrographs is being used to characterize the continuum and the evolution of emission lines, including Hα, Hβ, and Ca II H & K. These spectra reveal temperature, density, and velocity structures in the flare plasma.

The RDG was launched under the guidance of Bob Buchheim, who oversaw operations between 2020 through 2023. The program was announced in AAVSO Alert Notice 789. This first campaign resulted in a number of publications [4, 5, 6, 7]. Gary Hawkins took over coordination of the RDG in 2024, announcing activities in AAVSO Alert Notice 880. RDG members have submitted more than 400,000 observations to the AID so far and aim to maintain continuous monitoring of EV Lac and AD Leo through 2027.

2.2 Benefits

The work of the RDG is significant to the broader scientific community because it provides continuous, high-cadence monitoring of M-dwarf flare activity—an area often under-sampled by professional observatories. Large telescopes and space missions like TESS or Swift are optimized for short campaigns or limited fields of view, leaving major gaps in long-term temporal coverage. RDG's distributed network of small observatories attempts to fill this gap, producing a multi-year dataset of unprecedented temporal density. These observations allow for accurate flare

frequency distributions, energy scaling relations, and color–temperature calibrations that potentially could refine existing models of stellar magnetic activity.

Beyond its immediate scientific outputs, RDG's work enhances the integration of amateur and professional astronomy in time-domain research. By providing calibrated, openly shared photometric data, the group supports cross-validation with survey and ground-based missions. RDG's efforts also inform exoplanetary science by characterizing the flare environments around potentially habitable stars, improving our understanding of atmospheric erosion and habitability limits. The combination of rigorous methodology, open collaboration, and large-scale participation makes RDG's dataset a vital and enduring resource for stellar and planetary scientists alike.

Members of the RDG gain access to a collaborative and scientifically rigorous community that bridges the gap between amateur and professional astronomy. Participation offers opportunities to contribute meaningful data to peer-reviewed research, develop advanced skills in photometric and spectroscopic analysis, and engage directly with experts in stellar astrophysics. Through coordinated observing campaigns, shared calibration standards, and mentoring in tools such as *PhotoStats* and AAVSO workflows, members enhance both their technical proficiency and scientific understanding. The group's cooperative structure also fosters friendships, shared learning, and a sense of purpose—allowing each observer to see their individual work become part of a global effort to advance our knowledge of stellar activity and its effects on exoplanetary environments.

2.3 Challenges

Bringing multi-user data together is one of the greatest technical challenges faced by any collaborative observing group. Each observer operates with unique hardware—different telescope apertures, detectors, filters, and image calibration pipelines. Even when all data are of high quality, small systematic differences in zero-points, filter transmission, or processing methods can lead to measurable offsets. These inconsistencies complicate the generation of uniform light curves and can introduce biases into flare amplitude and color-temperature measurements. The RDG commitment to common comparison stars, consistent procedures, and transformation into standard photometric systems is therefore critical to achieving reliable, scientifically meaningful results.

To minimize these variations, RDG members adhere to a shared set of standard operating procedures and comparison/check star lists for each target. During post-processing, the group applies normalization and bias correction to align datasets from multiple observers into a coherent ensemble light curve. Where data gaps exist, interpolation and scaling algorithms ensure temporal continuity without distorting flare profiles. This attention to calibration consistency and statistical rigor allows the combined dataset to reach a level of precision comparable to professional survey work—demonstrating how coordinated citizen science can generate robust, publishable results in time-domain astrophysics.

3. Areas of Analysis

The Red Dwarf Group's analytical work is focused on quantifying the physical properties of stellar flares through systematic, multi-observer photometry and spectroscopy. By combining high-cadence, multi-band light curves with spectral diagnostics, RDG aims to characterize how energy is released, distributed, and dissipated during magnetic reconnection events on active M-dwarfs. This includes deriving flare amplitudes, durations, and color-temperature evolution from time-series photometry and, when applicable, correlating these with spectroscopic indicators such as Balmer line broadening and continuum enhancement. Through rigorous statistical normalization and temperature modeling, RDG's analyses transform raw observational data into calibrated, physics-based insights—linking observed brightness variations to underlying plasma processes and magnetic energy release. The result is a coherent, quantitative framework for studying stellar flare energetics that complements both professional observatory data and theoretical models.

The sections below discuss a few areas RDG team members have been investigating.

3.1 Stellar Spot Variance and Rotational Period

By collecting high-quality photometric data and applying careful post-processing, we are able to analyze not only the flare events themselves but also the slowly varying quiescent state of the star. This quiescent light curve frequently reveals subtle stellar-spot modulation—often only tens to at most a few hundred millimagnitudes (Figure1)—arising as active regions rotate into and out of view. Using periodogram analysis, we can determine the star's rotation period with good precision, while monitoring the variance in the quiescent level provides valuable insight into the evolution of spot coverage and magnetic activity. These changes typically unfold over timescales ranging from tens to hundreds of days, making long-duration, multi-observer coverage essential.

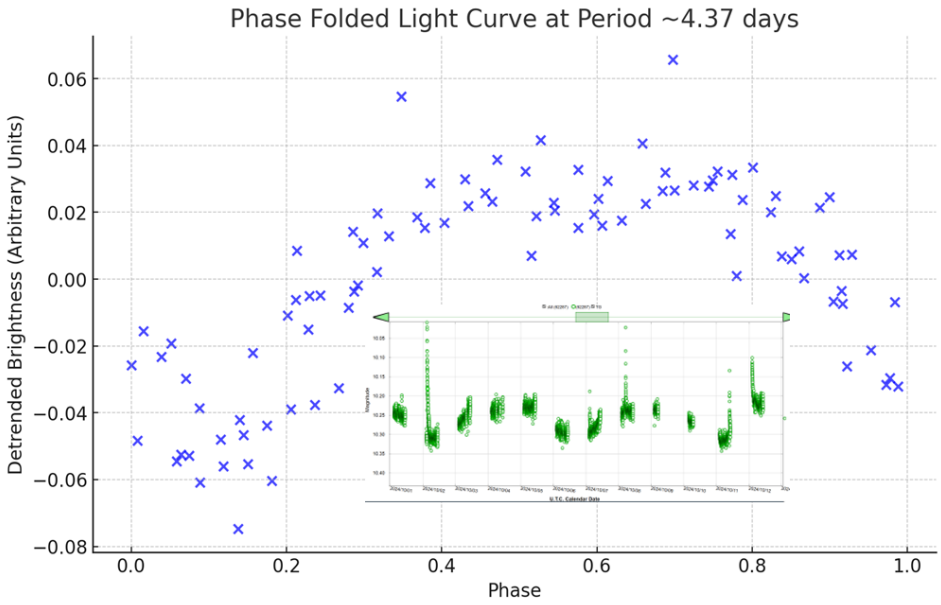

Figure 1. Example Phase Folded Light Curve for EV Lac

Period analysis using Lomb–Scargle methods yields rotation periods of 2.3 and 4.8 days for EV Lac and AD Leo, respectively (Figure 2). Long-term monitoring demonstrates differential rotation and migration of active longitudes.

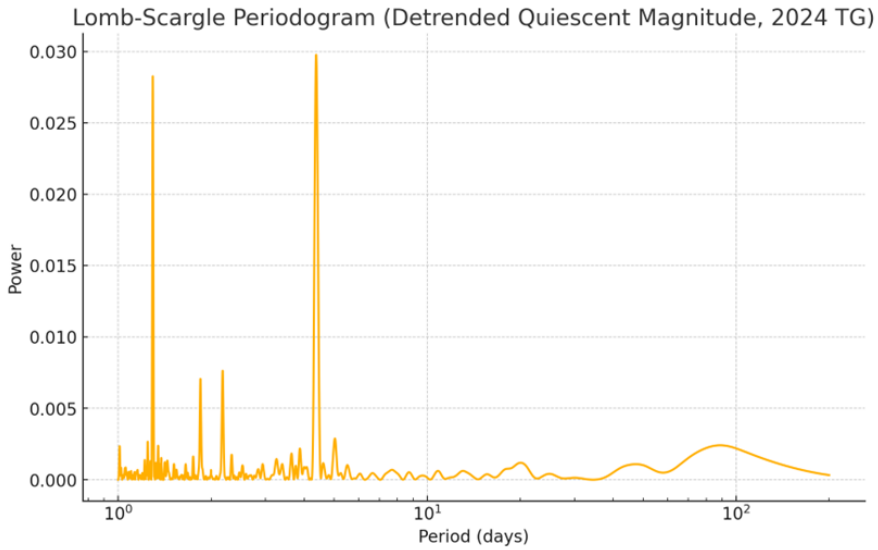

Figure 2. Example Periodogram for EV Lac

3.2 Flare Frequency Diagrams

Once the energy of individual flares across an observing season have been characterized, it is possible to construct a flare frequency diagram (FFD), a fundamental tool for characterizing the flare energy distribution of an active star (Figure 3).

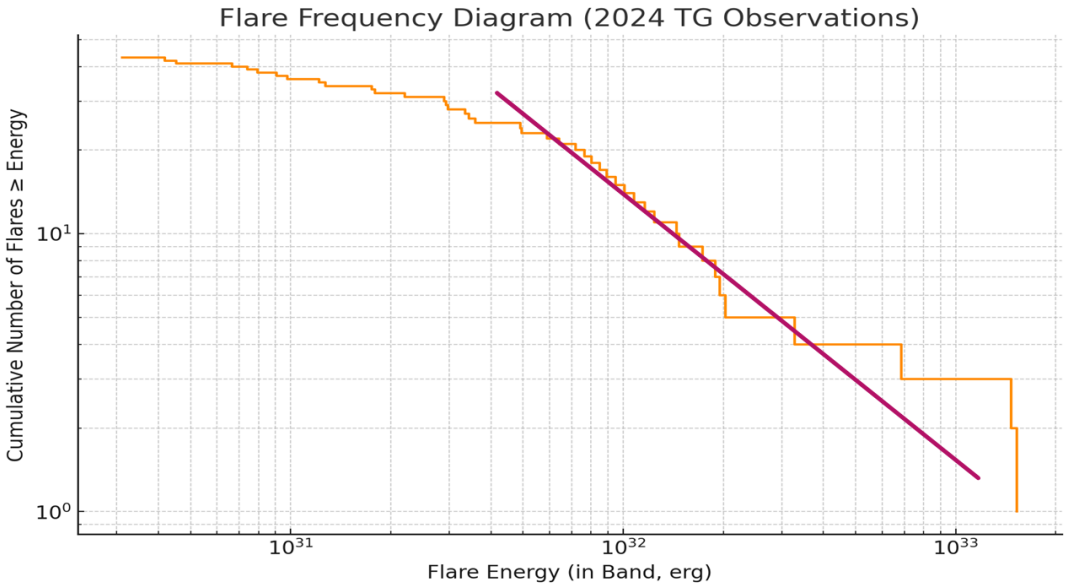

Figure 3. Example Flare Frequency Diagram for EV Lac

An FFD shows how often flares of different energies occur, typically expressed as the cumulative number of flares over a given period above a given energy. This allows us to quantify both the overall activity level and the relative abundance of low-, medium-, and high-energy events. By repeating this analysis over multiple observing seasons, we can begin to probe deeper scientific questions about the long-term evolution of magnetic activity in M dwarfs. For example, we can examine whether the flare frequency rate is increasing or decreasing over time, whether the star is becoming more or less active as its magnetic cycle progresses, and whether patterns emerge that resemble solar-cycle behavior but scaled to the physics of low-mass stars. With sufficient temporal coverage, these trends can reveal how magnetic energy builds, dissipates, and reorganizes in these highly active stellar dynamos.

3.3 Single-Band to Multiband Photometric Conversion

A recent area of investigation within the Red Dwarf Group has been to assess whether photometric data collected in a single band — for example, the *B*-band — can be used to predict corresponding measurements in another band, such as *V*. Our initial results have been promising (Figure 4).

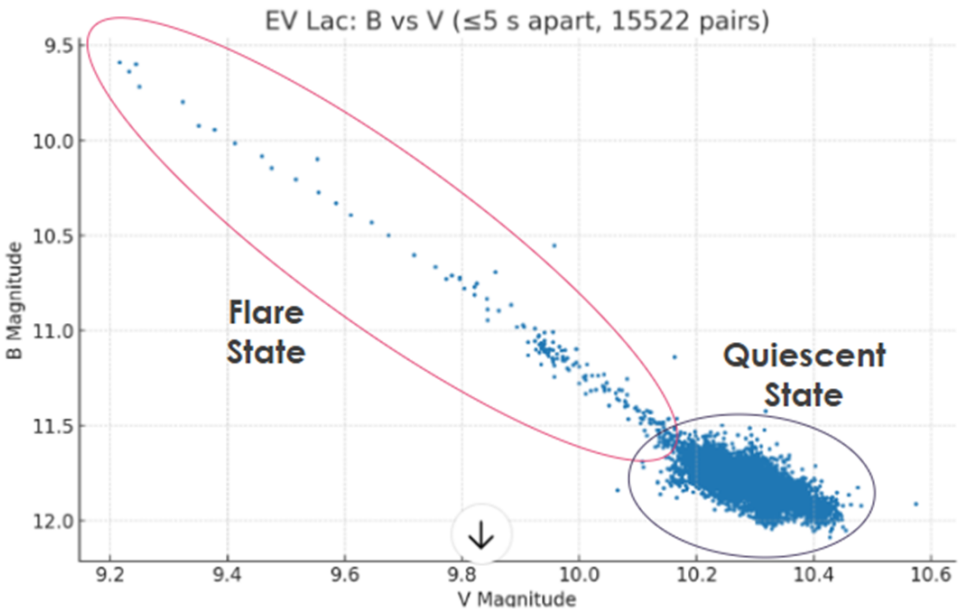

Figure 4. Example B Magnitude vs. V Magnitude Relationship for EV Lac

During the flare phase in particular, the relationship between the bands appears well defined, enabling us to model one light curve directly from the other with surprising accuracy. This is scientifically useful because it allows observers to maximize temporal resolution without needing to alternate filters, a process that often sacrifices cadence at the very moment rapid changes are occurring. If we can reliably reconstruct *B*–*V* color from single-band data, we can derive temperature and energy evolution curves even when only one filter was used.

However, new analysis of a large "monster flare" observed in October 2025 — described in Section 6 — has introduced an important complication. In that event, the impulsive/decay locus in *B*–*V* space was not a straight line but instead formed a loop (Figure 5).

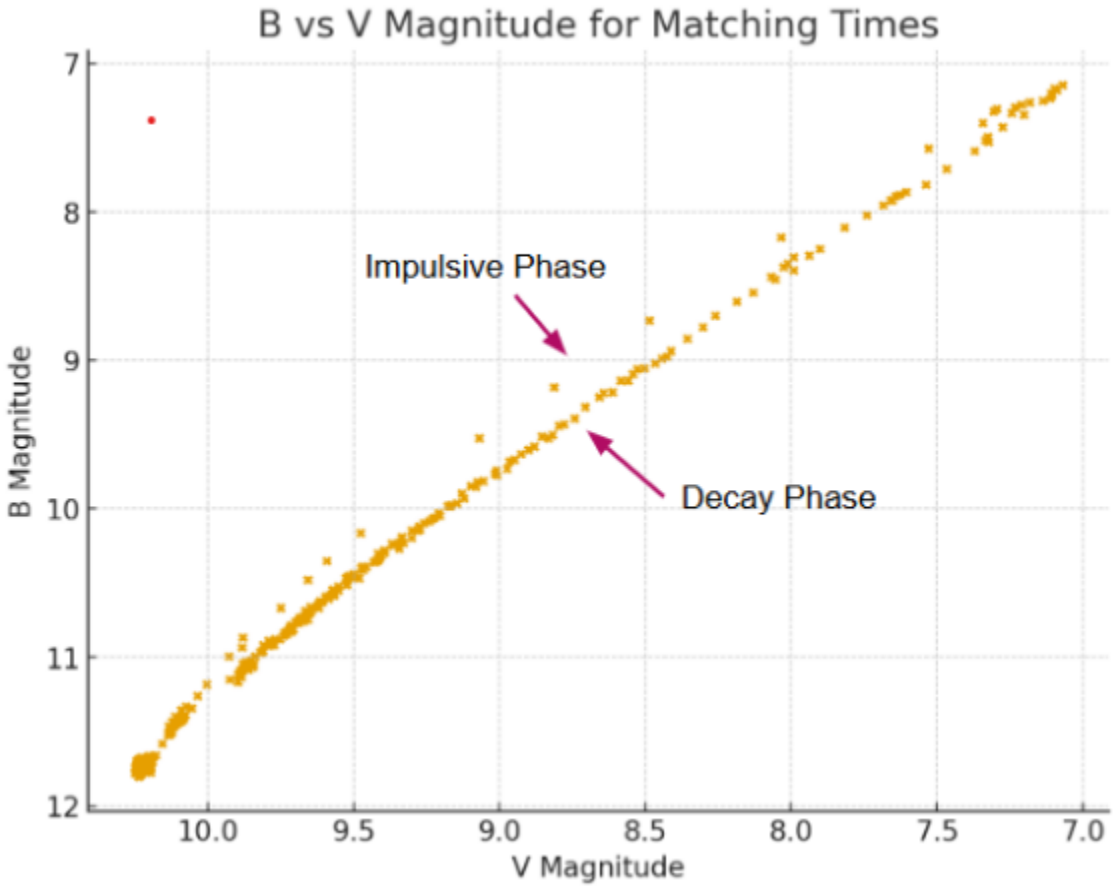

Figure 5. B vs. V Magnitude Relationship for EV Lac for a Monster Flare in October 2025

This behavior suggests that the mapping from one photometric band to another may not always be single-valued. In other words, the same *B* magnitude may correspond to different *V* magnitudes depending on where the flare is in its evolution. As a result, band-to-band prediction may only be valid for a subset of conditions, perhaps restricted to the impulsive phase where the relationship appears tighter. Continued multi-band observations will be essential to determine when and how these predictive models hold — and when they break down.

3.4 Spectroscopic Analysis

Spectroscopy has played an essential role in both phases of the Red Dwarf Group's work, complementing our photometric measurements and deepening our understanding of stellar flare physics. During Campaign #1, our spectroscopic strategy emphasized high-resolution but low-cadence observations. This approach allowed observers to capture exceptionally detailed line profiles across the Balmer series, enabling precise measurements of equivalent widths, amplitude variations, and subtle changes in the line wings. Although these observations were not

frequent enough to track rapid flare evolution in real time, they provided high-fidelity snapshots of the chromospheric structure and energy distribution during both quiescent and active states. These datasets helped establish a baseline understanding of EV Lac and AD Leo's spectral behavior, laying the groundwork for more dynamic observing approaches in later campaigns.

In Campaign #2, the focus shifted toward higher-cadence spectroscopy to better align with our rapidly improving photometric capabilities. As our flare-detection methods grew more sophisticated — and as more observers adopted high-cadence photometry — it became clear that matching spectroscopic timing to photometric variability would potentially open a new window into flare physics. This led the group to experiment with exposure times short enough to resolve fast-evolving flare features while still maintaining the signal-to-noise ratio needed to extract meaningful spectral information. While this balance is technically demanding, the potential scientific payoff is substantial: high-cadence spectra allow us to observe how emission lines strengthen, broaden, and change shape on timescales of seconds to minutes, capturing the dynamic response of the chromosphere during the impulsive and decay phases of flares. The RDG hopes to report further on this line of investigation at a later date.

4. Photostats

PhotoStats is a specialized software tool designed to streamline the reduction and analysis of time-series photometry for stellar flare research. Originally released in late 2021, PhotoStats has matured into a robust workflow integrating quiescent-state modeling, peak-flare detection, flare duration calculation, and detailed flare energy estimates. Its design philosophy emphasizes simplicity for the user — especially those processing large volumes of data — while providing scientifically rigorous outputs suitable for publication.

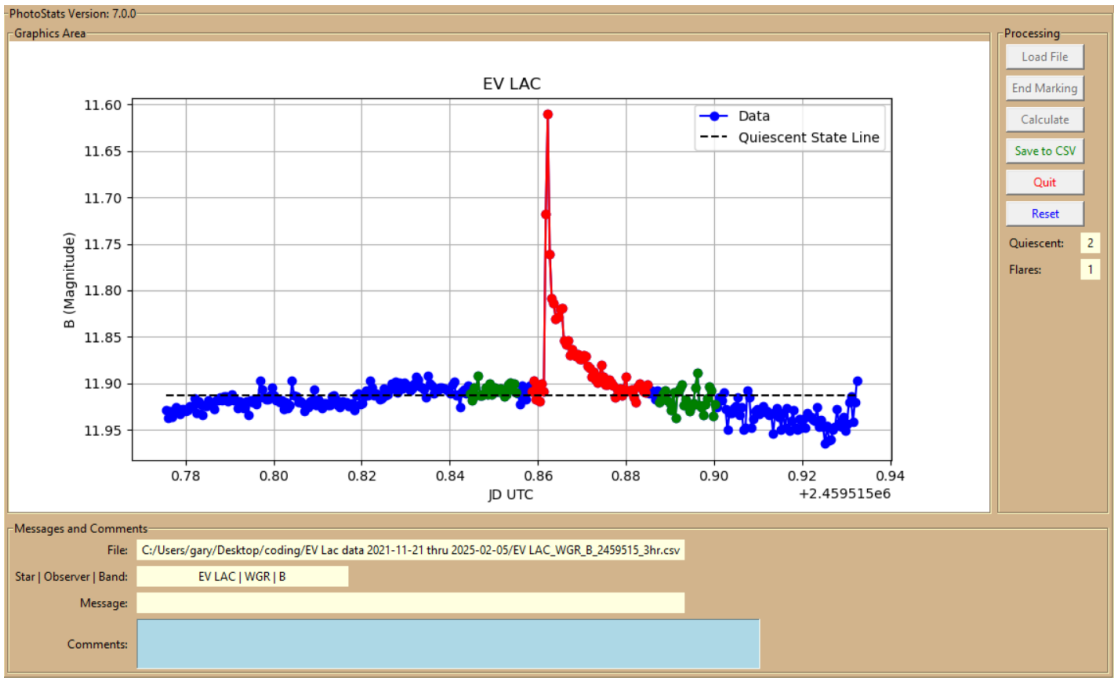

Figure 6. An Example Analysis Screen from PhotoStats Version 7.1

A major advancement came with the Version 6 and 7 series, which introduced a fully interactive GUI, improved visualization tools, expanded output parameters, and automated handling of file metadata. The program allows the user to load a photometry file, mark quiescent regions and flare boundaries directly on the plotted light curve using mouse clicks, and then automatically compute slope/intercept parameters, luminosities, delta magnitudes, flare energies, and bolometric corrections. Support for multiple photometric bands (B, V, R, Sloan tricolor, TESS, GAIA) is integrated through band-dependent solar luminosities, bolometric constants, and star-specific parallaxes. (Figure 6).

The collaboration between developers — including code refinements, GUI enhancements, and scientific validation — reflects the iterative nature of community-driven astronomical tools. Today, PhotoStats serves as a central element in the RDG's processing pipeline, enabling observers to extract accurate, consistent flare parameters across diverse telescopes, filters, and observers. Its emphasis on reproducibility, transparency, and ease of use has made it a cornerstone for transforming raw photometric measurements into reliable scientific results.

5. AI Is Your Friend

Artificial intelligence — and tools like ChatGPT — have become powerful partners in data analysis. These systems don't replace our understanding of the underlying astrophysics, but they significantly accelerate the process of making discoveries. AI can rapidly test hypotheses, explore parameter space, and suggest relationships or trends that might take much longer to uncover manually. This is particularly valuable in flare-star research, where large datasets, multi-band observations, and complex temporal structures demand both speed and precision in the exploratory phase of analysis.

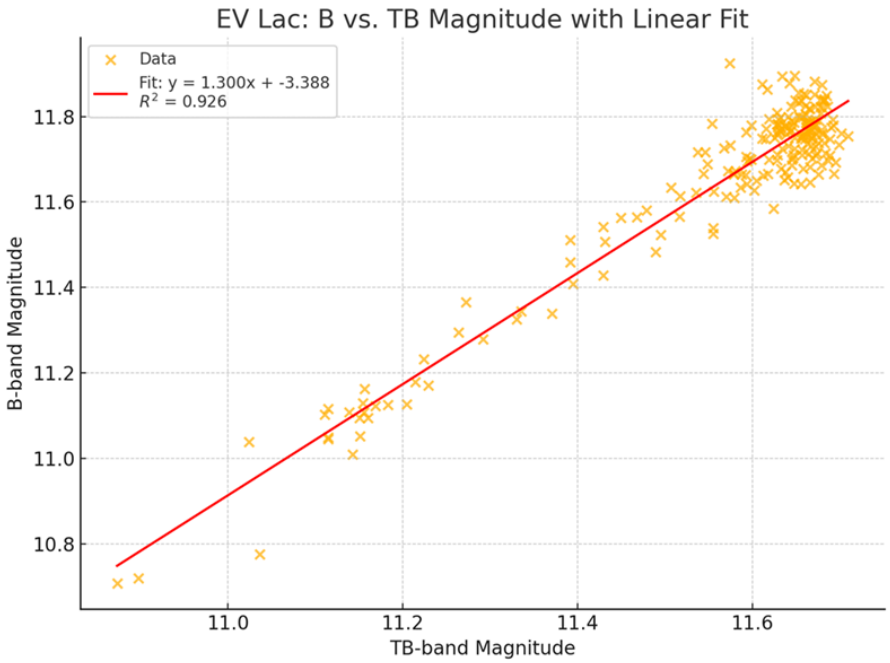

Figure 7. Example of Analysis Using ChatGPT

By combining human expertise with AI-assisted workflows, we can spend less time writing and debugging code and more time interpreting what the data actually mean in an astrophysical context. Figure 7 shows a regression analysis that was performed using ChatGPT after removing the observing session quiescent data — an excellent example of how AI can enhance, streamline, and even inspire deeper scientific investigation. When used thoughtfully, AI becomes a force multiplier: helping us move from raw data to meaningful insight more efficiently, while keeping humans firmly in charge of the science.

It should also be mentioned that ChatGPT and Gemini were used to develop a significant amount of the Python code for PhotoStats.

6. Monster Flares

With thousands of hours of high-cadence observations collected across multiple Red Dwarf Group campaigns, we have been fortunate to capture several exceptionally energetic stellar flares — events that push the upper limits of what active M dwarfs like EV Lac are capable of producing. These so-called monster flares are rare and extraordinarily luminous, offering a unique window into the physics of magnetic reconnection on low-mass stars. Their intensities far exceed those of typical flares, and they provide some of the most scientifically valuable datasets in our archive. Understanding these extreme events is essential for probing stellar magnetic processes, estimating flare energy budgets, and assessing their potential impact on surrounding planetary environments.

One such event was observed in November 2023 and remains one of the most striking flares the group has recorded. During that flare, EV Lac brightened by an extraordinary four magnitudes in the B-band, corresponding to a dramatic increase in luminosity over a very short interval [8].

An even more extraordinary event occurred in October 2025, representing the largest flare yet captured by RDG members (Figure 8). This flare exceeded even the 2023 event in brightness, duration, and total radiated energy. It is estimated the bolometric energy of both of these flares exceeds 10^{35} erg.

Further analysis of the October 2025 flare has revealed unexpected complexity in its color behavior. In particular, the B–V trajectory did not follow the nearly linear impulsive/decay locus typical of many flares; instead, it traced out a loop, indicating that the relationship between the bands changed over the course of the event. This finding has significant implications: it suggests that predicting one photometric band from another may only be valid during certain evolutionary phases of a flare, such as the early impulsive rise.

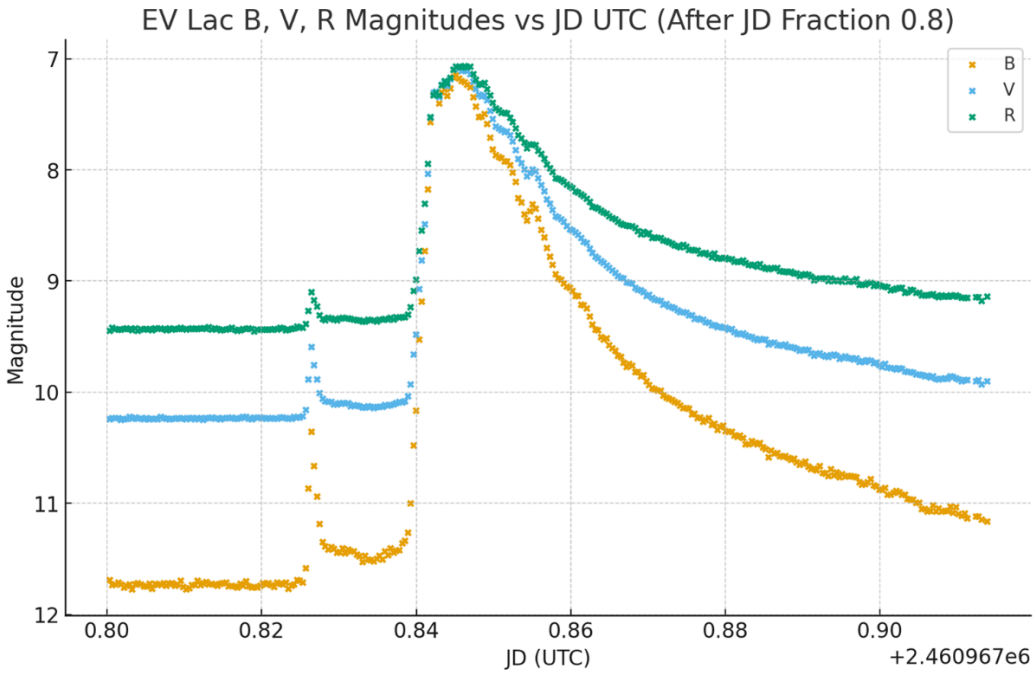

Figure 8. October 2025 Superflare Observed for EV Lac

7. Conclusions

The coordinated work of the Red Dwarf Group has demonstrated the value of sustained, distributed monitoring of M-dwarf flare activity. By combining thousands of observations, RDG has refined methods for flare detection, temperature estimation, and energy analysis. The project bridges amateur and professional astronomy, contributing both to scientific understanding and to community engagement.

Ongoing work with professional partners and the integration of AI-driven analysis promises to further enhance the scientific return of future campaigns. Ultimately, the RDG initiative provides a scalable framework for collaborative time-domain astronomy in the era of global observation networks.

If you are interested in becoming part of the RDG, please reach out to the author at astrogary8@gmail.com.

Acknowledgements

The author thanks all the past and current members of the Red Dwarf Group for their dedication and contributions. The author also acknowledges the AAVSO for maintaining the AAVSO International Database and for supporting citizen science in variable star research.

References

1. The Character of M Dwarfs. Todd J. Henry and Wei-Chun Jao. 2024, Annual Reviews of Astronomy and Astrophysics.
2. Time-Resolved Properties and Global Trends in dMe Flares from Simultaneous Photometry and Spectra, Adam F. Kowalski, Suzanne L. Hawley, John P. Wisniewski, Rachel A. Osten, Eric J. Hilton, Jon A. Holtzman, Sarah J. Schmidt, and James R. A. Davenport. 2013, The Astrophysical Journal Supplement Series, Volume 207, Number 1.
3. Autonomy on a Budget: Transforming a Small Observatory into a Photometric Powerhouse, Gary Hawkins, 2025, JAAVSO Volume 53, Number 1.
4. Combined Spectroscopic and Photometric Analysis of Flares in the Dwarf M Star EV Lacertae. Boyd, David & Buchheim, Robert & Curry, Sean & Parks, Frank & Shank, Keith & Sims, Forrest & Walker, Gary & Wetmore, John & Jackman, James. 2023, 10.48550/arXiv.2304.08578.
5. Spectroscopic And Photometric Investigation of Red Dwarf Flares, Forrest Sims, Sean Curry, & Robert K. Buchheim. 2022, Proceedings for the 41st Annual Conference of the Society for Astronomical Sciences.
6. Time-Series Spectroscopy of Flare Star AD Leo In 2021, Robert K. Buchheim, Forrest Sims, Sean Curry, & Jack Martin. 2022, Proceedings for the 41st Annual Conference of the Society for Astronomical Sciences.
7. Combined Spectroscopic and Photometric Analysis of Flares in the dM3.5e Star EV Lacertae, David Boyd, Robert K. Buchheim, Sean Curry, Frank Parks, Keith Shank, Forest Sims, Gary Walker, John Wetmore, & James Jackman. 2022, Proceedings for the 41st Annual Conference of the Society for Astronomical Sciences.
8. The Mouse that Roared Again: Another Monster Superflare from EV Lacertae. 2024, JAAVSO Volume 52, Number 1.

Scriblerian Satires of 1716 and Early Observations of Variable Stars

Kristine Larsen

Central Connecticut State University, 1615 Stanley St., New Britain, Connecticut, 06053, USA;
larsen@ccsu.edu

Subject Keywords

History of astronomy; interdisciplinary astronomy; novae, historical; stars: individual (P Cyg, chi Cyg, CK Vul)

Abstract

As noted in previous work (Larsen 2022; 2024), while literary scholars have connected numerous astronomical references in pre-20th century works of fiction to real-world astronomical events and contemporaneous hypotheses, such analyses are open to two problems: incompleteness and erroneous alignment with 20th century astronomical knowledge. These issues are exacerbated by serial quoting by later scholars without further analysis. This paper focuses on literary analysis of two short "Scriblerian" satires published within a few weeks of each other in 1716, demonstrating how, while literary scholars correctly note their connection to observations of variable stars of the time, their analysis both misses additional connections and perpetrates astronomical errors.

1. Introduction

The term "Scriblerian" refers to the literary group founded in early 1714 from the merger of two social groups: one led by essayist and cleric Jonathan Swift and including polymath Dr. John Arbuthnot (physician-in-ordinary to Queen Anne), poet and clergyman Thomas Parnell, and Robert Harley, 1st earl of Oxford; the other, led by poet Alexander Pope and including dramatist and poet John Gay (Kerby-Miller 1988). Their formal meetings, held in Arbuthnot's rooms in St. James's Palace, lasted only a few months, during which they planned a grand satirical scheme to invent a fictional scientist and publish his hagiographic biography, accompanied by fabricated scientific papers by said scientist (both under his name and pseudonyms – a common literary conceit in the 18th century). To complete the plot, they would also claim as his work various scientific discoveries and publications for the purpose of satirizing them (paralleling the then not uncommon practices of plagiarism and falsely claiming authorship of anonymous publications) (Kerby-Miller 1988).

The overarching purpose was to draw attention to several issues that vexed them in the scientific publications of the day, including the non-critical acceptance of such works by the (gullible) general public (even works of a clearly sensational nature), the use of scientific publications for the purpose of self-aggrandizement, pretentious language and the explosion of invented terminology, claims of having reached the ultimate truth, and the misuse of science to further

political or religious viewpoints (Kerby-Miller 1988; Lynall 2012). While the death of Queen Anne soon after led to the end of their formal meetings, various members remained in contact and published numerous satirical works over the next decades, including the biography of their fictitious scientist, *The Memoirs of Martinus Scriblerus*, a work begun in 1714 but not published until 1741. Due to the use of pseudonyms, it is not often easy to discern the true author of any individual satire, and they are sometimes simply ascribed to one of the two most famous members, Swift or Pope.

2. Understanding of Transient and Periodic Astronomical Objects circa 1700

2.1 Comets

The astronomical knowledge of the Scriblerians has been well documented (e.g. Lynall 2012; Nicholson & Mohler 1937; Nicholson & Rousseau 1968; Rogers 2022), especially that of Dr. Arbuthnot, who was friends with Sir Isaac Newton and was high-connected with the Greenwich Royal Observatory as an Official Visitor and a member of a Royal Society committee tasked with overseeing Astronomer Royal John Flamsteed's observations. It is therefore not surprising that three of their satirical targets were astronomers: Edmund Halley, William Whiston, and John Flamsteed. The third of these would obviously be fair game for (especially) Arbuthnot; the Scriblerians' tweaking of Halley and Whiston is largely related to comets. For historical context, it is important to note that while Halley's groundbreaking calculations of the orbit of the comet that became associated with his name (and the prediction that it would return in 1758-1759) were published in 1705, the possibility of periodic cometary orbits had been proposed far earlier, for example by Jean-Dominique Cassini (Genuth 1997; Halley 1705). Halley's confident prediction of what became his eponymous comet's return became the target of Swift's satirical eye in *Gulliver's Travels* (1726), in the Laputans' fear of a catastrophic terrestrial encounter with the comet upon its next return (Genuth 1997; Nicholson and Mohler 1937). The connection was Halley's 1687 paper published in the *Transactions of the Royal Society*, and two 1694 papers he read to the society but did not publish until 1724, in which he noted that the Noachian flood of the Bible (or a similar historical catastrophe) might be explained by a close encounter with a comet (Halley 1687; 1724a; 1724b).

Similar ideas were widely publicized by William Whiston in his *A New Theory of the Earth* (1696). Whiston, a rising star at Cambridge and Newton's successor in the Lucasian Professorship, was a controversial figure, who lost his position at Cambridge in 1710 after being condemned as an Arian heretic (Force 1985). He afterwards supported his family through public lectures and publications considered sensational in nature, capitalizing on his detailed hypotheses of a cometary cause for both past and future Biblical catastrophes. He became infamous for connecting all manner of astronomical events with potential catastrophes, although comets were his favorite trope. Of particular interest here is his pamphlet *The Cause of the Deluge Demonstrated* (published as an appendix to later editions of *A New Theory* and as a separate work beginning in 1714) in which he identified the Great Comet of 1680 as the perpetrator of many of these events, and which he predicted would return to bring about the end of the world on its next return (based on Halley's erroneous period of 575 ½ years) (Whiston 1717).

Interestingly, some literary scholars discussing Whiston's work confuse the comet of 1680 with Halley's Comet in their analysis (e.g., Rousseau 1988). Not only were the Scriblerians well-aware of Whiston's sensational pronouncements, but some had attended his popular lectures in person (Rousseau 1988).

The multitude of Whiston's "sins" made him a clear and continuous target of Scriblerian satires (Nicolson and Rousseau 1968; Rousseau 1988). For example, the satirical short story "A True and Faithful Narrative of What Passed in London," written under the Scriblerians' shared pseudonym "J. Baker" but argued to be the work of John Gay (circa 1729-32), purports to be a recounting of a 1714 public lecture by Whiston in which he erroneously pronounces that a comet will destroy the world a week later (Osborn 1962; Rousseau 1988).

2.2 Results

Comets were not the only astronomical objects then transitioning from seemingly random and erratic to possibly well-regulated and predictable. Given that there had not been a total solar eclipse visible in the UK for nearly 600 years, independent calculations by Halley and Whiston predicting the timing and eclipse path of such an event on April 22, 1715, garnered much public attention. Whiston openly fanned this interest in order to sell seats in his public talks, pamphlets, and an instrument he had developed for making such calculations, which he called "The Copernicus" (Whiston 1715). Letters from Pope and Gay to John Caryll suggest that at least these two Scriblerians had experience using a 'Copernicus' (Rousseau 1988). While Whiston later bragged in his memoirs that the eclipse had been "exactly foretold by Mr. Flamsteed, Dr. Halley and myself," both the timing and eclipse paths were slightly off, opening the door to Scriblerian satirical treatment (qtd. in Nicolson and Rousseau 1968, 156; Westfall and Sheehan 2015).

2.3 Variable Stars

A third type of astronomical object was simultaneously showing signs of predictability, the so-called 'new-star' or nova. The term 'nova' had been used to describe any celestial object that suddenly appeared to the unaided eye since at least Pliny's *Naturae Historia* (c. 75 CE), including comets, meteors, true novae and supernovae (themselves not clearly distinguished until the 20th century), and other types of variables. By 1716 only six stellar 'novae' had been unequivocally described by Western astronomers (Figure 1); the first and fourth – Tycho's Star in 1572 and Kepler's in 1604 – were later shown to be supernovae. Their sudden appearance and gradual disappearance led astronomers to posit a connection between them. The second, Mira, was discovered by David Fabricius in 1596, and its roughly 11-month period first documented by Johann Holwarda in 1638 (Hoffleit 1997). The third, discovered in Cygnus by Willem Jansz Blaeu on August 18, 1600, remained a third magnitude object for several years before dimming to barely visible to the unaided eye, brightening to nearly its maximum in 1655, fading again, and afterwards varying between roughly magnitudes 4.6-5.6 (de Groot et al. 2001). The physical differences between this S Doradus variable (Luminous Blue Variable), now named P Cygni, and the Long Period Variable Mira were not known in the 18th century, but the

fact that both varied in brightness in a repetitive (if not periodic) way meant that they were not the same type as Tycho's and Kepler's stars.

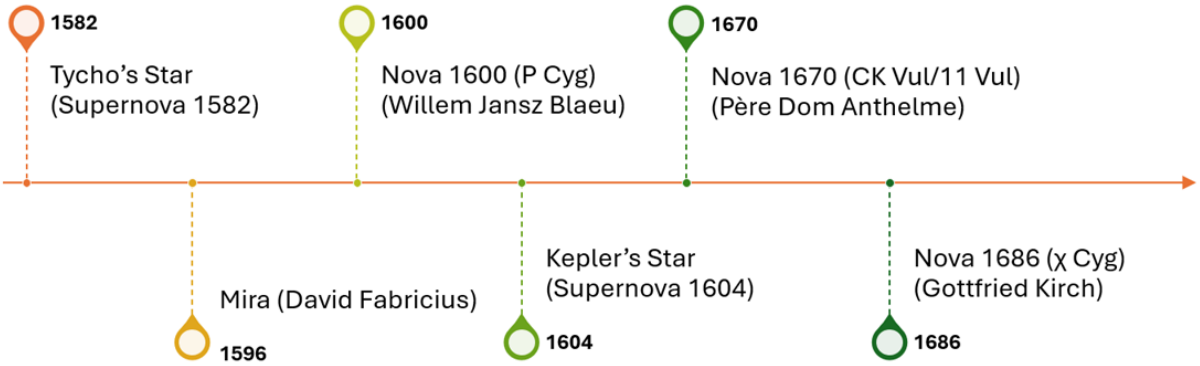

Figure 1. The six 'novae' listed by Halley (1715).

In 1670 a 'nova' was discovered by Père Dom Anthelme in Vulpecula, near the head of Cygnus (Figure 2). Like P Cygni, it reached third magnitude, dimmed significantly, and then reached an even higher peak brightness (~2.6). After dimming, it brightened a final time, and disappeared from view on May 22, 1672 (Shara et al. 1985). This V838 Mon type (Luminous Red Nova) variable, designated 11 Vul or CK Vul, was repeatedly sought for even into the 18th century (Kamiński et al. 1999; Halley 1715).

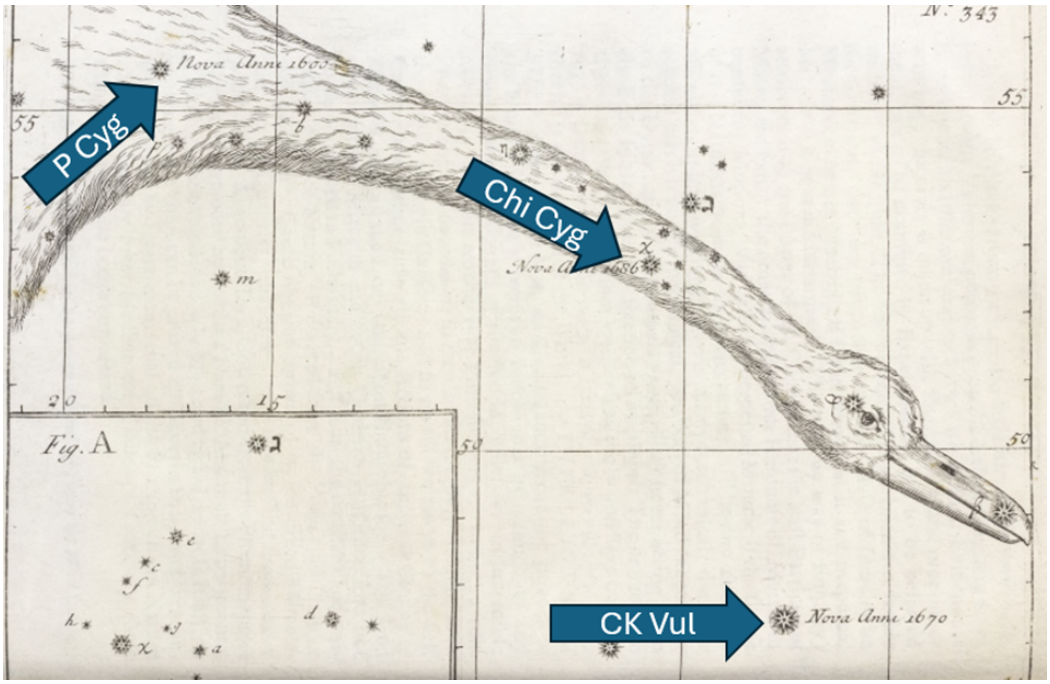

Figure 2. Three early 'novae' observed in Cygnus. Adapted from Kirch (1715).

The sixth star was most similar to Mira, having a relatively regular periodicity. In July 1686 Gottfried Kirch was looking for CK Vul and noted that the star χ Cygni, cataloged in Bayer's 1603 *Uranometria*, was invisible. He suspected it, too, might be a repeating 'nova,' and recovered it on October 19, 1686 (Sterken et. 1999). He continued to observe the star and before his death in 1710 reported its period as 404.5 days (Kirch 1715). While as early as 1713 Maraldi noted that the periodicity was not perfect, varying between 13-14 months, the pattern was sufficiently regular for astronomers to make confident predictions of the star's return to unaided eye visibility (normally a maximum of mag. 4-5) (Rosenberg 1905). Observations by Halley noted maxima in July 1714 and September 1715, agreeing with Kirch's predictions (Rosenberg 1905).

By the late 17th century, sufficient 'novae' were known to attempt a classification. Zsoldos (2010) describes two early systems, both of which include comets as types of 'novae.' The first, published in Erhard Weigel's 1680 *Cosmologia*, differentiated between extraordinary temporary stars (Tycho's and Kepler's supernovae), stars that repeatedly appear, disappear, and return (his known examples being Mira, P Cygni, and CK Vulpeculae), and comets, which are also temporary but move relative to the first two types (Weigel 1680). The second system, by Johann Christoph Sturm (1635-1703), appeared in his math textbook, *Mathesis Juvenilis* (originally published in 1699). His three classes were periodic stars such as Mira, one-and-done stars such as Tycho's supernova, and comets (Sturm 1708). Therefore, while comets were known to have properties different from other 'new-stars,' they were often discussed in the same breath as stellar 'novae,' confusing the general public. For example, in their work on astronomical references in Scriblerian satires Nicholson and Rousseau (1968) and Rousseau (1988) heavily reference Edmund Halley's December 1715 paper in the Royal Society's *Philosophical Transactions* summarizing these six aforementioned known stellar 'novae.' Halley ends his paper by touting the scientific success in predicting the 1714 and 1715 returns to visibility of χ Cygni and makes the unequivocal prognostication that "Those that please to seek for it may expect its first Appearance in July next" (Halley 1715, 6). The star did return to the unaided eye's gaze as predicted, with Kirch's son, Christfried, observing its next peak on October 16, 1716 (Rosenberg 1905).

Despite these scientific successes, some astronomical events still took the public unawares. An important example is a particularly vivid March 6, 1716, auroral display seen over much of England, including London. Not unexpectedly, it fanned apocalyptic fears among segments of the general public, especially as such a display had not been seen that far south in living memory and it occurred soon after the public execution of two Jacobite leaders (Jankovic 2002). While explanations ranged from a strange comet to peculiar lightning, Halley correctly described the event as an aurora (Halley 1716). Predictably, Whiston took advantage of the situation for his own financial gain (Nicolson & Rousseau 1968; Rousseau 1988). He had similarly taken the general public's generic use of 'comet' to describe the periodic return of χ Cygni as an opportunity to connect it with other "strange portents in the heavens" that could foretell unfortunate events (Rousseau 1988, 28).

3. Scriblerian Satires of 1716

3.1 Overview

Summarizing the historical context of 1714-1716, we find the following:

1) The general public hearing both sensational prognostications relating the heavens to possible catastrophes and staid scientific predictions of astronomical events (both presented with confidence and observed with varying degrees of accuracy);

2) Confusing and inconsistent usage of terms such as 'comet' and 'new-star' in both the common and scientific vernacular;

3) A series of specific astronomical events both predicted and unexpected to which this inconsistent terminology was applied (the total solar eclipse, several maxima of χ Cygni, and an auroral outburst)

4) The Scriblerian satirists following all of these events – what Nicolson and Rousseau describe as "an annus mirabilis in England" – with interest and sufficient astronomical knowledge to turn it all on its ear (1968, 161).

Two short 1716 works by members of the Scriblerians, "God's Revenge Against Punning" and the more obscure "Mr. Joanidion Fielding His True and Faithful Account of the Strange and Miraculous Comet which was seen by the Mufti at Constantinople," reference specific astronomical events, including some described as 'comets.'

3.2 "God's Revenge Against Punning"

"God's Revenge" appeared in early November 1716, signed with the aforementioned shared pseudonym "J. Baker, knight." Literary scholars have debated its authorship, but a solid case has been made for John Gay, in part due to similarities with the later "A True and Faithful Narrative" (Rousseau 1988). Like that work, William Whiston is openly lampooned, but so, too, are astronomical predictions. The author bemoans three widespread heresies – "Socinianism, Arianism, and Whistonism" – before announcing that an even greater "contagion" has infected society, "the woful [sic] practice of PUNNING" (Baker 1814, 286). Before listing supposed examples of God's wrath against punsters, the author enumerates a series of astronomical events that foretold this epidemic: "that unparalleled eclipse in 1714... the dreadful coruscation in the air this year... [and] nine comets seen at once over Soho Square, by Mrs. Katharine Wadlington and others" (Baker 1814, 286). The erroneous year given for the solar eclipse is an often-used Scriblerian trope undercutting the pompous self-assurance of the narrator (Rogers 2022). The "deadly coruscation" clearly refers to the March 1716 aurora.

The "nine comets" have been suggested as "an exaggeration of that other celestial phenomenon which appeared during the annus mirabilis 1715-16, the reappearance of a nova, visible to the

naked eye, which many laymen thought a comet" (Nicolson & Rousseau 1968, 184). Nicholson and Rousseau cite Halley's 1715 prediction that χ Cygni would be visible again in 1716, but confuse the September 10, 1715, maximum with the October 16, 1716, maximum (Nicolson & Rousseau 1968). While they correctly point out that the use of visions of multiple celestial objects is a common literary trope, often meant as an omen (Nicolson & Rousseau 1968; Heninger 1960), the multiplicity could also be a direct jab at Halley's listing of six 'novae' in his 1715 paper (the difference between the numbers six and nine being unimportant in satire). The apparent lack of comets in the astronomical record between 1707-17 and the previously described blurring of comets with 'novae' in the common (and even scientific) vernacular add weight to this interpretation (Kronk 1999). Comets may have been in the public imagination (thanks to Whiston), but the public's memory of what a comet actually looked like would have been fuzzy indeed.

3.3 "Mr. Joanidion Fielding His True and Faithful Account...."

A month later another brief Scriblerian work appeared under the pseudonym "E. Parker, Philomath." "Mr. Joanidion Fielding His True and Faithful Account of the Strange and Miraculous Comet which was seen by the Mufti at Constantinople" only survives in three copies, and has not been the topic of detailed analysis, with the exception of a 2022 paper by Pat Rogers. Similar to "God's Revenge," this work satirizes both false prophecies and astronomical predictions, set within ongoing wars involving the Ottoman Empire (Rogers 2022). Nicolson and Rousseau correctly cite an item from the *Paris News Letter* published in the November 15, 1716, edition of *The Daily Courant* as the source of the "miraculous comet," reproduced here in full:

> They write from Malta, that an English Ship arrived there from the Isles of the Archipelago reports, that there had been seen at Constantinople for eight days, a Comet, hairy, with a long Tail; which appeared soon after Sun-rising, and extended itself from North to South. This has very much frightened those people, who are not used to such Appearances in the Heavens. ("From the *Paris News Letter*" 1716, 1-2).

Rogers claims (with no evidence) that the comet "held no outstanding interest to British astronomers" (2022, 6) and does not appear to appreciate that (1) the Western astronomical record does not mention any comets in this time period; (2) a comet that is visible after sunrise would be very bright and noticeable indeed; and (3) the overall claimed appearance of the object does not align with comets in general. While no alternate astronomical explanation will be offered here, it is possible that a member of the Scriblerians would have noticed the astronomical inconsistencies in the description – especially if the author was Dr. John Arbuthnot, as Rogers argues. In addition, Rogers makes a convincing case that the target of the satire was Astronomer Royal John Flamsteed (who shares initials with the fictional narrator), with whom Arbuthnot had a long-standing and tense professional relationship (Rogers 2022).

The piece begins with a bombastic pronouncement by Fielding, proclaiming himself

> Surveyor of the Zodiack, House-keeper of the Twelve Apartments of the Primum Mobile, Comptroller of the Sun and Moon, Inspector of the Luminaries Errant, with their Several Attendants, Pursuivant of the Blazing Stars, with their Train, Lord of the Parallax of the Pole-Star, Quarter-Master-General of the Heavenly Host, and Retailer of their Influences to the Inhabitants of the earth (Parker 1716, 3).

He shares a list of things he has both seen and not seen, and after describing the comet and its supposed role as an omen, lists prognostications of events that both will and will not happen. Of relevance here, he explains that he

> did not see the famous total Eclipse of the Sun in 1714, being 17 Minutes too late.... I did not see the Coruscations, which Mr. Whiston rightly judges to be the Fire-works of Aerial Spirits, being intent upon burning my erroneous Catalogue of the Fixed Stars. Neither did I, but a Friend of mine did see the Nine Comets at Mrs. Wadlington's in Soho-Square, when he was going to celebrate a Geocentrick Conjunction. I have not observ'd the New Building at Greenwich Hospital, but I beheld the New Star in the Swan (Parker 1716, 4).

The catalog burning clearly points to Flamsteed, as in April 1716 he burned an estimated 13,500 pages taken from the majority of the extant copies of the 1712 edition of his *Historia Coelestis*, an edition published without his permission by Newton and Halley (Dean 2025). References to the eclipse of 1715 (again, including the Scriblerian trope of an erroneous date and deriding the imperfect time calculation) and the 1716 aurora are unequivocal, and the same vague hyperbolic portent of the "Nine Comets" used in "God's Revenge" makes an appearance. The new addition is a clear reference to the predicted return of χ Cygni.

These astronomical references are all noted by Rogers (2022), although introducing astronomical error in the process: "In reality Flamsteed did not discover the star [sic] Cygni within the Cygnus constellation, which is visible to the naked eye, but he did catalog it and it was later given the name Cygni68 [sic] in the Flamsteed designation system" (Rogers 2022, 4). While the omission of the Greek letter χ may have been a typesetting error, the designation of the star as "Cygni68" is clearly an error. 68 Cygni is in a completely different part of the constellation; instead, as noted by Olbers (1816), χ Cygni became erroneously identified with 17 Cygni, an error found on some star lists (Hagen 1918). The error is possibly due to Kirch's identification of 17 Cygni (Figure 3) as a finder star on his charts (Kirch 1715). As it is now known that the Flamsteed numbers were not designated by Flamsteed himself, it is unfortunate that Rogers includes compounded errors here (Steinicke 2014).

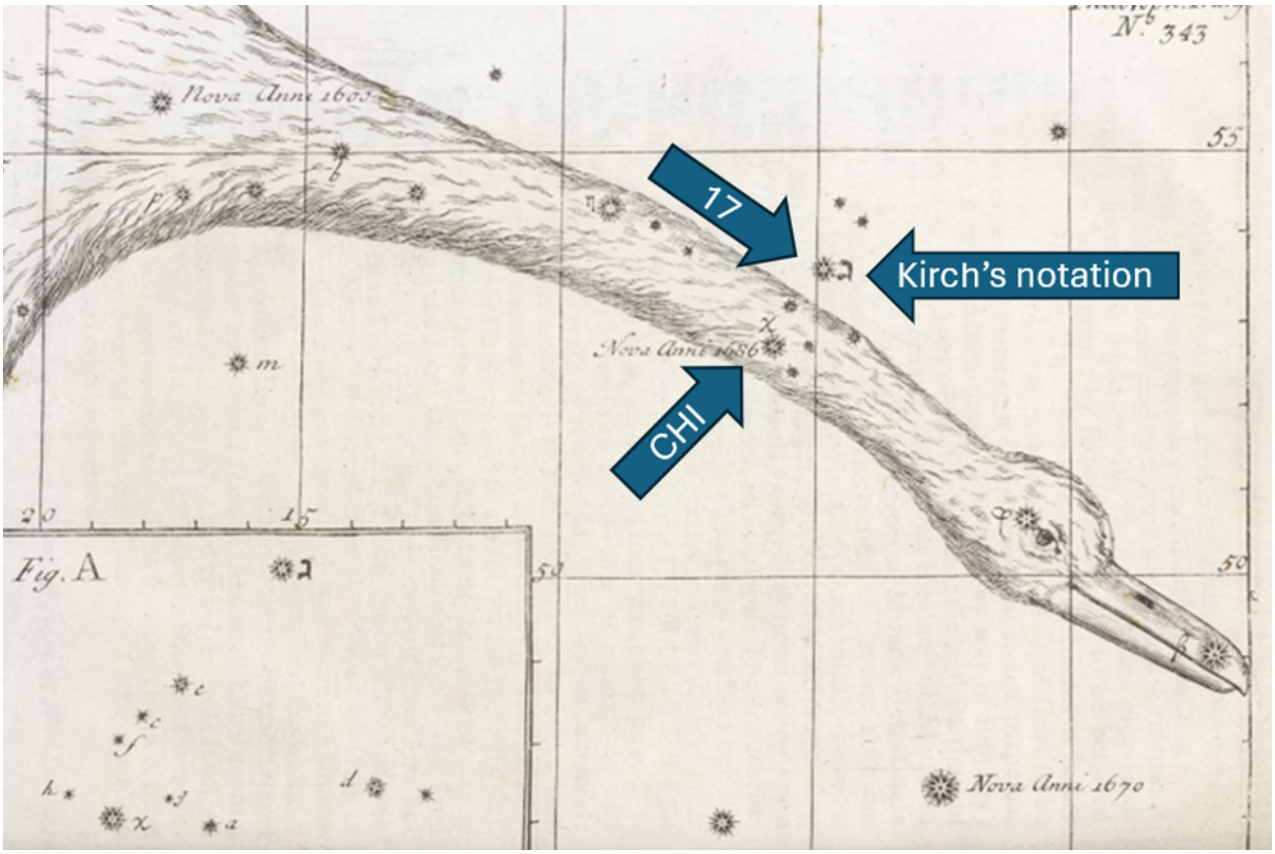

Figure 3. Relative positions of Chi Cygni and 17 Cygni. Adapted from Kirch (1715).

4. Discussion

Nicholson and Rousseau confidently conclude their analysis of Alexander Pope's engagement with astronomy by opining that "The spectacular celestial phenomena of the years 1714, 1715, 1716 were completely understood, even when they had not been anticipated, by members of the Royal Society" (1968, 186). While it is certainly true that the 1715 solar eclipse path and timing had been calculated with relative accuracy, the 1716 atmospheric light show correctly identified as an aurora, and several maxima of χ Cygni correctly predicted, the causes of the last two of these phenomenon eluded astronomers until the 20th century. In addition, while Halley had published both an orbit and forecasted return for the comet he had seen in 1682, it would be several decades before he could be proven right. It is therefore ironic that the Scriblerians might have considered the confident – and in some cases clearly erroneous – pronouncements of literary scholars studying the astronomical allusions in their works to be worthy targets of their satirical talents.

5. Conclusions

Careful, detailed analysis of astronomical references in works of literature and other media can provide valuable information on the scientific literacy of both the creators of that media and their intended audiences. Evidence concerning the more general reception of scientific ideas (and

related pseudosciences) and the effectiveness of scientists as communicators can also be discovered. Astronomers can provide a valuable service to literary scholars by working alongside them in an interdisciplinary type of data mining. Through such a partnership the propagation of astronomical errors can be minimized in the scholarly literature while the cultivation of creative insights can be simultaneously maximized. This is especially important when dealing with interdisciplinary and polymathic historical figures such as the Scriblerians.

References

Baker, J. (pseud.) 1814, in *The Works of Jonathan Swift, Vol. 13.,* Archibald Constable and Co., Edinburgh, 285.

De Groot, M., Sterken, C., and van Genderen, A.M. 2001, *Astron. Astrophys.*, **376**, 224.

Dean, J. 2025, *New Acquisition: John Flamsteed's Historia Coelestis.* https://www.lindahall.org/about/news/new-acquisition-john-flamsteed-historia-coelestis/.

Force, J. E. 1985, *William Whiston: Honest Newtonian*, Cambridge Univ. Press, Cambridge.

"From the *Paris News Letter*," 1716, *The Daily Courant*, 15 Nov., 1.

Genuth, S. S. 1997, *Comets, Popular Culture, and the Birth of Modern Cosmology*, Princeton Univ. Press, Princeton.

Hagen, J.G. 1918, *Mon. Not. Roy. Astron. Soc.*, **78**, 682.

Halley, E. 1687, *Phil. Trans. Roy. Soc. London*, **16**, 403.

Halley, E. 1705, *A Synopsis of the Astronomy of Comets*, John Senex, London.

Halley, E. 1715, *Phil. Trans. Roy. Soc. London*, **29**, 354.

Halley, E. 1716, *Phil. Trans. Roy. Soc. London*, **29**, 406.

Halley, E. 1724a, *Phil. Trans. Roy. Soc. London*, **33**, 118.

Halley, E. 1724b, *Phil. Trans. Roy. Soc. London,* **33**, 123.

Heninger, Jr., S.K. 1960, *A Handbook of Renaissance Meteorology*, Duke Univ. Press, Durham.

Hoffleit, D. 1997, J. *Amer. Assoc. Var. Star Obs.,* **25**, 115.

Jankovic, V. 2002, J. Brit. Stud., **41**, 429.

Kamiński, T., et al. 2015, *Nature*, **520**, 322.

Kerby-Miller, C., (ed.). 1988, *Memoirs of the Extraordinary Life, Works, and Discoveries of Martinus Scriblerus*, Oxford Univ. Press, New York.

Kirch, G. 1715, *Phil. Trans. Roy. Soc. London*, **29**, 226.

Kronk, G. W. 1999, *Cometography Vol 1. Ancient – 1799*, Cambridge Univ. Press, Cambridge.

Larsen, K. 2022, in *Proc. of the 111th Ann. Meeting of the Amer. Assoc. Var. Star Obs*., ed. J. A. Guzik, 99.

Larsen, K. 2024, T*he Sun We Share: Our Star in Popular Media and Science.* McFarland and Company, Jefferson.

Lynall, G. 2012, *Swift and Science*, Palgrave Macmillan, New York.

Nicolson, M., and Mohler, N.M. 1937, *Ann. Sci.,* **2**, 299.

Nicolson, M., and Rousseau, G.S. 1968, *"This Long Disease, My Life": Alexander Pope and the Sciences*. Princeton Univ. Press, Princeton.

Olbers, D.W. 1816, *Zeits. für Astron. und verwandte Wissenschaften*, **2**, 181.

Osborn, J. M. 1962, *Papers Biograph. Soc. Amer.,* **56**, 73.

Parker, E. (pseud.) 1716, *Mr. Joanidion Fielding His True and Faithful Account....,* Berington, London.

Rogers, P. 2022, *J Lit. and Sci*., **15**, 1.

Rosenberg, H. 1905, *Der Veränderliche χ Cygni*, Ehrhardt Karras, Halle.

Rousseau, G.S. 1988, *Stud. Eighteenth-Cen. Cult.,* **17**, 17.

Shara, M. M., Moffat, A. F. J., and Webbink, R.F. 1985, *Astrophys. J.,* **294**, 271.

Steinicke, W. 2014, *J. Hist. Astron.,* **45**, No. 3, 287.

Sterken, C., et al. 1999, *Astron. Astrophys.,* **342**, 167.

Sturm, J. C. 1708, *Mathesis Juvenilis: Or a Course of Mathematicks for Young Students*, Dan. Midwinter, London.

Weigel, Erhard. 1680, *Cosmologia*, Johan Meyer, Jena.

Westfall, J., and Sheehan, W. 2015, *Celestial Shadows*, Springer-Verlag, New York.

Whiston, W. 1696, *A New Theory of the Earth*, Benj. Tooke, London.

Whiston, W. 1715, *The Copernicus Explain'd*. https://catalog.hathitrust.org/Record/001989855.

Whiston, W. 1717, *The Cause of the Deluge Demonstrated*. https://archive.org/details/bim_eighteenth-century_the-cause-of-the-deluge-_whiston-william_1717/mode/2up.

Zsoldos, E. 2010, J*. Hist. Astron*., **41**, 105.

Give it a SPIN: Introducing the Solar Precision Image Normalizer (SPIN) Tool

Dipankar Maitra[1], Douglas Scobel[2], and Biswajit Bose[3]

[1]Wheaton College, 26 E. Main St., Norton, MA, 02766, USA; maitra_dipankar@wheatoncollege.edu; [2]University Lowbrow Astronomers, PO Box 131446, Ann Arbor, MI 48113-1446, USA; [3]Institute of Astronomy Space and Earth Science, P-177 CIT Road, Kolkata, WB, 700054, India

Subject Keywords

Sun; Sunspots; Education; Public Outreach; Software; stars: individual (Sun)

Abstract

We present a new open-source, web-based, free tool, the "Solar Precision Image Normalizer" (SPIN). SPIN rotates a user-provided full-disk, white-light image of the Sun, obtained on or after 2010 May 1st, so that the solar north pole is in the upward direction in the output image, and the east limb is towards the left. One may think of SPIN as a tool for "plate-solving" the Sun. Solar images processed using SPIN allow for comparing images across time and between users, as well as with images obtained using professional solar observatories. The user can optionally overlay a Heliographic Stonyhurst grid on their image and/or show the size of Earth for scale, before downloading their output image. The SPIN tool can be accessed and used by pointing a web browser to the URL https://is.gd/spincode or the QR code shown adjacent to the title above.

1. Introduction

Thanks to advances in digital imaging as well as the recent introduction of smart telescopes, an increasing number of amateur astronomers frequently obtain full-disk white-light images of the Sun, using safe, neutral-density solar filters attached to their equipment.

However, the Sun's rotation axis is neither aligned with the Earth's rotation axis nor is it aligned perpendicular to the plane of the ecliptic. Furthermore, there are no permanent features on the solar surface. All these factors make the task of aligning solar images nontrivial, unless the exact orientation of the imaging sensor is very precisely known (which is often not the case for most amateur equipment).

Rather than relying on knowing the exact orientation of the observer's imaging sensor, our SPIN tool uses contemporaneous solar images obtained by the Solar Dynamics Observatory (SDO[1]), to determine the orientation of the user-provided image. An obvious limitation of SPIN therefore is that it can only work on images for which contemporaneous SDO data exists, i.e., on images taken

[1] https://sdo.gsfc.nasa.gov

on or after 2010 May 1st. SPIN uses the continuum images obtained by SDO's Helioseismic and Magnetic Imager (HMI) since these images closely match the white-light images taken by most amateur solar observers. The quick-look SDO/HMI continuum images are made publicly available within about 15-20 minutes of observation, by the Joint Science Operations Center (JSOC[2]). Thanks to the JSOC team, these images are already oriented so that the solar north is towards the top, and the east (approaching limb) is towards the left.

Note that even though the SDO is in a geosynchronous orbit at an altitude of about 35,800 km (about 22,250 miles) above Earth's surface, the SDO is still less than 0.04% the distance to the Sun for any Earth-based observer. This implies that SDO's view of the Sun is essentially the same as that of an observer on the Earth to within 0.02 degrees, thereby justifying our use of SDO images to orient an Earth-based observer's solar image.

In Section 2 we describe how to obtain images that SPIN can process, and how to access the SPIN tool. Section 3 describes how to use SPIN. The working of SPIN is described in Section 4. Finally, a summary of our work, known caveats, conclusions, and future work is contained in Section 5.

2. Obtaining Input Image and Accessing the SPIN Tool

In order to use SPIN, the user needs a white-light digital image of the Sun (i.e., an image obtained using safe neutral-density filter, but not using a narrowband filter like Hα, or Calcium, or any other narrowband filters), saved in JPEG or PNG format. The entire Sun must be visible in the image, preferably with the solar center close to the image center so that none of the edges of the solar disc are too close to the edges of the image. A sample image is shown in Fig. 1.

Besides a full-disk, white-light image of the Sun, the only other requirement is that the user has to have a Google email account. This is because the SPIN tool is written using open-source python and associated packages hosted on the web-based Google Colab platform. As of writing these proceedings, obtaining a Google email address is free.

The code can be accessed by pointing a web browser to the shortened URL https://is.gd/spincode or the QR code shown in the title. SPIN is a web-based tool and does not need to be installed on the user's computer or smartphone. When using SPIN, all computations are done on a cloud-based server. Since SPIN only needs a web browser, it can be used from any device supporting a modern web browser. We have successfully tested it on Google's Chrome browser on several desktops and laptops running Linux, Mac, or Windows operating systems, as well as on different iPhones and Android smartphones. Using SPIN on a smartphone can come in handy when working with images obtained with smart telescopes that save their images directly on the user's phones.

When SPIN is used for the first time, a pop-up window will appear warning that the code is not authored by Google. Other than uploading the user-provided image, SPIN does not access any

[2] http://jsoc.stanford.edu/

other data on the user's device, and it does not engage in any other nefarious activities. In fact, the user can view all of SPIN's code by clicking the "Show code" link next to the play icon for each step. If convinced by these disclaimers, the user may hit the "Run anyway" button when that warning shows up.

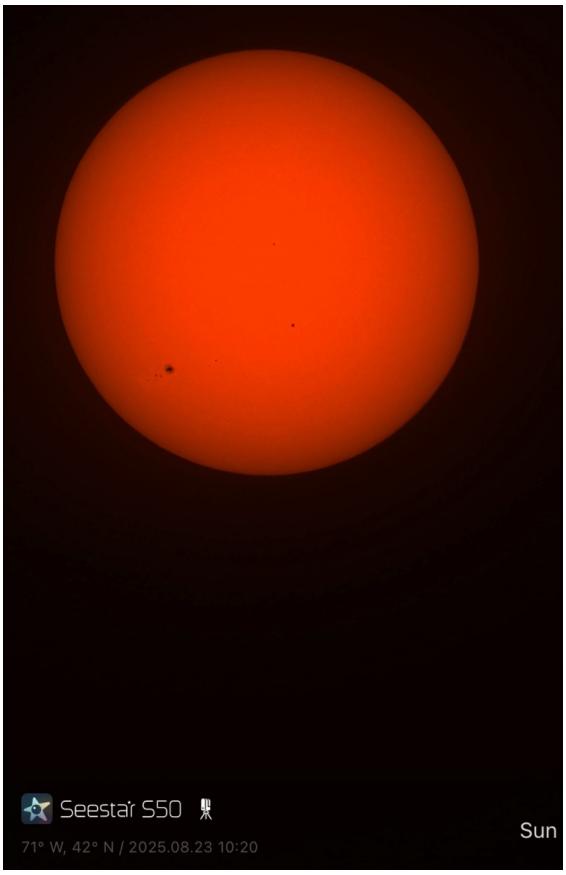

Figure 1. A sample input image for SPIN, obtained using a Seestar S50 telescope on 2025 August 23, at 14h 20m UTC. Note the manufacturer's logo and other text near the bottom were not cropped out.

3. Using SPIN

The user first uploads their image and provides the date and time of their image in UTC. It is crucial that the date and time is in UTC and not in the user's local time[3]. Given the relatively slow rotation of the Sun, we don't require the observation time to be correct to second-level precision. Timing uncertainties of a few minutes will introduce less than sub-pixel errors due to the Sun's rotation and can be safely ignored.

[3] While it is possible to extract the date and time information from the image metadata, different hardware manufacturers use different keywords for time-related metadata such as date, time, time zone, daylight savings etc. Therefore, we have deliberately left this step manual so that the user can ensure that the correct UTC date and time is provided to SPIN.

Besides providing the input image and its observation date/time, the user can choose whether to overlay the Heliographic Stonyhurst grid (see, e.g., Thompson 2006 and Çakmak 2014) on a grayscale version of the output image. The default is to skip overlaying the Stonyhurst grid. The user can also choose whether to draw the Earth as a circle, for scale, near the top-right of the output image. The default is to skip drawing the Earth for scale.

Once these inputs have been provided, the user hits the *Submit* button and waits for SPIN to complete the task[4].

4. How SPIN works

4.1. Installing the necessary libraries

SPIN uses several specialized open-source python libraries. Amongst these libraries, some are not installed by default on Google Colab's cloud-based compute environment. Therefore, once the user hits the Submit button after providing all inputs, the code first installs the missing libraries. This unfortunately is the slowest part of the code, and can sometimes take up to 30 or 40 seconds.

4.2. Finding the Sun in the user-provided image, and tightly cropping around the Sun

Once all required libraries have been installed, SPIN attempts to find the center and radius of the Sun, in pixels, in the user-provided image. To begin this process, the user-provided image is converted into a grayscale image using the *rgb2gray* function in the *scikit-image* package. For a rough, initial estimate of the solar disk's center, the light centroid of the entire grayscale image is computed. Then the best-fit 2D Gaussian model is determined, with the image centroid as the starting guess, to refine the position of the solar center. Thereafter we compute radial intensity profiles about the refined solar disk center. The radial intensity profile allows us to determine the radius, in pixels, of the Sun's disk based on solar limb-darkening laws[5]. Having determined the center and radius of the disk, we now create a tightly cropped, square, grayscale image with sides equal to the diameter of the Sun. We call this image the processed user image, or P_u.

4.3. Retrieving the nearest SDO/HMI continuum image

SPIN uses the observation date and time provided by the user to retrieve the 4096 x 4096-pixel resolution HMI continuum image closest to the observation time, from the JSOC data archive[6].

[4] Hopefully without any errors! However, a detailed progress log is printed on the screen, so that the user can keep track of what is going on. These logs are also usually helpful when tracking down any errors.
[5] As noted in Cox (2000), for the Sun at 550 nm, the intensity at the edge of the limb-darkened solar disk is 30% of the intensity at the disk's center.
[6] https://jsoc1.stanford.edu/data/hmi/images/

4.4. Finding the Sun in the SDO/HMI image

Inspecting several tens of SDO/HMI images we determined that average (i.e. [R+G+B]/3) pixel values less than 10 corresponded to pixels that were either beyond the Sun's disk or were located in the umbral regions of prominent sunspots. This allowed us to tightly crop the SDO/HMI image into a square image with sides equal to the diameter of the Sun. This grayscale, square, SDO/HMI image is then resized so that the diameter of the Sun is the same as that of the Sun in P_u (created in step 4.2). We call this image the processed HMI image, or P_h. Steps 4.1 through 4.4 ensure that both P_u and P_h are of the same size, the Sun is at the center of both, and the solar disks are of equal size as well.

4.5. *Rotating the user-provided image to match the orientation of the SDO/HMI image*

We polar-transform both P_u and P_h using the *warp_polar* function in scikit-image library. Cross-correlating the two polar-transformed images allows us an initial estimate of the rotation between P_u and P_h. A more refined estimate of the required rotation is obtained by minimizing the quantity *sum of squared residuals* (SSR), where the SSR is computed as follows:

1. Rotate P_u by a certain angle θ to obtain the rotated image $P_{u\theta}$
2. Create the residual image $D = P_{u\theta} - P_h$
3. Create the squared residual image by squaring each pixel of D
4. SSR = sum of all pixel values of the squared residual image

SPIN uses Nelder-Mead algorithm as implemented in *scipy* library (Virtanen et al. 2020, Gao & Han 2012) to minimize SSR as a function of the rotation angle. Unless the user requests overlaying the Stonyhurst grid and/or a circle representing the Earth for scale, the color version of $\boldsymbol{P_u}$ rotated by the optimal rotation angle determined above, is made available to the user for downloading. The output of SPIN on the image shown in Fig. 1 is shown in the left panel of Fig. 2. For comparison, the contemporaneous SDO/HMI image is shown in the right panel of Fig. 2.

A limitation of this approach is that it can only find the correct rotation where the imaging optics has an even number of reflections. Examples of such setups include a refracting telescope where the imaging sensor is directly placed on the focal plane of the objective lens(es), such as a DSLR camera with a solar filter in front of its lens, the *Seestar S30/S50* smart telescopes, and any similar setups that have zero reflections. Solar images obtained with the imaging sensor at the focal plane of a Newtonian reflector or a Schmidt–Cassegrain reflector, where light has been reflected twice (once by the primary mirror and again by the secondary mirror) should also work with SPIN. However, for setups with an odd number of reflections, e.g., a refractor with a star diagonal between the objective and the imaging sensor, SPIN will fail if the image is directly provided as input. *In cases involving an odd number of reflections the user should flip the image either horizontally or vertically (but not both!) before offering it to SPIN.* Future versions of SPIN will give the user options to specify whether their image has even or odd reflections, along with a third "try both" option for cases where the number of reflections is unknown.

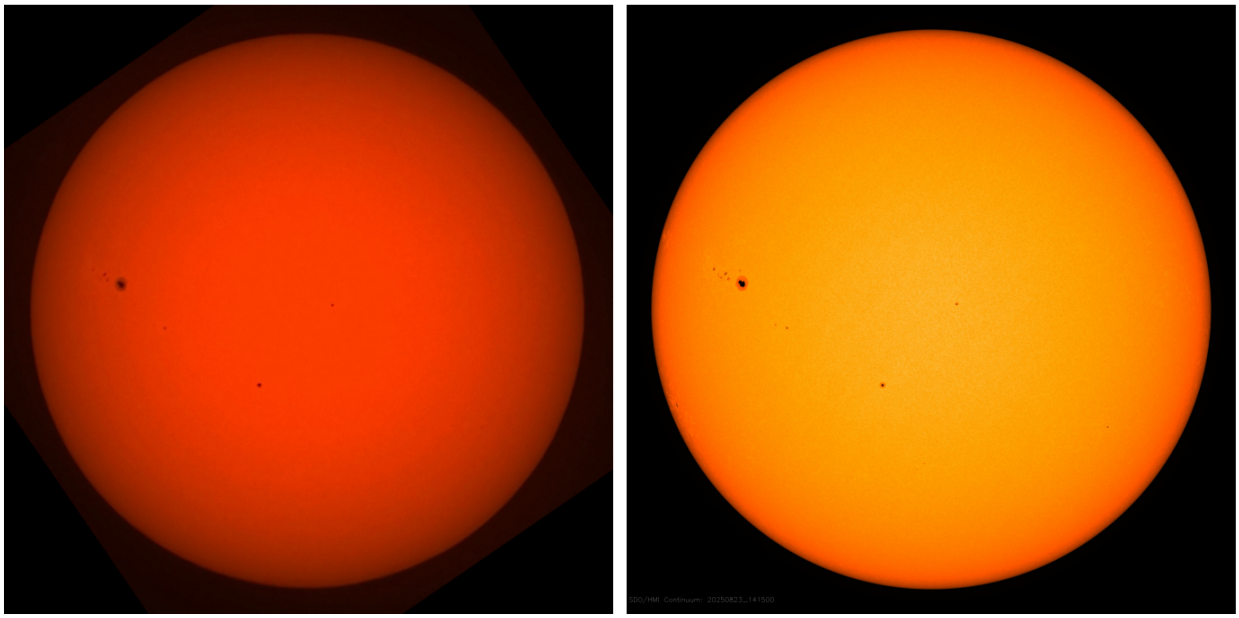

Figure 1. The left panel shows the optimally rotated solar image, for the input image shown in Fig. 1. The right panel shows the contemporaneous SDO/HMI image.

4.6. Overlaying Stonyhurst grid and/or a circle representing the Earth for scale (optional)

If the user requests overlaying the Stonyhurst grid and/or a circle representing the Earth for scale, then we use the *sunpy* package (The SunPy Community et al 2020) to obtain the Sun's distance from the Earth at the time of the observation. This is used to compute the angular size of the Earth if it were placed as far as the Sun, and thereby draw a circle near the top-right of the rotated image, depicting the Earth for scale. *Sunpy* is used again to get the Sun's angular radius at the time of observation. Since we already know the radius of the solar disk in the user-provided image (from step 4.2), the solar angular radius divided by the solar disk's radius in pixels gives us the plate-scale of the user-provided image. The *sunpy* package also uses the date and time information to compute the tilt of the solar north rotational axis toward Earth (which is equivalently the heliographic latitude of the central point of the solar disk, and often denoted as B_0 in the literature), as well as the angle between geocentric north and solar north as seen from Earth measured eastward from geocentric north (often denoted as P). The quantities B_0, P and the image plate-scale are used by *sunpy* to overlay the Stonyhurst grid on a grayscale version of the correctly rotated version of $\boldsymbol{P_u}$, and then made available to the user for downloading. The output of SPIN on the image shown in Fig. 1, with both 'Display Stonyhurst Grid' and 'Display Earth for Scale' options enabled, is shown in Fig. 3.

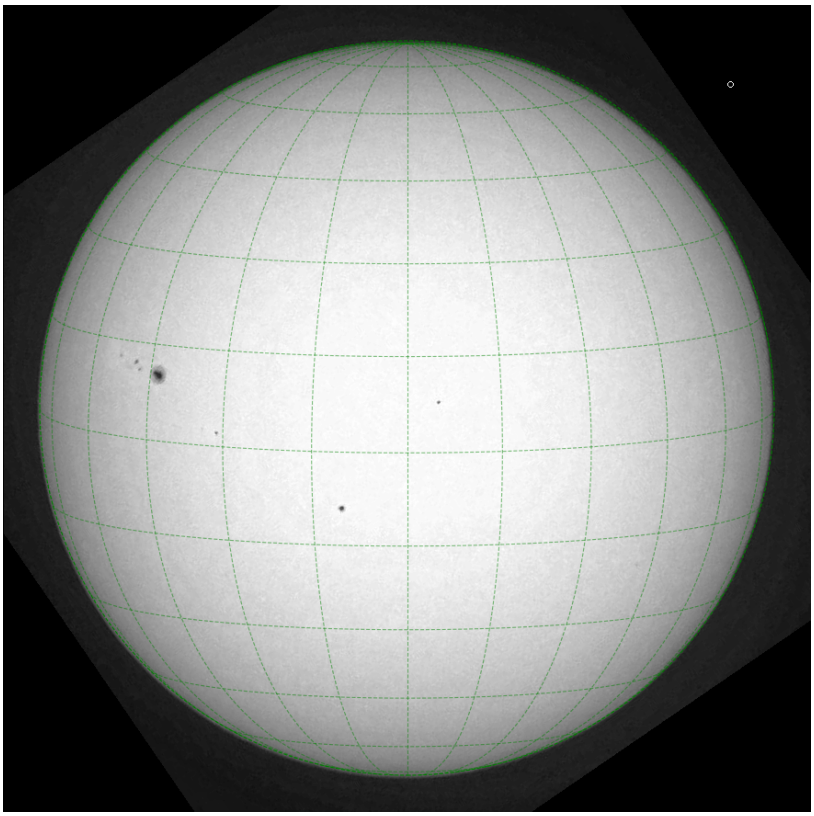

Figure 3. The output of SPIN on the image shown in Fig. 1, with both 'Display Stonyhurst Grid' and 'Display Earth for Scale' options enabled.

5. Summary, Caveats, Conclusions, and Future Work

We have developed an entirely web-based, open-source software tool "Solar Precision Image Normalizer" (SPIN) to facilitate standardizing the orientation of solar images taken for education, research, public outreach, or sheer entertainment. Once standardly oriented, e.g., using SPIN, the output images can readily show remarkable and fascinating properties of our Sun such as (but definitely not limited to):

(i) Rotation of the Sun by following the locations of sunspots (as illustrated in Fig. 4),
(ii) Differential rotation of the solar photosphere by following sunspots at different latitudes,
(iii) Formation and evolution of sunspots,
(iv) The axial tilt of the Sun's rotation axis, by following sunspots over a year,
(v) Creating 3D stereoscopic images of the Sun by taking images separated by a few hours (as illustrated in Fig. 5).

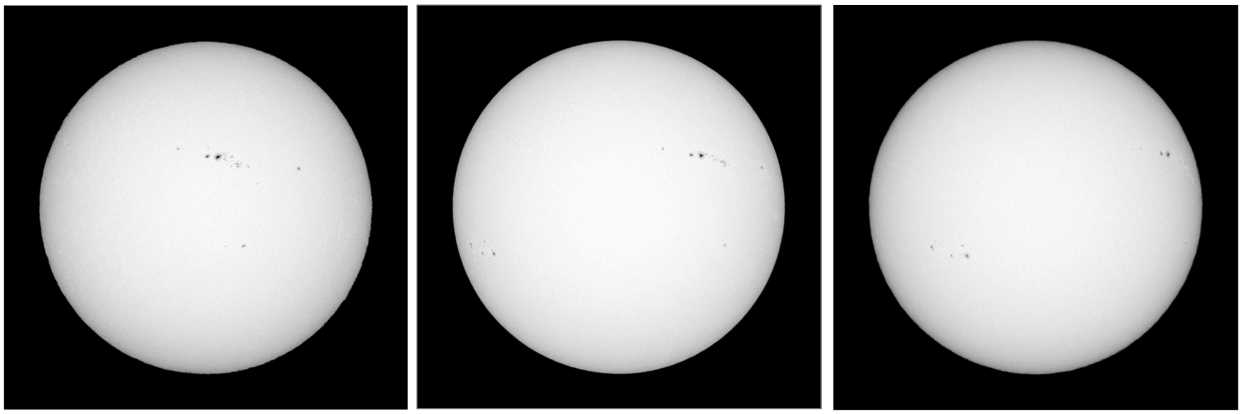

Figure 2. Three images taken on 2025 June 17, 19, 21, by one of the authors (DS) using a DSLR camera, and de-rotated using SPIN so that solar north is towards the top and the east limb is towards the left in each image. Solar rotation is evident from the motion of the sunspots.

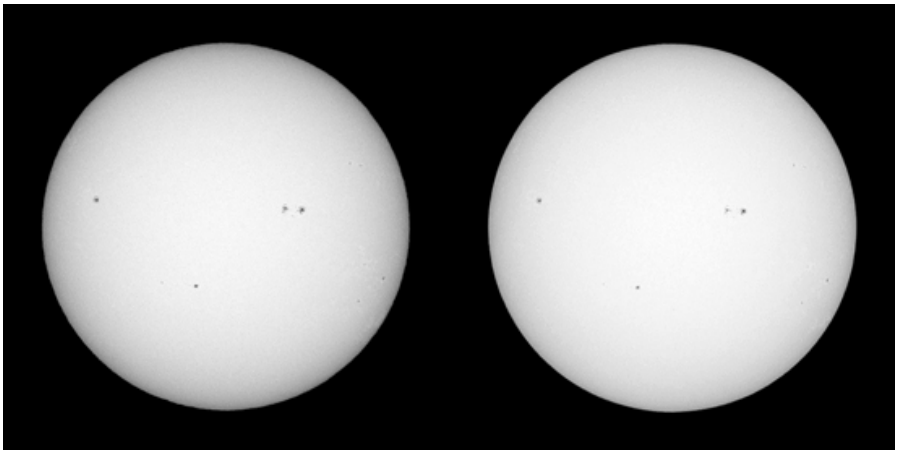

Figure 3. A composite of two solar images processed by SPIN, taken about 7 hours apart on 2025 Aug 01 by co-author DS. The later image is on the left side and earlier image is on the right side. When this composite image is viewed using a 3D stereoscopic viewer[7], the Sun "pops out" in 3D. Trained viewers may also be able to use the "free fuse technique"[8] by focusing beyond the screen, to combine the two images mentally into a 3D image without any viewer.

Some of the current limitations of SPIN are:

(a) Since SPIN uses contemporaneous SDO/HMI images, only images obtained on or after 2010 May 1st can be processed by SPIN.
(b) The images must be broad-band white-light images, and not obtained using any narrowband filter.

[7] Such as this one designed by astronomer and musician Sir Brian May: https://thespacestore.com/products/lite-owl-3-d-viewer [Disclaimer: The authors receive no financial gain from Sir May for highlighting his design!]
[8] See, e.g., https://stereoscopy.blog/2022/03/11/learning-to-free-view-see-stereoscopic-images-with-the-naked-eye/

(c) The images must contain the entire solar disk, reasonably well centered so that no part of the solar limb is too close to the edges of the image.
(d) Images where the optical train includes an even number of reflections need to be flipped either horizontally or vertically before providing them to SPIN as input.
(e) After taking a solar image the user is advised to wait for about 30 minutes or so before giving it a SPIN. This is because it typically takes about 15-20 minutes for the latest images from the SDO observatory to appear on the JSOC website.

We are currently working on adding features such as sunspot detection and sunspot area measurement, which will allow users to contribute scientifically valuable information from their images, and track sunspot evolution.

Acknowledgements

It is a great pleasure to acknowledge constructive criticism from numerous users of SPIN who have not only provided feedback and reported bugs, but also suggested additional features (of which we have been able to incorporate only a few so far!). We encourage users to please continue sending their thoughts and feedback so that the tool can continue to improve.

References

Çakmak, H. 2014, Experimental Astronomy **38**, 77.
Cox, Arthur N., ed. 2000, *Allen's Astrophysical Quantities*, Springer-Verlag, NY.
Gao, F. and Han, L. 2012, Computational Optimization and Applications **51**, 259.
The SunPy Community et al. 2020, ApJ **890**, 68.
Thompson, W. T. 2006, A&A **449**, 791.
Virtanen, P. et al. 2020, Nature Methods **17**, 261.

Mining the AAVSO Database to Determine Period Evolution of Intermediate Polars

Ryan McCrone[1] and Dipankar Maitra[2]

[1]Rhode Island College, Department of Physical Sciences, Providence, RI, 02908;
[2]Wheaton College, Department of Computer Science, Mathematics, and Physics, 26 E. Main St., Norton, MA 02766

Subject Keywords

AAVSO International Database; Photometry; Intermediate Polars; stars: individual (AO Psc,FO Aqr, V1062 Tau, V405 Aur)

Abstract

We carried out systematic analysis of V- and CV-band photometric observations of the intermediate polars AO Psc, FO Aqr, V1062 Tau, and V405 Aur in the AAVSO database. We searched for signatures of spin period and orbital period, and the change in period over time of these intermediate polars. Lomb-Scargle periodograms were used to find these periods after all the observation times were barycenter corrected for a geo-centered observer. These periods were identified to within a few hundredths of a second when there were at least a few thousand observations in any given observing season. Our results on the spin-period evolution in systems such as AO Psc and FO Aqr agree with prior work on these systems, whereas our new results on V1062 Tau and V405 Aur indicate that they are interesting sources that need more observations. Our promising results demonstrate the power of long-term monitoring when it comes to answering fundamental astrophysical questions, and the need for databases like AAVSO.

1. Introduction

Intermediate polars (IP) are a class of binary star system where a white dwarf (WD) accretes from a companion star. The magnetic field of the WD disrupts the accretion disk near the dwarf, and the accreted matter is instead channeled via the WD's magnetic field lines, onto its magnetic poles similar to how solar winds enter the Earth's upper atmosphere following the Earth's magnetic field lines. Previous studies of period histories of IPs (e.g., Patterson et al., 2020) demonstrate that they typically have spin periods of minutes or hours and their spin periods change by a small fraction of a second every year. Therefore, these studies typically require analysing multiple years of data. Given the AAVSO database contains years of photometric observations, submitted by observers around the world, we decided to test whether changes in spin periods of IPs can be studied via a careful analysis of their data in the AAVSO database. We present our source-selection and analysis methodology in Sec. 2, describe our results in Sec. 3, and summarize our conclusions as well as future work in Sec. 4.

2. Source Selection and Data Analysis Methodology

We used the comprehensive list of IPs curated by Dr. Koji Mukai at NASA/GSFC (Mukai, K., n.d.). We started our work with AO Psc and FO Aqr since their spin period histories have been recently published by Patterson et al. (2020), thereby allowing us to cross-check our results. Thereafter we chose V1062 Tau since its spin-period appeared to be poorly constrained and we wanted to probe whether our work can provide tighter constraints of its spin period history. Finally, we analyzed data from V405 Aur because it exhibits a strong harmonic of its spin period, rather than its actual spin period, and we wanted to test whether our methodology was sensitive to detecting this harmonic.

For a given source, the first step was to download all V- and CV-band photometry data from the AAVSO database. Once the data were downloaded, the resulting light curve was visually inspected so that obvious outliers in the light curve could be removed.

We then grouped data from each observing season by requiring that observing seasons were separated by at least 80 days. Furthermore, data from seasons with less than 100 observations were merged with that of the preceding observing season to enhance period detection precision. For each group of data, the Lomb-Scargle periodogram (Lomb 1976, Scargle 1982) as implemented in the *astropy* package (VanderPlas 2018, Astropy Collaboration 2022) was used to find the period for that group. Search ranges were set 100 seconds above and below the expected period. One million frequencies were searched in the range to estimate the periodicity.

Our Lomb-Scargle periodograms showed that for groups which had more than a few thousand observations submitted, our results were close to the periods in literature for AO Psc and FO Aqr. However, the scatter in the periodicities was significantly larger than those reported, e.g., by Patterson et al. (2020). The precision of our analyses was significantly improved by barycenter correcting the observation times. The python package *barycorrpy* (Kanodia & Wright 2018) was used to carry out barycenter correction to the timestamps of our data. One concession that had to be made was to treat the location of all observers as being at the center of the Earth, as geolocation data is not included in the AAVSO database. However, even with the 'every observer was at geocenter' approximation, the precision in period determination increased by almost an order of magnitude, compared with raw data not corrected for barycenter. The importance of barycenter correction is illustrated in Fig. 1. Figure 2 shows how the volume of data affects the precision of period determination.

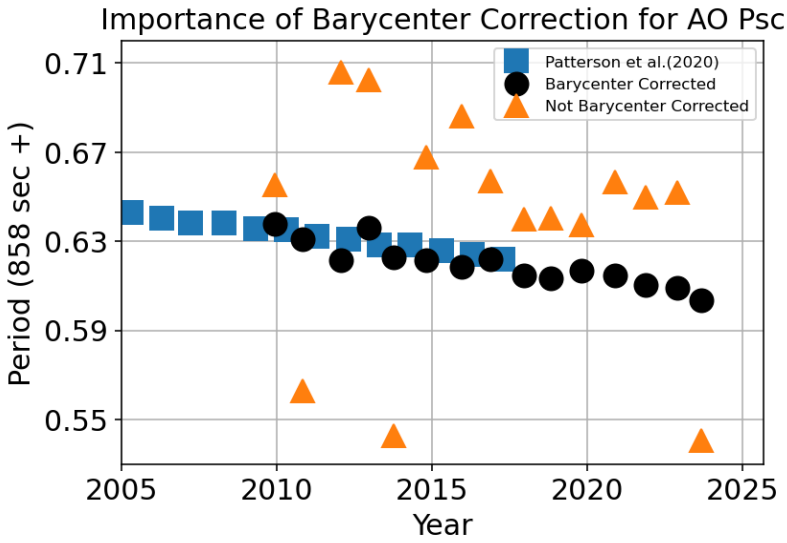

Figure 1. A plot of the period history of AO Psc showing the difference between barycenter uncorrected AAVSO data (orange triangles) and barycenter corrected AAVSO data (black circles). Results from Patterson et al. (2020; shown as blue squares) are shown for reference.

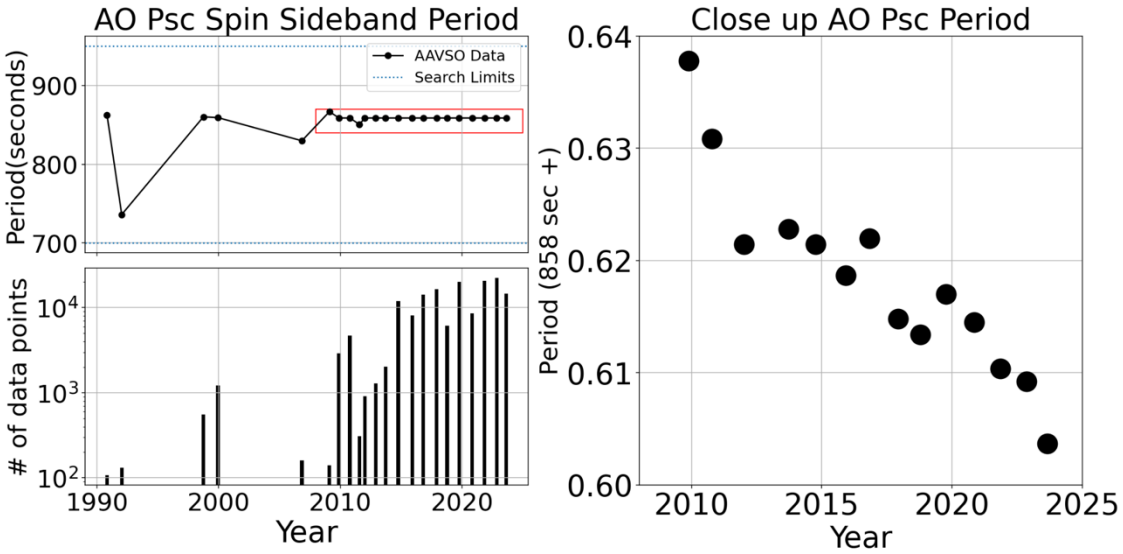

Figure 2. The top-left panel shows the periods with observing seasons that had less than 100 observations grouped together. The bottom-left histogram shows the number of observations for each such group. In years prior to 2010, the number of observations per observing season is not sufficient to constrain the period adequately. The right panel is a close-up of the last 17 years when enough observations were recorded in the database to allow for precise periods estimation.

3. Results and Future Work

As expected, the observing seasons with more observations typically had better results than ones with less observations, with an observing season typically needing at least a few thousand data points to yield an accurate and precise period.

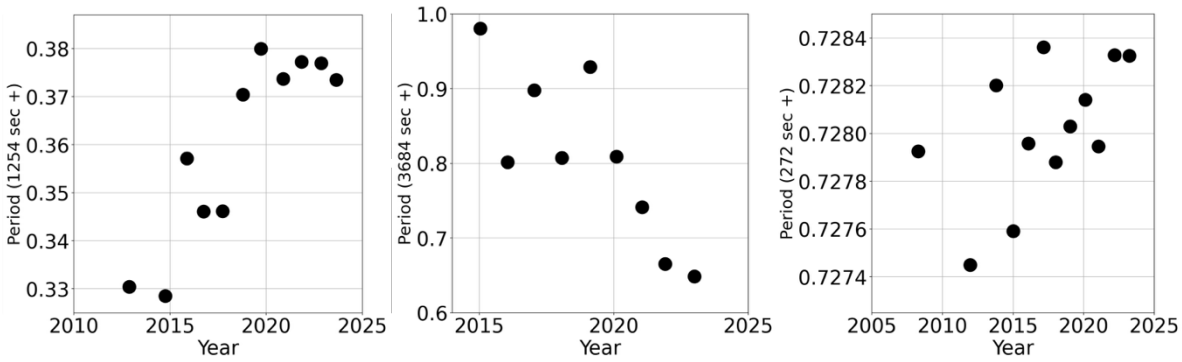

Figure 3. The spin period evolution of FO Aqr (left panel), V1062 Tau (middle panel) and the half spin period of V405 Aur (right panel) as determined from our analysis of their AAVSO data.

AO Psc was one of the two stars that formed the core of our hypothesis that the AAVSO data could be used to find the period histories. The period history of this star was compared to the period history found and the AAVSO data agreed with what had been found by Patterson et al. (2020). The full period history of this star is shown in Fig. 2

FO Aqr was the other star that was used as the basis for our hypothesis. It is notable that the spin period was decreasing for the majority of the data seen in Patterson et al. (2020) with the period increasing in the last few points. The AAVSO data are able to show that the spin period has appeared to continue this increase over the last few years. We also see that the spin period appears to have plateaued and may have begun to decrease again in the last few years, as is seen in the left panel of Fig. 3.

V1062 Tau was initially chosen due the spin period listed by K. Mukai, being ill-defined at exactly 3800 seconds. Further analysis by Lipkin, Leibowitz, & Orio, 2004 defined a period of 3685.8 ± 3 seconds. We had found that according to the AAVSO data this star had a spin period of 3684.65 seconds during the 2022-2023 observing season. The spin period for this system since 2015 is shown in the middle panel of Fig. 3.

Finally, V405 Aur was chosen due to interesting behavior in its period. While the spin period of the star was weakly defined in the AAVSO data, the half spin period was more well defined. We determined that the half spin period is about 272.728 seconds (as shown in the right panel of Fig. 3). Additional high-precision photometry is needed to statistically quantify any time-dependent trend in this source.

4. Conclusions and Future Work

From the results presented in this pilot study of four IPs it is clear that even though the AAVSO database is somewhat heterogenous in terms of quality, our analysis procedure can robustly constrain spin period evolution of IPs based on V- and CV-band photometric observations submitted to the AAVSO database, especially when a few thousand or more observations were submitted during any given observing season. If the observers could ensure that (a) the observation times are precise, and (b) include their observatory location, e.g., in the comments when submitting the observations [which would improve the barycentering process], then the spin evolutions can be constrained even better. We are currently working on systematically analyzing all IPs in the AAVSO database to study their spin period evolution.

Acknowledgements

We acknowledge with thanks the variable star observations from the AAVSO International Database contributed by observers worldwide and used in this research. We are also grateful to the group of AAVSO members who contributed data to the Patterson et al. (2020) campaign, for discussing their work with us.

References

Astropy Collaboration. 2022, *ApJ* **935**, 167

Kanodia, S. & Wright, J. 2018, *Res. Notes AAS* **2**, 4

Lomb, N. R. 1976, Ap&SS **3**, 447

Lipkin, Y. M., Leibowitz, E. M., & Orio, M. 2004, *MNRAS*, **349**, 1323

Mukai, K. n.d., *The intermediate polars*, NASA, https://asd.gsfc.nasa.gov/Koji.Mukai/iphome/iphome.html

Patterson, J., et al. 2020, *ApJ* **897**, 70

Scargle, J. D. 1982, *ApJ* **263**, 835

VanderPlas, J. 2018, *ApJS* **236,** 16

Tracing the Universe with Variable Stars: RR Lyrae in Nearby Systems and Cepheids Across Galaxies: Integrating Research, Education, and Public Engagement

Abbas Mokhtarzadeh, Ph.D., PE

Amateur Astronomer, IAU CoNOC USA, NASA/JPL Solar System Ambassador;
lookingupastro@gmail.com

Subject Keywords

RR Lyrae; Cepheids; Cosmic Distance Ladder; AAVSO International Database; STEM, STEAM Education; Public Outreach; Cultural Astronomy

Abstract

RR Lyrae and Cepheid variable stars are essential tools for measuring cosmic distances and understanding galactic structures within and beyond the Local Group. This study presents results from a multi-year program integrating scientific research, structured education, and public engagement. Students and community participants conducted CCD photometry using robotic telescopes through the Skynet network, constructed light curves, determined periods, and compared results with archival AAVSO data. Incorporating cultural astronomy and highlighting historical contributions of women astronomers connected participants to the broader context of the field. These activities enhanced understanding of cosmic distances, fostered STEM/STEAM skills, and promoted inclusive citizen-science participation. The results demonstrate that variable star research can simultaneously advance astrophysical knowledge and community engagement.

1. Introduction

1.1 Historical Overview

The study of variable stars has a long and storied history, dating back to observations by ancient civilizations. Babylonian, Chinese, and Greek astronomers documented unusual stellar phenomena in the context of celestial omens, agricultural calendars, and navigation. These early records, though descriptive, demonstrated careful observation of stellar brightness and periodicity (Kanas 2007; Chapman 1990).

With the advent of the telescope, astronomers such as Tycho Brahe and Johannes Kepler refined positional and brightness measurements of stars. John Goodricke's pioneering study of Algol in 1783 was the first to identify a predictable eclipsing variable star, showing that stellar variability could be quantified and systematically studied (Goodricke 1783). Friedrich Wilhelm Herschel extended these observations to other stars, contributing to early catalogs and classifications of variable stars.

The early 20th century marked a turning point with Henrietta Swan Leavitt's discovery of the period-luminosity relationship in Cepheid variables within the Magellanic Clouds (Leavitt 1908). By correlating pulsation periods with intrinsic luminosity, Leavitt provided a method for measuring extragalactic distances. Edwin Hubble subsequently applied this relationship to spiral nebulae, confirming their extragalactic nature and demonstrating the expansion of the universe (Hubble 1925).

Figure 1. Henrietta Swan Leavitt - Period–Luminosity Relationship

RR Lyrae stars, pulsating horizontal branch stars, provide complementary distance measures within the Milky Way and nearby dwarf galaxies. These stars, with shorter periods and lower luminosities than Cepheids, occupy a critical rung in the cosmic distance ladder. Modern observations, combined with stellar evolution modeling, allow precise distance measurements and mapping of Galactic structures (Madore and Freedman 1991; Riess et al. 2016).

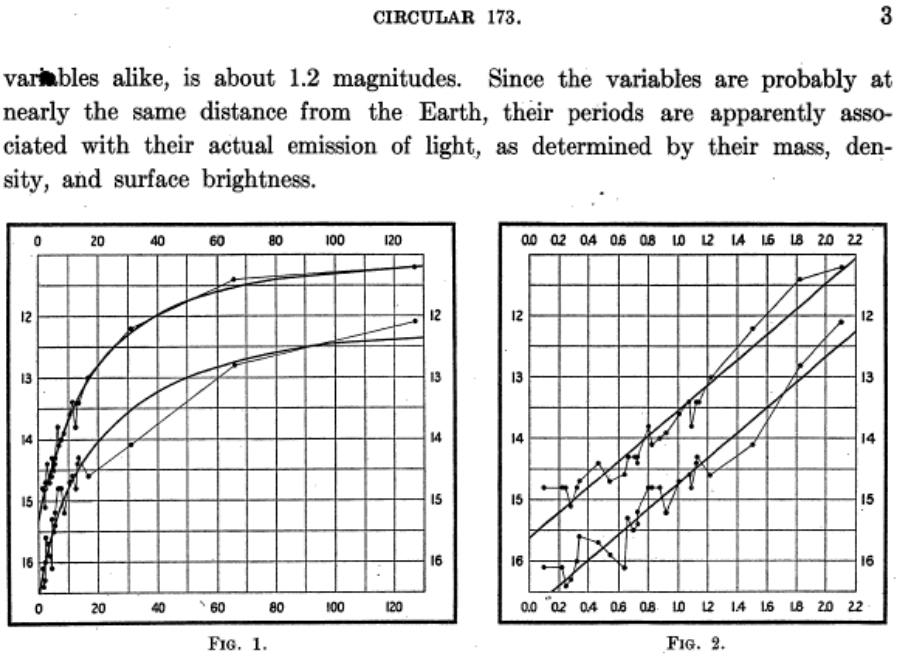

CIRCULAR 173. 3

variables alike, is about 1.2 magnitudes. Since the variables are probably at nearly the same distance from the Earth, their periods are apparently associated with their actual emission of light, as determined by their mass, density, and surface brightness.

FIG. 1. FIG. 2.

Figure 2. Period–Luminosity Relationship of Variable Stars in the Magellanic Clouds. Adapted from Henrietta S. Leavitt, 1777 Variables in the Magellanic Clouds (Harvard College Observatory, 1908).

1.2 Educational and Outreach Context

Historical narratives, particularly the contributions of women astronomers like Henrietta Leavitt, Annie Jump Cannon, Antonia Maury, and Cecilia Payne-Gaposchkin, offer rich material for inclusive STEM and STEAM education (IAU OAO 2025). Integrating these narratives with hands-on observational research fosters engagement among diverse learners, providing authentic experiences in scientific inquiry while emphasizing cultural heritage and inclusivity.

1.3 Archaeoastronomy, Cultural Astronomy, and Inclusive Astronomy

Astronomy is deeply intertwined with human culture, history, and society, giving rise to archaeoastronomy and cultural astronomy. Archaeoastronomy studies how ancient civilizations observed and interpreted celestial phenomena, often integrating them into calendars, architecture, rituals, and mythology (Ruggles 1999; Krupp 2000). Iconic structures such as Stonehenge, Chichen Itza, and the Egyptian Pyramids exemplify alignments to solar, lunar, and stellar events, linking human cognition with astronomical phenomena.

Cultural astronomy examines the societal role of astronomy, including navigation, agriculture, timekeeping, and religious practices. In recent decades, the field has expanded to emphasize cross-cultural perspectives and contributions of historically marginalized groups, bringing an inclusive lens to astronomical studies (Aveni 2001; Belmonte et al. 2020).

Inclusive astronomy promotes participation for all learners, regardless of gender, race, socioeconomic status, physical ability, or prior knowledge. Initiatives such as Women and Girls in Astronomy, citizen science projects, and community-driven outreach have significantly expanded engagement, providing authentic research experiences and bridging professional science with public learning.

Integrating archaeoastronomy, cultural astronomy, and inclusive astronomy into variable star programs enhances understanding in multiple ways:

- **Historical Context:** RR Lyrae and Cepheid observations are linked to centuries of human skywatching.
- **Cultural Literacy:** Diverse interpretations of celestial knowledge foster appreciation for global contributions.
- **Educational Engagement:** Inclusive approaches increase participation and learning gains.
- **Public Outreach:** Connecting science to cultural heritage captures public interest and encourages lifelong learning.

This integrative approach develops technical skills, curiosity, empathy, and engagement, demonstrating how scientific research and public education advance together.

Table 1. Historical Overview of Variable Stars as Distance Indicators and the Evolution of Astronomical Models from Antiquity to Modern Astronomy

Era	Key Objects	Notes	Scientific Insights
Ancient Observations (~3000 BCE – 1500 CE)	Sun, Moon, planets, constellations	Unaided-eye sky / constellations	Basic celestial patterns, calendars, seasonal cycles
Geocentric Model (4th – 16th Century CE)	Earth-centered orbits, fixed stars	Ptolemaic universe	Conceptual universe model, predictable planetary motion
Heliocentric Model (16th Century)	Planets orbit Sun, moons of Jupiter	Sun-centered concept	Corrected planetary system understanding, moons & planets observed
Deep-Sky Discoveries (17th–18th Century)	Nebulae, star clusters	Telescope + nebula/stars	Cataloging stars & nebulae, realization of "island universes"
Variable Stars & Distance Indicators (Early 20th Century)	**Cepheids, RR Lyrae**	**Light curve & Galaxies**	**Measurement of cosmic distances, first "standard candles"**
Modern Astronomy (20th Century–Present)	Exoplanets, galaxies, pulsars, black holes	Telescope + galaxy/exoplanet	Understanding universe structure, stellar evolution, extreme objects

2. Methods

2.1 Observational Approach

Data were collected using robotic telescopes via the Skynet University network, providing access to instruments in both hemispheres for synchronous and asynchronous observations. Targets were selected for both scientific value and educational engagement.

RR Lyrae variables were observed in globular clusters (M3, M15, M53, M92, NGC 5466) and nearby dwarf galaxies (Sculptor, Fornax, Carina). Classical Cepheids were observed in Local Group galaxies (LMC, SMC, M31, M33). Observation planning included airmass calculations, exposure optimization, field-of-view analysis, and selection of multiple stable comparison stars. Multiple exposures were obtained to fully resolve periods of RR Lyrae (0.1–1 day) and Cepheids (1–100 days).

Data reduction utilized Afterglow and Astromancer online tools for batch photometry, light curve construction, and period determination. Standard CCD reductions—bias subtraction, dark frame correction, and flat-field normalization—were applied. Differential photometry minimized systematic errors, while multi-filter observations enabled amplitude and color analyses. Period determination employed Fourier transforms, phase dispersion minimization, and cross-validation with archival AAVSO datasets. Quality control included signal-to-noise verification and sigma-clipping for outlier removal.

The integrated use of Skynet, Afterglow, and Astromancer allowed students and citizen scientists to perform authentic astronomical research efficiently, calibrating magnitudes, constructing light curves, and deriving distances to RR Lyrae and Cepheids while developing STEM/STEAM skills.

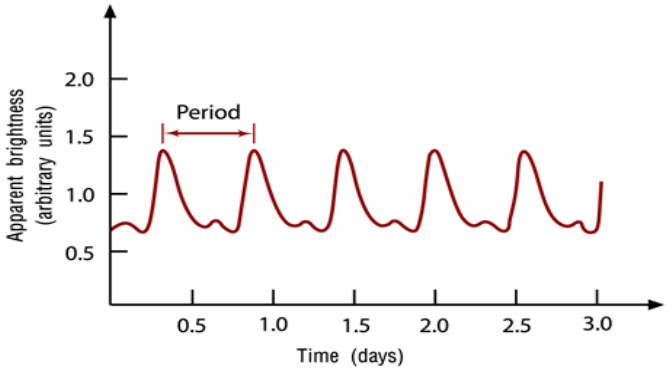

Figure 3a. Typical RR Lyrae Light Curves

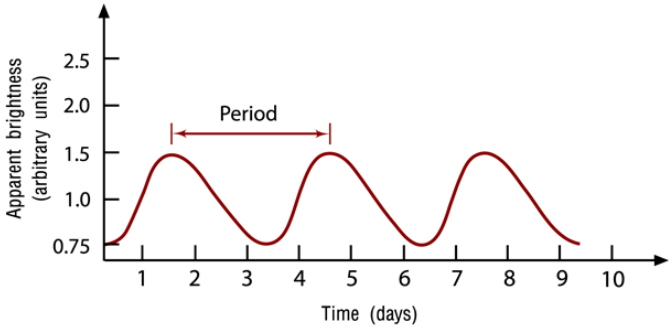

Figure 3b. Typical Cepheid Light Curves

Adapted from UNC SkyNet University, University of North Carolina at Chapel Hill, Department of Physics and Astronomy, n.d. (https://skynet.unc.edu/university)

Variable stars, including Classical Cepheids and RR Lyrae stars, serve as fundamental distance indicators in astronomy through their well-established Period–Luminosity (P–L) relationships.

For Cepheids, the absolute magnitude M_V can be calculated from the pulsation period using:

$$M_V = a\log_{10}(P) + b \quad (1)$$

where $a \approx -2.76$ and $b \approx -1.40$ for V-band observations (Leavitt & Pickering 1912; Freedman & Madore 2010).

For RR Lyrae stars, the relation is simpler because their periods are shorter and their luminosities are nearly constant:

$$M_V \approx 0.75 \quad (2)$$

with slight adjustments depending on metallicity.

The distance "d" to a variable star is then determined via the distance modulus formula:

$$d = 10^{(m-M+5)/5} \text{ pc} \quad (3)$$

where m is the apparent magnitude. Using these methods, astronomers can measure distances to stars within our Galaxy and nearby galaxies, providing crucial constraints for the cosmic distance scale and the calibration of the extragalactic distance ladder.

The following rearranged approximate formulas have been implemented in the Skynet OPIS program to calculate the absolute magnitudes and distances of variable stars:

$$M_V \approx -1.43 - 2.81 \log \frac{P}{1 \text{ day}} \quad (4)$$

$$D = 0.01 \text{ kpc} \times 1.585^{(m-M)} \quad (5)$$

2.2 OPIS Curriculum and Learner Engagement

The **OPIS curriculum** (Reichart 2008–2025) was originally designed to provide structured engagement for learners conducting hands-on investigations of variable stars, focusing on measuring cosmological distances. In this study, the curriculum has been expanded to integrate historical context, cultural perspectives, and inclusive educational practices. The enhanced curriculum emphasizes iterative laboratory practice, reflective thinking, and active participation to promote both scientific understanding and engagement in citizen science initiatives.

Key Parts and Their Development:

The OPIS curriculum is structured into six interrelated parts. Parts 1–4 are adapted from the original modules, incorporating contextual and reflective enhancements to connect technical skills with historical and cultural understanding. Parts 5 and 6 represent newly added or evolved components, extending the original curriculum to emphasize scientific communication, public engagement, and integrative reflection. Each part is designed to build specific technical competencies while reinforcing historical, cultural, and societal connections.

- **Part 1: Introduction to Variable Stars**: Derived from the original OPIS Module 1, this part provides foundational knowledge of variable stars, including classification, pulsation mechanisms, and historical discoveries. Learners examine the roles of RR Lyrae and Cepheid stars in mapping cosmic distances and explore the contributions of early women astronomers and global skywatching traditions. Enhancements include explicit reflection on the cultural and historical contexts of variable star research to foster holistic understanding.

- **Part 2: Telescope Operation and Observational Planning.** Based on OPIS Module 2, this part provides hands-on experience in robotic telescope operation, including alignment, field-of-view analysis, exposure calculations, and observation scheduling. Observations utilize the Skynet University network, providing access to telescopes in both hemispheres. Enhancements focus on optimizing observation schedules for scientific rigor and participant engagement, facilitating authentic contributions to citizen science datasets.

- **Part 3: CCD Photometry and Data Reduction**. Derived from OPIS Module 3, learners process raw telescope images using Afterglow and Astromancer online tools. Techniques include bias, dark, and flat-field corrections, differential photometry, and error analysis. Instruction emphasizes reproducibility, data quality assessment, and collaborative problem-solving. Enhancements include explicit connections to historical and cultural perspectives, reinforcing the broader relevance of data analysis.

- **Part 4: Period Analysis and Distance Measurement**. Based on OPIS Module 4, learners apply Fourier analysis, phase folding, and period determination to RR Lyrae and Cepheid stars. Distances to globular clusters and nearby galaxies are calculated from calibrated magnitudes. Enhancements embed historical and cultural perspectives on the cosmic distance ladder, emphasizing the global legacy of variable star research and its role in shaping our understanding of galactic structure.

- **Part 5: Scientific Communication and Public Engagement (Enhanced/Evolved Module 5)**. This evolved part extends the original OPIS Module 5, integrating scientific communication with public outreach and inclusive participation. Learners synthesize results, prepare visualizations, and communicate findings to both scientific and general audiences. Instruction emphasizes narrative storytelling that integrates historical contributions, cultural context, and the role of women in astronomy, translating observational research into accessible narratives for classrooms, community programs, and online platforms.

- **Part 6: Reflective and Integrative Practices (New Addition/Evolved Module 6)**. This newly developed part emphasizes holistic integration of observational data with historical, cultural, and educational perspectives. Learners engage in iterative problem-solving, uncertainty evaluation, collaborative discussion, and participation in citizen science initiatives. This component fosters critical thinking, scientific reasoning, and inclusive engagement, highlighting the societal relevance of variable star research while reinforcing experiential learning.

The enhanced OPIS curriculum incorporates a comprehensive set of instructional strategies designed to foster technical competence, scientific reasoning, and inclusive engagement in variable star research. These pedagogical approaches provide structure while allowing flexibility for learners at different experience levels, and they integrate historical, cultural, and societal contexts to enrich the learning experience. Key elements include**:**

1. Scaffolding for multiple experience levels: Activities progress from foundational to advanced, supporting gradual skill development.
2. Reflective exercises: Learners explicitly link scientific findings to historical, cultural, and societal narratives, emphasizing contributions from women and underrepresented groups in astronomy.
3. Iterative practice: Repeated cycles of observation, data analysis, and interpretation reinforce technical competencies and conceptual understanding.
4. Citizen science integration: Participants contribute authentic observations to research datasets, gaining experience in real scientific workflows.
5. Public engagement emphasis: Reporting and communication exercises enable dissemination of scientific knowledge to diverse audiences, enhancing STEM or STEAM literacy and fostering lifelong learning.

Through these enhancements and additions, the OPIS curriculum provides learners with both technical skills and a holistic understanding of how variable star research intersects with culture, history, and community participation. This integrative approach promotes curiosity, critical thinking, and inclusive engagement in science, demonstrating how structured curricula can simultaneously advance education, research, and outreach.

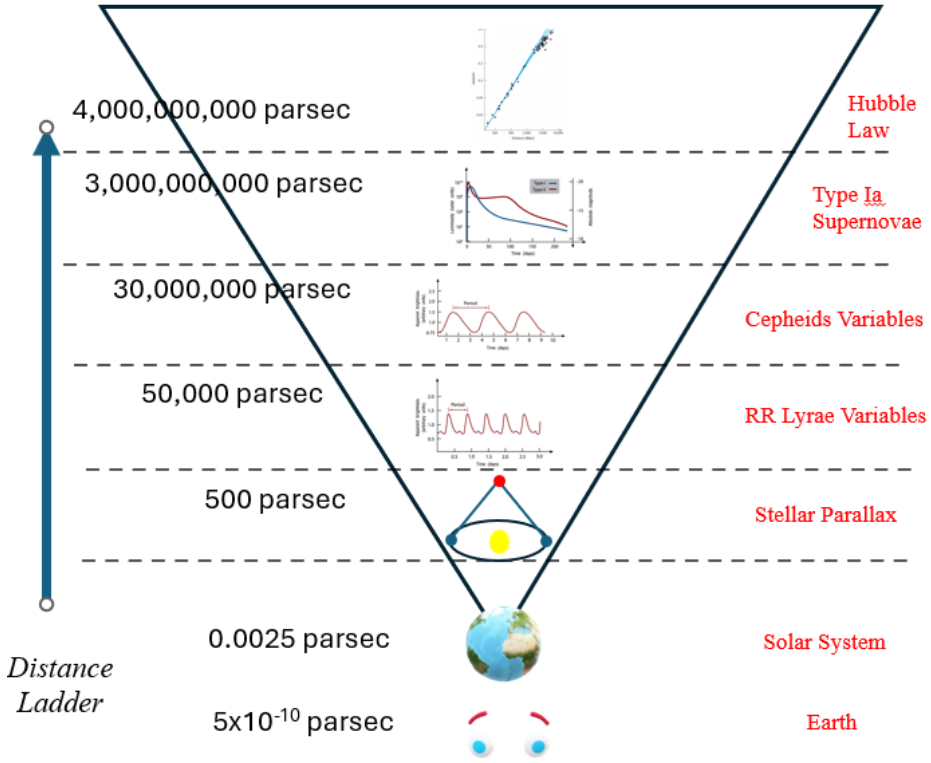

Figure 4. Curriculum integration diagram

2.3 Public Engagement and Inclusive Learning

Public engagement activities encompassed star parties, workshops, and interactive sessions designed to accommodate diverse participants. Accessibility features, including tactile star charts, large-print guides, and color-blind–friendly visuals, ensured inclusive participation. Mentorship paired experienced amateur astronomers with learners, providing guidance in telescope operation, photometry, and data analysis. Historical narratives highlighting the contributions of women and underrepresented groups were integrated to reinforce cultural awareness and inclusivity.

Participant learning outcomes were assessed through pre- and post-activity surveys, demonstrating measurable gains in:

1. Observational skills and practical data collection
2. Understanding of stellar variability and distance measurement techniques
3. Participation in authentic research experiences
4. Confidence, interest, and motivation in STEM or STEAM fields

Outreach efforts intentionally targeted a broad spectrum of the community, including underrepresented populations and lifelong learners. Participants actively constructed light curves, analyzed observational data, and contributed their findings to the AAVSO International Database, thereby participating in meaningful citizen science initiatives while reinforcing both scientific literacy and community engagement.

Figure 5. Public engagement workflow diagram

3. Lab Practice Results

3.1 RR Lyrae Lab Observations Procedure

RR Lyrae stars in this program exhibited pulsation periods of 0.1–1.0 day and V-band amplitudes of 0.3–1.2 mag. Observed targets included RR Lyrae stars in globular clusters NGC 1261, M3, M15, M53, M92 and in dwarf spheroidal galaxies Sculptor, Fornax, and Carina. NGC 1261 is presented as a representative example. Distances derived using horizontal-branch absolute magnitude calibration agreed with published values within 5–10%.

Finder charts identified each RR Lyrae variable and reference stars for differential photometry, accommodating telescope flips and rotations. Observations were obtained via Skynet Robotic Telescope Network, validated with AAVSO datasets, and analyzed using standard photometric procedures, enabling authentic variable star research within a collaborative framework.

The period of the RR Lyrae star in NGC 1261 was P = 0.329 days from the period-folded light curve and P = 0.330 days from the Astromancer periodogram, consistent with RR Lyrae characteristics. The average absolute magnitude was M_V = 0.75, with an apparent magnitude of m_V = 16.699 ± 0.05 mag. Using the distance modulus formula, the derived distance was D = 15.29 kpc, a 6.8% deviation from reference values, demonstrating reliable educational and citizen-science measurement.

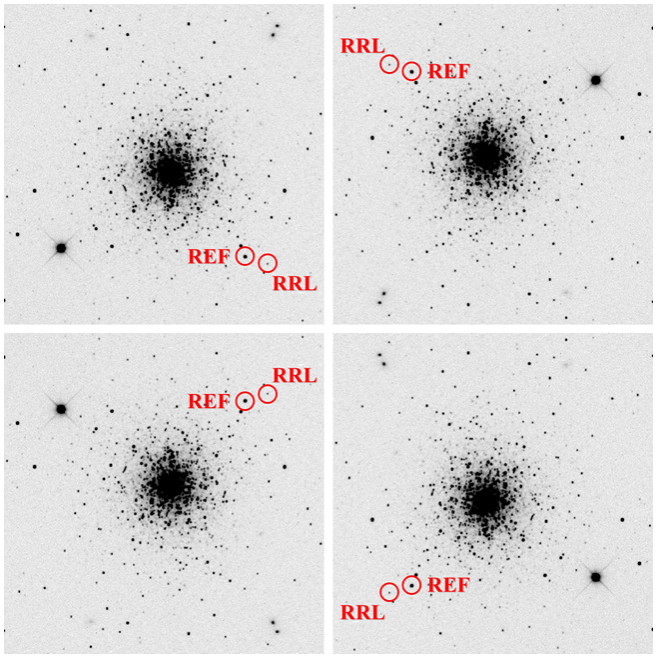

Figure 6. Finder Chart for RR Lyrae Observation in NGC 1261. Four astronomical images of crowded star fields. The globular cluster NGC 1261, an RR Lyrae star, and a reference star appear in all four images in various orientations. The reference star and RR Lyrae star are close together. The RR Lyrae star is circled and labeled "RRL" and the reference star is circled and labeled "REF."

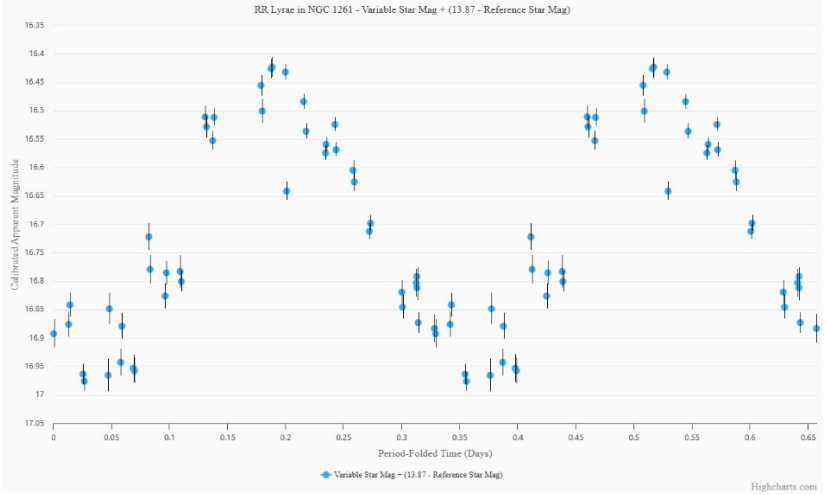

Figure 7. Period-folded RR Lyrae light curves

Table 2a. RR Lyrae Observational Properties

Target System	Variable Star ID	RA (J2000)	Dec (J2000)	⟨V⟩ (mag)	Period (days)	V Amplitude (mag)
NGC 1261	RRL-1	03:12:15.4	−55:12:58	16.70	0.331	0.95
M3	RRL-12	13:42:11.6	+28:22:38	15.65	0.553	0.78
M15	RRL-7	21:29:59.1	+12:10:05	15.90	0.642	1.10
M53	RRL-4	13:12:55.8	+18:10:09	16.95	0.487	0.65
M92	RRL-3	17:17:07.2	+43:08:12	15.20	0.529	0.72
Sculptor dSph	RRL-2	01:00:09.4	−33:42:31	20.10	0.587	0.68
Fornax dSph	RRL-5	02:40:02.3	−34:27:08	20.85	0.613	0.60
Carina dSph	RRL-9	06:41:36.5	−50:57:58	20.70	0.642	0.73

Table 2b. RR Lyrae Observational Coverage and Derived Distances

Target System	No. of Observations	Filters	Distance (kpc)	Distance Uncertainty (%)	Validation Dataset
NGC 1261	52	V	15.5	5.5	AAVSO
M3	61	V	10.4	6.0	AAVSO
M15	58	V	10.8	7.0	AAVSO
M53	49	V	18.3	8.0	AAVSO
M92	55	V	8.3	5.0	AAVSO
Sculptor dSph	45	V	86.0	10.0	AAVSO
Fornax dSph	42	V	147.0	10.0	AAVSO
Carina dSph	39	V	105.0	10.0	AAVSO

Mean magnitudes ⟨V⟩ were derived from phase-folded light curves using extinction-corrected differential photometry. Periods were determined using Fourier analysis and phase dispersion minimization. Distances were calculated by assuming an RR Lyrae absolute magnitude of $M_V \approx 0.75$ mag. Distance uncertainties reflect combined photometric scatter, period uncertainty, and

intrinsic RR Lyrae luminosity dispersion. Validation against the AAVSO International Database confirms consistency with published results.

3.1.1 RR Lyrae Lab Observation Results

The period of the observed RR Lyrae star in NGC 1261 was determined from a period-folded light curve as P =0.329 days and from the Astromancer periodogram as P = 0.330 days. Both measurements are fully consistent with the expected period range for RR Lyrae variables (0.1–1 day; Samolyk 2015; AAVSO 2024), confirming the classification of the star as an RR Lyrae pulsator.

The star's average absolute magnitude was adopted as $M_V = 0.75$, in line with standard calibrations for RR Lyrae stars (Madore & Freedman 1991; Riess et al. 2016). The average apparent magnitude, measured as the midpoint between the light curve's peak and trough, was $m_V = 16.699 \pm 0.05$mag. Using the distance modulus relation of equation 5, the calculated distance to the star, and hence to the NGC 1261 globular cluster, is D= 15.29 kpc. This value is slightly lower than the reference distance of D = 16.4 kpc reported in NASA/IPAC and other IAU-supported databases (Harris 2010; NASA/IPAC 2025), resulting in a percent error of approximately 6.8%. This level of agreement is considered excellent for educational and citizen-science observations, demonstrating that the methodology reproduces reliable scientific measurements.

3.1.2 Sources of Uncertainty

The principal contributors to measurement uncertainty include:

1. **Apparent Magnitude Estimation:** Sampling the light curve may leave gaps near the maximum or minimum, especially when observations are limited in cadence, leading to uncertainty in the determination of the average apparent magnitude.
2. **Intrinsic Scatter in Absolute Magnitude:** While Mv= 0.75 is standard for RR Lyrae stars, individual stars can deviate slightly due to metallicity effects or evolutionary stage, introducing systematic uncertainty.

Minor contributors such as instrumental photometric error, period determination accuracy, and reference star extinction corrections were assessed and found to have negligible impact relative to the above uncertainties. Care was taken to select the correct variable and comparison stars, perform differential photometry accurately, and fold the light curve correctly, minimizing procedural errors.

3.2 Cepheid Observations

Classical Cepheids in the Large Magellanic Cloud (LMC), Small Magellanic Cloud (SMC), M31, and M33 displayed pulsation periods ranging from 1 to 100 days. Multi-band photometry in Johnson-Cousins and Sloan filters confirmed amplitude and color variations characteristic of fundamental mode pulsation. Periods were determined using Fourier analysis and period folding with

Astromancer and Afterglow, following the same methodology described in Section 3.1 for RR Lyrae stars, and the resulting measurements closely reproduce Leavitt's period-luminosity relation.

For example, Cepheid in NGC 6822, the derived period was P =66.7 days. Using the calibrated period-luminosity relation or Equation 4, the average absolute magnitude was calculated as Mv= -6.56. The corresponding average apparent magnitude, measured at the midpoint between the light curve's peak and trough, was $m_V = 17.0 \pm 0.05$mag. Applying the distance modulus relation or equation 5, yielded a distance of D = 515 kpc. This is in good agreement with published distances to NGC 6822, $D \approx 500$kpc (NASA/IPAC 2025; Riess et al. 2016), corresponding to a percent error of approximately 3%.

3.2.1. Sources of Uncertainty

The main contributors to uncertainty in Cepheid distance determination include:

1. Light Curve Sampling: Sparse observations can lead to imprecise determination of the average apparent magnitude, especially for long-period Cepheids.
2. Intrinsic Scatter in the Period-Luminosity Relation: Individual Cepheids may deviate slightly due to metallicity differences or evolutionary stage, producing systematic variation in M_V.

Minor contributors, such as photometric calibration errors, period estimation accuracy, and interstellar extinction corrections, were assessed and found to be secondary relative to the above factors. Careful selection of reference stars, proper differential photometry, and accurate period folding minimized procedural errors.

3.3 Summary of RR Lyrae and Cepheid Lab Examples

The derived periods, average magnitudes, and distances for both RR Lyrae stars (e.g., NGC 1261) and classical Cepheids in NGC 6822 are consistent with published values, validating the observational and data reduction procedures employed in this study. RR Lyrae results demonstrate the reliability of horizontal branch calibration for Galactic globular clusters, while Cepheid measurements confirm the robustness of Leavitt's period-luminosity relation as a standard candle for extragalactic distance determination.

These outcomes highlight the effectiveness of combining robotic telescope networks (Skynet University), online photometry tools (Afterglow, Astromancer), and archival datasets (AAVSO International Database) in facilitating authentic, scientifically rigorous observations. Participants were able to determine periods, calibrate magnitudes, construct light curves, and derive distances while adhering to community-accepted photometric standards. Integration with the AAVSO database further enabled data validation, reproducibility, and contribution to a global citizen-science effort.

Overall, the lab examples illustrate how structured curricula, supported by advanced observing networks and online analysis tools, can provide learners with a seamless, hands-on research experience that bridges education and professional astronomical practice.

3.4 Educational Outcomes

Over 200 participants completed the enhanced curriculum over two years. Assessment data indicated:

1. 35–50% improvement in understanding of stellar variability
2. Increased proficiency in telescope operation, photometry, and period analysis
3. Enhanced competence in data interpretation, error estimation, and scientific communication

Participants reported increased confidence, motivation, and interest in STEM or STEAM fields.

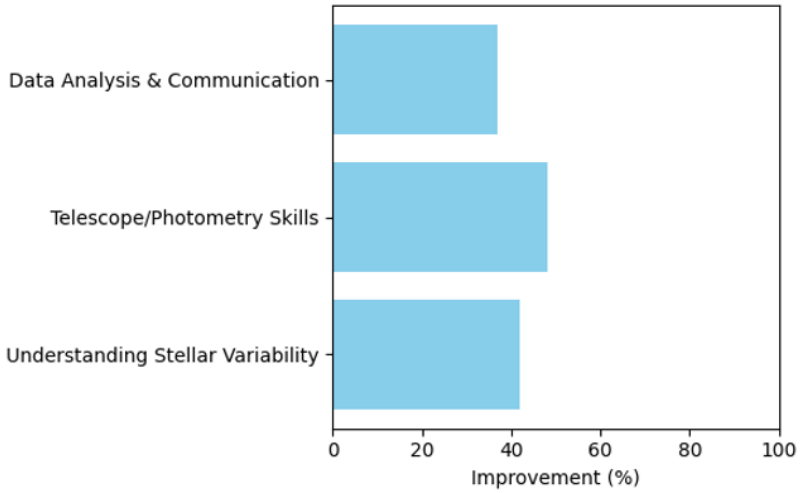

Figure 8. Educational assessment results

3.5 Public Engagement Outcomes

Public outreach activities reached approximately 500 participants. Survey responses indicated:

- 92% reported improved understanding of variable stars
- 87% valued the integration of historical and cultural content
- 78% expressed interest in further astronomy learning

These outcomes demonstrate the effectiveness of combining scientific rigor with historical, cultural, and inclusive engagement strategies.

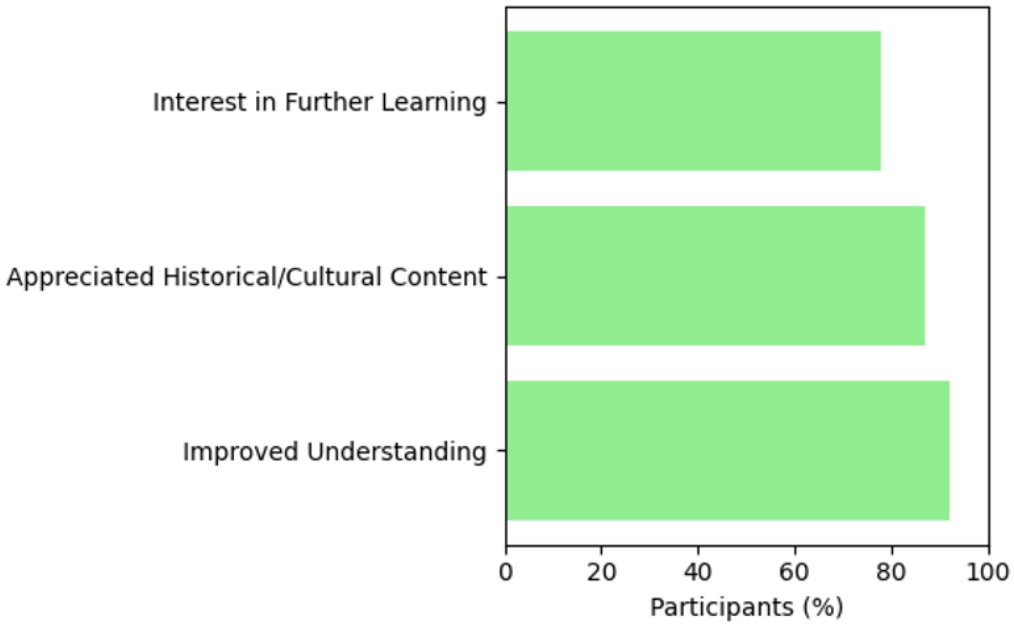

Figure 9. Survey and demographic results

4. Conclusions and Future Directions

This study demonstrates that RR Lyrae and Cepheid variable stars serve as precise tools for measuring cosmic distances and as effective instruments for education and public engagement. Observations via Skynet University, combined with Afterglow and Astromancer, produced high-quality light curves and distance estimates consistent with published values. RR Lyrae stars traced distances within globular clusters and dwarf galaxies, while Cepheids extended the cosmic distance ladder to Local Group galaxies.

Integrating historical and cultural context, including the contributions of Leavitt, Cannon, Maury, and Payne-Gaposchkin, enriched the educational experience and promoted inclusive participation. Students and community participants developed technical proficiency in telescope operation, photometry, and period analysis while gaining appreciation for the human and cultural dimensions of astronomy.

Key outcomes include:

- **Scientific Validation:** High-fidelity photometry and period analysis produced distances consistent with established results.
- **Educational Gains:** Learners improved observational skills, data analysis, scientific reasoning, and communication.
- **Community Engagement:** Public outreach broadened access to authentic research experiences.
- **Inclusive Participation:** Narratives of historically underrepresented contributors fostered belonging and inspiration.

Future directions include expanding to additional variable star types, multi-wavelength photometry, remote observing networks, computational modeling, and international collaboration, continuing to advance both science and education while cultivating scientifically literate citizens.

Acknowledgements

I gratefully acknowledge the AAVSO International Database for providing essential observational data. We thank the Skynet University network and the University of North Carolina at Chapel Hill, particularly Professor Dan Reichart, for their support in telescope access and curriculum development. I also wish to recognize John Taylor, Physics and Astronomy teacher at Marvin Ridge High School, for his guidance and invaluable support in student engagement, research, and public outreach. Historical inspiration from Henrietta Swan Leavitt, Annie Jump Cannon, Antonia Maury, and Cecilia Payne-Gaposchkin is gratefully acknowledged for their foundational contributions to variable star and modern astronomy research.

References

American Association of Variable Star Observers (AAVSO). 2024, *The AAVSO International Database: Variable Star Observations and Research Tools*, AAVSO, Cambridge, MA.

Aveni, A. F. 2001, *Skywatchers: A Revised and Updated Version of Skywatchers of Ancient Mexico*, Univ. of Texas Press, Austin.

Belmonte, J. A., et al. 2020, *Archaeoastronomy and Cultural Astronomy: Proceedings of the International Conference on Archaeoastronomy*, Springer, Cham.

Cadmus, R. R., Jr. 2014, "Long-Term Photometric and Spectroscopic Monitoring of Semiregular Variable Stars," *J. AAVSO*, prepub. No. 293.

Chapman, A. 1990, *Ancient Astronomy*, Routledge, London.

Goodricke, J. 1783, "Observations of the Variable Star Algol," *Philos. Trans. R. Soc. Lond.*, 73, 474.

Harris, W. E. 2010, "A Catalog of Parameters for Globular Clusters in the Milky Way," *Astronomical Journal*, 112, 1487.

Hubble, E. 1925, "Cepheids in Spiral Nebulae," *ApJ*, 62, 409.

IAU Office for Astronomy Outreach (OAO). 2025, *Women and Girls in Astronomy*, International Astronomical Union.

Kanas, N. 2007, *Star Maps and Astronomy in Ancient Cultures*, Springer, Berlin.

Krupp, E. C. 2000, *Echoes of the Ancient Skies: The Astronomy of Lost Civilizations*, Dover, New York.

Leavitt, H. S. 1908, "1777 Variables in the Magellanic Clouds," *Ann. Harvard Coll. Obs.*, 60, 87–108.

Madore, B. F., & Freedman, W. L. 1991, "The Cepheid Distance Scale," *PASP*, 103, 933–957.

NASA/IPAC Extragalactic Database. 2025, *NGC 1261 Distance Data*.

NASA/IPAC Extragalactic Database. 2025, *NGC 6822 Distance Data*.

Reichart, D. E. 2008–2025, *Our Place in Space! (OPIS) Curriculum*, Univ. of North Carolina at Chapel Hill.

Reichart, D. E., et al. 2018, "Skynet: A Global Robotic Telescope Network for Research and Education," *Bull. Am. Astron. Soc.*, 50, 423.

Riess, A. G., Macri, L., Casertano, S., et al. 2016, "A 2.4% Determination of the Local Value of the Hubble Constant," *ApJ*, 826, 56.

Samolyk, G. 2015, "Recent Maxima of 67 Short-Period Pulsating Stars," *J. AAVSO*, prepub. No. 294.

Streamer, M., Byron, J., Moriarty, D. J. W., et al. 2014, "Revised Light Elements of 78 Southern Eclipsing Binary Systems," *J. AAVSO*, prepub. No. 292.

Templeton, M. R., et al. 2017, "Scientific Use of the AAVSO International Database," *J. AAVSO*, 45, 1.

A Study of Unusual Behaviors in a Sample of Pulsating Red Giants

John R. Percy, Malaika Malik, and Ana Florella Pago

Department of Astronomy & Astrophysics, University of Toronto, 50 St. George Street, Toronto ON M5S 3H4, Canada; john.percy@utoronto.ca

Subject Keywords

AAVSO International Database; Photometry, Time-Series Analysis, Long-Period Variables

Abstract

Pulsating red giants (PRGs) display a wide range of non-periodic behaviors, including slightly wandering periods, variable amplitudes and, in about a third of them, long secondary periods which are believed to be due to eclipses by a dust-enshrouded companion. In this paper, we analyze 54 PRGs in the AAVSO LPV observing program – the so-called Percy List on the long-period variables (LPV) Observing Section website – plus a handful of other stars from the literature which display unusual or extreme behavior.

We used light curve analysis, and the Fourier and wavelet routines available in the AAVSO's VSTAR time-series analysis software package. We call attention to spurious long period variability which can arise in stars with periods near one year.

Based on preliminary analysis, we divided the stars into two groups: about a third which show primarily unusually large or complicated amplitude variability, and about two-thirds which show other unusual or extreme behaviors. The latter group's behaviors include: large, rapid period changes, presumably due to evolution; multiple pulsation modes and/or mode-switching; non-sinusoidal light curves; very slow, cyclic variability of unknown nature and cause; long-period eclipse-like variability (as in V Hya); significant changes in mean magnitude (as in L2 Pup); and "nature and cause unknown".

The study of the 19 stars in the former group, with notable amplitude variability, focused on the possible causes of the variability, which are poorly understood. We built on a similar study by Kiss *et al.* (2000 A&AS, 145, 283), who used a similar approach, but with a smaller sample and a shorter database. They proposed four possible causes: changes in the type or mode of variability; amplitude modulation due to beating; interaction between pulsation and rotation; and repetitive switches in pulsation mode. In our sample, we find 1 star with beating and mode-switching; 9 with beating only; 2 with rotation and pulsation, but no beating; 3 with pulsation and rotation, and also beating; 1 with all three; and 2 which may not fit any of the proposed causes. Given the large random convective cells in the outer layers of the stars, and the stars' pulsation and rotation, this mixture of results is not unexpected.

Our results emphasize the complexity of the variability, and the need to continue the systematic, sustained observation of this group of stars. There is still much that we do not know about these stars, and about LPVs in general. As always, observation and analysis of their complex variability may help.

1. Introduction

Note: an extended presentation of the content of this paper, including more notes, figures, tables, and discussion can be found published in the Journal of the AAVSO (Percy and Malik 2025; Percy and Pago 2025). These articles are freely available on the AAVSO website. We provide a summary here.

Red giants vary in brightness in many and complex ways. They pulsate, and the pulsation period "wanders" by a few percent, probably due to large random convection cells in the outer layers of the star. The pulsation amplitude can vary by up to a factor of ten; see below for a discussion. In at least a third of these stars, there is a "long secondary period" (LSP), five to ten times the pulsation period. Soszynski et al. (2021) make a strong case that it is due to eclipses by a dust-enshrouded low-mass companion. See Percy and Zhitkova (2023) for the results of analysis of AAVSO observations of a large number of LPVs in the AAVSO Binocular Observing Program.

There are stars whose variability is even more interesting and/or unusual and/or extreme. One of us (JRP) compiled a list ("the Percy list") of about 50 such stars. It is posted on the website of the AAVSO Long-Period Variable (LPV) Observing Program, to provide guidance to observers as to which stars were most deserving of observation. The purpose of the present project was to examine the behavior of these stars in more detail.

The project was divided into two parts: (1) a study of 37 stars whose behavior appeared to be most unusual (Percy and Malik 2025, in press), and (2) the rest: primarily stars with large and/or unusual amplitude variability (Percy and Pago 2025). The division of the stars was based on a preliminary analysis, but the division of stars between the two groups was somewhat fuzzy. In the second project, the emphasis was on clarifying the cause of the amplitude variability.

In an important paper, Kiss et al. (2000) provided the first comprehensive study of amplitude variability. Our work builds on theirs. They identified and discussed four possible mechanisms: (1) Changing type of variability (e.g. Y Per), such as a sudden switch in pulsation mode. (2) Beating between two or more close modes which interact. (3) Interaction between pulsation and rotation of the star. (4) Repetitive mode changes.

2. Data and Analysis

We used visual and Johnson V observations from the AAVSO International Database to study the variability of these stars. Light curve, phase curve, Fourier and wavelet analysis were done using the AAVSO time-series analysis package VSTAR (Benn 2012). We emphasize the importance of

inspecting the light curve of the star before doing time-series analysis. Note that the amplitudes given in this paper are actually semi-amplitudes as given by VSTAR.

Virtually all the stars had seasonal gaps in the data, when the sun was in the same general part of the sky as the star. In Fourier analysis of the data, using VSTAR or the like, the gaps produce spurious or "alias" peaks in the spectra, at frequencies separated from the true frequency by N/365.25 where N is a small integer; the strongest is at N = 1.

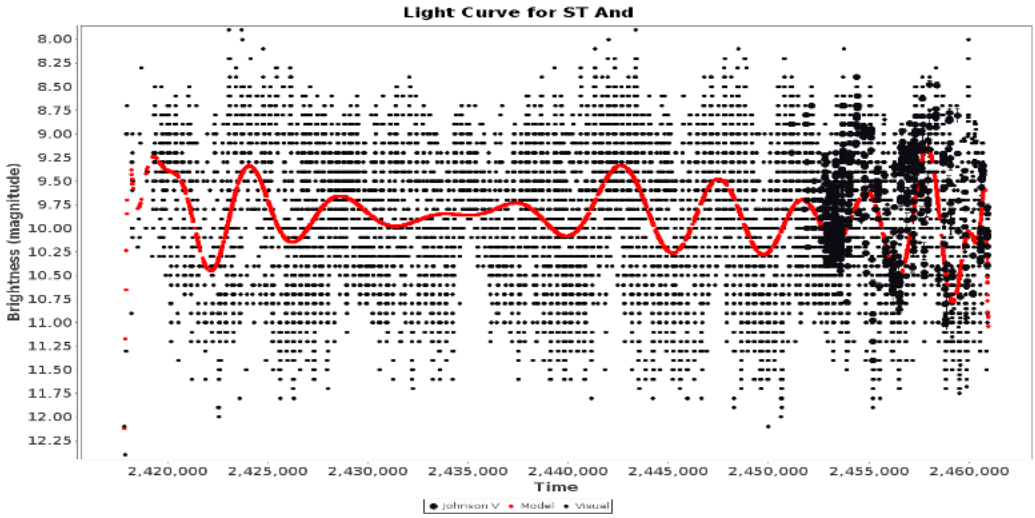

Figure 1. The long-term visual light curve of ST And. There is a cyclic variation in mean magnitude with a time scale of about 2750 days. It is spurious – the result of the long-period alias (LPA) effect, which occurs in stars with pulsation periods close to a year when there are seasonal gaps in the data. The solid red curve is a high-order polynomial fit.

Many LPVs have pulsation periods close to a year. When this is the case, the seasonal gaps migrate slowly along the light curve, producing a very long spurious period. It is, in fact, the low-frequency alias (LFA) of the pulsation period, at a frequency close to zero. This effect is not strictly periodic, because of the random "meandering" of the pulsation period. Figure 1 shows the light curve of ST And, with a pulsation period of 326.6 days. The red curve is a polynomial fit to the data, and the variability is almost all spurious. If the pulsation period is exactly one year, the seasonal gaps will always fall on the same part of the light curve, and that part will never be observed. We urge observers to observe these stars throughout their observable period.

3. Results

Aside from the stars whose slow variations are spurious, and due to the long-period alias effect, the following are the types of unusual behavior that we have identified, and some examples of each:

- Large, rapid, continuous changes in period, likely due to evolution (Templeton et al. 2005, Merchan-Benitez et al. 2023); examples R Aql, R Cen, LX Cyg, Z Tau, T UMi (Figure 2), RU Vul.
- Presence of two or more pulsation periods, in most cases with variable amplitudes, resulting in some cases in apparent period "switches"; examples: Z Aur, RZ Cyg, R Dor.
- Non-sinusoidal phase curves, which produce harmonics in the Fourier spectrum; examples: R Cnc, SV Cas, R Nor.
- Slow, quasi-sinusoidal variations in mean magnitude, not due to the LPA effect; examples: S Aur, S Cep, RU Vir.
- Deep, periodic, eclipse-like minima in the light curve; example: V Hya – a complex system, in which the red giant has one or more companions.
- Decrease or increase in mean magnitude of several magnitudes; example: L2 Pup, with a decrease of 3 magnitudes.
- Unusually large period "wandering" and/or amplitude variation; example W Tau.
- Unknown nature and/or cause, sometimes because of inadequate data; examples: V Boo, RY Leo, S Lyr.

In the second part of this project, we looked specifically at the variation in the pulsation amplitude and compared it to that predicted by each of Kiss et al.'s (2000) proposed mechanisms. We also looked carefully at the amplitude-time graphs for each star. These ranged from ones showing a slow, steady increase or decrease in amplitude, to ones showing more rapid, quasi-periodic increases and decreases which may be due to beating. The former may be stars with cyclic increases and decreases, but on a longer scale – longer than the extent of the observations.

Indeed, most of the stars in our sample (14 out of 19) showed evidence of beating, either on its own (9 stars) or in combination with one of the other proposed mechanisms. None of the stars showed an amplitude variation due to an abrupt transition from one variability type to another, as Y Per did. For at least two of the stars, the mechanism(s) is uncertain.

A few of the stars in our sample underwent a form of mode-switching (Figure 3). This occurred because there were two modes present, usually the fundamental and first overtone, both with variable amplitude. They do not actually appear and disappear. One mode may have a larger amplitude than the other. Then the amplitudes slowly vary, so that the other mode then has the larger amplitude. The process of "period switching" is slow, rather than abrupt.

We find evidence of beating in the fine structure of the pulsation peaks in the Fourier spectrum (Figure 4), which may represent different closely spaced modes. We also find evidence of beating in the amplitude-time diagram, which shows evidence of cyclic increases and decreases which are typical of beating (Figure 5). These closely spaced modes may arise from the non-spherical shape of the outer layers of the star, which results from the large, random convection cells.

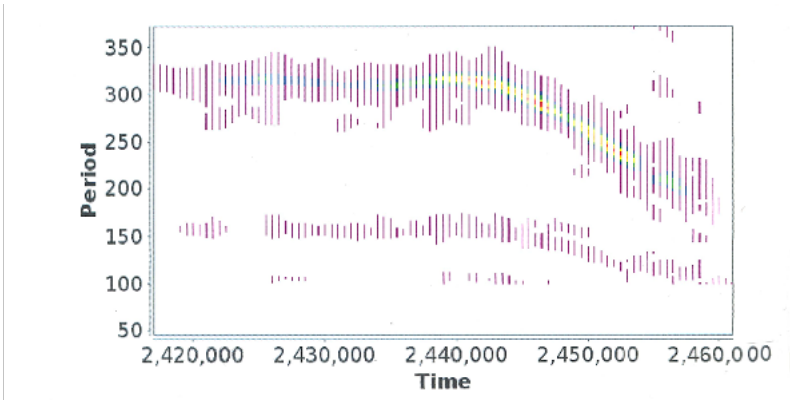

Figure 2. The visual wavelet contour diagram for T UMi, showing the period in days as a function of Julian Date, with the amplitude given by the contours. The dominant (shorter) period has decreased from 160 to 120 days, while the amplitude has decreased from 1.8 to 0.1 magnitude; the 312-day period has decreased substantially, also.

4. Discussion

For a discussion of the evolutionary origin of large, rapid, sustained period changes in LPVs, and lists of stars showing such changes, see Templeton et al. (2005) and Merchan-Benitez et al. (2023). Both studied the period changes in over 500 stars.

As for multiperiodicity in LPVs, Kiss et al. (1999) have used AAVSO data to identify 44 stars which are bi-periodic, 12 which are tri-periodic (including an LSP); 29 were monoperiodic. The amplitudes of the modes are invariably variable (Kiss et al. 2000, Percy and Abachi 2013, Percy and Pago 2025, in press). The existence of large, bright, *random* convection cells in the outer layers of red giants is sure to introduce irregularity in the variability of the star.

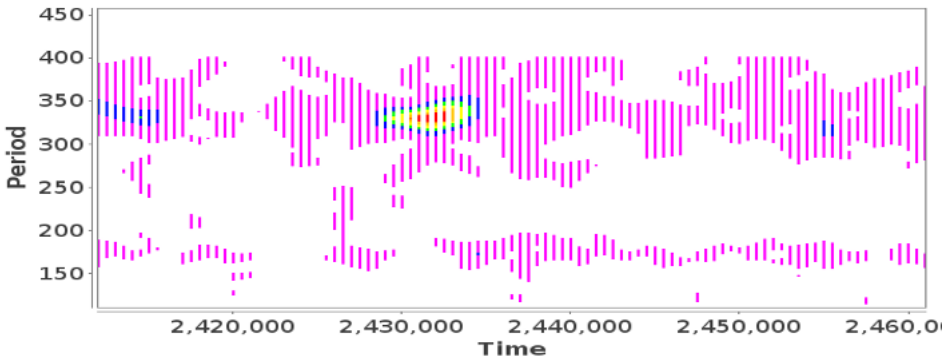

Figure 3. A contour plot of the amplitude of R Dor as a function of time and period; the contours show a measure of the amplitude. Both the longer (fundamental) and the shorter (first overtone) periods vary in amplitude and undergo apparent period "switches".

Red giant stars have winds; the more luminous the star, the stronger the wind. Because of the large, random convection cells, the winds will be stronger in some directions than in others.

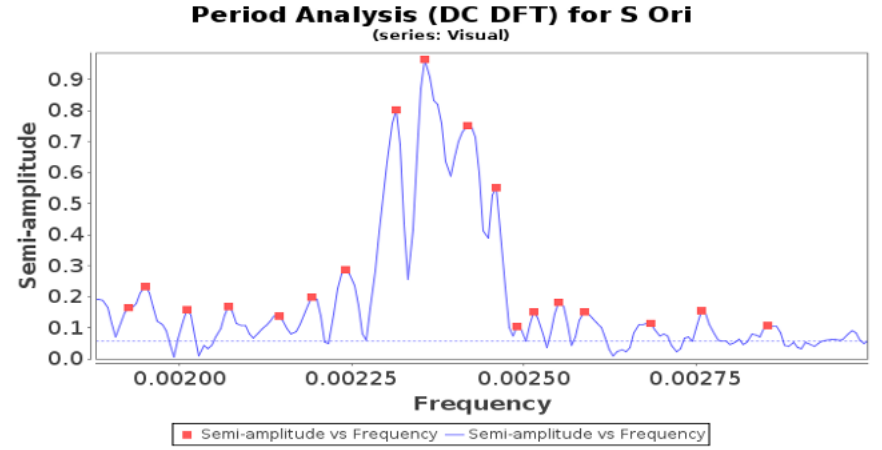

Figure 4. The fine structure of the peak, in frequency space of the 424-day period in the Fourier spectrum of S Ori. The fine structure may be due to closely spaced modes which then undergo beating.

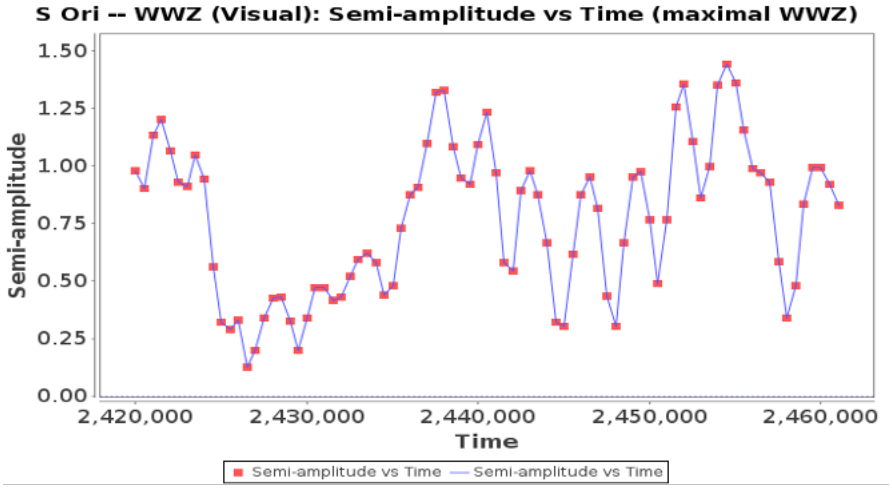

Figure 5. The amplitude of S Ori as a function of time, for the period range 205 to 225 days, encompassing the first overtone period of 214 days. The amplitude rises and falls in a quasi-periodic way, typical of beating.

Binarity is a factor in LSPs and appears to be in rare stars such as V Hya, which shows deep periodic minima. In the case of LSPs, the mechanism proposed by Soszynski et al. (2021) suggests that the dust-enshrouded companion was originally a planet which gained mass from the LPV to become a brown dwarf or low-mass star. Recent research on exoplanets is consistent with their existence around many red giant stars. In our own solar system, the Sun will eventually become a red giant, and the gas giants should survive as its planets.

Finally: we note that co-authors Malik and Pago are talented undergraduate students in our astronomy and physics program. In this project, they have developed and integrated their science, math, and computing skills by doing real science, with real data – your data!

5. Conclusions

Our work confirms that the types of variability in LPVs are many and complex, and generally not well understood. For this reason, we recommend that observers continue to concentrate on these stars on "the Percy list" for the foreseeable future. The longer the time span of the observations (it's typically almost a century now), the more likely it is that we can find explanations for their behavior – especially because most of the variability occurs on a long timescale. AAVSO observers play a unique role in this respect. We also hope that theoreticians will use the AAVSO data, as Kiss et al. (2000) did, to model the behavior to help us understand the causes of the behavior.

Acknowledgements

We acknowledge with thanks the variable star observations from the AAVSO International Database contributed by observers worldwide and used in this research. We also thank the headquarters staff, and those who have created and maintained VSTAR and made it publicly available. Our project was supported by the University of Toronto Work-Study Program, and the Dunlap Institute, which is funded by an endowment established by the David Dunlap Family and by the University of Toronto.

References

AAVSO. 2025, observations from the AAVSO International Database (http://www.aavso.org).

Benn, D. 2102, *J. Amer. Assoc. Var. Star Obs.,* **40**, 852.

Kiss, L.L. et al. 1999, *Astron. Astrophys.*, **346**, 542.

Kiss, L.L. et al. 2000, *Astron. Astrophys. Suppl.*, **145,** 283.

Merchan-Benitez, P. et al. 2023, *Astron. Astrophys.,* **672A**, 165.

Percy, J.R. and Abachi, R. 2013, *J. Amer. Assoc. Var. Star Obs.*, **41**, 193.

Percy, J.R. and Zhitkova, S. 2023, *J. Amer. Assoc. Var. Star Obs.,* **51***, 230.*

Percy, J.R. and Malik, M. 2025, *J. Amer. Assoc. Var. Star Obs.*, **53**, 109

Percy, J.R. and Pago, A.F. 2025, *J. Amer. Assoc. Var. Star Obs.*, **53**, 150

Soszynski, I. et al. 2021*, Astrophys. J. Lett.*, **911,** L22.

Templeton, M. et al. 2005, *Astron. J.*, **130**, 776.

First Light of the Whoppshel Spectrograph on the USAFA One-Meter Telescope

Benjamin D. Roth, Scott Donnell, Zion D. Porter, Timothy Giblin, and Francis Chun

United States Air Force Academy, 2345 Fairchild Dr, Air Force Academy, CO 80840, USA;
donnellsp@gmail.com, benjamin.roth@afacademy.af.edu, C26Zion.Porter@afacademy.af.edu, Timothy.Giblin.CTR@afacademy.af.edu, Francis.Chun@afacademy.af.edu

Subject Keywords

Echelle, Whoppshel, Spectrograph, Spectroscope, Spectroscopy

Abstract

The integration of the Shelyak Whoppshel Spectrograph with the United States Air Force Academy's one-meter Ritchey Chrétien f/6.76 optical telescope greatly advances both stellar and satellite spectroscopy capabilities at the United States Air Force Academy (USAFA) Observatory. This expanded capability will strengthen the Academy's role in various astronomical research fields including the high-resolution spectroscopic monitoring of satellites, stars, and exoplanets, while bolstering cadet education in general space situational awareness.

The integration process consisted of designing and fabricating the telescope spectrograph physical interface to maximize light delivery into the Fiber Injection and Guiding Unit (FIGU). The FIGU collects light at the telescope focal plane and feeds it through a fiber optic cable to the spectrograph. A major operational challenge is maintaining connectivity of the main camera, guide camera, and FIGU to enable simultaneous operations. The Whoppshel FIGU is physically integrated onto one of the two telescope guide star camera ports preserving the large format science camera at the primary focal plane. A focal reducer placed before the FIGU decreases the effective focal length, expanding the field of view for efficient target acquisition and centering. Alignment and field-of-view tests ensured that light was consistently directed into the FIGU which allowed for successful Whoppshel integration. We validated our system's performance by evaluating the spectra of well-known stars Deneb and Vega.

The USAFA one-meter telescope currently uses transmission grating filters at a spectral resolving power of $R \approx 200$. The Whoppshel provides more than 100 times the spectral resolution with a resolving power of $R \approx 30000$. The spectrograph increases observational capabilities to allow for high precision radial velocity measurements, chemical abundance studies of stars and exoplanets, and high-resolution monitoring of both stars and satellites. The addition of this high-resolution spectrograph brings USAFA's astronomical capabilities to the state-of-the-art, which will enable collaboration with premier organizations. Looking forward, the Whoppshel's enhanced resolution will enable cadets and faculty to carry out projects ranging from detailed stellar classification to satellite spectroscopy.

1. Introduction

Only a handful of observatories around the world have successfully integrated the Whoppshel Spectrograph with a one-meter telescope, making this setup at the United States Air Force Academy unique and cutting edge (Garde 2023; Yorulmaz et al. 2025; Matthews et al. 2023). The legacy spectroscopic capabilities at the United States Air Force Academy primarily rely on transmission grating filters installed in the telescope's filter wheel that provide a spectral resolving power of $R \approx 200$. The spectral resolving power is defined as

$$R = \frac{\lambda}{\Delta\lambda} \qquad (1)$$

where λ is the wavelength and $\Delta\lambda$ is the wavelength width of a spectral line often defined as the full-width-half-max (FWHM). Although transmission grating filters provide spectra across the visible range, their R value limits the ability to resolve closely spaced spectral lines. The Whoppshel spectrograph, however, provides users with a spectral resolving power of $R \approx 30000$ while also covering a wavelength range of 3900 Å to 7600 Å. The combination of high resolution and broad wavelength coverage in the visible spectrum opens the door to more precise spectroscopy than previously capable with transmission gratings at the USAFA Observatory.

The Whoppshel spectrograph is produced by Shelyak Instruments and is built around two optical components, an echelle reflection grating and a series of prisms (Garde 2019). The echelle grating maximizes dispersion and spectral range with a high incidence angle, high blaze angle ($63° 26"$), and typical echelle groove spacing (31.6 g/mm) (Palmer 2020). Figure 1 shows the diffraction geometry for a reflection grating where the grating obeys the grating equation

$$m\lambda = d(sin\alpha + sin\beta) \qquad (2)$$

where m is the diffraction order, d is the groove spacing, and α and β represent the incident and reflection angles respectively.

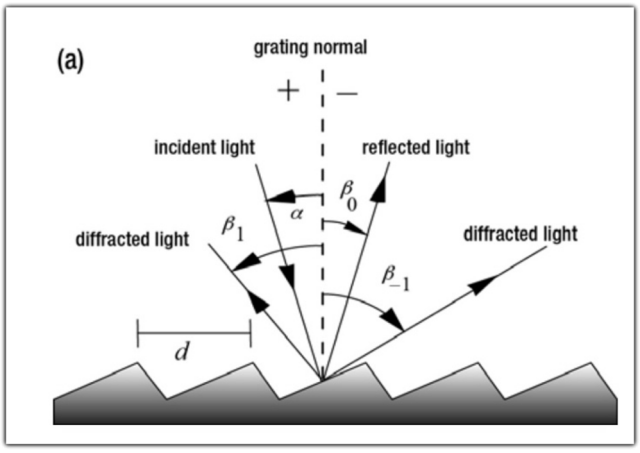

Figure 1. Diffraction Geometry for a Reflection Grating. The subscripts on the diffraction angle, β represent the diffraction order. Image from Diffraction Grating Handbook (Palmer 2020).

Echelle gratings operate in a near-Littrow configuration where the incident angle striking the grating is equal to the diffraction angle for the target wavelength. The grating equation then reduces to

$$m\lambda = 2dsin\theta \qquad (3)$$

where θ is the incident and reflection angle. Rearranging the formula and solving for the central blaze angle where peak efficiency occurs for each diffraction order gives

$$\lambda_b = \frac{2d}{m} sin\theta_b \qquad (4)$$

where $\lambda_b$is the blaze wavelength and θ_b is the blaze angle, satisfying the max efficiency condition (Palmer 2020). While the echelle grating disperses each spectral order, these orders remain physically overlapped. The second optical component, the series of prisms, provides cross dispersion vertically separating each order as seen in the left image of Figure 2. A spectrum from the transmission grating in the one-meter's filter wheel is also shown in the right image of Figure 2 for comparison. The Whoppshel produces a cross-dispersed compilation of many narrow, high-dispersion orders across the detector, each covering a small wavelength range at high resolving power. The transmission grating produces a single, continuous first-order spectrum at much lower resolution.

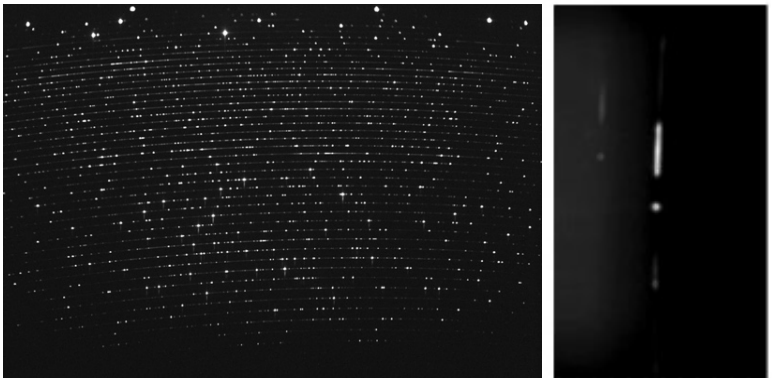

Figure 2. Whoppshel spectrum image (left) vs. transmission grating spectrum image (right). The left image displays the light as collected by the Whoppshel camera. Each horizontal row represents a different spectral order, orders ~42-87. The right image is the light captured by the 200 g/mm transmission grating, the first-order spectrum shown as a vertical line above the zero-order spot.

Light makes its way to the Whoppshel from the telescope through a fiber optic cable attached to the Fiber Injection and Guiding Unit (FIGU). This fiber is then coupled into the Whoppshel through a fiber connector and afocal optics. Figure 3 shows the light's path through the Whoppshel and into the camera. Once entering the Whoppshel housing, it is collimated and directed toward the input mirror. This mirror reflects the beam through one of two Takahashi FSQ-106 telescopes, which focuses the light onto the reflection grating (Garde 2019). The grating spreads the incident

light, producing a dispersed spectrum of overlapping orders and is directed back through both telescopes. The beam then passes through a set of cross-dispersing prisms, which vertically separate the spectral orders. The dispersed and cross-dispersed light is finally reimaged by the objective lens onto the CCD camera.

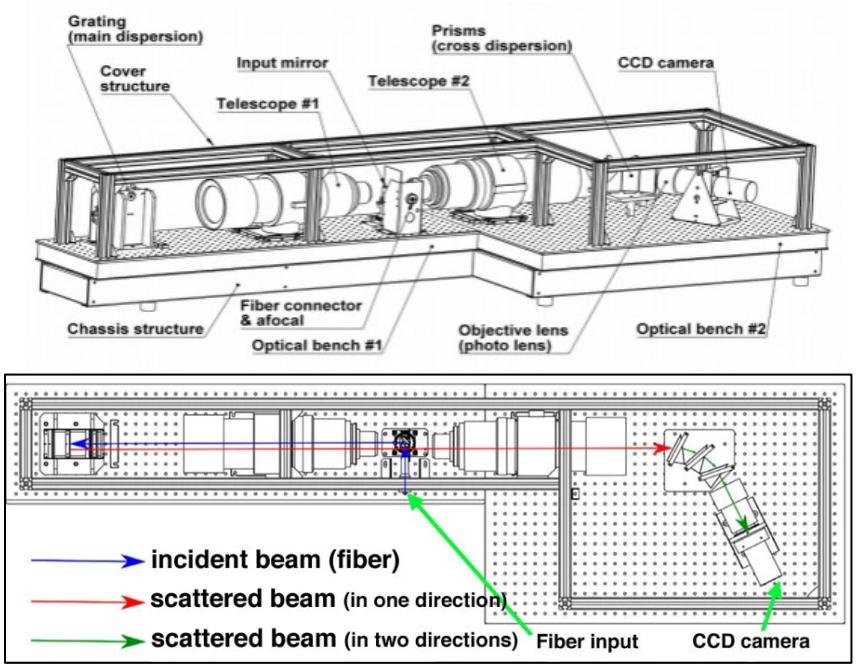

Figure 3. These diagrams illustrate the optical layout of the Whoppshel spectrograph (top), and the light path through the system (bottom). Light is collected by the telescope, enters through the fiber, collimated, dispersed by the transmission grating, cross dispersed by the prisms and recorded by the CCD camera. Images from "The Whoppshel, a high resolution echelle spectroscope" (Garde 2019).

2. Instrumentation

The spectroscope was integrated into the USAFA one-meter system in an unconventional manner making use of one of two guide camera ports on the filter wheel designed and fabricated by ACE Instruments. Integrating the FIGU into one of the guide camera ports allows for operations of the main science camera (Spectral Instruments 1110s E2V) at the primary focal plane to continue without having to swap instruments ("1110S CCD Camera Data Sheet" 2019). Nominally, the FIGU collects light at the telescope focal plane, however, the guide port contains a pickoff mirror and a 40 mm focal length Hastings triplet collimating lens that is focused by a second 40 mm focal length lens in front of the guide camera (ACE Instruments 2019). Once light enters the FIGU it is focused on the fiber optic cable that then takes light to the spectrograph. Figure 4 below displays the location of the FIGU on the backend of the telescope and the fiber from the FIGU entering the Whoppshel.

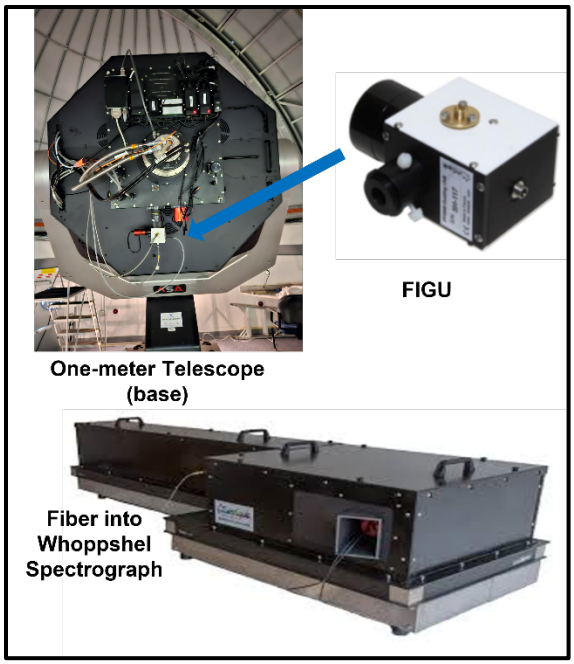

Figure 4. The FIGU integration location on the telescope base is shown in the top image with a zoomed image of the FIGU. The lower image displays the Whoppshel indicating the location the fiber enters the instrument.

The integration process also consisted of designing an optical interface into the FIGU as the original 40 mm Hastings lens focal length was too short for the back focus of the FIGU. An 85 mm focal length focal reducer lens was incorporated to allow focus onto the fiber within the FIGU as shown in the diagram of Figure 5. A 40mm relay lens is native to the system, which creates an effective focal length of infinity. Another focal reduction lens is required to back focus the light from the primary plane to the FIGU, so that it can then be guided into the fiber optic cable.

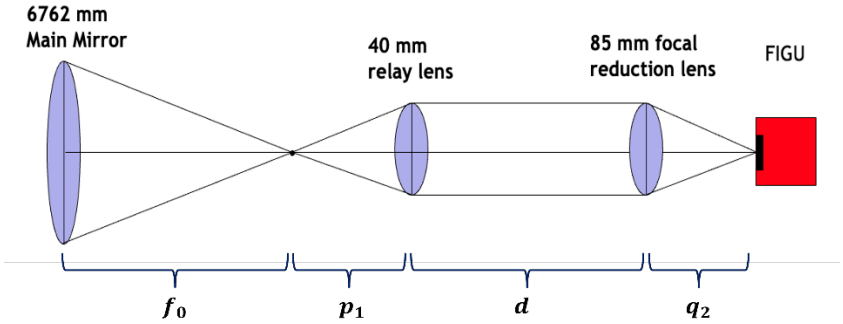

Figure 5. Schematic of the current optical relay into the FIGU. The 40 mm relay lens images light from the 6762 mm focal length, f_0, primary mirror with an object distance of p_1 resulting in a near infinite image distance. The 85 mm focal-reduction lens at distance d from the first lens then focuses the light into the FIGU at image distance q_2.

An important term to understand when designing an optical system to couple star light into an optical fiber is the star image diameter to fiber image diameter ratio, γ. This can be found using thin lens equations to determine the magnification and image scale of the system. We start by

finding the image distance, q_1 from the first lens

$$q_1 = \left(\frac{1}{f_1} - \frac{1}{p_1}\right)^{-1} \qquad (5)$$

Where f_1 is the 40 mm lens focal length, and p_1 is the object distance, the distance from the lens to the primary mirror focus. Note that a small offset from the 40 mm distance is used for p_1 to prevent divide by zero errors. The magnification M_1 from the first lens is then

$$M_1 = -\frac{q_1}{p_1} \qquad (6)$$

Now that we know q_1, the object distance, p_2 for the 85 mm lens is just $-q_1 + d$, where d is the distance between the lenses. The image distance q_2 of the 85 mm lens can now be found along with its magnification M_2 in the same manner as q_1 and M_2. The total magnification of the system, M now is just the product of M_1 and M_2

$$M = (M_1)(M_2). \qquad (7)$$

The diameter of the fiber, α_{fiber} can now be calculated in arcsec

$$\alpha_{fiber} = D_{fiber} \frac{S_0}{M} \left(\frac{1\text{ mm}}{1000\ \mu\text{m}}\right) \text{[arcsec]} \qquad (8)$$

where D_{fiber} is the fiber diameter in μm and S_0 is the native image scale for the main camera. The term $\frac{S_0}{M}$ is then the image scale. The star to fiber diameter ratio is now simply

$$\gamma = \frac{\alpha_{star}}{\alpha_{fiber}} \qquad (9)$$

where α_{star} is the typical star Point Spread Function (PSF) Full-Width-Half-Max (FWHM). The typical seeing FWHM at the USAFA observatory is about two arcseconds. The current optical configuration results in an approximate γ value of 2.8. We recognize that for efficient light collection a value close to one is desirable. Future work will reconfigure the optical system to achieve a better γ ratio.

3. Procedures

We obtained spectra of Vega and Deneb, both of which are commonly analyzed bright stars. Though both stars are well studied, Deneb, is known to show slight variability in its brightness and radial velocity (Richardson 2006). Image acquisition and guiding were carried out using SI Image, Sequence, and PHD2 software (Spectral Instruments 2016; Puchner, M 2019; Stark et al. 2023). We utilize three different cameras with their own respective field-of-view. The main camera is operated by using SI image software which is used for initial capture and identification.

Once the target is centered in the main camera, an offset is applied to center the star into the FIGU camera. PHD2 is used for both the FIGU camera and the remaining guiding camera. Fine guiding controls in PHD2 allows for precise placement of the target star over the fiber as viewed in the FIGU camera. Stable tracking is achieved with PHD2 on the telescopes guide camera. A top-level system architecture diagram is shown in Figure 6 that helps visualize the software and hardware component connections for spectra collection.

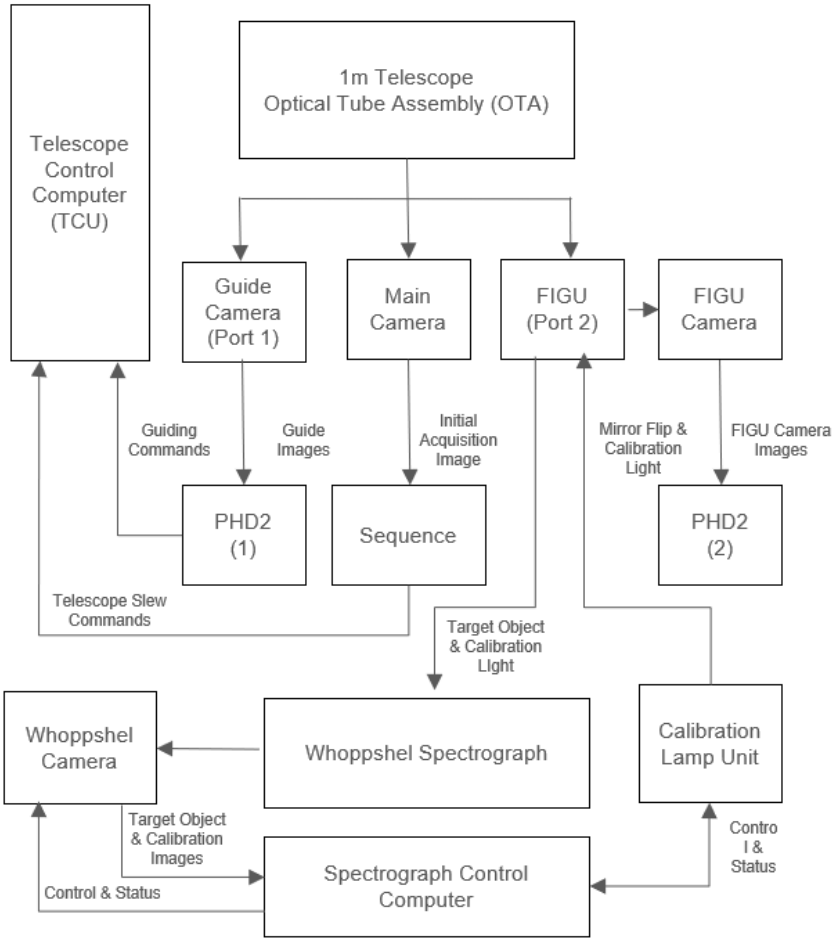

Figure 6. System architecture for the USAFA Whoppshel spectrograph and integration to the one-meter system. Light collected by the OTA is focused onto the main camera and into two guide ports, one which is used for mount control guiding and the second has the Whoppshel FIGU. Note that the light from the spectra calibration lamp unit makes its way to the Whoppshel by first going to the FIGU and then to the Whoppshel via fiber.

Spectral data collection and reduction are then performed using Demetra software produced by Shelyak Instruments (Shelyak Instruments 2025). Each observing sequence includes a set of bias and dark frames to remove electronic and thermal noise, flat frames from calibration lamps to correct for sensitivity variations, and calibration spectra from Th-Ar lamps for wavelength calibration. Multiple exposures are often taken to reduce the signal-to-noise. The spectra are then ready for additional post processing, including alignment, normalization, and finetuning

wavelength calibration within the Demetra software.

An important step in the Demtra software is to manually link pixel ranges to known wavelengths to establish a baseline for calibration of all other spectral orders. For instance, Deneb, the central wavelengths of orders 50 and 81 were linked to 6834 Å and 4215 Å respectively.

4. Results

Upon completion of data reduction and calibration, the resulting spectra are available for analysis. The resulting spectral orders for Deneb combined into a single full spectrum profile resembles the expected blackbody curve validating the Whoppshel configuration as seen in Figure 7. The Vega spectrum is displayed in the presented poster for this work (Roth et al. 2025).

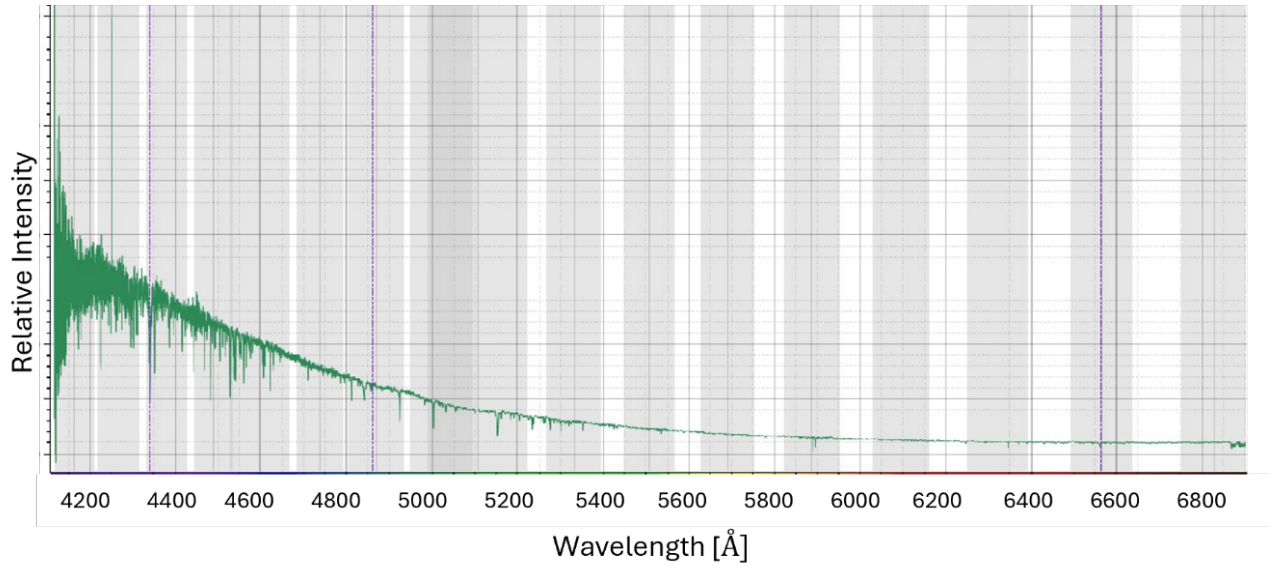

Figure 7. Spectral Profile of Deneb. Wavelength in Angstroms on the x-axis, and Relative Intensity on the y-axis.

Note that the spectrum is very noisy towards the blue, attributed to atmospheric turbulence, sensitivity of the CCD camera and potentially the 85 mm lens in the optical chain. Individual orders were inspected and confirm the fidelity of the spectral profile. We examined order 52, which covers a 15 nm wavelength range centered on the H-alpha absorption line at 656 nm. The H-alpha line is seen at its expected location at about 6560 Å in Figure 8 below. This qualitative agreement also supports the accuracy of our configuration. However, the next step is to quantitatively compare the gathered Whoppshel spectral data to known spectral data.

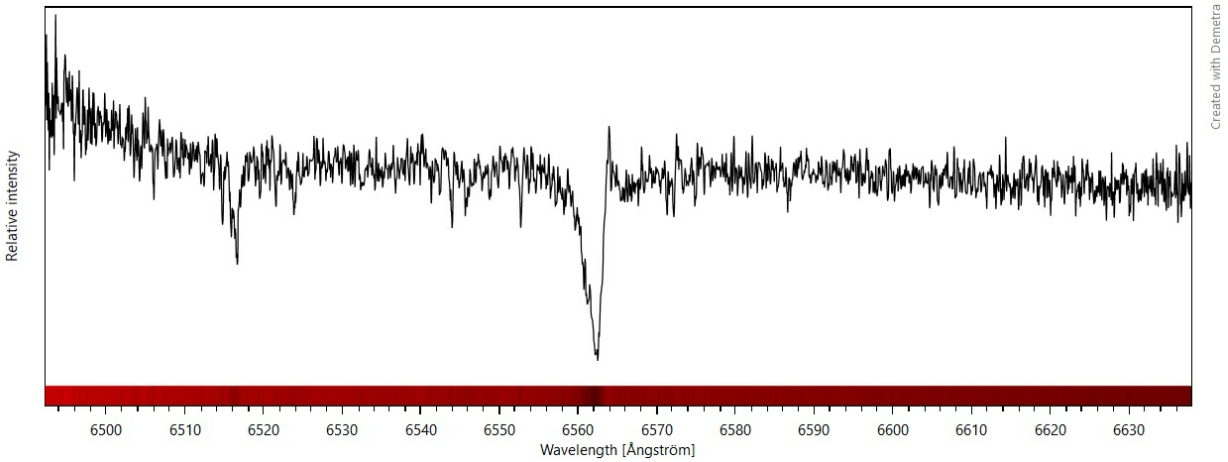

Figure 8. Order 52 Spectral Plot containing Hydrogen-Alpha absorption line.

After gathering the spectral data, we used the BASS Project software to measure the spectral resolution at selected wavelengths using three spectral lines in each order from 50 to 82 (Paraskeva 2024). BASS provides the Full Width at Half Maximum (FWHM) for each line, which we used to compute the resolving power. Our goal was to examine how the measured resolution varied with wavelength and how much it deviated from the nominal value of $R \approx 30000$.

The average resolving power over all data points is $R \approx 21338$, which is about 29 percent lower than the nominal value. Measurements show that the resolving power remains relatively high at longer wavelengths, clustering around $R \approx 27000$ for $\lambda > 550$ nm, but it drops noticeably for wavelengths shorter than 500 nm and becomes much noisier. In particular, the 400–500 nm range has significant resolution differences from order to order. Distortions from the 85 mm lens in the nonstandard optical chain likely suppress the measured resolution, masking the capability of the Whoppshel.

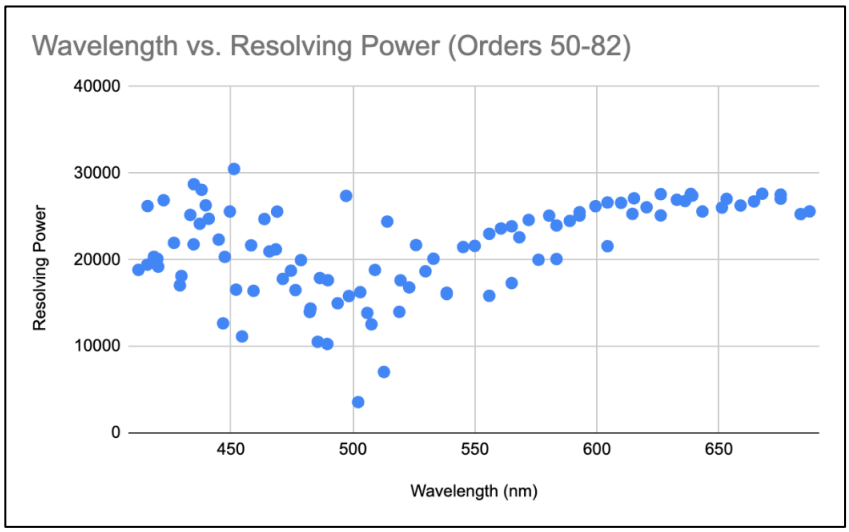

Figure 9. Wavelength vs. Spectral Resolving Power for orders 50-82 using FWHM values from Bass Project.

5. Conclusion

In summary, we successfully achieved first light with the integrated Whoppshel spectrograph on the USAFA one-meter telescope system while also qualitatively and quantitatively assessing the resulting spectra. High resolution spectra across orders 50-82 were obtained on Deneb verifying stable fiber injection of starlight, spectral data collection and spectral processing. The results confirmed both the blackbody spectral shape and the expected position of the H-alpha absorption line. Resolution measurements show the current optical configuration underperforms the nominal design value, particularly at shorter wavelengths. The average resolving power over all data points was determined to be $R \approx 21338$.

Future efforts will modify the optical chain to improve performance. Replacing the current focal reduction optics with a more optimal design to minimize distortions is expected to increase the instrument's performance, particularly in the blue. Repeat observations of Deneb and spectroscopic standard stars will be made to measure increased performance and further characterize the USAFA Whoppshel.

Acknowledgements

We would like to express our gratitude to Dr. Brian Kloppenborg for his invaluable guidance throughout this project. His insights into current astronomical requirements and his direction regarding future research pathways were instrumental to our work.

Distribution A. Approved for public release, distribution unlimited. (PA#: USAFA-DF-2026-56)

References

"1110S CCD Camera Data Sheet." 2019, Spectral Instruments Inc.

ACE Instruments. 2019, "ACE Instrumentation Dual Filter Wheel, 8 Position 110 Mm Square With Dual Guider Ports For USAFA," Astronomical Consultans & Equipment, https://faculty1.coloradocollege.edu/~sburns/Courses/22-23/PC362/ACE%20Filter%20Wheel%20with%20Guider%20Ports%20for%20USAFA%20User%20Manual.pdf

Garde, Olivier. 2019, "The Whoppshel, a High Resolution Echelle Spectroscope," Shelyak Instruments. https://www.shelyak.com/le-woppshel-un-spectro-echelle-a-grande-resolution/?lang=en

Garde, Olivier. 2023, "The Whoppshel on a 1m Telescope." Shelyak Instruments, December 18. https://www.shelyak.com/the-whoppshel-on-a-1m-telescope/?lang=en

Matthews, Nolan, Jean-Pierre Rivet, David Vernet, et al. 2023, “Intensity Interferometry Observations of the Hα Envelope of γ Cas with MéO and a Portable Telescope.” The Astronomical Journal **165** (3), 117

Palmer, Christopher. 2020, Diffraction Grating Handbook. 8th ed. MKS Instruments, Inc.

Paraskeva, John 2024, BASS Project. V. 1.9.9, Released, Windows, https://groups.io/g/BassSpectro/wiki/13559

Puchner, M. 2019, “EQ1000 User Manual,” ASA Astro Systeme Austria, October 10, 2019

Richardson, Noel Douglas. 2006, A Five-Year Spectroscopic and Photometric Campaign on the Supergiant Star Deneb

Roth, Benjamin, Scott Donnell, Zion Porter, Timothy Giblin, and Francis Chun. 2025, “First Light of the Whoppshell Spectrograph on the USAFA One-Meter Telescope (Poster Abstract),” American Association of Variable Star Observers (AAVSO) 114th Annual Meeting. https://www.aavso.org/114/annual-meeting-abstracts#Posters

Shelyak Instruments. 2025, Demetra. V. 7.3.1, Released, https://www.shelyak.com/software/demetra

Spectral Instruments. 2016, “SI Image SGL II Software Manual,” Spectral Instruments Inc.

Stark, Craig, Bret McKee, Andy Galasso, and Bruce Waddington. 2023, PHD2 v2.6.13. V. 2.6.13. Released. https://openphdguiding.org/

Yorulmaz, EB, I Ozavci, ENGİN Bahar, HV Senavci, GAJ Hussain, and Oleg Kochukhov. 2025, “Doppler Imaging of the Contact Binary DU Boo.” Contributions of the Astronomical Observatory Skalnate Pleso **55** (3): 117–21

SNR and Exposure Times for Differential Photometry

Mark L. Spearman, PhD

Regina Caelorum Observatory, Wheelock, Texas 77882, USA; spearman@factoryphysics.com

Subject Keywords

Differential Photometry, Poisson Statistics, Scintillation Noise, Signal to Noise Ratio

Abstract

The signal to noise ratio (SNR) is an important measure of the quality of a science frame in that the greater the SNR the better the accuracy. SNR is also associated with intensity where the larger the intensity the greater the SNR and the better the accuracy. However, this study finds that there is a "maximum practical intensity" in which the error due to scintillation limits the observed SNR for a single measurement.

1. Introduction

This paper recounts a personal quest to find a way to determine how long one must image a given star in order to obtain good photometry. "Good photometry" means providing estimates of magnitude with low error. In this work, I will use the terms "error," and "noise" interchangeably and reference the standard deviation of the associated random variable as the measure of the error or noise.

Given a good reference star's magnitude and its intensity (i.e., counts for a given exposure time), I need to find an exposure time for a reasonable intensity for my target star. I began with the basic equation relating magnitudes,

$$m_1 - m_0 = -2.5 \log(I_1/I_0) \tag{1}$$

where m is the apparent magnitude and I is the intensity. The zero indicates a known magnitude and intensity. Since I know the magnitudes and the intensity of the comparison star, I can use the above relationship to obtain the intensity of the target star with the same exposure time. Solving for I_1, I obtain,

$$I_1 = I_0 \cdot 10^{((m_0 - m_1)2.5)} \tag{2}$$

If the exposure time for the comparison star is t_0 and I would like the intensity of the target star to be I_t, then the required exposure time is,

$$t_1 = \frac{I_t}{I_0} \cdot t_0$$

For instance, suppose I want to image a 13.5 magnitude star and have imaged a 10.55 magnitude star with an intensity of 97,847 counts using a 30 s exposure. If I image the 13.5 magnitude star for 30 s, the resulting intensity is 6,489. But I do not think this is sufficient and would like to have an intensity of 20,000. Using the above I get an exposure time of 92.5 s so I will use 90 s (since I have dark frames for 90 s).

However, although I decided 20,000 counts would be enough, I am just going on my experience and "gut feel." 20,000 might not be enough and it may be overkill. To make a good decision, I need to know the signal to noise ratio (SNR) of a given exposure time.

To this end, I began searching for SNR formulae and found many different and varied ones. Here are a few examples from various texts and software documentation that I found,

$$SNR = \frac{S\sqrt{T}}{\sqrt{S + \sum(B + D + R^2/t)}}$$

$$SNR = \frac{S}{\sqrt{S/(G + N_s + \sigma^2(1 + 1/N_r))}}$$

$$SNR = \frac{N_{star}}{\sqrt{N_{star} + n\left(N_{sky} + N_{dark} + N_{readnoise}^2\right)}}$$

$$SNR = \frac{N_{ADU} G}{\sqrt{N_{ADU}\, G + n_{pix}\left(\left(N_{ADU\, sky} + N_{ADU\, dark}\right)G + N_{readnoise}^2\right)}}$$

While the notation is different in each formula, the general idea is that the numerator indicates the signal with the denominator being the noise terms added in quadrature. These terms are composed of shot noise of the star itself plus more shot noise from the sky measurement and dark current along with the read noise.

After this investigation, I had three questions: (1) why do some formulae have a gain term and others do not? (2) what happened to scintillation error which, for brighter stars, can result in more noise than the Poisson variation of the star itself, and (3) which of these, if any, is correct?

The answer to the first question is rather simple. Gain is a multiplicative constant converting the number of electrons detected at a pixel in the CCD to analog digital units or ADU's. Since SNR is a dimensionless ratio, any gain factor will cancel out. If there is a gain factor in a formula then

one is adding electrons and ADU's, different quantities with different dimensions, which is always incorrect (like adding inches and millimeters).

Before addressing questions 2 and 3, we need to review the basics of differential photometry.

2. Review of Differential Photometry

The magnitude estimate of the target star is given by the magnitude of a comparison star minus the difference in the instrumental magnitudes of the target and the comparison stars.

$$\widehat{m}_t = m_c - 2.5 \log \frac{I_t}{I_c}$$
$$\widehat{m}_t = m_c - 2.5(\log I_t - \log I_c) \quad (3)$$

where the I values are the average intensities that are computed from the average of the aperture, $\overline{X}_0$, and the average of the annulus, $\overline{X}_b$, viz.

$$\overline{I} = p_0(\overline{X}_0 - \overline{X}_b) \quad (4)$$

where $\overline{X}_0$ is the average aperture and $\overline{X}_b$ is the average annulus and p_0 is the number of pixels in the aperture. The sources of error are in the magnitude of comparison star and in the value of the two intensity values. The error of the comparison star is usually quoted in the VSP sequence while the error of the intensities is determined by their respective SNR, ξ, where

$$\widehat{\sigma} = \overline{I}/\xi \quad (5)$$

The variance of the magnitude estimate is the sum of the standard deviations added in quadrature,

$$\widehat{\sigma}_t^2 = \sigma_c^2 + 2.5^2\left(V(\log I_t) + V(\log I_c)\right) \quad (6)$$

It is clear then that we must be concerned with not one SNR value but with two, one for the target and one for the comparison star. Now we need to address how to obtain those variances.

Star light is distributed, for our purpose, as a Poisson random variable. As such, the mean and the variance of the intensity are equal. If the average value is larger than 25 then the SNR is greater than 5 and the normal distribution will be a good approximation. If we have fewer than 25 counts, the star may be too dim to measure! So, the Poisson can be approximated by the normal distribution with the same mean and a standard deviation that is the square root of the mean.

The instrumental magnitude is -2.5 times the base 10 logarithm of the intensity. The minus sign is due to the fact that the magnitude scale is decreasing with increasing intensity. The 2.5 and base 10 logarithms imply that a hundred-fold increase in intensity represents a decrease of 5 in magnitude. But base 10 logarithms are a bit awkward so we will convert these into a natural logarithm by $\log x = \ln x / \ln 10$. Then the magnitude estimate becomes

$$\hat{m}_t = m_c - \left(\frac{2.5}{\ln 10}\right)(\ln I_t - \ln I_c)$$

The log function is an increasing concave function so if a Poisson random variable has an SNR>5 and can be approximated by a normal random variable, then the log of the Poisson random variable will have an even larger SNR and so is more readily approximated by a normal random variable. Thus, we have the natural log of a random variable that is normally distributed. Such random variables are distributed according to a *lognormal* distribution whose variance is related to the SNR, ξ, of the random variable itself by

$$\sigma^2 = \ln(1 + 1/\xi^2) \tag{7}$$

If $1/\xi^2 \ll 1$ then, $\ln(1 + 1/\xi^2) \approx 1/\xi^2$. If $\xi = 20$ then the approximation is 0.1249% greater than the actual term. When the SNR is 100, the difference is 0.0050%. So, we can approximate,

$$\sigma_t = \sqrt{\sigma_c^2 + \left(\frac{2.5}{\ln 10}\right)^2 \left(\frac{1}{\xi_t^2} + \frac{1}{\xi_c^2}\right)} \tag{8}$$

The coefficient is approximately unity which may account for the multiple texts that report the average error as 1/SNR. Those texts are correct for absolute photometry where there is no comparison star, but not for differential photometry where we have two additional error terms, the error in the comparison star magnitude and its intensity.

Suppose the comparison star has an error of 0.01 magnitudes and the SNR of both the target and comparison stars is 100. Then,

$$\begin{aligned}\sigma_t &= \sqrt{\sigma_c^2 + \left(\frac{2.5}{\ln 10}\right)^2 \left(\frac{1}{\xi_t^2} + \frac{1}{\xi_c^2}\right)} \\ &= \sqrt{0.001 + 1.18\left(\frac{1}{10,000} + \frac{1}{10,000}\right)} \\ &= 0.0183\end{aligned}$$

In many cases, the error of the comparison star is greater than the error of the measurements.

3. Sources of Error

A comprehensive list of errors found in photometry is from the classic text by Henden and Kaitchuck (1982), Appendix K.4. The total error will be the sum of the individual errors added in quadrature. These errors are:

1. Shot noise from the star light itself.
2. Background shot noise from the sky.
3. Scintillation noise from the atmosphere.
4. Dark current[1]
5. Read error

The light from the star has a Poisson probability distribution *in space.* The sky background should also have a Poisson distribution. Again, the variance is equal to the mean. If $\boldsymbol{I_0}$ is the mean for the star and $\boldsymbol{I_b}$ the mean for the sky (background) then the variances of those random variables are the same as those means. However, when we subtract sky (annulus) from star + sky (aperture) it is no longer Poisson. Fortunately, if the mean is large enough (e.g., $> \mathbf{25}$) then the distribution is well approximated by a normal distribution with the same mean and standard deviation. In that case, the difference is also normal with a mean of $\boldsymbol{I_0 - I_b}$ and a variance of $\boldsymbol{\sigma_o^2 + \sigma_b^2}$.

The error caused by scintillation is more subtle. While the light received in space from a star may be Poisson, the star light coming through the atmosphere is definitely not Poisson. Indeed, the added variation of scintillation can be greater than that from the shot noise for brighter stars. Thus, the second source of error is the scintillation of the star itself. Young (1967) provides an estimate of the RMS fractional scintillation noise as,

$$\frac{\boldsymbol{\sigma_{scint}}}{\boldsymbol{I}} = \mathbf{0.09}\, \boldsymbol{D^{-2/3}}\, \boldsymbol{X^{3/2}} \boldsymbol{e^{-h/H_0}} / \sqrt{\boldsymbol{t}} \tag{9}$$

where $\boldsymbol{D}$ is the diameter of the telescope in cm, $\boldsymbol{X}$ is the airmass, $\boldsymbol{h}$ is the altitude of the observatory in meters, $\boldsymbol{H_0} \approx \mathbf{8,000}$ m is the scale height of the atmosphere, and $\boldsymbol{t}$ is the exposure time in seconds. The development of this function continued in 1997-98 with three papers by Dravins, et al. (1997a), (1997b), (1998) and with Osborn, et al. (2015). The AAVSO Guide to CCD/CMOS (2022) Photometry recommends Radu Corlan's tables of scintillation (Corlan 2025).

Equation (9) shows that the right-hand side is constant for any telescope configuration and airmass. Consequently, the scintillation noise is *proportional* to the intensity and not the square root of the intensity. For large intensities, the scintillation noise is dominate.

[1] With temperature-controlled cameras, the error due to dark current is very small compared to the other sources.

Equation (9) shows that the right-hand side is constant for any telescope configuration and airmass. Consequently, the scintillation noise is *proportional* to the intensity and not the square root of the intensity. For large intensities, the scintillation noise is dominate.

Kornilov (2012) developed the covariance between two measurements separated by a given angular distance. He finds that when the distance between the target and comparison star is very small, the correlations very nearly cancel the scintillation noise. But, with the exception of crowded fields, the scintillation noise simply doubles.

Given that there is no scintillation error term in the above referenced SNR formulae, it appears that all are assuming that the target and comparison star are dim enough so that scintillation noise is not significant. However, scintillation appears to be significant in many frames that are far from being saturated. So, the second question as to why scintillation noise is not included in the SNR calculation has not been satisfactorily answered.

4. SNR for Differential Photometry

Define

$\boldsymbol{X_{0,i}} =$ count in aperture of ith pixel of a particular frame
$\boldsymbol{X_{b,k}} =$ count in annulus of kth pixel of a particular frame
$\boldsymbol{X_{e,j}} =$ count of dark plus read error of jth pixel of a particular frame
$\boldsymbol{\mu_{e,j}} =$ mean count of dark plus read error of jth pixel
$\boldsymbol{\sigma^2_{e,j}} =$ variance of dark plus read error of jth pixel
$\boldsymbol{p_0} =$ number of pixels in the aperture
$\boldsymbol{p_b} =$ number of pixels in the annulus

I am ignoring other sources such as flat field error and non-linearity in the CCD because these are small in comparison to the others. Dark and read error (bias) are measured together because I take dark frames at the same temperature as the science frames. The $\boldsymbol{\mu}$ and $\boldsymbol{\sigma^2}$ values represent the true average and variance of the pixel in dark and bias frame. Although we do not know the exact values, we estimate these by taking numerous dark/bias frames and choosing the median value. The median prevents hot and dead pixels from distorting the statistic. The $\boldsymbol{p_0}$ and $\boldsymbol{p_b}$pixel numbers could be fractional to accommodate pixels on the border of the aperture (annulus).

The average intensity is

$$\begin{aligned}\bar{\boldsymbol{I}} &= \boldsymbol{p_0}\left(\frac{\sum_{\boldsymbol{i}\in\boldsymbol{p_0}}\boldsymbol{X_{0,i}}+\boldsymbol{X_{e,i}}-\boldsymbol{\mu_{e,i}}}{\boldsymbol{p_0}}-\frac{\sum_{\boldsymbol{j}\in\boldsymbol{p_b}}\boldsymbol{X_{b,j}}+\boldsymbol{X_{e,j}}-\boldsymbol{\mu_{e,j}}}{\boldsymbol{p_b}}\right)\\ &= \boldsymbol{p_0}\left(\bar{\boldsymbol{X}}_{\boldsymbol{0}}+\bar{\boldsymbol{X}}_{\boldsymbol{0,e}}-\boldsymbol{\mu_{e,i}}-\bar{\boldsymbol{X}}_{\boldsymbol{b}}-\bar{\boldsymbol{X}}_{\boldsymbol{b,e}}+\boldsymbol{\mu_{e,j}}\right)\end{aligned} \tag{10}$$

where $\sum_{\boldsymbol{i}\in\boldsymbol{p_0}}\boldsymbol{X_{0,i}}$ indicates the summing of the pixel counts over all the pixels in the aperture. With good dark/bias frames, the average and mean error terms will cancel, leaving,

$$\bar{\boldsymbol{I}} = \boldsymbol{p_0}(\bar{\boldsymbol{X}}_\mathbf{0} - \bar{\boldsymbol{X}}_\boldsymbol{b})$$

which is what we first wrote in equation (4). Note that $\bar{\boldsymbol{X}}_\mathbf{0}$ is the average of the sum of the counts of the star and the counts of the background sky. So, if we let X_s be the counts from the star (which we do not know but are attempting to measure), then $\boldsymbol{X_0} = \boldsymbol{X_s} + \boldsymbol{X_b}$. So

$$E[I] = E[X_s]$$

is the true intensity of the star.

Thus, the *signal* will be $\bar{\boldsymbol{I}}$ and the noise will be the standard deviation of $\boldsymbol{I}$. This standard deviation is a bit more complicated since no terms cancel and because X_0 and X_b are correlated. But we want the variance of X_s.

$$\boldsymbol{Var}(\boldsymbol{X_0}) = \boldsymbol{Var}(\boldsymbol{X_s}) + \boldsymbol{Var}(\boldsymbol{X_b}) + \mathbf{2}\,\boldsymbol{Cov}(\boldsymbol{X_s}, \boldsymbol{X_b})$$

But since $\boldsymbol{X_s}$ and $\boldsymbol{X_b}$ are not correlated, $\boldsymbol{Var}(\boldsymbol{X_0}) = \boldsymbol{Var}(\boldsymbol{X_s}) + \boldsymbol{Var}(\boldsymbol{X_b})$

since $\boldsymbol{X_s}$ and $\boldsymbol{X_b}$ are independent. Consequently, $\boldsymbol{Var}(\boldsymbol{X_s}) = \boldsymbol{Var}(\boldsymbol{X_0}) - \boldsymbol{Var}(\boldsymbol{X_b})$. Also, note that the variance of an average is $\boldsymbol{V}(\bar{\boldsymbol{X}}) = \boldsymbol{\sigma^2}/\boldsymbol{n}$, where $\boldsymbol{n}$ is the number of frames averaged. So, the variance of I is approximately

$$\boldsymbol{S^2(I)} \approx \boldsymbol{p_0^2}\left(\frac{\boldsymbol{S_0^2}}{\boldsymbol{p_0}} - \frac{\boldsymbol{S_b^2}}{\boldsymbol{p_a}} + \frac{\boldsymbol{S_e^2}}{\boldsymbol{p_0}} + \frac{\boldsymbol{S_e^2}}{\boldsymbol{p_b}}\right)$$

where S_e^2 is the variance estimate of the background plus the read error. Assuming a Poisson distribution, we can substitute the mean for the variances of the aperture and annulus

$$\begin{aligned}\boldsymbol{S^2(I)} &\approx \boldsymbol{p_0^2}\left(\frac{\bar{\boldsymbol{X}}_\mathbf{0} - \bar{\boldsymbol{X}}_\boldsymbol{b}}{\boldsymbol{p_0}} + \boldsymbol{S_e^2}\left(\frac{\mathbf{1}}{\boldsymbol{p_0}} + \frac{\mathbf{1}}{\boldsymbol{p_b}}\right)\right) \\ &\approx \boldsymbol{p_0}(\bar{\boldsymbol{X}}_\mathbf{0} - \bar{\boldsymbol{X}}_\boldsymbol{b}) + \frac{\boldsymbol{p_0}}{\boldsymbol{p_b}}(\boldsymbol{p_0} + \boldsymbol{p_b})\boldsymbol{S_e^2}\end{aligned}$$

Then, ignoring scintillation noise, the SNR becomes

$$\boldsymbol{SNR} = \frac{\boldsymbol{p_0}(\bar{\boldsymbol{X}}_\mathbf{0} - \bar{\boldsymbol{X}}_\boldsymbol{b})}{\sqrt{\boldsymbol{p_0}(\bar{\boldsymbol{X}}_\mathbf{0} - \bar{\boldsymbol{X}}_\boldsymbol{b}) + \frac{\boldsymbol{p_0}}{\boldsymbol{p_b}}(\boldsymbol{p_0} + \boldsymbol{p_b})\boldsymbol{S_e^2}}} \tag{11}$$

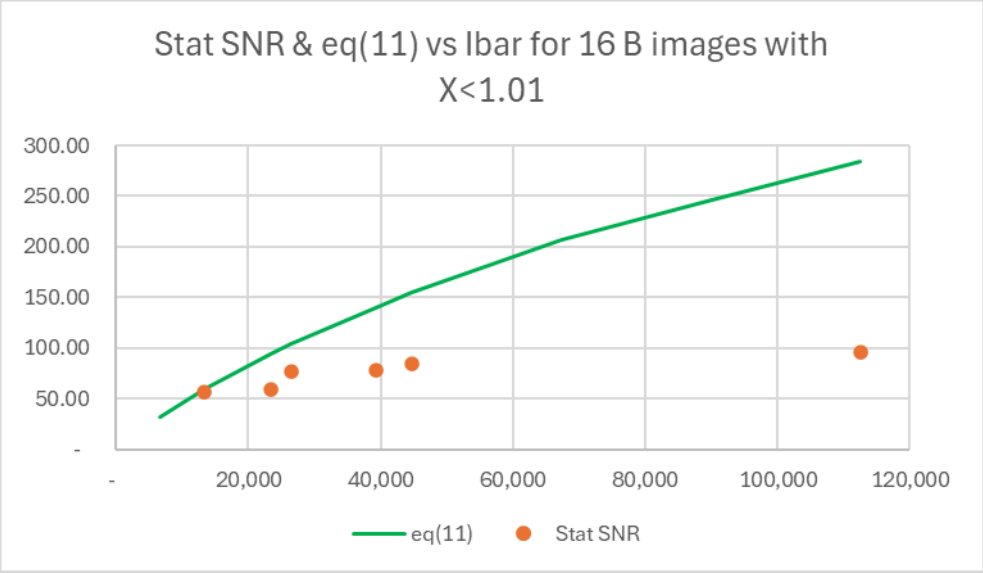

Figure 1: Statistical SNR and eq (11) versus $\bar{I}$

If we add scintillation noise, we obtain,

$$\boldsymbol{SNR = \frac{p_0(\bar{X}_0 - \bar{X}_b)}{\sqrt{\sigma_{scint}^2 \cdot p_0^2(\bar{X}_0 - \bar{X}_b)^2 + p_0(\bar{X}_0 - \bar{X}_b) + \frac{p_0}{p_b}(p_0 + p_b)S_e^2}}}$$

(12)

Now consider the estimated SNR using equation (11) with the "statistical" SNR measured by dividing the average by the standard deviation of a number of $\bar{I}$ estimates with low airmass values. Figure 1 compares these with the approximation given in equation (11). Once we are beyond around 30,000 for the intensity, the $\boldsymbol{SNR_{stat}}$ no longer increases due to scintillation noise. The maximum of any of the 16 apertures was far below the saturation level of around 60,000.

5. Practical Considerations

The main practical consideration from this study is to realize that there is a maximum practical intensity (MPI) and increasing exposure times beyond this level does not improve the SNR. If the error is too large with the MPI, then multiple images must be averaged to reduce the measurement error.

For example, suppose the MPI = 100,000 with a 60 s exposure yielding a SNR of 200. This implies a standard deviation of 500. If we desire a standard deviation of 200 or a SNR of 500. To achieve this, we image n science frames, where

$$\boldsymbol{n \geq \left(\frac{500}{200}\right)^2 = 6.25}$$

So, we must image 7 science frames and average the estimates.

6. Conclusions

The answer to question 3, "which if any of the foregoing formulae is correct?" is that none are exactly correct for differential photometry since none consider the different pixel counts in the aperture and the annulus and none have a scintillation error term. The reason for omitting the scintillation term may be because the various sources give different equations for this term ranging from 1.3×10^{-3} to 2.3×10^{-3} for a 10" diameter scope at a zenith distance of 45 degrees with a 60 s exposure at low altitude.

The question as to what SNR is sufficient turns out to be more complicated that I had first thought. Clearly, equation (11) is an upper bound and is not far below the simplest upper bound of $SNR \leq \sqrt{\bar{I}}$.

Perhaps the best suggestion is to paraphrase Socrates, "Know thy rig!" If your scope and camera achieve a maximum practical intensity near 25,000 then you need only to use equations (2) and (8) and then, possibly, (13) to determine exposure times and/or number of science frames to achieve a given error

Acknowledgements

I would like to acknowledge Dr. Arne Henden for his guidance during the AAVSO Observational Best Practices CHOICE course. I also acknowledge with thanks the variable star observations from the AAVSO International Database contributed by observers worldwide and used in this research.

References

AAVSO, 2022, "AAVSO Guide to CCD/CMOS Photometry with Monochrome Cameras," AAVSO, Cambridge, MA

Corlan, R., "Estimated scintillation noise tables," http://astro.corlan.net/gcx/scint.txt, accessed 15 August 2025.

Dravins, D., Lindegren, L., Mezey, E., & Young, A. T. 1997, *PASP*, **109**, 173

Dravins, D., Lindegren, L., Mezey, E., & Young, A. T. 1997, *PASP*, **109**, 725

Dravins, D., Lindegren, L., Mezey, E., & Young, A. T. 1998, *PASP*, **110**, 610–633

Henden, A. A., and Kaitchuk, R. H. 1982, Astronomical Photometry, New York: Van Nostrand Reinhold Company.

Kornilov, V. 2012, "Angular correlation of the stellar scintillation for large telescopes," *MNRAS*, **425**, 1549

Osborn, J., Föhring, D., Dhillon, V.S., and Wilson, R.W. 2015, "Atmospheric scintillation in astronomical photometry," *MNRAS*, **452**, 1707-1716

Sterken, C. and Manfroid, J. 1992, Astronomical Photometry: A Guide, Kluwer, §15.4

Young, A. T., 1967, "Photometric Error Analysis. VI. Confirmation of Reigen's Theory of Scintillation," *ApJ*, **72**, 747

Results from the HST Treasury Program on Accreting White Dwarfs as Probes of Compact Binary Evolution

Paula Szkody[1], Anna Pala[2], Thomas Kupfer[3], Weitian Yu[3], Gagik Tovmassian[4], and HST Consortium

[1]University of Washington, Astronomy Department, Seattle, WA 98105, USA (szkody@uw.edu); [2]ESO, Karl Schwarzschild Strasse 2, Garching, Germany (annafrancesca.pala@eso.org); [3]University of Hamburg, Gojenbergsweg 112, Hamburg, Germany; [4]UNAM, Mexico

Subject Keywords

Cataclysmic Variables; stars: spectroscopy

Abstract

About 4 years ago, a large Consortium of 30 astronomers was awarded an HST Treasury Program to obtain ultraviolet observations of accreting white dwarfs to explore the previously poorly studied regions of very short and very long orbital periods. The goal of these observations was to determine accurate temperatures, gravity, masses and compositions of the white dwarfs in order to test models of compact binary evolution. The project has now ended with observations of 14 dwarf novae/novalikes and 12 AM CVn systems that were completed with help from monitoring by AAVSO observers. The data reveal differences in detection of the white dwarf, anomalies in ratios of N/C and a disk wind in some systems. Detailed analysis has been completed for the cataclysmic variable V479 And and the AM CVn ZTF J225237.05-051917.4.

1. Introduction

Cataclysmic variables (CVs) are close binary systems that involve a white dwarf primary, a low mass secondary (usually a late M star or brown dwarf but can also be a hydrogen deficient star like another white dwarf), and actively transfer mass. The orbital periods of these objects range from 10 minutes in the AM CVns to several days for a few dwarf novae. While thousands of accreting white dwarfs are now known, detailed knowledge such as mass and temperature are lacking for the shortest and longest period systems. These parameters are important for modelling of how these common endpoints of stellar evolution evolve from widely separated members of a binary to the short periods that are observed. To improve the situation, a consortium of 30 astronomers from 10 countries proposed a Hubble Space Telescope (HST) Treasury program to explore these regions of parameter space to test available models of close binary evolution.

2. The HST Program

The Cycle 29 three-year Treasury Program was awarded in 2021 to observe 43 CVs using 132 HST orbits with the Cosmic Origins Spectrograph (COS) covering ultraviolet wavelengths from 1100-

1900 Angstroms. The ultraviolet is necessary to obtain light from the white dwarf, as the optical wavelengths are swamped by the light from the accretion disk surrounding the primary. However, optical observations from the ground close in time to the HST scheduled ones are necessary to ensure the objects are at quiescence since the outburst fluxes could damage the HST detectors and would also prevent detection of the white dwarf. The monitoring by AAVSO observers around the world was invaluable in this regard. Due to various issues such as the complexity of the program requiring safe holds and HST issues with degrading pointing stability, the program was extended to four years but only managed to obtain spectra for 14 dwarf novae/novalikes (DN/NL), the systems that show outbursts or high and low accretion states, and 12 AM CVns, the systems with hydrogen deficient secondaries.

3. Results

The UV spectra of the 26 systems reveal a wide variety. The white dwarf is evident in the spectra by the presence of absorption lines, especially around Lyman alpha, where the depth of the absorption allows an estimate of the contribution of the white dwarf. This is complicated by the airglow emission at the center of the line. However, if the object was caught close to a dwarf nova outburst or a high state of accretion in a novalike, broad absorption lines from the disk are also possible and can even result in a P Cygni profile (absorption on the blue side of the line with emission at the central wavelength) that is indicative of an outflowing wind. Emission lines from Carbon, Silicon, Nitrogen and Helium are also present and originate from the accretion disk. Nine of the 14 dwarf novae/novalikes (DN/NL) show absorption lines consistent with an origin from the white dwarf and will be able to be modeled to obtain temperature and mass. Two spectra are consistent with winds. Five spectra reveal inverted N/C ratios that indicate an evolution path from an evolved secondary star. One of these systems (V479 And) also shows an unusually strong ionized helium line that indicates a highly magnetic white dwarf (details may be viewed in Tovmassian et al. 2025). The AM CVn spectra are generally fainter but show a wide variety of absorption and emission lines. One system (ZTF J225237.05-051917.4) has currently been modelled (Yu et al. 2025) that results in the temperature and mass and provides constraints on the evolution path. Several others are in process.

4. Conclusions

It is clear that UV spectra provide a unique method to explore white dwarf parameters. However, our program demonstrates that it is not easy to acquire large UV spectral datasets on CVs with HST. Despite the lower than expected number of completed observations in our program, the data show that there is a relatively large percentage of inverted N/C ratios among the long period CVs, and white dwarf models will be able to be fit to many of the systems. Results so far on V479 And have confirmed this object contains a highly magnetic white dwarf, while a detailed model fit to the spectrum of the AM CVn system ZTF J225237.05-051917.4 shows that the UV spectra can constrain evolution channels. The major problem for the future is going to be the lack of UV spectral capability on faint objects once HST is decommissioned.

Acknowledgements

We acknowledge with thanks the variable star observations from the AAVSO International Database contributed by observers worldwide and used in this research. PS acknowledges grant HST-GO-16659.007A for partial support.

References

Tovmassian, G., et al. 2025, Astronomy & Astrophysics, 703, 119, arXiv:2508.21358

Yu, W., Pala, A. F., Kupfer, T., et al. 2025, arXiv:2512.04147

The NASA Landolt Mission

Arlo Landolt Lecturer: Dr. Peter Plavchan

Peter Plavchan is an Associate Professor of Physics and Astronomy at George Mason University and the Executive Director of George Mason Observatories. Previously, he was an Assistant Professor at Missouri State University and a Research Scientist at the NASA Exoplanet Science Institute. His research focuses on exoplanets around low-mass stars, specializing in precise radial velocity techniques at near-infrared wavelengths. He discovered the AU Mic planetary system. Currently, Plavchan is Principal Investigator of the NASA Landolt mission and the HaZE mission concept. He has built instrumentation for the NASA Infrared Telescope Facility and uses ground-based telescopes worldwide and in space with the Spitzer, Kepler, TESS, and James Webb Space Telescope missions.

Dr. Plavchan is an observational exoplanet astronomer, with a focus on the formation and demographics of planets around cool dwarfs, utilizing the radial velocity and transit detection methods. He is the Principal Investigator of a NASA Probe Mission concept called EarthFinder, is a Co-PI of the MINERVA-Australis telescope array, regularly uses the NASA Infrared Telescope Facility iSHELL spectrometer for precise radial velocities, has served as an Executive Committee member of the NASA Exoplanet Program Analysis Group (ExoPAG), and has received multiple NASA Group Honor Achievement Awards. His research is currently supported by NASA, NSF, and the Mt. Cuba Astronomical Foundation, and his work has appeared in numerous local and national publications.

Resources for Doing Variable Star Science with the Vera C. Rubin Observatory

Keynote Speaker: Dr. Melissa L. Graham

Melissa Lynn Graham is currently a research staff scientist in the Department of Astronomy at the University of Washington in Seattle, Washington, where she works with the Rubin Observatory and its Legacy Survey of Space and Time as a Data Management Science Analyst during construction and as the Lead Community Scientist for operations. Her main research focus is supernovae, especially those of Type Ia.

The Vera C. Rubin Observatory will capture the cosmos in exquisite detail. Using the largest camera ever built, Rubin will repeatedly scan the sky for 10 years and create an ultra-wide, ultra-high-definition time-lapse record of our Universe: the Legacy Survey of Space and Time (LSST). In her talk, Dr. Graham will cover the LSST survey strategy, the image processing pipelines, and the science-ready data products that astronomers worldwide are using for their analyses. She will focus especially on the practical aspects of data access via the Rubin Science Platform and Alert Brokers, how to find documentation and tutorials, where to go to ask questions and get support, and opportunities for engagement and collaboration.

Narrowband Visual Observations of the Solar Photosphere

Dr. David Cowall

After many decades of conducting nocturnal variable star observations for submission to the AID, I have transitioned to the AAVSO Solar Observing Section to focus on daytime visual observations of the solar photosphere. The optical system employed consists of a 72-millimeter aperture f/5.8 apochromatic refractor, a Herschel Wedge, a broadband ND#3 filter, a narrowband 540 nanometer filter, and a 9-millimeter eyepiece, yielding a magnification of 46X and a 1.8-degree field of view. The addition of the narrowband filter significantly enhances resolution by improving contrast and by mitigating atmospheric turbulence effects. The system's solar mount automatically slews to the sun and maintains the solar image centered in the eyepiece. This setup allows for detailed observations of the ever-changing sunspots and faculae. The Zurich sunspot numbers generated are submitted via SunEntry to the AAVSO American Relative Sunspot Program for analysis and are included in the monthly Solar Bulletin.

W Ursae Majoris-Type Eclipsing Binary V0512 Cam

Adreana Dillabough and Jenna Martodam

Minnesota State University, Moorhead, Minnesota

I aim to conduct time-series photometry on V0512 Cam, a contact eclipsing binary. This target is an Ursae Majoris variable type with a light curve that displays ellipsoidal components and shares a similar eclipse depth during the primary and secondary minima. Utilizing data collected by the 0.5-meter ARCSAT at Apache Point Observatory in New Mexico on the nights of September 9th to 14th, I will create a light curve to more accurately constrain the period and update the ephemeris. SA38-326 to estimate magnitudes for the system. I plan to achieve this with Lomb-Scargle and Monte Carlo analysis in python.

Transformed Magnitudes of a Flare Star (EV Lac) - A Warning and Solutions

Kenneth Menzies and Gary Hawkins

Red Dwarf Group

The Red Dwarf Observing Group has monitored the Flares of EV Lacerta during the current 2025 observing season to determine its Flare Frequency and Energy Distribution. In order to generate accurate magnitudes in both the blue (B) and green (V) bandpasses, observing procedures were selected to provide transformed magnitudes based on careful selection of the reference star and/or imaging with multi-band filters. However, it became clear that the short duration of flares significantly impacts the accuracy of multi-band magnitude measurements due to difficulty balancing target magnitude, filter exposure, filter cadence, flare duration, and the need to match equivalent flare magnitudes in two bandpasses.

As expected, it was determined that careful selection of comparison star improves data consistency/accuracy from multiple observers, rapid measurement cadence improves the ability to track the rapid flare duration, and simultaneous color imaging can provide accurate transformed magnitudes. However, it was observed that filter image cadences such as BBBBV degrade magnitude accuracy due to the inability to match sampling frequency with flare duration. A comparison of B and V magnitudes of flare events indicates that single filter magnitudes may be used as accurate predictors of the second bandpass.

The AAVSO Smart Telescope Working Group: Re-Thinking the Stellar Photometry Workflow

Mark Munkascy

The AAVSO created a Smart Telescope Working Group last year to explore ways that the AAVSO can leverage the growing number of smart telescope owners with an interest in using their scopes to participate in real scientific discovery. The working group has been measuring photometric quality from smart telescope images using a new generation of software tools created by the group. Some of their findings have confirmed long-held rules of thumb for photometry with one-shot-color sensors, while other findings have been surprising. The working group has been able to identify error sources and reduce some types of error to the point where photometric accuracy images were shifted to Landolt standard fields to enable measuring the relatively small residual magnitude errors. Because smart telescope exposure times are often short (typically 10 seconds), many images are used to make individual photometric measurements; to reduce the AAVSO computing workload (and out-of-pocket cost), the working group developed a new standard file interface format (called the AAVSO Starlist) that reduces the information transfer from the smart telescope to AAVSO servers by two orders of magnitude compared to transferring FITS images. This talk explores some of these measurements, the AAVSO's motivation for rethinking how images are processed, and the emerging new architecture that will enable any smart telescope observer to contribute scientific data from anywhere in the world.

Initial Results from a Two-Month Spectroscopic Study of Deneb

Katelyn Osterhoudt, Jean Perkins, Daniel Cotton, and Derek L. Buzasi

Monterey Institute for Research in Astronomy [MIRA], Marina, CA

Deneb (A2 Ia) is the prototype of the alpha Cygni class of variable stars and has been the subject of many recent articles and discussions (Abt et al. 2023, Cotton et al. 2024, Guzik et al. 2023, 2024). In particular, the nature of both the abrupt photometric excursions on an interval of ~75 days, and the resumption of a quickly damped, high-amplitude 12-day photometric period about every 100 days, noted by Guzik et al. 2024, is still poorly understood.

At this meeting we present a preliminary analysis of a new spectroscopic dataset. For two months in the fall of 2024, we took twice-nightly, high-resolution (R~35,000) spectroscopic data of Deneb. We used the BACHES Echelle Spectrograph mounted to the 36-inch telescope at MIRA's Oliver Observing Station. The data were obtained concurrently with the sector 82 and 83 TESS observations of Deneb. Additionally, five-color, broadband linear polarization was measured at the same time.

We examine the radial velocity variations to look for variability correlated with the photometric and polarimetric variation and explore changes in the line profile of H-alpha over this period. Some small periodic variations over the data set are detected. A significant high-velocity absorption event, as was seen in the Richardson et al. 2011 data, does not appear to be present in our H-alpha data. We note a possible correlation between the polarimetric data and the emission in the H-alpha profile.

Waiting for T CrB: The Trials and Triumphs of an AAVSO Observer

Dr. Bert Pablo

AAVSO, Cambridge, Massachusetts

As the variable star community continues to hold its breath for the long-anticipated eruption of T Coronae Borealis, the AAVSO finds itself at the center of both excitement and endurance. This talk reflects on the past year's scientific highlights, a period marked by intense monitoring, data-driven collaboration, and the remarkable persistence of observers around the globe. From long-term photometric campaigns and cross-mission coordination to rapid-response alerts and community data analysis, our members have turned anticipation into opportunity. Along the way, new tools, new relationships, and new insights have emerged, reinforcing the AAVSO's vital role in bridging the professional and citizen-scientist communities. Despite its continued quiescence, "waiting for T CrB" has become emblematic of our community's uniqueness: Patience, precision, and passion in the face of an unpredictable universe.

Engaging Amateur Astronomers, Citizen Scientists, and Students in Astronomy Research at MIRA

Jean Perkins

Monterey Institute for Research in Astronomy, Marina, CA

The Monterey Institute for Research in Astronomy (MIRA) is a private, non-profit institute that has been dedicated to research and education in astronomy for more than 50 years. In this presentation I highlight several of the ways that students, volunteer citizen scientists, and amateur astronomers engage in research with our astronomers—with the results often leading to publications in astronomical journals.

Our thriving internship program offers high school and college students the unique opportunity to get hands-on experience through a variety of observational, theoretical, and instrumentation-based research projects over the summer months. These experiences are often cited as a major factor in their pursuit of STEM-focused careers. Recent projects include the design and fabrication of a new polarimeter, custom guiding software, and several observing based projects.

Citizen scientist volunteers and amateur astronomers with the aptitude and availability often contribute to projects that require longer completion times than available to summer students. Examples of the work being done by our volunteers include a data processing pipeline for echelle spectra, an analysis of Deneb's variability in spectroscopy, modeling of pulsations in red giant stars, and occultations by solar system bodies.

MIRA operates the Oliver Observing Station—home to our main 36-inch telescope and co-mounted 14-inch telescope—and the Weaver Student Observatory which hosts a second 14-inch telescope. The primary research areas of MIRA include stellar astronomy, comets and solar system bodies, instrumentation, and observational techniques.

The Starchive – A Needed Resource for the AAVSO Community

Angelle Tanner and Demitri Muna

Mississippi State University, Starkville, MS

Have you struggled to find all the data you need on a star or many stars only to resort to Wikipedia for physical parameters along with five to ten to fifty different references? There has got to be a better way! SIMBAD is useful for looking up stellar coordinates and some physical parameters, but it lacks versatility, ease of use and complete content. Over the past few years, I have been assembling data and developing the web application for a resource I call the Starchive. It currently contains over 50,000 stars and brown dwarfs, 430,000 fluxes and photometry, 236,000 coordinates, 1.6 million stellar, planet and disk parameters and 23,000 references. The straight-forward front-end is designed to be used by educators, amateurs, and professionals in any phase of their career. It has filter, single and list search functions. There are specific samples that can be queried including the nearest, brightest, and youngest stars; stars with planets; stars with disks; brown dwarfs and white dwarfs. When looking at a single star page, there are finder charts, an airmass chart, a spectral energy distribution with the photometry and a host of physical properties. High contrast images, spectra and time series can be accessed there too. When multiple stars are queried, the page contains a sortable, customizable, and downloadable table along with a set of different plotting tools in 2-D and 3-D. This has been a significant undertaking which will serve a menagerie of research programs. My poster will depict many of the features of the Starchive and I will be available for live demonstrations. I want this to be a resource the AAVSO community can use, so I'd love feedback on what features or content you'd like added to the Starchive!

A Low Noise Approach to Photometric Transformation Leading to the Potential Detection of 0.01 to 0.02 Magnitude Spots on EV Lac

Gary Walker

AAS, MMO, AAVSO

The Red Dwarf Group undertook a Project to investigate the Flare Star EV Lac. Considerable discussion on the benefits and compromises with Transforming one's data took place. The detection of low-level flares requires the data to be as high in precision as possible, while calculations of energy etc. require the data to be Transformed so that multiple observers' data can be combined for analysis. The author developed a method to Transform photometric data without the traditional increase in scatter—i.e., loss of precision. The data transformed with the new method is compared to other observers who transformed data with the traditional method. As a result of the Transformed Data, a 4.3-day period variation of 0.12 magnitudes in B is accurately resolved.